Interplay of Disorder and Transverse-Field Induced Quantum Fluctuations in the $LiHo_xY_{1-x}F_4$ Ising Magnetic Material

by

Seyed Mohiaddeen Ali Tabei

A thesis
presented to the University of Waterloo
in fulfilment of the
thesis requirement for the degree of
Doctor of Philosophy
in
Physics

Waterloo, Ontario, Canada, 2008

I hereby declare that I am the sole author of this thesis. This is a true copy of the thesis, including any required final revisions, as accepted by my examiners.

I understand that my thesis may be made electronically available to the public.

Abstract

The $LiHo_xY_{1-x}F_4$ magnetic material in a transverse magnetic field B_x perpendicular to the Ising spin direction has long been used to study tunable quantum phase transitions in pure and random disordered systems. We first present analytical and numerical evidences for the validity of an effective spin$\frac{1}{2}$ approach to the description of a general dipolar spin glass model with strong uniaxial Ising anisotropy and subject to weak B_x. We relate this toy model to the $LiHo_xY_{1-x}F_4$ transverse field Ising material. We show that an effective spin-$\frac{1}{2}$ model is able to capture both the qualitative and *quantitative* aspects of the physics at small B_x. After confirming the validity of the effective spin$\frac{1}{2}$ approach, we show that the field-induced magnetization along the $\hat{x}$ direction, combined with the local random dilution-induced destruction of crystalline mirror symmetries generates, via the predominant dipolar interactions between Ho^{3+} ions, *random fields* along the Ising $\hat{z}$ direction. This identifies $LiHo_xY_{1-x}F_4$ in B_x as a new random field Ising system. We show that the random fields explain the smearing of the nonlinear susceptibility at the spin glass transition with increasing B_x. In this thesis, we also investigate the phase diagram of non-diluted $LiHoF_4$ in the presence of B_x, by performing Monte-Carlo simulations. A previous quantum Monte Carlo (QMC) simulation found that even for small B_x where quantum fluctuations are small, close to the classical critical point, there is a discrepancy between experiment and the QMC results. We revisit this problem, focusing on weak B_x close to the classical Tc, using an alternative approach. For small B_x, by applying a so-called cumulant expansion, the quantum fluctuations around the classical T_c are taken into account perturbatively. We derived an effective perturbative classical Hamiltonian, on which MC simulations are performed. With this method we investigate different proposed sources of uncertainty which can affect the numerical results. We fully reproduce the previous QMC results at small B_x. Unfortunately, we find that none of the modifications to the microscopic Hamiltonian that we explore are able to provide a $B_x - T$ phase diagram compatible with the experiments in the small semi-classical B_x regime.

Acknowledgements

I would like to take this opportunity to express my extreme gratitude to my supervisor Prof. Michel Gingras, who has been a very good friend, an excellent advisor and with whom it has been a pleasure and privilege to work. I would like to thank him for his excellent advice and free donation of his time. My research was greatly improved by the high standards with which he conducts his own work.

I would like to acknowledge my Ph.D. advisory committee Prof. Tom Devereaux, Prof. Rob Hill, Prof. Holger Kleinke, and Prof. Robert Mann for their useful suggestions and comments during my study at Waterloo. Also, I would like to thank Prof. Manjeri Anantram, Prof. Karin Dahmen, and Prof. Roger Melko, who accepted to be my Ph.D examiners and read my thesis.

During my PhD, I had the great opportunity to collaborate with J.-Y. Fortin, Ying-Jer Kao, Pawel Stasiak, François Vernay, and Taras Yavorskyy.

I enjoyed many discussions with the other members of the condensed matter theory group Prof. Anton Burkov, J.-Y. Delannoy, Tom Fennell, Mahmoud Ghaznavi, Steve Johnston, Paul McClarty, Hamid Molavian, Mohammad Moraghebi, Sattar Taheri, Kam-Ming Tam and, Martin Weigel.

I would like to acknowledge Vadim Oganesyan, and Jeffrey Quilliam for very useful discussions. Specially, Jeffrey, who made many valuable comments on the manuscript. I would also like to thank Brad Moores, Robert Schaffer and Mischa Thesberg for helping me with the grammar.

I would like to acknowledge my beloved parents, for their endless love and support, without which I would not have succeeded. I am forever indebted to them.

At last, but not the least, I would like to appreciate my wife, Faezeh, for her support and patience and my daughter, Sana, for making home a place full of joy and happiness.

Dedication

To my dear wife Faezeh.

Contents

List of Figures

List of Tables

Chapter 1

Introduction

The study of magnetism and magnetic materials has allowed physicists to profoundly develop our understanding of the collective behaviour of systems with many interacting degrees of freedom. To understand how the interactions between a very large number of individual microscopic degrees of freedom lead to the fascinating macroscopic behaviours observed in magnetic materials is one of the major theoretical challenges faced by the community. To theoretically study these magnetic systems, after identifying the most relevant physics, one can construct an abstract theoretical model that hopefully captures the essential features of the properties of the real magnetic materials. The advantage of this approach is that the insights obtained from such a generic model may apply to whole classes of materials rather than just a specific material.

Early theoretical works, aiming to address the general collective behaviour of magnetic materials, concentrated on classical models, and assumed the system to be pure and perfect. However, in the real world, such an ideal situation does not exist. Most materials contain a certain amount of frozen (quenched) random disorder[1] such as impurities or vacancies. Some strongly disordered systems (i.e. spin glasses) have competing interactions which lead to random frustration[2]. The question of how quenched disorder influences phase transitions and critical points is

[1] In statistical physics, a system is said to present quenched disorder when some parameters defining its behaviour are random variables which do not evolve with time.

[2] In a physical system with competing interactions, frustration occurs when all the interactions

conceptually very interesting and of fundamental importance. Most early studies of spin glass systems and other systems with strong disorder were performed in the regime where the quantum mechanical nature of the microscopic degrees of freedom was neglected. Later on, it turned out that when only a classical framework is considered to describe disordered systems, then the understanding of the experimental behaviour of some realistic disordered systems becomes problematic. The physics becomes more interesting and complicated when quantum fluctuations come into play. The interplay between disorder and quantum mechanics can lead to behaviour which is qualitatively distinct from the clean situation. The physics becomes even more interesting when one goes to very low temperatures, where thermal fluctuations are weak and the system overcomes energy barriers by the aid of quantum tunnelling.

In the last 30 years, there has been a large effort to produce simplified theoretical models in order to capture the physics of realistic disordered systems. However, a large number of interesting disordered quantum systems, such as high-temperature superconductors, are rather complex. Therefore, it is desirable to identify a real system with a well defined Hamiltonian, in which disorder and quantum fluctuations are tunable in a simple manner. In this thesis, we focus on a quantum magnetic material, $LiHo_xY_{1-x}F_4$. This material, because of the quite simple form of its Hamiltonian, is one of those desired systems which is the host to a wide variety of collective quantum effects. For example, for $x = 1$, when an external magnetic field B_x is applied transverse (perpendicular) to the crystallographic Ising $c-$axis direction $LiHoF_4$ becomes one of the rare physical realizations [1] of the transverse field Ising model (TFIM) [2, 3, 4, 5, 6], where quantum fluctuations are tunable via the external magnetic field. This material is such that one is able to investigate the influence of thermal and quantum fluctuations in a single physical system. On the other hand, in the absence of an external field, the system can be recast as a diluted dipolar Ising model with the low-temperature phase being either a ferromagnet or a spin glass depending on the concentration x of magnetic ions [7, 8, 9]. Therefore, when an external transverse magnetic field is turned on, this material potentially can help us to establish a quantitative understanding of the interplay of

among its degrees of freedom are not fully satisfied.

quenched random disorder and quantum fluctuations in a system, especially when we are at relatively very low temperatures (close to $T = 0$). There are a number of puzzling experimental observations pertaining to $LiHo_xY_{1-x}F_4$, for which the physics is not well understood yet. Later on in this chapter (see Section 1.4), we will briefly discuss some of these paradoxical experimental results of $LiHo_xY_{1-x}F_4$. This thesis addresses theoretically some of the mysterious behaviours of this insulating magnetic material, hoping to shed light on the underlying physics and provide a better understanding of this system.

Prior to a review of the physics of the real material $LiHo_xY_{1-x}F_4$, it will prove useful as background to have a short introduction to some of the theoretical models which have been developed to study quantum magnetic materials and disordered magnetic materials. In this chapter, the theoretical models, which are discussed in the following sections, are useful for our later discussions related to the real material $LiHo_xY_{1-x}F_4$ depending on the concentration x and depending on whether it is subject to an external magnetic field B_x or not. These models and some of the related techniques and methods used to study these models are fruitfully applied to the theoretical studies we perform in this thesis.

In this chapter, in Section 1.1, we give a brief introduction to the transverse field Ising model (TFIM), which is the simplest theoretical model exhibiting a quantum phase transition. It has generally been believed that pure $LiHoF_4$ with an applied external B_x is an ideal host for this model. Then, we make a simple mean field study of this model. As we discussed above, diluting $LiHo_xY_{1-x}F_4$ enough drives the system into a spin glass phase. Quantum fluctuations can be induced via an external B_x. Therefore, in Section 1.2, we introduce the classical and quantum Ising spin glass models as the simplest models to study spin glass systems without and with quantum fluctuations, respectively. In Section 1.3, we introduce yet another class of interesting class of disordered materials known as the random field Ising model. The motivation behind introducing this model will be more apparent when we discuss in Chapter 3 the possibility that random fields may be effectively induced by an external B_x in diluted $LiHo_xY_{1-x}F_4$. After the theoretical background of Section 1.4, we give a brief review of some of the interesting phenomena observed in the real $LiHo_xY_{1-x}F_4$ material. In Section 1.5, we give an overall outline of the

rest of this thesis.

1.1 Transverse Field Ising Model

As we mentioned earlier, and it will be discussed in more detail later (see Section 1.4), $LiHoF_4$ with an applied external B_x is quite well explained by a transverse field Ising model (TFIM)[3], in which the pair-wise interactions are long-range dipole-dipole interactions. This motivates us to start with an introduction to the simple transverse field Ising model.

Phase transitions into a highly fluctuating disordered phase are most commonly driven by thermal fluctuations. However, near absolute zero temperature, a system can, via *quantum* fluctuations associated with the Heisenberg uncertainty principle, undergo a quantum phase transition (QPT) [4, 10]. Quantum phase transitions can differ fundamentally from their classical counterparts because of the large influence of the dynamics on the static critical behaviour at zero temperature. In other words, at $T = 0$, a phase transition occurs by a transition of the ground state to another state via, i.e, level crossing. Such transitions, in the absence of thermal fluctuations, are governed by varying a non thermal controllable parameter (i.e magnetic field, pressure, etc.). Naively speaking, considering for example the $\Delta E \Delta t \approx \hbar$ version of the Heisenberg uncertainty principle, quantum mechanics can admix the dynamics with statics. Approaching the phase transition where level crossing between the ground states occur, we will have $\Delta E \to 0$ for the energy gap between the states. Therefore we will have a diverging time scale ($\Delta t \to 0$). During this characteristic time scale, there will be correlation between events. This diverging time scale can be considered as adding an additional effective dimension (*imaginary time* dimension) to the existing spatial dimension. Hence, each microscopic degree of freedom is correlated with itself during the diverging time scale [4].

The transverse field Ising model (TFIM), first proposed by de Gennes to describe proton tunneling in ferroelectric systems [2], is perhaps the simplest model that

[3]In Chapter 3, it is shown that at low energies the Hamiltonian of $LiHoF_4$ is approximately mapped to an effective spin-$\frac{1}{2}$ TFIM.

exhibits a QPT [3, 4, 5]. The Hamiltonian of the TFIM is given by

$$H_{\rm TFIM} = -\frac{1}{2}\sum_{i,j} J_{ij}\sigma_i^z\sigma_j^z - \Gamma\sum_i \sigma_i^x \ , \tag{1.1}$$

where σ_i^μ ($\mu = x, y, z$) are the Pauli matrices. The Pauli spin matrix, σ^z, has two eigenvalues (± 1), which denotes that if the expectation value of the $\hat{z}$-projection of the spin is aligned either along the $\hat{z}$ direction or along the opposite direction, respectively. The eigenstate corresponding to eigenvalue ($+1$) is symbolically denoted by $|\uparrow\rangle$, while that corresponding to (-1) is denoted by $|\downarrow\rangle$. By taking these two eigenvectors as a basis, the Pauli matrices have the following representation

$$\sigma^x = \begin{pmatrix} 0 & 1 \\ 1 & 0 \end{pmatrix}, \ \sigma^y = \begin{pmatrix} 0 & -i \\ i & 0 \end{pmatrix}, \ \sigma^z = \begin{pmatrix} 1 & 0 \\ 0 & -1 \end{pmatrix}.$$

The Pauli matrices satisfy the commutation relation[4]

$$[\sigma_i^\alpha, \sigma_j^\beta] = 2i\delta_{ij}\epsilon_{\alpha\beta\gamma}\sigma_i^\gamma \ ,$$

where i and j denote the position of the spins and α, β, γ indicate a permutation of x, y, z. δ_{ij} is the Kronecker delta and $\epsilon_{\alpha\beta\gamma}$ is the Levi-Civita fully antisymmetric tensor. Since σ_i^x and σ_i^z do not commute, a nonzero field Γ, transverse to the Ising $\hat{z}$ direction, causes quantum tunneling between the spin-up and spin-down eigenstates of σ_i^z, hence causing quantum spin fluctuations. These fluctuations decrease the critical temperature T_c at which the spins develop long-range order. In the simplest scenario, where $J_{ij} > 0$, the ordered phase is ferromagnetic [3, 5]. As it is schematically shown in Fig. 1.1.1, at a critical field Γ_c, T_c vanishes and a quantum phase transition between the quantum paramagnet (PM) and a long-range ordered ferromagnetic state occurs. Via a Trotter-Suzuki transformation [11], the partition function of the transverse field Ising model in d space dimensions is equivalent to that of a classical Ising model in $d+1$ space dimensions [11] with imaginary time playing the role of the extra dimension (In Appendix A we derive the equivalent $d+1$ dimension classical Hamiltonian for a TFIM.). Therefore, to

[4]The Pauli matrices σ^x, σ^y and σ^z with the Identity operator $\sigma^0 = \begin{pmatrix} 1 & 0 \\ 0 & 1 \end{pmatrix}$ form a group. Therefore, any 2×2 matrix can be written as a linear superposition of σ^x, σ^y, σ^z, and σ^0.

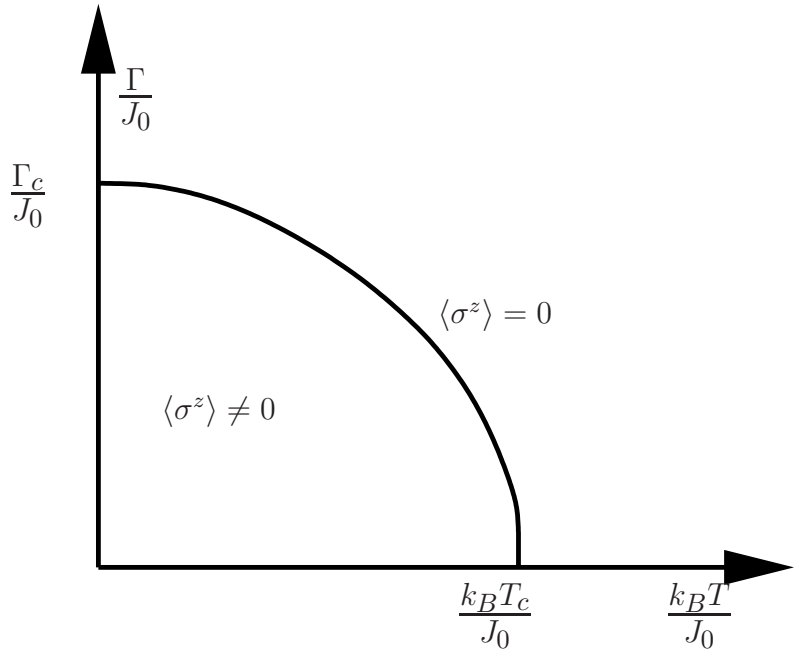

Figure 1.1: Schematic mean field phase diagram of a simple TFIM.

study quantum phase transitions of the d-dimensional, disorder-free transverse-field Ising model, one can study the equivalent $d+1$ dimensional classical Ising model. In the following subsection, we will use a simple mean field framework to show that for the TFIM, the quantum fluctuations induced by the transverse field reduce the paramagnetic to ferromagnetic phase transition temperature. Subsequently, within the same mean field framework, we will see that at $T = 0$ there exists a finite Γ_c, such that for $\Gamma > \Gamma_c$ collective ferromagnetic order disappears.

1.1.1 Mean Field Theory for the TFIM

The standard mean field approximation can be extended to study the TFIM of Eq. (1.1) at non-zero temperature. Writing $\sigma_i^z = \langle\sigma_i^z\rangle + (\sigma_i^z - \langle\sigma_i^z\rangle)$ and using the mean field approximation ansatz, which neglects the fluctuation term $(\sigma_i^z - \langle\sigma_i^z\rangle)(\sigma_j^z - \langle\sigma_j^z\rangle) \approx 0$, the TFIM Hamiltonian is approximated as

$$H_{\text{TFIM}} \approx -\frac{1}{2}\sum_{i,j} J_{ij}\langle\sigma_i^z\rangle\langle\sigma_j^z\rangle - \sum_i \left(h_i^x\sigma_i^x + h_i^z\sigma_i^z\right) \ , \tag{1.2}$$

where $h_i^x = \Gamma$ is a local transverse field and $h_i^z = \left(\frac{1}{2}\sum_j J_{ij}\langle\sigma_j^z\rangle\right)$ is a local longitudinal mean field, which interacts with each spin at site i. Therefore, the mean field partition function reads

$$Z_{\rm MF} = \mathcal{C}\prod_i \mathbf{Tr}\exp\left[\beta\left(h_i^x\sigma_i^x + h_i^z\sigma_i^z\right)\right] \ , \tag{1.3}$$

where $\beta = 1/k_BT$ and $\mathcal{C} = \exp\left[\frac{1}{2}\beta\sum_{i,j} J_{ij}\langle\sigma_i^z\rangle\langle\sigma_j^z\rangle\right]$. If $\lambda_\pm^i = \pm|\mathbf{h}_i|$ denote the eigenvalues of the 2×2 matrix

$$h_i^x\sigma_i^x + h_i^z\sigma_i^z = \begin{pmatrix} h_i^z & h_i^x \\ h_i^x & -h_i^z \end{pmatrix} \ , \tag{1.4}$$

then, $Z_{\rm MF}$ reads

$$Z_{\rm MF} = \mathcal{C}\prod_i \left(e^{+|\mathbf{h}_i|} + e^{-|\mathbf{h}_i|}\right) = \mathcal{C}\prod_i \left[2\cosh\left(\beta|\mathbf{h}_i|\right)\right] \ , \tag{1.5}$$

where $|\mathbf{h}_i| = \sqrt{(h_i^x)^2 + (h_i^z)^2}$. For a non-random case, where the system is translationally invariant, $|\mathbf{h_i}|$ is replaced by $|\mathbf{h}| = \sqrt{\Gamma^2 + (J_0\langle\sigma^z\rangle)^2}$, where $J_0 = \sum_j J_{ij}$. Therefore the mean field equation for $\langle\sigma^z\rangle$ and $\langle\sigma^x\rangle$ reads

$$\langle\sigma^z\rangle = \left(\frac{J_0\langle\sigma^z\rangle}{|\mathbf{h}|}\right)[\tanh(\beta|\mathbf{h}|)], \qquad \langle\sigma^x\rangle = \frac{\Gamma}{|\mathbf{h}|}[\tanh(\beta|\mathbf{h}|)]. \tag{1.6}$$

Equation (1.6) is the self-consistency equation needed to obtain the order parameter $\langle\sigma^z\rangle$ at any temperature T and transverse field Γ. Clearly, the order-disorder transition is tuned both by Γ and T (see Fig. 1.1.1). For $\Gamma = 0$, where the transition is driven by T

$$\langle\sigma^z\rangle = \tanh\left(\frac{J_0\langle\sigma^z\rangle}{k_BT}\right) \quad \text{and} \quad \langle\sigma^x\rangle = 0 \ . \tag{1.7}$$

This equation has a nontrivial solution only if $k_BT < J_0$, i.e.,

$$\begin{aligned} \langle\sigma^z\rangle &\neq 0 \qquad \text{for} \quad k_BT < J_0 \\ \langle\sigma^z\rangle &= 0 \qquad \text{for} \quad k_BT > J_0 \ . \end{aligned} \tag{1.8}$$

Therefore, there is a critical temperature $T_c = J_0$ above which, there is no order and the system is in the paramagnetic phase. When $k_BT \to 0$, the transition is driven by Γ, which implies

$$\langle\sigma^z\rangle = \frac{J_0\langle\sigma^z\rangle}{\sqrt{(\Gamma)^2 + (J_0\langle\sigma^z\rangle)^2}} \qquad \left(\text{since,} \quad \tanh x\Big|_{x\to\infty} = 1\right). \tag{1.9}$$

From this equation we easily find that in the limit $\frac{\Gamma}{J_0} \to 1$, the only real nontrivial solution is

$$\langle\sigma^z\rangle \to 0$$

and

$$\langle\sigma^x\rangle = \frac{\Gamma}{\sqrt{(\Gamma)^2 + (J_0\langle\sigma^z\rangle)^2}} \to 1, \qquad \text{as} \quad \frac{\Gamma}{J_0} \to 1.$$

Thus, we see that there is a critical transverse field $\Gamma_c = J_0$ ($\Gamma_c = zJ$ for nearest neighbor interactions) such that for any $\Gamma > \Gamma_c$ there is no ferromagnetic order ($\langle\sigma^z\rangle = 0$) even at zero temperature. In general one sees that for any temperature $T < T_c$, there exists some transverse field Γ_c at which the transition from the ferromagnetic ordered state ($\langle\sigma^z\rangle \neq 0$) to the paramagnetic state ($\langle\sigma^z\rangle = 0$) occurs. The equation for the phase boundary in the $(\Gamma - T)$ - plane is obtained by putting $\langle\sigma^z\rangle \to 0$ in Eq. (1.6). The equation gives a relation between Γ_c and T_c as follows:

$$\tanh\left(\frac{\Gamma_c}{k_BT}\right) = \frac{\Gamma_c}{J_0}. \tag{1.10}$$

One may note that for the ferromagnetic phase, since $\langle\sigma^z\rangle \neq 0$,

$$\frac{1}{|\mathbf{h}|}\tanh(\beta|\mathbf{h}|) = \frac{1}{J_0} = \text{Constant}.$$

Hence, independent of temperature in the ferromagnetic phase, the $\hat{x}$ component of the average/static moment $\langle\sigma^x\rangle$ is $\langle\sigma^x\rangle = \frac{\Gamma}{|\mathbf{h}|}\tanh(\beta|\mathbf{h}|) = \frac{\Gamma}{J_0}$. While for the paramagnetic phase, since $\langle\sigma^z\rangle = 0$, $\langle\sigma^x\rangle = \tanh(\beta\Gamma)$. In this section we saw that a tunable transverse field induces quantum fluctuations and how the simple TFIM toy model exhibits a quantum phase transition. In Section 1.4, we see that $LiHoF_4$ with an applied transverse field maps onto a TFIM. The simple Ising model and TFIM are simple abstract models introduced to capture some of the general collective characteristics of clean (dilution free) classical and quantum magnetic systems. In the next Sections 1.2 and 1.3, the Ising model and the TFIM are generalized such that they model simple systems with quenched disorder and random interactions.

1.2 Spin Glasses

In the real world, no pure, perfect and disorder free system exists. One of the theoretical and experimental challenges in the study of magnetic systems is to understand the physics of quenched disorder and random interactions in magnetic systems. In $LiHo_xY_{1-x}F_4$, which is the material on which we focus in this thesis, the effect of random disorder can be studied by randomly substituting a fraction $1-x$ of the magnetic Ho^{3+} ions by nonmagnetic Y^{3+} ions. It is expected that, if the system is diluted enough, the system will be a spin glass. As we discussed earlier, one of the aims of this chapter is to introduce several of the theoretical models that seem to be useful in benchmarking some of the physics pertaining to $LiHo_xY_{1-x}F_4$.

In the previous section, motivated by pure $LiHoF_4$ with an applied external magnetic field B_x, we looked at the TFIM. Now, in this section, inspired by diluted $LiHo_xY_{1-x}F_4$ with/without an external B_x, we introduce a generalized variation of the classical Ising model and the quantum TFIM which incorporates random interactions. In this generalization, the J_{ij}'s in Eq. (1.1) are considered to be quenched (frozen) random interactions. Competing ferromagnetic $J_{ij} > 0$ and antiferromagnetic $J_{ij} < 0$ couplings generate random frustration (see Fig. 1.2). For a three dimensional case, the system freezes into an (Ising) spin glass state at a spin glass critical temperature T_g [12, 13]. Similarly to the simple TFIM in Eq. (1.1) in the presence of $\Gamma \neq 0$, $T_g(\Gamma)$ decreases as Γ is increased until at $\Gamma = \Gamma_c$, a quantum phase transition between a quantum paramagnet and a spin glass phase occurs.

In this section, we first have a look at spin glass phenomena and then review some of the models and methods developed to study classical Ising spin glasses. In a separate subsection, we discuss the magnetic nonlinear susceptibility as a general experimental probe for determining spin glass transition temperatures. Also, in analogy with $LiHo_xY_{1-x}F_4$ with an applied B_x, we look through the topic of quantum spin glasses, particularly the Ising spin glass model with a transverse field as a prototype of a quantum spin glass.

1.2.1 General Overview

Spin glasses were first studied in dilute magnetic alloys *Au*Fe, *Ag*Mn and *Cu*Mn. In these systems, the magnetic impurities are coupled via the Ruderman-Kittel-Kasuya-Yosida (RKKY) interaction [14, 15, 16] $J(r_{ij}) \propto \cos(2k_F r_{ij})/r_{ij}^3$, where k_F is the Fermi wave vector and r_{ij} is the spatial distance between two magnetic impurities positioned at i and j. Since the polarization is oscillating spatially, the coupling between two randomly positioned impurities is random, and may be positive or negative, resulting in competing interactions. A number of unusual behaviour were observed in these materials. For example, in the measurement of the AC susceptibility as a function of temperature, a cusp is observed in the magnetic susceptibility. What is unusual about the susceptibility is that it strongly depends on the frequency f at which it is measured [17]. The cusp appears at a temperature $T_g(f)$, and moves to lower temperatures as the frequency is lowered. As another example, these materials also exhibit significant remanence effects in their magnetization and susceptibility below T_g. Very different values of the static susceptibility will be measured if the sample is field cooled or zero-field cooled even for very small magnetic fields [18][5]. These experiments along with a series of other experimental evidence are consistent with a scenario in which the spins in the material enter a *"frozen"* state with very slow dynamics. The same generic experimental features are also observed for the insulating magnet $Eu_xSr_{1-x}S$, which was discovered to behave as a spin glass for certain values of x [19]. The exchange interaction between the magnetic Eu ions are ferromagnetic between nearest neighbors and antiferromagnetic between next-nearest neighbors. When the Eu moments are sufficiently diluted, because of randomness and frustration, the system becomes a spin glass. The fact that this very different type of magnet also demonstrates spin glass behaviour indicates that there is some degree of universality in these materials which have been named "*spin glass*" materials.

Generally spin glasses are random magnetic systems, with competing (frus-

[5]In susceptibility measurements, if a longitudinal magnetic field is applied when the system is above T_g and the system in this field is subsequently cooled down below T_g the measurement is a so called "field-cooled" measurement. In contrary, "zero-field-cooled" susceptibility is obtained after cooling down the system in zero field, below T_g.

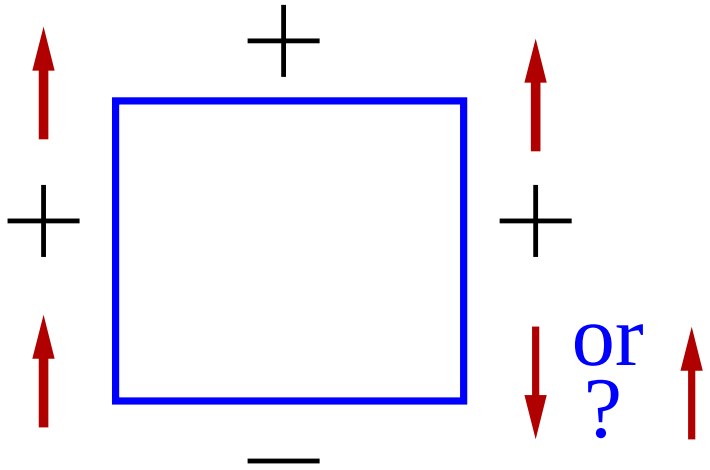

Figure 1.2: A simple illustration of frustration. If the interaction on the bond is "+" (ferromagnetic), the spins tend to be parallel and if the interaction on the bond is " - " (antiferromagnetic), the spins tend to be antiparallel. Such condition can not lead to a simultaneous satisfaction of all the bonds. Therefore, there is *frustration* in the system.

trated) interactions. Here, frustration in the context of spin glasses, arises due to the competition between ferromagnetic and antiferromagnetic quenched random interactions. Therefore, it is not possible for the spins to energetically satisfy every bond associated with them simultaneously. Fig. 1.2 simply illustrates an example of such competitions. In the spin glass phase, frustration and the random interactions introduce large energy barriers between states that are closely spaced in energy. This leads to very long relaxation times and the occurrence of spontaneous cooperative freezing of the (random) spin orientations.

An important concept required for understanding measurements of systems which equilibrate slowly is that of ergodicity. If the time scale for an experiment is much longer than any relaxation time, then the system explores all regions of phase space with its equilibrium probability. In this case, the time average of a physical quantity corresponds to the statistical average of the same quantity. However, in a spin glass phase there are very long relaxation times, and on any time-scale only some portion of the phase space will be sampled. Hence the glassy state is non-

ergodic, so that time averages and thermodynamic averages may not be identical due to the system spending large amounts of time in metastable states.

As we briefly discussed, spin glass materials possess a class of generic characteristics which are in common in all these disordered systems, no matter what the precise underlying microscopic disordered interactions among the spins. Therefore, studying a simple toy model which possesses the generic character of spin glasses (frustration and random interactions), can be useful in understanding spin glass materials better. In the next subsection, we introduce the Edwards Anderson model as one of those generic toy models.

1.2.2 Classical Ising Spin-Glass model (Γ=0)

The Edward-Anderson (EA) model [20]

$$H_{\rm EA} = -\frac{1}{2}\sum_{i,j} J_{ij}\sigma_i^z\sigma_j^z - h\sum_i \sigma_i^z \ , \tag{1.11}$$

is perhaps the simplest model that features random disorder and frustration. Here h denotes a longitudinal external field in the $\hat{z}$ direction of the Ising spins. J_{ij} couplings are independent random variables with a symmetric distribution such that $[J_{ij}]_{\rm av} = 0$ and $[J_{ij}^2]_{\rm av}^{1/2} = J$, where $[\cdots]_{\rm av}$ means an average over the disorder. To be more precise, for example, if $\{J_{ij}\}$ denotes a specific realization of random variables and $P(\{J_{ij}\})$ stands for the probability of that specific realization then the disorder average of a general quantity $A(\{J_{ij}\})$ reads

$$[A(\{J_{ij}\})]_{\rm av} = \sum_{\{J_{ij}\}} P(\{J_{ij}\})A(\{J_{ij}\}) \ . \tag{1.12}$$

In a spin glass phase, because of the frozen random direction of the spins, the magnetization

$$m_z = [\langle\sigma_i^z\rangle]_{\rm av} \tag{1.13}$$

is zero and obviously is not a suitable order parameter. One choice of order parameter which distinguishes between a paramagnetic phase and spin glass (frozen

configuration) phase is the Edwards-Anderson order parameter defined as

$$q \equiv \left[\langle \sigma_i^z \rangle^2\right]_{\text{av}} \ . \tag{1.14}$$

Despite the simple form of the EA model, it is not an easy model to solve exactly. Sherrington and Kirkpatrick [21] proposed that the mean field theory of spin glasses should be the exact solution of an infinite-range version of the EA model in which the distribution of the J_{ij} is the same for all distinct pairs i and j. The distribution is considered to be Gaussian $P(J_{ij}) \propto \exp\left[-NJ_{ij}^2/J^2\right]$, where $[J_{ij}]_{\text{av}} = 0$ and $[J_{ij}^2]_{\text{av}} = J^2/N$. The variance of the distribution is scaled by the number of spins N, such that at a fixed temperature the total free energy scales with N and the free energy density is independent of N.

For a specific configuration of random variables $\{J_{ij}\}$ the partition function $Z\{J_{ij}\}$ can be evaluated. To calculate thermodynamical quantities properly one should average over extensive quantities such as the free energy density $[f\{J_{ij}\}]_{\text{av}}$, where $Z\{J_{ij}\} = \exp\left(-N\beta f\{J_{ij}\}\right)$. In this case the free energy density will be

$$f = [f\{J_{ij}\}]_{\text{av}} = -\frac{k_B T}{N}[\ln Z\{J_{ij}\}]_{\text{av}}, \tag{1.15}$$

which in practice is difficult to calculate[6]. If we consider a large system and divide it into n macroscopic subsystems (replicas) with different configurations and assume that the coupling between the subsystems is negligible, then it can be argued that the average of the extensive quantity of each replica should be equal to the average over the whole system. The idea of the replica trick is based on the use of the exact relation

$$[\ln Z\{J_{ij}\}]_{\text{av}} = \lim_{n\to 0}\frac{1}{n}\left([Z^n\{J_{ij}\}]_{\text{av}} - 1\right) = \lim_{n\to 0}\frac{\partial}{\partial n}[Z^n\{J_{ij}\}]_{\text{av}} \ , \tag{1.16}$$

[6]For example, to calculate $f = -\frac{k_B T}{N}\sum_{\{J_{ij}\}} P(\{J_{ij}\})\ln Z[\{J_{ij}\}]$, before averaging over the quenched disorder variables $\{J_{ij}\}$, we need to calculate the logarithm of the partition function for each specific configuration of $\{J_{ij}\}$ quenched variables. But the specific $\{J_{ij}\}$'s are not known a priori. Knowing the distribution function $P(\{J_{ij}\})$, one can overcome this difficulty, if there is a way to integrate out the disorder before tracing out the different configurations of the microscopic degrees of freedom (i.e. the configuration of spin variables $\{\sigma_1, \sigma_2, \cdots, \sigma_N\}$ in a spin system). The replica trick provides us with a way to overcome this difficulty.

where we used the identity as $n \to 0$, $Z^n = \exp(n \ln Z) \approx 1 + n \ln Z$. Now, momentarily, if we assume that n is a positive integer, we can say that we have made n copies (*replicas*) of the system and we can express $Z^n \{J_{ij}\}$ as the partition function of a larger system consisting of n replicas of the original system. If $H[\{\sigma_i\}, \{J_{ij}\}]$ denote the Hamiltonian of the original system with a specific configuration of N spins $\{\sigma_i\}$ (the microscopic thermodynamical variables) and a specific configuration of quenched random variables $\{J_{ij}\}$, then

$$\begin{aligned} Z^n &= \left[\mathbf{Tr}_{\{\sigma_i\}} \exp\left\{-\beta H\left[\{\sigma_i\}, \{J_{ij}\}\right]\right\}\right]^n \\ &= \mathbf{Tr}_{\left\{\sigma_i^1\right\}} \mathbf{Tr}_{\left\{\sigma_i^2\right\}} \cdots \mathbf{Tr}_{\left\{\sigma_i^n\right\}} \exp\left\{-\beta \sum_{\alpha=1}^{n} H\left[\{\sigma_i^\alpha\}, \{J_{ij}\}\right]\right\} , \end{aligned} \quad (1.17)$$

where $H[\{\sigma_i^\alpha\}, \{J_{ij}\}]$ is the Hamiltonian of the α-th replica. Employing this trick, for example for the EA model, we can average over the $\{J_{ij}\}$ before tracing over a set of N spins with n components, where each component specifies one of the replicas. After solving the problem by whatever tool which can be implemented, we have to restore the $n \to 0$ limit in the final result.

Sherrington and Kirkpatrick [21], in order to find a mean-field solution for their proposed infinite range model, assumed that the replicated system has replica symmetry, which means that the total replicated system is invariant under permutations of replicas. If n is an integer number this assumption is correct. However, in the case that n is real and $n \to 0$ it is not obvious that if the replica symmetry assumption is still valid. One can use the replica trick and the replica symmetry assumption to calculate the EA order parameter

$$q = \left[\langle \sigma_i^z \rangle^2\right]_{\text{av}} = \left[\frac{\left[\mathbf{Tr}\sigma_i^z \exp\left\{-\beta H\left[\{\sigma_i\}, \{J_{ij}\}\right]\right\}\right]\left[\mathbf{Tr}\sigma_i^z \exp\left\{-\beta H\left[\{\sigma_i\}, \{J_{ij}\}\right]\right\}\right]}{Z^2}\right]_{\text{av}} . \quad (1.18)$$

Multiplying the numerator and the denominator in Z^{n-2}, and letting $n \to 0$, we obtain

$$q = \left\langle \sigma_i^{z\alpha} \sigma_i^{z\beta} \right\rangle \quad (1.19)$$

for the order parameter q, where α and β correspond to different replicas. The replica symmetry assumption says that q should not depend on the choice of α and β. Sherrington and Kirkpatrick [21] in their mean-field replica symmetric solution,

as an ansatz, before applying the $n \to 0$ limit, use the replica symmetry ansatz ($q^{\alpha\beta}$ independent of α and β). Under this assumption, the mean-field solution shows a phase transition at temperature $T_g = J$, where below T_g the order parameter q has a nonzero value.

However, the mean-field replica symmetric model fails to describe the low temperature behaviour correctly (i.e. at low temperature the entropy becomes negative). Subsequently, Almeida and Thouless [22] analyzed the stability of the replica symmetric solution of the classical Sherrington-Kirkpatrick (SK) model as a function of temperature and the external field h . They found that in the temperature-external field plane, the mean-field replica symmetric solution is only stable above a so-called AT line, and for the values of T and h below this line the replica symmetric solution is not stable. Thus, the replica symmetric assumption is not valid below the AT line. As we previously discussed, it is not obvious that when n is real and $n \to 0$, then the assumption that the system is invariant under the permutation of the replicas, is still valid. Parisi [23] assumed that the permutation symmetry of the replicas is spontaneously broken in the spin glass phase below the AT line and instead of a single q, there is a distribution $P(q)$ in the spin glass phase.

Later, in this thesis (Chapter 5), in the context of diluted $LiHo_xY_{1-x}F_4$ with an applied B_x in the spin glass phase, for a variant of a generalized Sherrington and Kirkpatrick model with a transverse field and a random longitudinal field, we shall perform a mean field calculation and obtain the stability criteria of our mean field solution, where the replica symmetry assumption is valid.

Droplet Picture

In this subsection, we introduce another framework developed to study spin glasses which is based on phenomenological scaling arguments, known as the *"droplet picture"*. The droplet picture is another well known paradigm on spin glasses. The droplet picture competes with the replica symmetry breaking picture and produces quite different conclusions for a number of quantities. One reason for mentioning the droplet picture here, is that in this thesis, we discuss a phenomenological scaling approach using droplet picture arguments, which was applied [24, 25] in a

recent work to study the evolution of domains with spin glass order in the context of diluted $LiHo_xY_{1-x}F_4$ with an applied B_x.

As discussed in the previous section, even though mean-field models of spin glasses have proved very useful in the understanding of glassy phenomena, they are constructed in the limit of infinite dimensions. To compare with real glasses, it would be useful to have an understanding of what happens in lower physically relevant dimensions, such as three. A phenomenological approach to the finite dimensional problem was developed by McMillan [26], Bray and Moore [27], and Fisher and Huse [28, 29, 30]. A key difference between their approach and the replica symmetry breaking scenario is that their scaling theory assumes that the phase transition is "somewhat" as trivial as in a ferromagnet. Instead of the multiplicity of ground states found in mean-field theory, there are only two ground states, which are related by a global spin flip. The droplet approach is based on an ansatz for the scaling of low-energy large-scale droplet excitations in the system. By droplet excitation, we mean a compact domain, in which the spins within the domain are flipped. The droplet has a typical size of L in d dimensions. It is assumed that the low-energy excitations that dominate long distance and long time correlations are clusters or droplets of coherently flipped spins. The density of states of the droplets is assumed to scale as $\rho_{\text{droplets}}(E) \sim L^{-\theta}$, where θ is a scaling exponent, with $0 < \theta < (d-1)/2$ [28, 29, 30]. The barriers to activation of the droplets are assumed to scale as L^{ψ} . These barriers correspond to the energy required to flip the spins in a domain wall between the two ground states. The domain walls are assumed to have a non-trivial fractal dimension $d_s > d-1$. The scaling and fractal dimensions are not determined a priori but need to be determined from computer simulations or other types of numerical approaches.

Nonlinear Susceptibility

For magnetic systems, one of the methods commonly used to observe a phase transition from an ordered ferromagnetic phase to a disordered paramagnetic phase is to measure the linear susceptibility. The linear response of the magnetization to a small external field diverges as one approaches temperatures close to the ferromagnet transition temperature. This can be understood by the connection of

the linear susceptibility with the spin-spin correlation $\left\langle \sigma_i^z \sigma_j^z \right\rangle$ which diverges at the ferromagnetic critical temperature. What about spin glass materials? In spin glasses, because of strong quenched randomness, the spin correlation $\left\langle \sigma_i^z \sigma_j^z \right\rangle$ does not extend over more than a few spins and there are no long range correlations. One of the characteristic features of spin glasses is their very slow dynamics at low temperature. This property is due to the presence of a complicated energy landscape with many metastable valleys separated by barriers. Therefore dynamical measurements such as AC susceptibility measurements are useful tools. However, here we shall focus on another important feature of spin glasses, namely that they can have a sharp thermodynamic phase transition. For a temperature T less than the spin glass transition temperature T_g, the spins are frozen in a quenched random arrangement as $T \to T_g^+$. In the spin-glass regime the bulk magnetization $m_z = [\langle \sigma_i^z \rangle]_{\rm av}$ is zero, while the spin glass order parameter $q = \left[\langle \sigma_i^z \rangle^2\right]_{\rm av}$ is nonzero in the spin glass phase and zero in the paramagnetic phase. For spin glasses the linear susceptibility is not a diverging quantity as $T \to T_g^+$. Hence, for spin glass systems it is useful to study the so called *spin glass (order parameter) susceptibility*, which is defined as [12]

$$\chi_{\rm SG} = \frac{1}{N} \sum_{i,j} \left[\left(\langle \sigma_i \sigma_j \rangle - \langle \sigma_i \rangle \langle \sigma_j \rangle \right)^2 \right]_{\rm av} \ . \tag{1.20}$$

The order parameter susceptibility $\chi_{\rm SG}$ diverges when the ordering temperature T_g is approached. The practical way to study the order parameter susceptibility experimentally and observe the spin glass transition is to measure the nonlinear susceptibility χ_3. The nonlinear susceptibility is obtained from the nonlinear response of the longitudinal magnetization with respect to an external longitudinal magnetic field h_z. Generally the longitudinal magnetization $m_z(T, h_z)$ can be written as [12]

$$m_z(T, h) = \chi_1(T) h_z - \chi_3(T) h_z^3 + \chi_5(T) h_z^5 - \cdots \ . \tag{1.21}$$

where

$$m_z(T, h_z) = \frac{1}{N} \sum_i \left[\langle \sigma_i^z \rangle \right]_{\rm av} = \frac{k_B T}{N} \frac{\partial \left[\ln Z(\{J_{ij}\}, T, h_z) \right]_{\rm av}}{\partial h_z} \ .$$

By calculating $\chi_3 = -\frac{1}{6} \frac{\partial^3 m_z}{\partial h_z^3} |_{h_z=0}$ and considering the definition of $\chi_{\rm SG}$ in Eq. (1.20), it can be shown that for the regime where $[\langle \sigma_i^z \rangle]_{\rm av} = 0$, χ_3 is a function of $\chi_{\rm SG}$ via

the linear relation [12, 31]

$$\chi_3 = \left[\frac{1}{k_B T}\right]^3 (\chi_{\rm SG} - \frac{2}{3}) \ . \tag{1.22}$$

Close to the transition temperature $\chi_3 \propto (T - T_g)^{-\gamma}$, where $\gamma > 0$ [12]. Therefore, measuring the nonlinear susceptibility is a useful technique to probe the spin glass transition in disordered magnetic materials.

1.2.3 Quantum Spin-Glasses

Now that the classical spin glass Ising model has been introduced, we proceed to generalize the theoretical models developed to study classical spin glasses in order to incorporate quantum effects. Since one of the main intent of this thesis is to study the interplay of quantum fluctuations in the presence of random disorder, which is induced by diluting $LiHo_xY_{1-x}F_4$, it is now sensible to open a discussion of quantum spin glasses.

Only recently has the interplay between quantum effects and disorder in quantum statistical models begun to attract interest. Quantum spin glasses [5, 32, 33, 34, 35, 36, 37] have the interesting feature that the transition in randomly frustrated (competing) cooperatively interacting systems can be driven both by thermal fluctuations and by quantum fluctuations. The main question is how quantum mechanics influences the phases and phase diagram of these disordered magnetic systems. The early studies of quantum spin glasses were focused on quantum Heisenberg spin glasses introduced by Bray and Moore [38]. Quantum fluctuations cannot be tuned in such systems. Bray and Moore [38] studied the infinite range SK version of the quantum Heisenberg spin glass model using the so called "*static approximation*". The idea behind this approach is simply that in addition to the usual mean field approximation, in which the spatial fluctuations are neglected, one may also neglect the fluctuations of the order parameter in the imaginary time direction. Hence, the mean field approximation is actually extended to the quantum regime (the imaginary time direction). Bray and Moore [38] found that mean field calculations show a decrease in the critical temperature due to quantum effects. Another class of quantum spin glass models is generated by perturbing the classical spin

glass via tunable quantum fluctuations, for example, by applying a field transverse to the Ising direction [37, 5]. The transverse field Ising spin glass (TFISG) model is perhaps the simplest model that exhibits a tunable quantum phase transition.

$$H_{\rm TFISG} = -\frac{1}{2}\sum_{i,j} J_{ij}\sigma_i^z\sigma_j^z - \Gamma\sum_i \sigma_i^x \ . \tag{1.23}$$

Here the J_{ij}'s are quenched (frozen) random interactions and Γ causes quantum spin fluctuations (as in the simple transverse field Ising model of Eq. (1.1)). These quantum fluctuations decrease the spin glass transition temperature T_g as Γ increases. The transverse field is increased until, at $\Gamma = \Gamma_c$, a quantum phase transition between a quantum paramagnet and a spin glass phase occurs. For example, in the classical SK model, the free energy landscape consists of high barriers which separate deep valleys from each other. In the thermodynamical limit, below T_g, thermal fluctuations are unable to assist the system in crossing the barriers, so the system becomes non-ergodic. However, if one considers quantum fluctuations, then there exists a finite probability for the system to tunnel through the barriers. Hence, quantum fluctuations allow the system to explore the free energy landscape easily. The TFISG model is perhaps one of the simplest models in which the quantum effects in a random system can be and have been studied extensively [5, 37].

An interesting phenomenon which is studied in quantum spin glasses is the occurrence of Griffiths-McCoy singularities [39, 40, 41]. In an infinite system one can locally find arbitrarily large spatial regions, which do not have impurities. When the total bulk system is not in a paramagnetic phase yet, and the total magnetization is zero, these rare regions show local magnetic order and can lead to a singularity in the free energy. In classical systems with uncorrelated or short-range correlated disorder, the probability of finding such rare regions is small and the possibility that Griffiths singularities may effect the thermodynamics of the system is very weak. Long-range disorder correlations can increase the rare region effects qualitatively if the disorder is perfectly correlated in some spatial directions. Such a situation may occur for a quantum disordered system at the $T = 0$ quantum critical point. At $T = 0$, the rare regions are extended objects with an infinite correlation in the imaginary time direction. Now these strongly correlated rare regions can have much stronger effects, ranging from strong power-law singularities in the free energy to

a complete destruction of the phase transition [41]. Therefore there is a possible influence on the critical behaviour in the vicinity of the quantum critical point.

The possibility of finding a rare region with a volume v_{RR} and a typical length of L_{RR} ($v_{\mathrm{RR}} \propto L_{\mathrm{RR}}^{d}$) decreases exponentially with the volume of the rare region, therefore it is expected that the effect of Griffiths physics decreases by increasing the dimension of the system [37, 41]. Obviously, the Griffiths physics is not captured by the mean field study of the infinite range transverse field Ising spin glass model, where the spatial dimension is considered infinite ($d = \infty$). However, in the opposite limit, where the spatial dimension is $d = 1$, Fisher [42] used the renormalization group method to show how the Griffiths-McCoy singularities influence the critical behaviour of a random Ising spin chain with a transverse field close to the quantum critical point. For higher dimensions ($d > 1$), extensive numerical studies have found that in proximity to a quantum phase transition between a quantum paramagnetic phase and a spin glass phase [43, 44, 45], Griffiths-McCoy singularities [39, 40] occur. For example, a divergence in the nonlinear susceptibility is observed in a range of transverse field Γ in the vicinity of the critical transverse field Γ_c, as one approaches $T = 0$ for $d = 1, 2, 3$

1.3 Random Field Ising Model

In this section, we finish our discussion of those theoretical models that provide an important background to the work presented in this thesis by introducing the random field (RF) Ising model. In the previous sections, in order to study disordered magnetic models, we made a generalization to the Ising model (or TFIM) by imposing disorder to the pairwise spin-spin couplings J_{ij}, for example by considering them to be random. We previously discussed that, especially when the random interactions lead to frustration, the disordered variant of the Ising model (i.e EA model) is used to model spin glass magnetic systems. One can consider another way to adding disorder to the Ising model. Instead of considering the interactions to be random, one can consider the linear longitudinal field, which is coupled to the Ising spin to be random. Models with quenched random fields provide another class of disordered magnetic models, which have been studied extensively.

In this thesis, we propose that for diluted $LiHo_xY_{1-x}F_4$, applying B_x effectively induces random fields, which couple locally to the Ho^{3+} magnetic moments. The presence of RF physics in $LiHo_xY_{1-x}F_4$ motivates us enough to include a short background on the RF Ising model.

Here, disorder manifests itself as a generalized random field coupled directly to the order parameter of the otherwise clean (dilution free) system. In a RF problem, the system attempts to lower its energy by adjusting locally to the RFs while the tendency of the system toward order opposes this local deformation. The competition between these two trends brings out very interesting and rich physics. The prototype of such models is the generic random field (RF) Ising model

$$H_{\mathrm{RF}} = -\frac{1}{2}\sum_{i,j} J_{ij}\sigma_i^z\sigma_j^z - \sum_i h_i\sigma_i^z \ , \tag{1.24}$$

where there is a field that varies randomly from site to site with zero mean. Despite all the interesting rigorous theoretical studies related to random-field models [46, 47, 48, 49, 50], site-random fields are difficult to tune experimentally, and the random field model seemed quite abstract and not amenable to quantitative investigation until Aharony and [51, 52] showed that site-diluted antiferromagnets in tunable, uniform external magnetic fields should behave like ferromagnets in tunable random fields. A simple Hamiltonian, which describes a random diluted antiferromagnet in a uniform magnetic field h reads as

$$H_{\mathrm{AF}}^{\mathrm{dil}} = \frac{1}{2}\sum_{\langle i,j\rangle} \epsilon_i\epsilon_j J_{ij}\sigma_i^z\sigma_j^z - h\sum_i \epsilon_i\sigma_i^z \ , \tag{1.25}$$

in which $\epsilon_i = 1$ if site i is occupied and 0 if empty. In the case of antiferromagnetic interactions, where the system is not diluted and the external field is absent, the spins order in two sublattices. The spins in the same sublattice order parallel to each other and antiparallel respect to spins in the other sublattice. Adding random dilution imposes a local statistical imbalance of spins on each sublattice. The uniform field attempts to align the local spins with itself, while the neighboring spins from the other sublattice attempt to force the local spin to align antiparallel with respect to their direction. Therefore, the sublattice which locally has a greater number of spins will attempt to have its spins pointing along the uniform field.

In a general RF Ising model, the RFs tend to destroy order, which effectively reduces the ferromagnet to paramagnet transition temperature T_c relative to that of a classical Ising system. As the distribution width of the RFs, $h_r \equiv \sqrt{[h_i^2]_{\rm av}}$ increases, T_c decreases until, for a critical RF distribution width h_r^c, T_c goes to zero. Therefore for fields with $h_r \equiv \sqrt{[h_i^2]_{\rm av}}$ larger than h_r^c, the system is always disordered.

Imry and Ma [46] used a droplet picture framework and energy scaling arguments to show that for spatial dimension $d \leq 2$, even small RFs destroy the ordered phase of an Ising system. If one considers a droplet with a typical size of L, which is a compact domain of reversed spins opposite to the average magnetization of the bulk, then for the case that interactions are assumed to be ferromagnetic and nearest neighbor, the energy cost to flip a domain is proportional to the domain wall area $E_{\rm ex} \sim +JL^{d-1}$. This energy cost of flipping the spins should be compared with the energy gain which comes from the interaction of the spins with the random fields. For uncorrelated random fields, according to the central limit theorem, the mean square value of the random field energy $E_{\rm RF}^2$ inside a region of volume L^d is proportional to ${h_r}^2 L^d$. Therefore, the total energy cost for the formation of a domain is

$$E(L) \approx +JL^{d-1} - h_r L^{d/2} = JL^{d-1}\left[1 - \left(\frac{h}{J}\right) L^{\frac{2-d}{2}}\right] \tag{1.26}$$

Therefore, by this simple argument [46, 53], one can see from Eq. (1.26) that for h_r much smaller than J, the ferromagnetic state becomes unstable with respect to domain formation for $d < 2$, when L is large enough. In other words the system can not ferromagnetically order at $d < 2$ and $d_l = 2$ is the lower critical dimension of the RF Ising model.

Up to now, we have presented a minimum introductory back-ground material required for the discussion of the physics of $LiHo_xY_{1-x}F_4$ which follows in the rest of this thesis. The goal of this thesis is to study disordered magnetic materials in the context of $LiHo_xY_{1-x}F_4$ and to understand some of the paradoxical physics of that material. In the next section we preview the main properties of the magnetic material $LiHo_xY_{1-x}F_4$.

1.4 $\mathbf{LiHo_xY_{1-x}F_4}$

In the previous sections, we introduced some of the simple theoretical models which were developed to study disordered classical/quantum magnetic materials. From now on, we focus on the real magnetic material $LiHo_xY_{1-x}F_4$. Depending on x, the concentration of the magnetic Ho^{3+} ions, or B_x, the amplitude of the external magnetic field applied transverse to the $\hat{z}$ Ising direction, $LiHo_xY_{1-x}F_4$ provides an excellent framework to benchmark a variety of well-studied theoretical models, which were introduced in Sections 1.1, 1.2 and 1.3.

In $LiHoF_4$, the predominant J_{ij} interaction between the Ho^{3+} ions is the long range interaction between magnetic dipoles which decays as $1/r_{ij}^3$, where r_{ij} is the distance between the i and j ions. The sign of J_{ij} depends on the position of j respect to i. The existence of a large crystal field anisotropy acting on the magnetic Ho^{3+} ions [54] causes the system to behave as a classical Ising system with dipolar interactions for zero applied magnetic field B_x. The single ion crystal field ground state is an Ising doublet, meaning that the matrix elements of the raising and lowering angular momentum operators $J^{\pm}$ vanish within the space spanned by the two states of the doublet. The Ising direction is parallel to the
c-axis of the body centered tetragonal structure of $LiHoF_4$. In zero applied magnetic field B_x, the pure compound $LiHoF_4$ is well described by a low-energy effective spin-$\frac{1}{2}$ classical dipolar Ising model [55, 56]. For $B_x = 0$, $LiHoF_4$ is an Ising ferromagnet at low temperature with a critical phase transition at $T_c = 1.53$ K.

For Ho^{3+} in $LiHoF_4$, the energy gap between the ground state doublet and the first excited state singlet is fairly large compared to the J_{ij} couplings, so there is little quantum mechanical admixing between the ground state ad excited states that is induced by the interactions [55]. However, a nonzero B_x admixes the ground state doublet with the excited states thereby splitting the ground state doublet. It is this energy splitting which corresponds to the effective transverse field Γ in the TFIM description of $LiHoF_4$ in nonzero B_x [1, 56, 57].

Hence, $LiHoF_4$ with an applied external B_x can be advocated as one of the rare physical realizations [1] of the transverse field Ising model (TFIM) [2, 3, 4, 5, 6]. Here, quantum fluctuations are induced via an external B_x, which is experimentally

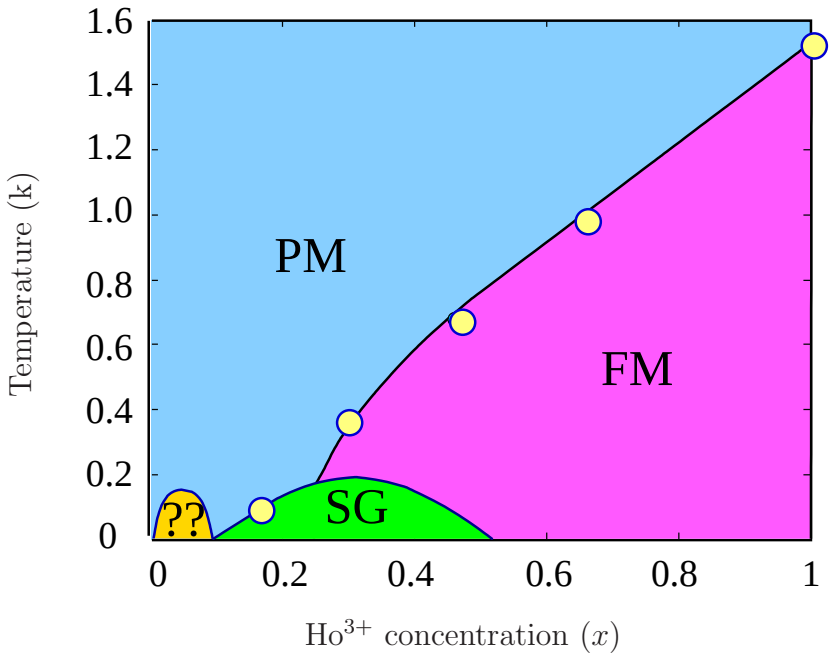

Figure 1.3: The phase diagram as a function of dipole concentration x for $LiHo_xY_{1-x}F_4$, showing paramagnetic (PM), ferromagnetic (FM), spin glass (SG) "anti-glass" (??) phases [7] .

tunable. Therefore, $LiHoF_4$ provides an ideal framework to study quantum phase transitions.

The Ho^{3+} ions may be substituted (i.e. randomly diluted) by non-magnetic yttrium (Y^{3+}) ions, with very little lattice distortion[7]. Therefore, the substitution of Ho^{3+} with Y^{3+} almost does not change the magnetic pairwise interactions between the magnetic moments of the remaining Ho^{3+} ions. This allows one to study the effects of disorder on $LiHo_xY_{1-x}F_4$ as an example of a diluted Ising model with quenched disorder.

Now, we momentarily set $B_x = 0$ and review different phases of $LiHo_xY_{1-x}F_4$ for different ranges of x in the absence of induced quantum fluctuations. Fig. 1.3 shows the temperature vs Ho^{3+} concentration (x) phase diagram of $LiHo_xY_{1-x}F_4$ [7]. As the concentration x is varied, $LiHo_xY_{1-x}F_4$ exhibits various phases. Starting from

[7]The ionic radius of the non-magnetic Y^{3+} is $\sim$ 104.0 pm, which is very close to the one of Ho^{3+} ($\sim$ 104.1 pm).

$x = 1$, as we mentioned earlier, the system maps on a simple classical Ising model with long range dipole-dipole interactions. By randomly diluting the system, the transition temperature is initially depressed linearly with dipole concentration down to $x \sim 0.5$ following the simple mean-field relationship $T_c(x) \approx xT_c(x = 1)$. The long-range ferromagnetic order survives down to $x \sim 0.25$ and the system is a ferromagnet with quenched disorder [1, 58, 59, 60]. For $x < 0.25$ the quenched disorder and the competition of the pairwise ferro/antiferro-magnetic interactions, which is inherent in dipolar interactions, dominate. The system cannot satisfy all the interactions, hence the system becomes very strongly randomly frustrated and a classical spin glass is observed [7, 9]. The spin glass transition is found by observing a sharp divergence in the nonlinear susceptibility, χ_3 (see Eq. (1.21)), and also from the dynamical signature in the dissipative component of the linear AC susceptibility, χ_1'' [36, 61][8].

What happens if we dilute the system further ($x \to 0$)? When $LiHo_xY_{1-x}F_4$ is highly diluted (e.g. $LiHo_{0.045}Y_{0.955}F_4$), very interesting and peculiar behaviours are observed. AC susceptibility data show that the distribution of relaxation times *narrows* upon cooling below 300 mK [7, 67, 8]. This behaviour is quite different from that observed in conventional spin glasses, where the distribution of relaxation times broadens upon approaching a spin glass transition at $T_g > 0$ [12, 68]. This so-called *antiglass* behaviour has been interpreted as evidence that the spin glass transition in $LiHo_xY_{1-x}F_4$ disappears at some nonzero $x_c > 0$ [9] and the system appears not to freeze at a finite temperature in this highly diluted regime. This is

[8]We note that the existence of a spin glass transition in $LiHo_xY_{1-x}F_4$ ($x \approx 0.17$) in *zero* transverse magnetic field has very recently been questioned. Recent numerical [62, 63, 64] and experimental works by Jönsson *et al.* [9, 65] claim that a finite temperature paramagnetic to spin glass phase transition may not occur for x as large as $x_c \approx 0.2$. However, Ancona-Torres *et al.* [66], in a more recent experimental work, remeasured the nonlinear susceptibility χ_3 for $x = 0.167$ and also for $x = 0.198$. They reclaim that $LiHo_xY_{1-x}F_4$ has a spin glass transition at $B_x = 0$ and question the results of Ref. [9]. They criticize the authors of Ref. [9] for having used large longitudinal magnetic fields and fast sweep rates in their measurements, probing the system far from equilibrium. However, subsequently in a rebuttal, Jönsson *et al.* [65] claim that their own measurements were performed at equilibrium and requestion the results of Ref. [66]. They emphasize that one can not justify a spin glass transition just from observing a sharp peak in χ_3 without performing a rigorous scaling analysis similar to the one presented in Ref. [9].

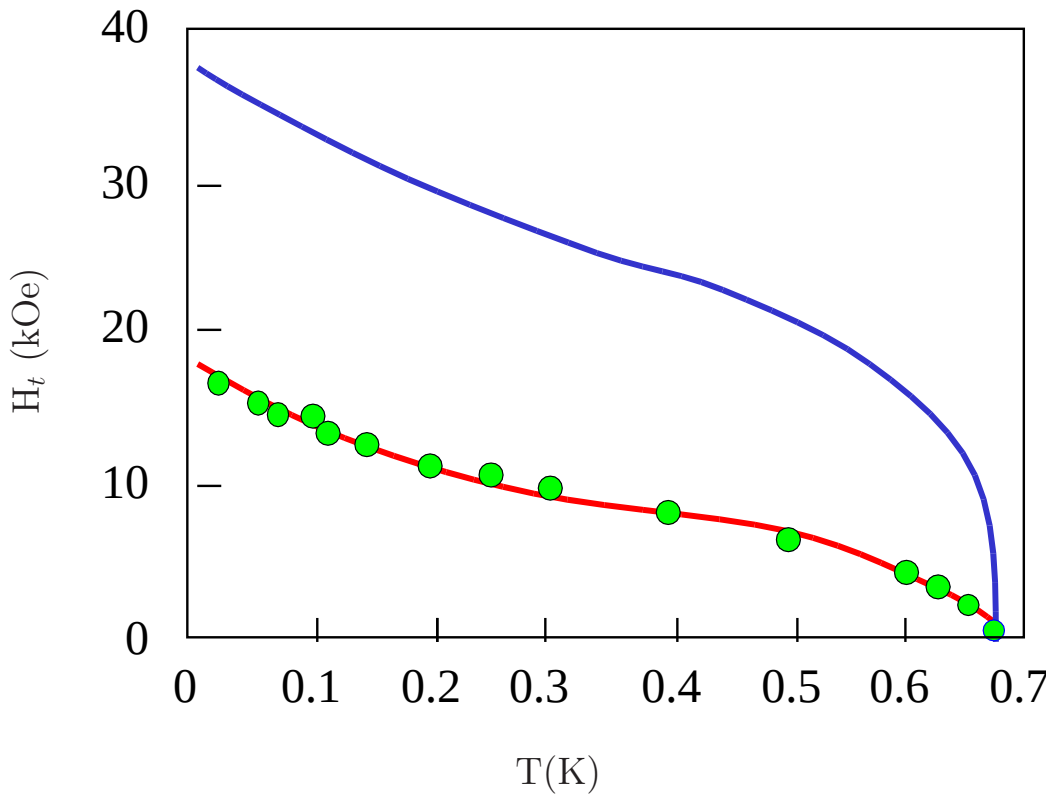

Figure 1.4: The phase diagram of diluted $LiHo_{0.44}Y_{0.56}F_4$ as a function of temperature and the external transverse magnetic field. The lower curve is an experimental curve reported in Ref. [70], while the upper curve is obtained from a simple mean field calculation. In nonzero B_x, with increasing B_x, $T_c(B_x)$ decreases faster than mean field theory predictions .

in contrast with theoretical arguments [69] which argue that, because of the long-ranged $1/r^3$ nature of dipolar interactions, classical dipolar Ising spin glasses should have $T_g(x) > 0$ for all $x > 0$.

Now, we induce quantum fluctuations in the system by applying an external transverse magnetic field $B_x \neq 0$ to $LiHo_xY_{1-x}F_4$, with $x < 1$. One may naively expect that in such a situation, $LiHo_xY_{1-x}F_4$ provides a framework to straightforwardly explore the physics of the TFIM in either a diluted ferromagnet or a spin glass, depending on the concentration x. However, it seems that the interplay of quenched disorder and quantum fluctuations leads to complex and nontrivial

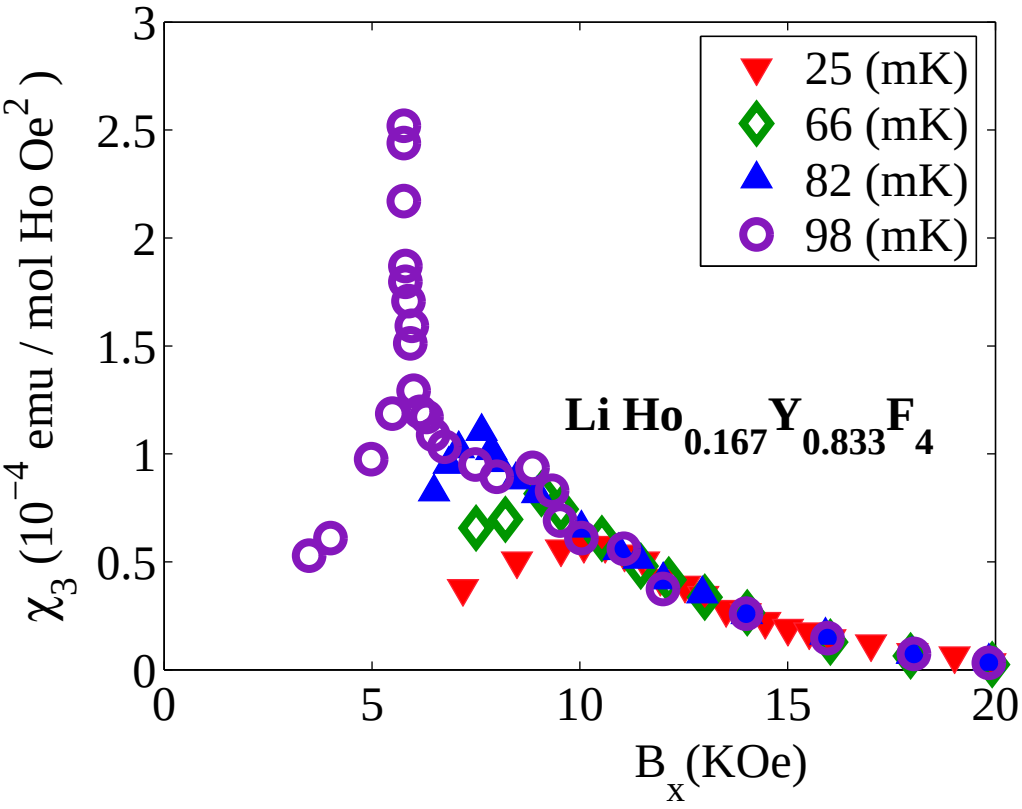

Figure 1.5: The evolution of the nonlinear susceptibility of $LiHo_{0.167}Y_{0.833}F_4$ with an external transverse magnetic field, measured by Wu *et al.* [36]. The divergence in the classical limit becomes quenched upon going to low temperature and/or the large B_x quantum limit.

physics in this material. One of the basic motivations for the work in this thesis was to understand some of the physics behind the puzzling behaviour of diluted $LiHo_xY_{1-x}F_4$ with $x < 1$ and $B_x \neq 0$.

One of the unusual behaviours which has been observed in experiment is in the range of $0.25 < x < 1.0$, where $LiHo_xY_{1-x}F_4$ is a ferromagnet. For $B_x = 0$, a mean-field behaviour $T_c(x) \propto x$ for the paramagnet to ferromagnet transition temperature is observed. However, as it is shown in Fig. 1.4, with increasing B_x, $T_c(B_x)$ decreases faster than what mean field theory predicts [70]. This implies that, compared with the energy scale for ferromagnetic order, set by $T_c(B_x = 0)$, the applied field B_x becomes progressively more efficient at destroying ferromagnetic order as x is lowered [70].

What about the range where $LiHo_xY_{1-x}F_4$ is diluted below $x \sim 0.25$? As we previously discussed, for $B_x = 0$, when $x < 0.25$, a conventional spin glass transition is observed [9, 36]. The general physics of $LiHo_xY_{1-x}F_4$ at $B_x = 0$ is captured by a classical Ising spin glass model, where the couplings are randomly diluted long range dipole dipole interactions. Therefore, at $B_x \neq 0$, one may naively expect that a transverse field Ising spin glass (TFISG) model is a suitable framework to study $LiHo_xY_{1-x}F_4$ theoretically. However, it turns out that in reality for $B_x \neq 0$, a TFISG model fails to capture some of the important macroscopic properties of the spin glass behaviour of $LiHo_xY_{1-x}F_4$ for $x < 0.25$. As was discussed earlier, the clearest signature of the spin glass transition is a divergence of the nonlinear magnetic susceptibility χ_3 at T_g [68]. However, surprisingly, $\chi_3(T)$ becomes less singular as B_x is increased from $B_x = 0$, suggesting that no quantum phase transition between a paramagnetic and spin glass state exists as $T \to 0$ [36, 71] (See Fig. 1.5). This behaviour is rather puzzling. For example, mean-field studies of infinite-range quantum Ising spin glasses, suggest that at $T = 0$ and $\Gamma_c = T_g(\Gamma = 0)$, the nonlinear susceptibility is divergent (see Chapter 5), where $T_g(\Gamma = 0)$ is the classical spin glass transition temperature. Also, numerical studies on the quantum version of the EA model with a transverse field for spatial dimension $d = 2$ [43] and $d = 3$ [45], indicate that the nonlinear susceptibility diverges at $T = 0$. This is in contrast with what is observed for $LiHo_xY_{1-x}F_4$.

Recently, theoretical studies [24, 25, 56, 72] have suggested that for dipole-

coupled Ho^{3+} in diluted $LiHo_xY_{1-x}F_4$, a nonzero B_x generates longitudinal (along the Ising $\hat{z}$ direction) random fields that couple to the magnetic moment and (i) lead to a faster decrease of $T_c(B_x)$ in the ferromagnetic regime and (ii) destroy the paramagnet to spin glass transition in $LiHo_xY_{1-x}F_4$ samples that otherwise show a SG transition when $B_x = 0$ [9]. In this thesis, we discuss the mechanism of this random field generation in detail. This induction of random fields in $LiHo_xY_{1-x}F_4$ via a tunable external transverse magnetic field may have a significant impact on the theory of random fields, which is currently an important problem in the field of disordered systems. As mentioned in Section 1.3, a direct manifestation of the RF phenomenon in real magnetic systems is extremely rare, because it is difficult to generate random fields at the atomic scale which couple directly to the spins.[9] Therefore $LiHo_xY_{1-x}F_4$, with $B_x \neq 0$ is seemingly the first realization of a random field Ising model in a ferromagnetic material providing a new venue for studying the random field problem with a direct probe, by measuring bulk properties such as magnetization and susceptibility. Recently, for the ferromagnetic regime, the influence of these induced random fields on the behaviour of the linear magnetic susceptibility χ in the presence of an external transverse magnetic field has been experimentally studied [58, 73].

The authors of Ref. [58] measured the linear susceptibility of diluted $LiHo_xY_{1-x}F_4$ in the presence of a transverse magnetic field for $x = 0.44$, where the system is a diluted ferromagnet. They observed that for $B_x \neq 0$, the linear susceptibility shows singular behaviour for temperatures above the Curie-Weiss temperature T_c. They discuss that, as a result of the induction of random fields, the susceptibility has a leading contribution proportional to $|B_x|$. This $|B_x|$ dependence is the origin of the singular behaviour of χ for temperatures in the proximity of the critical temperature. The authors of Ref. [58] claim that this is possibly evidence that $LiHo_xY_{1-x}F_4$ displays Griffiths singularities. However, the details of how this specific singular be-

[9] As discussed earlier in Section 1.3, Aharony and Fishman [51], showed that site-random antiferromagnets, such as $Fe_xZn_{1-x}F_2$, in a tunable uniform external magnetic field map onto a ferromagnet in tunable random fields. The experimental probe to study these diluted antiferromagnets is usually neutron scattering. Because, in practice one is not able to apply a staggered field (a field that is periodically alternating in space), direct bulk measurements such as magnetization and susceptibility measurements are not applicable for antiferromagnets.

haviour in the linear susceptibility is connected to the Griffiths physics for nonzero T is unclear. However, motivated by the discussion we had in Section 1.2, where numerical studies for a TFISG model in $d = 2, 3$ [43, 44, 45] observe Griffiths singularities at $T \to 0$ in the vicinity of the quantum critical point, it would be very interesting to investigate how these Griffiths rare regions influence the physics of $LiHo_xY_{1-x}F_4$ at low temperatures $T \to 0$, a subject beyond the scope of this thesis.

In addition to phenomena arising in the dilute regime of $LiHo_xY_{1-x}F_4$, the $x = 1$ regime also turns out to be interesting. There still exist problems for $LiHoF_4$, that require the properties of this system in nonzero B_x to be re-investigated more thoroughly. Perhaps surprisingly, it is just recently that the properties of $LiHoF_4$ in a transverse external magnetic field have been studied in quantitative detail starting from a truly microscopic spin Hamiltonian [57]. In Ref. [57], which reported results from a quantum Monte Carlo (QMC) study using the stochastic series expansion (SSE) technique [74], a general qualitative agreement between the microscopic model and experimental data was obtained [1]. However, as illustrated in Fig. 1.6, a significant quantitative discrepancy between the Monte Carlo results of Ref. [57] and the experimental data of Ref [1] was reported. In particular, the discrepancy between experiment and QMC results persists asymptotically close to the classical ferromagnetic to paramagnetic phase transition, where B_x/T_c and quantum fluctuations are *perturbatively small*. For very low temperatures and high B_x, it is crucial to consider the hyperfine interaction in order to explain the behaviour of the phase diagram close to the quantum critical point [1, 57, 75]. However, for very small B_x/T_c, the numerical results shown in Fig. 1.6 indicate that the effect of the hyperfine interaction is not important close to the classical transition at T_c, where T_c is much higher than typical energy scale of the hyperfine interactions and the effect of nuclear levels are effectively averaged out. In this thesis, we numerically re-investigate the temperature T, versus transverse field phase diagram of $LiHoF_4$ in the regime of weak B_x. Our goal in doing so is to scrutinize the individual role of a number of computational issues as potential culprits for the discrepancy between QMC and experiment observed in Fig. 1.6.

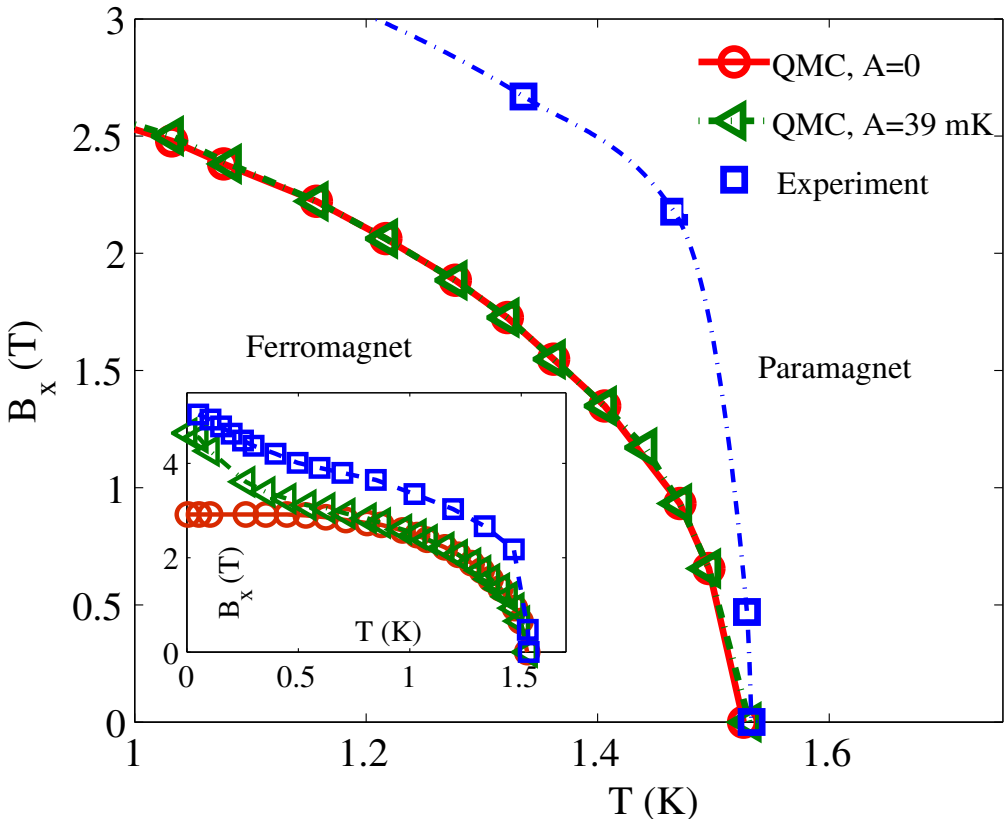

Figure 1.6: The discrepancy between the experimental [1] phase diagram of $LiHoF_4$ and quantum Monte Carlo (QMC) simulations using stochastic series expansion for small B_x from Ref. [57]. The whole phase diagram is shown in the inset. At low temperature and high B_x, neglecting the large hyperfine interaction A generates a significant discrepancy between the experimental quantum critical point and the one obtained from simulation. However, at low B_x and close to the classical critical point ($T_c \sim 1.53$K), we are in a temperature range where the hyperfine interaction does not quantitatively affect the phase boundary. Other possibilities for the origin of this discrepancy must be investigated in this regime.

1.5 Outline of the Thesis

The rest of the thesis is organized as follows. In Chapter 2, we review the crystal structure and the physical properties of $LiHo_xY_{1-x}F_4$ in a transverse field B_x and the effect of the electrostatic interaction of the atoms surrounding the magnetic ions, the so called crystal field effect. We discuss how to derive the crystal field Hamiltonian of $LiHo_xY_{1-x}F_4$ based on the crystal structure and the symmetry of the lattice. Then, we introduce the full microscopic Hamiltonian, which describes the magnetic interactions in the lattice.

In Chapter 3, we first discuss how, for sufficiently low temperatures, an effective spin-$\frac{1}{2}$ Hamiltonian is generated for a generalized simple $S > 1$ model with long range dipolar interactions and with strong uniaxial Ising anisotropy and subject to a weak external magnetic field B_x transverse to the Ising direction. Then, we focus on $LiHo_xY_{1-x}F_4$ and explain how such an effective spin-$\frac{1}{2}$ Hamiltonian can be constructed. We explain how one can picture pure $LiHoF_4$ in nonzero B_x as a dipolar TFIM and show how, in the case of dilution, magnetic field-induced longitudinal random fields naturally arise in the effective Hamiltonian.

In Chapter 4, we present analytical and numerical evidence for the validity of an effective spin-$\frac{1}{2}$ approach to the description of random field generation in $S \geq 1$, and especially for an $S = 1$, dipolar spin glass model with strong uniaxial Ising anisotropy and subject to a weak external magnetic field B_x transverse to the Ising direction. We show that the spin-$\frac{1}{2}$ approach is able to capture both qualitative and *quantitative* aspects of the physics at small B_x, giving results that agree with those obtained using conventional second order perturbation theory.

In Chapter 5, we study $LiHo_xY_{1-x}F_4$ in the spin glass regime. Motivated by the effective spin-$\frac{1}{2}$ Hamiltonian, proposed in Chapter 3 to describe the low temperature behaviour of the diluted quantum magnetic material $LiHo_xY_{1-x}F_4$ with an applied transverse magnetic field B_x, we investigate an infinite range quantum spin glass model with random field interactions in the Ising $\hat{z}$ direction. To study this model we use a mean field replica symmetric calculation and an imaginary time static approximation. We calculate the nonlinear susceptibility for this model and discuss the range of temperature and transverse field over which the mean field so-

lution is stable. Finally, we bring our results in contact with the real $LiHo_xY_{1-x}F_4$ material and discuss how one can expose in this model the smearing of the nonlinear susceptibility χ_3 with increasing external applied magnetic field B_x, similar to what is observed experimentally [36].

Chapter 6 is devoted to numerically re-investigating the temperature T, versus transverse field phase diagram of $LiHoF_4$ in the regime of weak B_x. We discuss how a semiclassical effective Hamiltonian is derived from the TFIM Hamiltonian by incorporating the transverse field term perturbatively via a cumulant expansion. We employ the semiclassical effective Hamiltonian in classical Monte Carlo simulations for small B_x. We investigate the influence on the phase diagram of various effects that may be at the source of the discrepancy between the previous QMC results and the experimental ones. For example, we consider two different ways of handling the long-range dipole-dipole interactions and explore how the $B_x - T$ phase diagram is modified when using different proposed values of the parameters for the microscopic crystal field Hamiltonian.

Finally, in Chapter 7, the thesis is summarized and avenues for future work are discussed. The thesis also contains five appendices. Appendix A introduces the Trotter-Suzuki method for transforming a d-dimensional TFIM to a $d+1$-dimensional classical Hamiltonian, which is useful to study a very simple TFIM. Appendix B gives some of the intermediate steps needed to construct an effective classical Hamiltonian out of the non-commuting terms in the quantum Hamiltonian of the TFIM, using a perturbative cumulant expansion. This perturbative effective Hamiltonian is used in our Monte Carlo simulations. Appendix C gives the formulae needed to calculate physical thermodynamic quantities when performing classical Monte Carlo simulations with the effective perturbative Hamiltonian. Appendix D gives a very brief introduction of the numerical Lanczos method, which is used to perform numeric exact diagonalization of spin Hamiltonians and which is used in the calculations presented in Chapter 4. In Appendix E, we discuss the details of the derivation for the stability condition of the replica symmetric solution under the static approximation for the generalized infinite range model with random interactions, studied in Chapter 5.

Chapter 2

Crystal Structure and the Microscopic Hamiltonian of $\mathbf{LiHo}_x\mathbf{Y}_{1-x}\mathbf{F}_4$

This chapter is devoted to the crystal structure of $LiHo_xY_{1-x}F_4$ and the microscopic interactions acting on the magnetic Ho^{3+} ion within the crystal. In Section 2.1, we introduce some of the basic properties of the magnetic Ho^{3+} ions within the $LiHoF_4$ lattice and discuss the crystal structure and the symmetry of the $LiHoF_4$ lattice. In Section 2.2, we review the effect of the electrostatic interaction of the atoms surrounding the magnetic ions, the so-called the crystal field effect. We discuss how to derive the crystal field Hamiltonian based on the crystal structure and the symmetry of the lattice. The crystal field interaction can partially lift the atomistic degeneracy of isolated ions within the lattice. We also discuss how the crystal field Hamiltonian of $LiHoF_4$ is obtained. In Section 2.3, we introduce the full microscopic Hamiltonian that describes the interactions of the magnetic Ho^{3+} ions within the $LiHoF_4$ lattice.

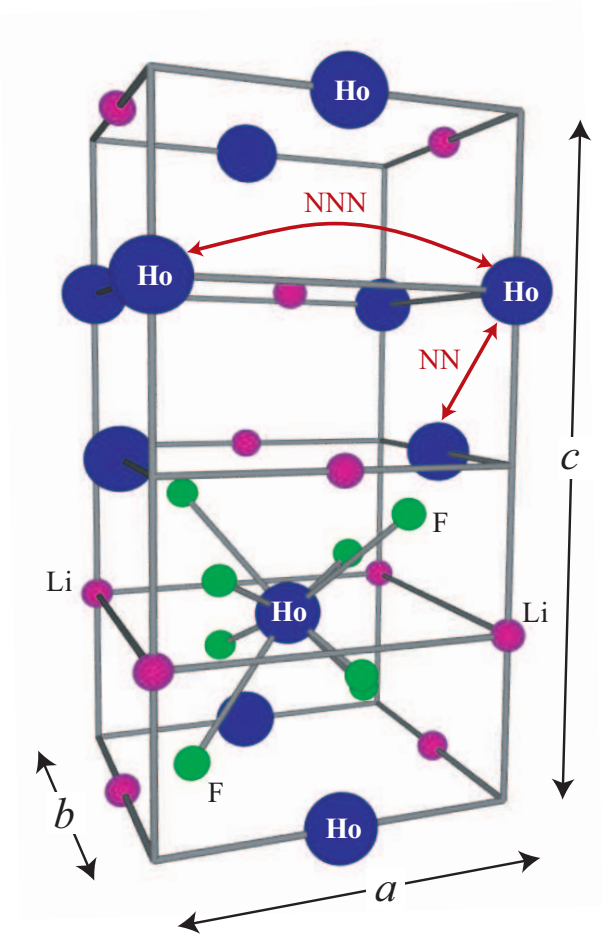

$$a = b = 5.176 \text{ Å}$$

$$c = 10.75 \text{ Å}$$

Figure 2.1: The crystal structure of $LiHoF_4$. NN identifies the first nearest neighbors and NNN identifies the next nearest neighbors

2.1 Structure and Crystal Properties

The magnetic material $LiHoF_4$ undergoes a second-order phase transition from a paramagnetic to a ferromagnetic state at a critical temperature of 1.53 K [36, 54]. The critical temperature can be reduced by applying a magnetic field B_x transverse to the Ising easy-axis direction. The magnetic field induces quantum fluctuations such that beyond a critical field of $B_x^c \approx 4.9$ Tesla, the system displays a quantum phase transition from a ferromagnetic state to a quantum paramagnetic state at zero temperature [1] (see Fig. 1.6). The magnetic properties of $LiHoF_4$ are due to Ho^{3+} rare earth magnetic ions. The electronic ground state of Ho^{3+} is $4f^{10}$, which gives small exchange coupling [57, 76, 77][1], such that the predominant magnetic interaction between the Ho^{3+} ions are long-range magnetic dipole-dipole interactions. Hund's rules dictate that the total angular momentum of a free ion Ho^{3+}, J = 8 (L = 6 and S = 2) and the electronic ground state configuration is ${}^5I_8$. $LiHoF_4$ is a compound with space-group $C_{4h}^6(I4_1/a)$ and lattice parameters $a = b = 5.175\mathring{A}$, $c = 10.75\mathring{A}$, and has 4 Ho^{3+} ions per unit cell positioned at $(0, 0, 1/2)$, $(0, 1/2, 3/4)$, $(1/2, 1/2, 0)$ and $(1/2, 0, 1/4)$ [76]. The lattice structure is shown in Fig. 2.1 The crystal has S_4 symmetry, which means the lattice is invariant with respect to a $\frac{\pi}{2}$ rotation about the z axis and reflection with respect to the $x - y$ plane[2].

In the crystal structure, the Ho^{3+} ions are surrounded by F^- and Li^+ ions, which create a strong crystal electric field with S_4 symmetry. This crystal field lifts the 17-fold degeneracy of the ${}^5I_8$ configuration giving a non-Kramers ground state doublet. The next excited state is a singlet with an energy gap of ≈ 11 K above the ground state doublet [54, 78, 79][3]. In Section 2.2, we discuss the crystal field Hamiltonian and the crystal field parametrization in more detail. Holmium is an isotopically

[1]The reason of weak exchange coupling in rare earth ions is that, the $4f$ orbitals are deeply buried within the electronic shell under the $5s$, $6s$ and $5d$ orbitals

[2]This reflection with respect to the $x - y$ plane makes the S_4 symmetry different from the C_4 symmetry, which the system is invariant respect to $\frac{\pi}{2}$ rotations around the $\hat{z}$ axis (i.e see Fig. 2.1).

[3]In $LiHoF_4$ there is an ambiguity in the value of the energy gap Δ between the ground state doublet and the excited state for $B_x = 0$ among different experimental works. For different estimations of Δ see Refs. [54, 78, 79].

pure element with nuclear spin I = 7/2, which is coupled to the electronic spin **J** via the hyperfine contact interaction $A\mathbf{I}\cdot\mathbf{J}$, where $A \approx 39$ mK [76, 80].

2.2 The Crystal Field Interaction

In this Section, we briefly discuss how the crystal field Hamiltonian of $LiHoF_4$ is written in terms of angular momentum operators and crystal field parameters.

The outer shell of the Ho^{3+} ion is an unfilled f-shell of 10 electrons, and the ground state configuration is (2J + 1) = 17-fold degenerate. However, the electrostatic interactions of the electrons in the unfilled shell with the neighboring charged ions partially lifts the degeneracy. The effect of these electrostatic interactions can be captured by an approximate model in which the overlap of the electronic wave-functions, centered on different ions, are neglected. This approximation is known as the *point-charge* approximation in which all the other ions and their electrons surrounding the ion of interest are treated as point-charges sitting at their equilibrium position in the crystal. In case of an insulator like $LiHoF_4$, where the individual electronic wave-functions are strongly localized on a single ion, this is not a totally bad approximation.

If we assume that the ions electrostatically interacting with the f-electrons of Ho^{3+} are close to point-charges, then the electrostatic energy is simply the sum of the point-charge Coulomb interaction energies. Thus, if we choose a reference frame such that the magnetic ion is at the center of the coordinates, the electrostatic interaction between the environmental ions and the f-electrons of the rare earth ions can be expressed as

$$V_{\mathrm{CF}} = -e\sum_{i,j}\frac{q_j}{|\mathbf{R}_j - \mathbf{r_i}|}\ , \tag{2.1}$$

where $\mathbf{r}_i$ is the position of the i'th f-electron of the rare earth ion, $\mathbf{R}_j$ denotes the position of the jth ion, which is surrounding the Ho^{3+} ion, $-e$ is the charge of an electron and q_j is the total electric charge of the j'th ion surrounding the Ho^{3+} ion. The sum over j includes all the other ions surrounding the rare earth ion of interest, and the sum of i is over all the f-electrons of the rare earth ion. In order to take advantage of the crystalline symmetry, it is useful to expand the crystal

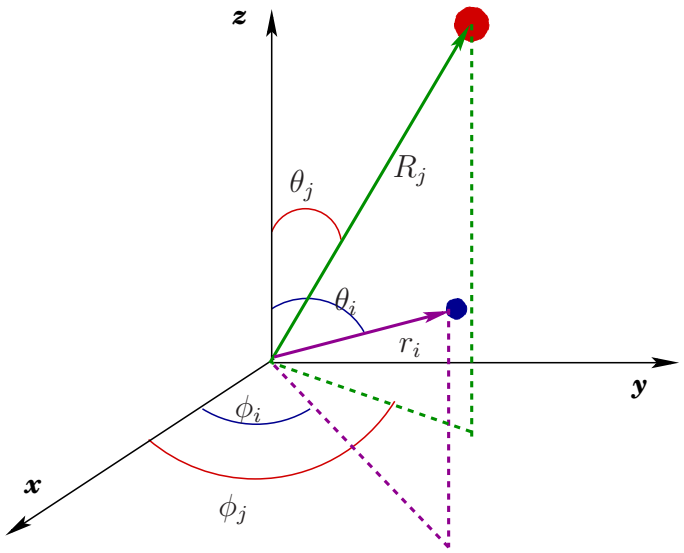

Figure 2.2: The position of the f-electrons (small, blue circle) of the rare earth ion and the position of the environmental ions (large, red circle), in spherical coordinates.

field energy in terms of the spherical harmonics. The components of $\mathbf{r}_i$=(r_i, θ_i, ϕ_i) and $\mathbf{R}_j$=(R_j, θ_j, ϕ_j) are written in terms of the spherical coordinates (See Fig. 2.2). In general $\frac{1}{|\mathbf{R}_j - \mathbf{r_i}|}$, in terms of the spherical harmonics for $R_j > r_i$, can be written as [4]

$$\frac{1}{|\mathbf{R}_j - \mathbf{r_i}|} = \sum_{n=0}^{\infty} \frac{4\pi}{2n+1} \frac{{r_i}^n}{{R_j}^{n+1}} \sum_{m=-n}^{n} (-1)^m Y_n^{-m}(\theta_j, \phi_j) Y_n^m(\theta_i, \phi_i) \ . \tag{2.2}$$

However, in order to avoid imaginary coefficients in the crystal field Hamiltonian, it is more convenient to work with tesseral harmonics [81], which are defined as

$$\begin{aligned} Z_{n0} &= Y_n^0 \ , \\ Z_{nm}^c &= \frac{1}{\sqrt{2}} \left[Y_n^{-m} + (-1)^m Y_n^m \right] \ , \\ Z_{nm}^s &= \frac{i}{\sqrt{2}} \left[Y_n^{-m} - (-1)^m Y_n^m \right] \ , \end{aligned} \tag{2.3}$$

[4] In the case of the rare earth, where the electronic wave-function of the f-electrons are strongly localized, $R_j > r_i$ is a fair assumption.

where $m > 0$. Rewriting, $\frac{1}{|\mathbf{R}_j - \mathbf{r_i}|}$ in terms of tesseral harmonics yields the expression

$$\frac{1}{|\mathbf{R}_j - \mathbf{r_i}|} = \sum_{n=0}^{\infty} \frac{4\pi}{2n+1} \frac{{r_i}^n}{{R_j}^{n+1}} \sum_{\alpha} Z_{n\alpha}(\theta_j, \phi_j) Z_{n\alpha}(\theta_i, \phi_i) \ , \tag{2.4}$$

where $m = 0, ..., n$. For each n in the summation over α there are terms Z_{n0} for $m = 0$, as well as Z^c_{nm}, and Z^s_{nm} for $m \neq 0$. Finally, by substituting Eq. (2.4) into Eq. (2.1), one derives the expression

$$V_{\mathrm{CF}} = -e \sum_i \sum_{n=0}^{\infty} \sum_{\alpha} r_i^n \gamma_{n\alpha} Z_{n\alpha}(\theta_i, \phi_i) \ , \tag{2.5}$$

where $\gamma_{n\alpha}$ is defined as

$$\gamma_{n\alpha} := \sum_j \frac{4\pi q_j}{(2n+1)} \frac{Z_{n\alpha}(\theta_j, \phi_j)}{{R_j}^{n+1}} \ . \tag{2.6}$$

Note that, the dependence of the crystal field potential on the positions of the neighboring ions is captured entirely by the $\gamma_{n\alpha}$ parameters. Thus, the symmetry of the crystal manifests itself through these parameters, causing some of the terms in the harmonic expansion of Eq. (2.5) to vanish identically.

2.2.1 A Discussion of Symmetry

The free ion wave-function of a rare earth ion is written as a Slater determinant of the wave-functions $\psi_{nlm}(r, \theta, \phi)$ of the free electrons in the $4f$ shell. $4f$ free electrons are denoted with quantum numbers $n = 4$, $l = 3$, and $m = -l, \cdots, l$, where the angular part of the $\psi_{nlm}(r, \theta, \phi)$ wave-function is proportional to $Y^m_l(r, \theta, \phi)$ [81, 82]. Therefore, in the calculation of the matrix elements of V_{CF} for $4f$ rare earth ions, we end up calculating expressions such as

$$\int (Y_3^{m_1})^* \ Z_n^m \ Y_3^{m_2} d\Omega \ . \tag{2.7}$$

However, as a result of the addition theorem for spherical harmonics, such matrix elements will be zero if $n > 6$. Thus, we only need to consider the $Z_{n\alpha}$ terms for which $n \leqslant 6$. It should be also noted that, in general, $\int \left(Y_{l_1}^{m_1}\right)^* Z_n^m \ Y_{l_2}^{m_2} d\Omega$ is zero,

unless $l_1 + l_2 + n$= even integer. This means that in Eq. (2.7), where $l_1 = l_2 = 3$, the integral vanishes if n is an odd integer. Therefore, when writing the crystal field Hamiltonian of Eq. (2.5), one can neglect those $\gamma_{n\alpha}$ terms for which n is odd and $n > 6$.

Of the remaining $\gamma_{n\alpha}$ terms, some will vanish due to the symmetries of the crystal. Thus, as a result of all this, the total number of terms required to completely characterize the crystal field Hamiltonian within the point charge approximation is finite.

$LiHoF_4$, which is our subject of interest, has S_4 symmetry. This means that the lattice remains invariant under a rotation of $\pi/2$ about the z-axis followed by a reflection about the x-y plane. Now, for example, if we concentrate on a Ho^{3+} ion positioned at the origin, the position of its four nearest-neighbor Ho^{3+}, in spherical co-ordinates, are given by

$$\begin{aligned} \boldsymbol{r_1} &= (r_{nn}, \theta_{nn}, \phi + \pi/2) \\ \boldsymbol{r_2} &= (r_{nn}, \theta_{nn}, \phi + 3\pi/2) \\ \boldsymbol{r_3} &= (r_{nn}, \pi - \theta_{nn}, \phi) \\ \boldsymbol{r_4} &= (r_{nn}, \pi - \theta_{nn}, \phi + \pi) \ , \end{aligned}$$

where $r_{nn} = \sqrt{(a/2)^2 + (c/4)^2}$ is the nearest neighbor distance and $\theta_{nn} = \arctan(2a/c)$. Therefore, since the m dependence of $Z_n^m(\theta, \phi)$ originates from the $\sin m\phi$ and $\cos m\phi$ terms, the γ_{nm} terms, for which $m \neq (0 \text{ and } 4)$ will vanish. Thus, the total nonzero $\gamma_{n\alpha}$ terms in Eq. (2.5), remaining for $LiHoF_4$ are γ_{20}, γ_{40}, γ_{44}^c, γ_{44}^s, γ_{60}, γ_{64}^c, and γ_{64}^s .

2.2.2 Steven Operators

According to arguments provided by Stevens [83] for evaluating the matrix elements of the crystal field Hamiltonian between wave-functions[5] $|LSJJ^z\rangle$ specified by the

[5]In rare earth elements, the spin orbit interaction is very strong and, as a result, the total angular momentum **J** is a good quantum number and the eigenstates of the total angular momentum operator **J** are good states.

angular momentum **J**, the crystal field Hamiltonian can be written in term of Stevens' operator equivalents O_n^α [81, 82][6].

To do so, we write $Z_{n\alpha}$ in Cartesian coordinates by making the substitutions

$$\begin{aligned} \sin(\theta_i)e^{i\phi_i} &\longrightarrow (x_i + iy_i)/r_i \ , \\ \sin(\theta_i)e^{-i\phi_i} &\longrightarrow (x_i - iy_i)/r_i \ , \text{and} \\ \cos(\theta_i) &\longrightarrow z_i/r_i \ . \end{aligned}$$

The Wigner-Eckart theorem [81, 82] states that $r_i^n Z_{n\alpha}(x_i, y_i, z_i)$, which is an explicit function of x_i, y_i, and z_i, can be replaced by combinations of the vector components of the **J** operator, resulting in equivalent Stevens' operators such that

$$\langle LSJJ^z|r_i^n Z_{n\alpha}(x_i, y_i, z_i)|LSJJ'^z\rangle \propto \langle LSJJ^z|O_n^\alpha|LSJJ'^z\rangle \ . \tag{2.8}$$

To write O_n^α, one can "simply" replace the x, y, and z operators by the J_x, J_y, and J_z total angular momentum operators respectively. However, because the angular momentum operators do not commute as the spatial coordinates do, products of x, y, and z have to be replaced by all the different combinations of J_x, J_y, and J_z divided by the total number of combinations. A simple example is

$$xy \longrightarrow \frac{1}{2}(J_xJ_y + J_yJ_x) \ .$$

As a result the crystal field Hamiltonian can be written in a compact form, in terms of the Stevens' operators, as

$$V_C = \sum_{n,\alpha} B_n^\alpha O_n^\alpha \ . \tag{2.9}$$

The Stevens' equivalent operators act on the angular momentum states of the wave-functions. The matrix element of the radial part of the wave-function is incorporated in the B_n^α parameters

$$B_n^\alpha = -eq\gamma_{n\alpha}\theta_n \langle r^n \rangle \ , \tag{2.10}$$

[6]The details of the method and conventions for expressing the crystal field Hamiltonian can be found in the review paper by Hutchings [81].

where the $c_{n\alpha}$'s are constants which are prefactors existing within the $Z_{n\alpha}$ terms [81]. $\theta_2 = \alpha_J$, $\theta_4 = \beta_J$, and $\theta_6 = \gamma_J$ are constants which depend on the angular momentum state of the ion in question. For Ho^{3+}, $\alpha_J = 1/2 \cdot 3^2 \cdot 5^2$, $\beta_J = 1/2 \cdot 3 \cdot 5 \cdot 7 \cdot 11 \cdot 13$ and $\gamma_J = 5/3^3 \cdot 7 \cdot 11^2 \cdot 13^2$ [81].

Since, B_n^α is proportional to $\gamma_{n\alpha}$, the zero B_n^α parameters are set by symmetry arguments. Therefore, from the discussion given in the last subsection, the remaining nonzero B_n^α parameters of the $LiHoF_4$ crystal field Hamiltonian are B_2^0, B_4^0, B_4^{4c}, B_4^{4c}, B_6^0, B_6^{4c}, and B_6^{4c}, due to the S_4 point group symmetry of $LiHoF_4$. However, because the complexity of the electrical charge distribution and the quantum effects are neglected in the point-charge approximation, the nonzero B_n^α's are usually determined semi-empirically by fitting to experimental (e.g. spectroscopic) data [54, 78, 79].

The crystal field Hamiltonian for $LiHoF_4$, in terms of Stevens' equivalent operators , is

$$\begin{aligned} V_C &= B_2^0 O_2^0 + B_4^0 O_4^0 + B_4^{4c} O_4^{4c} + B_4^{4s} O_4^{4s} \\ &\quad + B_6^0 O_6^0 + B_6^{4c} O_6^{4c} + B_6^{4s} O_6^{4s}. \end{aligned} \tag{2.11}$$

The relevant operator equivalents are given in terms of angular momentum operators [81] (J_z, J_+, J_-, J^2) by

$$\begin{aligned} O_2^0 &= 3J_z^2 - J^2 \ , \\ O_4^0 &= 35Jz^4 - 30J^2 J_z^2 + 25J_z^2 - 6J^2 + 3J^4 \ , \\ O_4^{4C} &= \frac{1}{2}(J_+^4 + J_-^4) \ , \\ O_4^{4S} &= \frac{1}{2i}(J_+^4 - J_-^4) \ , \\ O_6^0 &= 231J_z^6 - 315J^2 J_z^4 + 735J_z^4 + 105J^4 J_z^2 \\ &\quad -525J^2 J_z^2 + 294J_z^2 - 5J^6 + 40J^4 - 60J^2 \ , \\ O_6^{4C} &= \frac{1}{4}(J_+^4 + J_-^4)(11J_z^2 - J^2 - 38) + \text{H.c.} \ , \text{and} \\ O_6^{4S} &= \frac{1}{4i}(J_+^4 - J_-^4)(11J_z^2 - J^2 - 38) + \text{H.c.} \end{aligned} \tag{2.12}$$

Two different sets of experimentally determined crystal field parameters, B_n^α are given in Table 2.1. The first set of the parameters was determined by inelas-

Parameter	Ref. [78]	Ref. [79]
B_2^0	-0.696 K	-0.609 K
B_4^0	4.06×10^{-3} K	3.75×10^{-3} K
B_4^{4C}	4.18×10^{-2} K	3.15×10^{-2} K
B_4^{4S}	0 K	2.72×10^{-2} K
B_6^0	4.64×10^{-6} K	6.05×10^{-6} K
B_6^{4C}	8.12×10^{-4} K	6.78×10^{-4} K
B_6^{4S}	1.137×10^{-4} K	4.14×10^{-4} K

Table 2.1: The first column lists the crystal field parameters (CFP) for $LiHoF_4$, which were determined by fitting the results of random phase approximation spin-wave dynamics calculation to neutron scattering data from Ref. [78]. The second column gives the crystal field parameters estimated using data from an electron paramagnetic resonance (EPR) spectroscopy experiment [79].

tic neutron scattering reported in Ref. [78] and implemented in the calculations of Ref. [57]. The second set of B_n^α parameters was determined using electron paramagnetic resonance (EPR) spectroscopy, and reported in a recent work [79].

2.3 The Microscopic Hamiltonian of $LiHo_xY_{1-x}F_4$.

There are different type of interactions that play a role in the magnetic properties of $LiHo_xY_{1-x}F_4$. The strongest of these interactions is the crystal field interaction $V_{\rm CF}$, which is a single ion interaction. This interaction, which originates from the interaction of the Ho^{3+} ion with the electrical field of all the other surrounding ions, was discussed in the previous section.

In $LiHo_xY_{1-x}F_4$, the main pair-wise interaction between the magnetic ions is the long-range dipole-dipole interaction. These interactions, which are between the

magnetic moments of Ho^{3+} ions read as

$$H_{\rm dip} = \frac{1}{2}(g_L\mu_{\rm B})^2 \sum_{i\neq j}\sum_{\mu\nu} \epsilon_i\epsilon_j L_{ij}^{\mu\nu} \mathrm{J_i^\mu J_j^\nu} \ , \tag{2.13}$$

where $\mu,\nu{=}x,y,z$ and $\mathbf{J}_i$ is the total angular momentum of Ho^{3+} ion i. $L_{ij}^{\mu\nu}$ is the magnetic dipole interaction written in the form

$$L_{ij}^{\mu\nu} = \left[\delta^{\mu\nu}|\mathbf{r}_{ij}|^2 - 3(\mathbf{r}_{ij})^\mu(\mathbf{r}_{ij})^\nu\right]/|\mathbf{r}_{ij}|^5 \ , \tag{2.14}$$

where $\boldsymbol{r}_i$ are the crystalline positions occupied either by a magnetic Ho^{3+} ion ($\epsilon_i = 1$) or a non-magnetic Y^{3+} ion ($\epsilon_i = 0$), and $r_{ij} = |\boldsymbol{r}_j - \boldsymbol{r}_i|$ is the inter-ion distance. Here, $g_L = 1.25$ is the Landé g-factor of free Ho^{3+} and $\mu_{\rm B} = 0.6717$ K/T is the Bohr magneton. The dipolar interaction between the Ho^{3+} magnetic ions is complemented by a short range nearest-neighbor Heisenberg exchange interaction

$$H_{\rm exch} \ = \ \frac{1}{2}J_{\rm ex}\sum_{i,\rm NN} \epsilon_i\epsilon_{\rm NN}\ \mathbf{J}_i\cdot\mathbf{J}_{\rm NN} \ , \tag{2.15}$$

where NN denotes the nearest neighbors of site i. This exchange interaction is considered to be weak and isotropic [57, 84]. The third interaction is the hyperfine coupling between the electronic and nuclear magnetic moments of the Ho^{3+} magnetic ions.

$$H_{\rm hyp} = A\sum_i \epsilon_i(\mathbf{I}_i\cdot\mathbf{J}_i) \ . \tag{2.16}$$

The hyperfine constant $A \approx 39$ mK is anomalously large in Ho^{3+}-based materials [1, 57, 75]. Finally, if one applies an external magnetic field to the system, then the magnetic Ho^{3+} moment couples to the external magnetic field $\mathbf{B}$ via Zeeman interaction. Thus, the complete Hamiltonian of the system with an applied magnetic field B_x is written as

$$\begin{aligned} H \ &= \ \sum_i \epsilon_i V_{\rm CF}(\mathbf{J}_i) - g_L\mu_{\rm B}\sum_i \epsilon_i \mathbf{B}\cdot\mathbf{J}_i \\ &\quad + H_{\rm dip} + H_{\rm exch} + H_{\rm hyp} \ . \end{aligned} \tag{2.17}$$

The first two terms are single ion interactions, where $V_{\rm CF}$ describes the strong crystal field interactions which has been discussed in Section 2.2 . The second term is the Zeeman interaction.

In the next chapter we will see that, for sufficient low temperatures, an effective spin-$\frac{1}{2}$ Hamiltonian can be derived from the full microscopic Hamiltonian of Eq. (2.17). We will see how the low energy effective model can assist us in studying the low temperature behaviour of $LiHo_xY_{1-x}F_4$ analytically and numerically.

Chapter 3

Effective Spin-1/2 Theory

3.1 Introduction

In condensed matter physics systems with strongly interacting quantum mechanical degrees of freedom, it is often a challenge to explain physical phenomena from a truly first principle atomistic point of view. In systems where there are high energy scales well separated from a low-energy sector, effective low-energy theories offer the advantage of a reformulation of the problem with a Hilbert space with an exponentially smaller number of states. There are various methods to carry out this reformulation [85, 86]. These methods usually consists of projecting the Hamiltonian and operators onto the subspace of the low energy levels. The effect of higher orders are usually incorporated perturbatively. However, the reduction of the Hilbert space is not priceless. The price is a much complicated form for the effective operators associated to physical observables as well as the effective Hamiltonian in the new reduced subspace compared with the original fully microscopic Hamiltonian. A well known and topical example where such an approach is used is in the derivation of an effective spin-only model starting from a Hubbard model describing electrons hopping on a lattice. It is commonly accepted that the low-energy magnetic excitations of a Hubbard model with a large on-cite Coulomb repulsion U are easier to investigate within an effective spin Hamiltonian than the full spectrum of the Hubbard model [87, 86, 88]. At least, in the context of the

Hubbard model, it has been shown that different methods for constructing a low-energy effective Hamiltonian leads to equivalent results [86]. Generally speaking, the only requirement to be able to derive an effective model is to have a small parameter, which is t/U in the previous example, where t is the nearest-neighbor hopping constant.

In many magnetic materials, the ground state degeneracy of the otherwise free magnetic ions can be partially lifted by the crystal field effect. In a number of situations, the energy scales associated with the spin-spin interactions are much smaller than the energy gap between the single-ion ground state and the excited crystal field states. In such cases, one can, as a first approximation, often neglect the high energy states and reduce the relevant Hilbert space to a much smaller subspace of low energy states. In this chapter, we discuss how to construct a low energy effective spin-$\frac{1}{2}$ Hamiltonian from the full microscopic Hamiltonian of such magnetic systems with a strong crystal field effect. Then, targeting $LiHo_xY_{1-x}F_4$, which is the main focus of this thesis, we derive a low energy effective spin-$\frac{1}{2}$ Hamiltonian for $LiHo_xY_{1-x}F_4$.

In this chapter, prior to any discussion related to obtaining an effective Hamiltonian for $LiHo_xY_{1-x}F_4$, we first introduce in Section 3.2 an easy-axis spin-S ($S \geq 1$) dipolar spin glass toy model Hamiltonian, $\mathcal{H}^{\mathrm{S}}$, in the presence of a nonzero B_x. Motivated by the phenomena displayed by $LiHo_xY_{1-x}F_4$, this model was originally considered by Schechter and collaborators [24, 25, 89] to investigate the general phenomenology of induced random fields in $LiHo_xY_{1-x}F_4$. Based on the general model $\mathcal{H}^{\mathrm{S}}$ introduced in Section 3.2, we derive in Section 3.3 an effective spin-$\frac{1}{2}$ description for $\mathcal{H}^{\mathrm{S}}$.

There are two reasons, which persuade us to study this general anisotropic model and subsequently its effective spin-$\frac{1}{2}$ derivative:

- The anisotropic toy model $\mathcal{H}^{\mathrm{S}}$, which has a simplified structure compared to the actual full Hamiltonian of $LiHo_xY_{1-x}F_4$, is a general model that captures the basic interactions and characteristics that we want to address and investigate in relation with the phenomenology of diluted $LiHo_xY_{1-x}F_4$ in an applied transverse magnetic field. Broadly speaking, the model can be

used to model any dipolar system, where there is a strong Ising anisotropy and, in the absence of any external field, there is a degenerate ground state doublet [6][1,2].

- In a recent argument offered by the authors of Refs. [24, 25, 89], the usefulness of an effective spin-$\frac{1}{2}$ model to capture the physics of a "bare" microscopic (large-spin) anisotropic dipolar spin glass model in the small B_x regime was questioned. Therefore, one might interpret the conclusion of Refs. [24, 25, 89], regarding the inadequacies of an effective spin-$\frac{1}{2}$ model to describe $LiHo_xY_{1-x}F_4$ in $B_x \neq 0$, as a counter example of the precise quantitative usefulness of effective low-energy theories for quantum N-body systems. However, because of the simple structure of this anisotropic toy model, specially for the case that $S = 1$, we can rather easily compare the low energy spectrum of the effective spin-$\frac{1}{2}$ Hamiltonian, derived in Section 3.3, with the low energy spectrum of the full $S = 1$ model introduced in Section 3.2. By doing this, we can validate the general usefulness of the effective Hamiltonian approach. In Chapter 4, we perform an analytical and numerical investigation of the validity of the effective spin-$\frac{1}{2}$ Hamiltonian. Since we will convincingly demonstrate in this chapter the validity of the effective spin-$\frac{1}{2}$ approach, we shall within the following chapters of this thesis, we use an effective spin-$\frac{1}{2}$ description for $LiHo_xY_{1-x}F_4$ to investigate this material theoretically.

In Section 3.4, we return to the $LiHo_xY_{1-x}F_4$ problem and derive an effective spin-$\frac{1}{2}$ Hamiltonian from the full microscopic Hamiltonian of $LiHo_xY_{1-x}F_4$ given in Eq. (2.17). In $LiHo_xY_{1-x}F_4$ the energy scale for dipolar interactions between nearest-neighbor Ho^{3+} ions is about 0.31 K [3]. Collective behaviour in this material occurs at temperatures less than O(1 K) (when $x = 1$ the critical temperature

[1]P. Stasiak and M. J. P. Gingras, in a recent theoretical study, find that the $Ho(OH)_3$ and $Dy(OH)_3$ uniaxial dipolar ferromagnets may constitute a new class of suitable materials to investigate the problem of transverse field physics in an Ising system.

[2]The pairwise ion-ion interactions are considered small, compared to the Ising anisotropic interaction. Therefore, the possibility that these interactions lift the ground state degeneracy is neglected in the discussions that follows.

[3]The displacement $\mathbf{d}$ between two nearest neighbor ions positioned, for example, at $(0, 0, c/2)$ and $(0, a/2, 3c/4)$ in the unit cell of $LiHoF_4$, is $\mathbf{d} = (0, a/2, c/4)$. Therefore, the energy scale of the

is $T_c(B_x = 0) = 1.53$ K). This energy scale is much smaller than the energy gap Δ_E between the two lowest single ion energy states and the next higher crystal field states ($\Delta_E \sim 11$ K) [78]. In this energy scale only the ground doublet is significantly thermally populated. In this case, one can neglect the higher energy states and reduce the full Hamiltonian Hilbert space to a smaller subspace spanned by the two lowest energy states. This enables us to construct a low energy effective spin-$\frac{1}{2}$ Hamiltonian for $LiHo_xY_{1-x}F_4$ [57, 72] . The details of this calculation are discussed in Section 3.4 for both $x = 1$ and $x < 1$. In Sections 3.3 and 3.4, we also show how random fields, which couple to the effective spin-$\frac{1}{2}$ degree of freedom, develop in a natural apparent way, in a *microscopic model* of $LiHo_xY_{1-x}F_4$ for a nonzero B_x [72]. In Section 3.5 we discuss the physical origin of the induced random fields within a mean field picture. In particular, in Chapter 5, we will see that, in $LiHo_xY_{1-x}F_4$, the induced random fields are crucial for explaining how the nonlinear susceptibility χ_3 becomes progressively less singular at the putative paramagnetic to spin glass transition as B_x is increased.

3.2 Anisotropic Spin Hamiltonian

Schechter *et al.* [24, 25] proposed a generic anisotropic spin-S toy model Hamiltonian with long-range dipolar interactions

$$\begin{aligned} \mathcal{H}^{\mathrm{S}} &= -D\sum_i [(S_i^z)^2 - S^2] \\ &- \sum_{i\neq j}\left[\frac{1}{2}V_{ij}^{zz}S_i^zS_j^z + V_{ij}^{zx}S_i^zS_j^x\right] - H_x\sum_i S_i^x \ . \end{aligned} \tag{3.1}$$

This Hamiltonian is a simplified model that preserves the basic characteristics of the proposed microscopic Hamiltonian [57, 72] for $LiHo_xY_{1-x}F_4$. In the absence of an external magnetic field B_x, individual Ho^{3+} spins have an Ising like ground state doublet with a large energy gap between the lowest excited state and the

dipole-dipole interaction between the two nearest neighbor ions is $\left(\frac{g_\parallel \mu_B}{2}\right)^2 \left[|\mathbf{d}|^2 - 3{d_z}^2\right]/|\mathbf{d}|^5 = 0.31$ K ($a = 5.175\mathring{A}$, $c = 10.75\mathring{A}$, $g_\parallel = 13.8$ is the renormalized Lande g factor for $LiHoF_4$ [57], and μ_B is the Bohr magneton.).

ground doublet. Also, for $S = 1$, the excited state of the model in Eq. (3.1) is a singlet, as for Ho^{3+} in $LiHo_xY_{1-x}F_4$ [54, 78]. Here, $D > 0$ is the anisotropy constant mimicking the crystal field, and i, j are the positions of the randomly positioned magnetic moments. $V_{ij}^{\mu\nu}$ denotes the random long-range dipolar interaction between the spins [4], V_{ij}^{zz} stands for the Ising interaction and V_{ij}^{zx} stands for the off-diagonal interaction ($V_{ij}^{\mu\nu} = V_{ij}^{\nu\mu}$ for dipolar interactions). H_x is the field transverse to $\hat{z}$, the direction of the Ising anisotropy. H_x is proportional to the transverse magnetic field B_x. Here, we consider $D \gg H_x, V_{ij}^{\mu\nu}$. For $H_x = 0$, the ground state (GS) of a single spin is doubly degenerate with $S^z = \pm S$. The corresponding states of the doublet are denoted $|S\rangle$ and $|-S\rangle$. The first excited states have $S^z = \pm(S-1)$ and energy $\Omega_0 \equiv (2S-1)D$ with respect to the ground state doublet and with the corresponding states denoted as $|\pm(S-1)\rangle$. Ignoring momentarily the $V_{ij}^{\mu\nu}$ interactions, the Zeeman term, $-H_x \sum_i S_i^x$, lifts the GS degeneracy of the $|\pm S\rangle$ ground doublet, resulting in two new lowest energy states, $|\alpha(H_x)\rangle$ and $|\beta(H_x)\rangle$, with corresponding energies $E_\alpha(H_x)$ and $E_\beta(H_x)$, and with an energy gap

$$\Delta_E(H_x) = E_\alpha(H_x) - E_\beta(H_x) \tag{3.2}$$

between them. For $H_x \ll \Omega_0$, to leading order in perturbation theory, the gap $\Delta_E(H_x)$ is proportional to $(H_x)^{2S}$.[5]

3.3 Effective spin-$\frac{1}{2}$ Description

In this section we derive an effective spin-$\frac{1}{2}$ Hamiltonian for the anisotropic Hamiltonian (3.1). Firstly, we focus on a situation where the temperature considered is negligible compared to Ω_0, and project the spin S operators onto the two-dimensional subspace formed by the two lowest energy eigenstates, $|\alpha(H_x)\rangle$ and $|\beta(H_x)\rangle$. Following Refs. [57, 72], we define an Ising subspace, $|\uparrow\rangle$ and $|\downarrow\rangle$, by performing a

[4] The dipole-dipole coupling $V_{ij}^{\mu\nu}$ is proportional to $\epsilon_i\epsilon_j L_{ij}^{\mu\nu}$

[5] For S=1, using second order degenerate perturbation theory, one finds that $\Delta_E = H_x^2\langle 1|S^x|0\rangle\langle 0|S^x|-1\rangle/\Omega_0$. For $S > 1$, one should go to higher orders of perturbation theory to obtain the leading term proportional to $(H_x)^{2S}$.

rotation

$$\begin{aligned} |\uparrow\rangle &= \frac{1}{\sqrt{2}}(|\alpha\rangle + \exp(i\theta)|\beta\rangle) \\ |\downarrow\rangle &= \frac{1}{\sqrt{2}}(|\alpha\rangle - \exp(i\theta)|\beta\rangle) \ . \end{aligned} \tag{3.3}$$

The phase θ is chosen such that the matrix elements of the operator S^z within the new (Ising) subspace are real and diagonal. In this case, we introduce $S_i^z = C_{zz}\sigma_i^z$. When we are working in a regime where the temperature, H_x and the interactions are much smaller than the energy gap Ω_0, we are allowed to recast $\mathcal{H}^{\rm S}$ in Eq. (3.1) in terms of an effective spin$-\frac{1}{2}$ Hamiltonian, $\mathcal{H}^{\rm S}_{\rm eff}$, that involves the σ^μ Pauli matrices [57]. In this projected subspace, a transverse field $\Gamma = \frac{1}{2}\Delta_E(H_x)$ acts on the effective σ_i^x spin. The projected S_i^μ ($\mu = x, y, z$) operator may be written as:

$$S_i^\mu = C_{\mu 0}(H_x)\sigma^0 + \sum_\nu C_{\mu\nu}(H_x)\sigma_i^\nu \ , \tag{3.4}$$

where

$$\begin{aligned} C_{\mu 0} &= \frac{1}{2}\left[\langle\uparrow|S^\mu|\uparrow\rangle + \langle\downarrow|S^\mu|\downarrow\rangle\right] \ , \\ C_{\mu z} &= \frac{1}{2}\left[\langle\uparrow|S^\mu|\uparrow\rangle - \langle\downarrow|S^\mu|\downarrow\rangle\right] \ , \\ C_{\mu x} &= \frac{1}{2}\left[\langle\uparrow|S^\mu|\downarrow\rangle + \langle\downarrow|S^\mu|\uparrow\rangle\right] \quad \text{and} \\ C_{\mu y} &= \frac{1}{2i}\left[\langle\uparrow|S^\mu|\downarrow\rangle - \langle\downarrow|S^\mu|\uparrow\rangle\right] \ . \end{aligned}$$

The σ_i^μ's are Pauli matrices plus the unit matrix $\sigma^0 \equiv \mathbf{1}$. The $C_{\mu\nu}$ and Δ_E dependence on H_x can be obtained by exact diagonalization [57, 72] of the non-interacting part of $\mathcal{H}^{\rm S}$ (i.e. $V_{ij}^{\mu\nu} = 0$) in Eq. (3.1).

For zero transverse field, $H_x = 0$, the only nonzero $C_{\mu\nu}$ coefficient is $C_{zz}(0) = S$, giving a "*classical*" (effective) low-energy dipolar Ising model

$$\mathcal{H}_{\rm Ising} = -\frac{1}{2}S^2\sum_{i\neq j} V_{ij}^{zz}\sigma_i^z\sigma_j^z. \tag{3.5}$$

Turning on H_x, the coefficients C_{x0} and C_{xx} increase with H_x, while C_{zz} shows a slight decrease with increasing H_x, as shown in Fig. 3.1. Thus, by substituting S_i^z

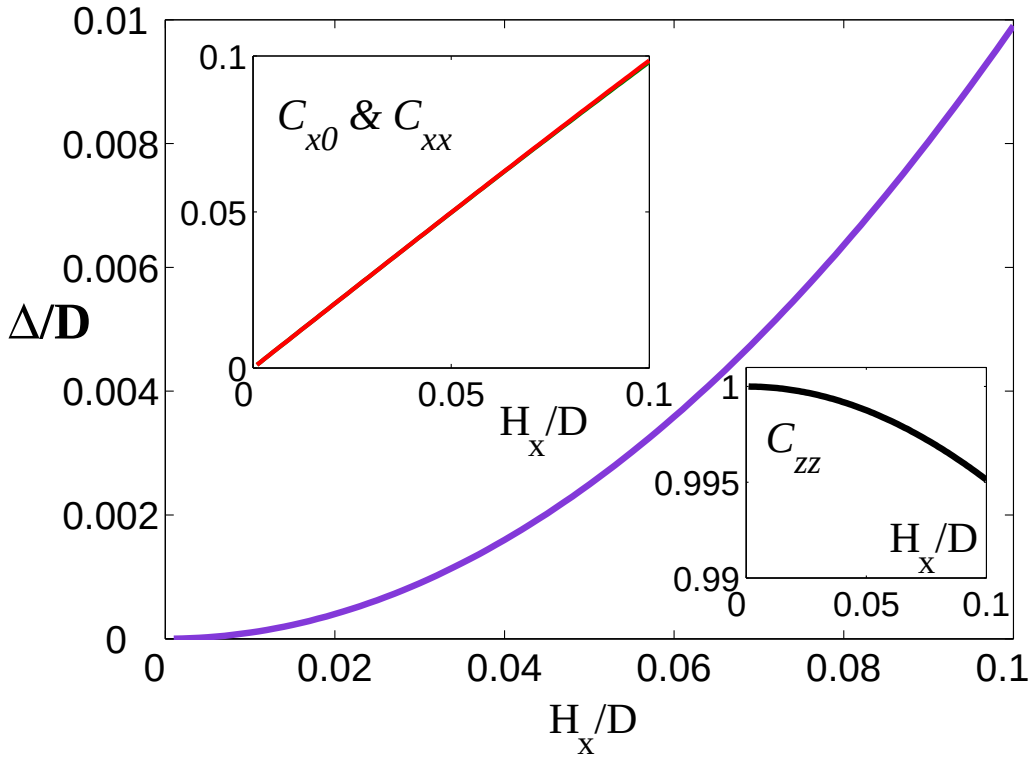

Figure 3.1: Evolution of Δ_E, C_{zz}, C_{x0}, and C_{xx} as a function of the external transverse field H_x for $S = 1$. Δ_E is the energy gap between the two lowest states $\langle\alpha\rangle$ and $\langle\beta\rangle$ in absence of interactions ($V_{ij}^{\mu\nu} = 0$). C_{zz}, C_{x0} and C_{xx} are the nonzero coefficients used to map the matrix elements of $\mathbf{S} = 1$ spin operator within the low-energy manifold spanned by $|\alpha\rangle$ and $|\beta\rangle$ to that of an effective spin-$\frac{1}{2}$ operator.

with $C_{zz}(H_x)\sigma_i^z$ and S_i^x with $C_{xx}(H_x)\sigma_i^x + C_{x0}(H_x)\sigma^0$ in Eq. (3.1), the following effective spin-$\frac{1}{2}$ Hamiltonian[6] $\mathcal{H}_{\rm eff}^{\rm S}$ is obtained

$$\begin{aligned}\mathcal{H}_{\rm eff}^{\rm S} &= -\frac{1}{2}C_{zz}^2(H_x)\sum_{i\neq j}V_{ij}^{zz}\sigma_i^z\sigma_j^z \\ &\quad -C_{zz}(H_x)\left\{C_{xx}(H_x)\sum_{i\neq j}V_{ij}^{zx}\sigma_i^z\sigma_j^x - C_{x0}(H_x)\sum_{i\neq j}V_{ij}^{zx}\sigma_i^z\right\} \\ &\quad -\frac{1}{2}\Delta_E(H_x)\sum_i\sigma_i^x \ . \end{aligned} \tag{3.6}$$

As can be seen, the projection of the $V_{ij}^{zx}S_i^zS_j^x$ term in Eq. (3.1) results in an induced bilinear coupling, $\propto V_{ij}^{zx}\sigma_i^z\sigma_j^x$, and a longitudinal field interaction, $\propto \sigma_i^z$, for $H_x \neq 0$. For low enough transverse field H_x, the Ising dipolar interaction ($\propto V_{ij}^{zz}$) is the dominant term. In Chapter 4 we shall present analytical and numerical evidence, using $\mathcal{H}_{\rm eff}^{\rm S}$, that confirms the validity of an effective spin-$\frac{1}{2}$ approach to the description of random field generation in $S \geq 1$, and especially for an $S = 1$, dipolar spin glass models with strong uniaxial Ising anisotropy and subject to weak external magnetic field H_x transverse to the Ising direction. We shall show that the effective spin-$\frac{1}{2}$ approach is able to capture both the qualitative and *quantitative* aspects of the physics at small H_x, giving results that agree with those obtained using conventional second order perturbation theory. In the next section, we use a similar approach to obtain an effective spin-$\frac{1}{2}$ Hamiltonian for the real microscopic Hamiltonian of $\mathrm{LiHo}_x\mathrm{Y}_{1-x}\mathrm{F}_4$ as opposed to the simple model of Eq. (3.1).

3.4 Effective Spin-$\frac{1}{2}$ Hamiltonian for $\mathbf{LiHo}_x\mathbf{Y}_{1-x}\mathbf{F}_4$

Postponing the demonstration of the quantitative validity of $\mathcal{H}_{\rm eff}^{\rm S}$ to Chapter 4, we carry on with the same procedure as in Section 3.3, used in the previous section to

[6]Recently, Chin and Eastham derived for $B_x = 0$ an effective two-state Hamiltonian for $\mathrm{LiHo}_x\mathrm{Y}_{1-x}\mathrm{F}_4$, via a general second order perturbation theory [55]. In general, the method of Ref. [55] can be implemented for $\mathcal{H}^{\rm S}$ with $H_x \neq 0$. The result to lowest order of perturbation theory is consistent with $\mathcal{H}_{\rm eff}^{\rm S}$ derived above, if we consider the H_x dependence of the $C_{\mu\nu}$ to leading order (see Ref. [55] and Chapter 4, Section 4.2).

derive a low energy effective spin-$\frac{1}{2}$ Hamiltonian for $LiHo_xY_{1-x}F_4$. As discussed in Section 2.3, in Eq. (2.16) the complete Hamiltonian, which describes the magnetic interactions of the Ho^{3+} ions in $LiHo_xY_{1-x}F_4$ in $\mathbf{B} = B_x\hat{x}$ is

$$\begin{aligned} H &= \sum_i \epsilon_i V_{\rm CF}(\mathbf{J}_i) - g_L\mu_{\rm B}\sum_i \epsilon_i B_x \mathrm{J}_i^x \\ &\quad + H_{\rm dip} + H_{\rm exch} + H_{\rm hyp} \ . \end{aligned} \tag{3.7}$$

The first two terms are single ion interactions where $V_{\rm CF}$ denotes the strong crystal field interactions. These crystal field interactions are discussed in detail in Chapter 2, Section 2.2. The second term is the Zeeman interaction, which couples the magnetic moments to the external transverse magnetic field B_x.

As stated previously, the magnetic Ho^{3+} ion in $LiHo_xY_{1-x}F_4$ is characterized by a relatively large hyperfine interaction between the electronic and nuclear moments, The hyperfine interaction plays an important role in a number of $Ho^{3+}-$based magnetic materials [1, 78, 90, 91, 92]. In particular, in $LiHoF_4$, it leads to a significant increase of the zero temperature critical transverse field for the dipolar ferromagnet to quantum paramagnet transition [1, 57]. It also plays an important role in setting the relevant critical transverse magnetic field scale in the dilute $LiHo_xY_{1-x}F_4$ [93].

When $LiHo_xY_{1-x}F_4$ is in a spin glass phase ($x < 0.20$), the system is in an energy range, in which hyperfine interactions are no longer negligible [93, 94](compare $A = 39$ mK with the classical spin glass transition, $T_g(B_x = 0) \sim 100$ mK.). However, in this thesis, we are specifically interested in studying the phenomenology of random fields along the Ising spin directions generated by applied transverse field (See Chapters 4 and 5). Although we discuss our results in the context of $LiHo_xY_{1-x}F_4$, we believe that the random field physics we investigate has a more general scope. The methods we apply to study random field physics in $LiHo_xY_{1-x}F_4$ can be fruitfully applied to other possible dipolar Ising magnetic materials, similar to $LiHo_xY_{1-x}F_4$, for which the hyperfine interactions may not be as strong as those in Ho^{3+}. To avoid possible complexities imposed by these hyperfine interactions, and to concentrate on the physics of the random field phenomena, of $LiHo_xY_{1-x}F_4$, we therefore neglect the role of hyperfine interactions in the process of deriving the effective spin-$\frac{1}{2}$ Hamiltonian[7]. However, in Chapter 5, we will discuss how

[7]The toy model of Eq. (3.1) was also developed to mainly study the random field phenomena

the hyperfine interactions may be somewhat incorporated by renormalizing the interaction parameters in the effective spin-$\frac{1}{2}$ Hamiltonian in order to achieve a closer match with the real system.

Also, in Chapter 6, which is focused on the non-diluted $LiHoF_4$, we will investigate the non-diluted $LiHoF_4$ for small B_x in the vicinity of the classical paramagnet to ferromagnet transition temperature ($T_c(B_x = 0) \sim 1.53$ K). Thus, in Chapter 6, we are interested in a temperature range, where hyperfine interactions can be neglected (see Fig. 1.6).

At this point, in the procedure of obtaining an effective low-energy spin-$\frac{1}{2}$ picture for $LiHo_xY_{1-x}F_4$, we ignore $H_{\rm hyp}$. Now, we consider the first two single ion (non-interacting) terms in H in Eq. (3.7), denoted as

$$H_{\rm single-ion} = V_{\rm CF}(\mathbf{J}) - g_L\mu_{\rm B}B_x{\rm J^x} \ . \tag{3.8}$$

$H_{\rm single-ion}$ can be easily numerically diagonalized for arbitrary transverse field B_x [57]. $|\alpha(B_x)\rangle$ and $|\beta(B_x)\rangle$ are the two lowest states of the single ion Hamiltonian (3.8) for a given B_x. Their corresponding energies are denoted by $E_\alpha(B_x)$ and $E_\beta(B_x)$.

At $B_x = 0$ these two states form a doublet, but $B_x \neq 0$ lifts the degeneracy. Similar to what we did in the previous section in Eq. (3.3), the Ising subspace $|\uparrow\rangle$ and $|\downarrow\rangle$ are chosen by performing a unitary rotation on the $|\alpha(B_x)\rangle$ and $|\beta(B_x)\rangle$ states :

$$\begin{aligned} |\uparrow\rangle &= \frac{1}{\sqrt{2}}(|\alpha\rangle + \exp(i\theta)|\beta\rangle) \\ |\downarrow\rangle &= \frac{1}{\sqrt{2}}(|\alpha\rangle - \exp(i\theta)|\beta\rangle). \end{aligned} \tag{3.9}$$

The phase θ is chosen such that the matrix element of the operator J^z between $|\uparrow\rangle$ and $|\downarrow\rangle$ is real and diagonal, giving $J_i^z = C_{zz}\sigma_i^z$. Since the first excited state, $|\gamma(B_x)\rangle$, above $|\alpha(B_x)\rangle$ and $|\beta(B_x)\rangle$, is at an energy at least seven times higher than $k_{\rm B}T_c(B_x)$, and is repelled for all B_x from the $|\alpha(B_x)\rangle$ and $|\beta(B_x)\rangle$ set (see

induced by an external B_x. Therefore, the hyperfine interaction is not considered in that model as well.

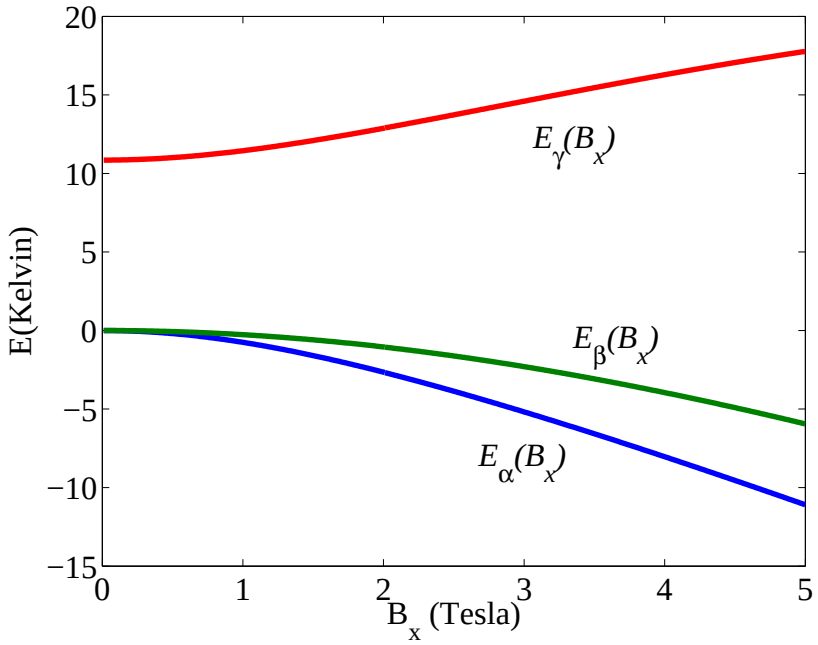

Figure 3.2: The evolution of the energy spectrum of the two lowest ground states $E_\alpha(B_x)$, $E_\beta(B_x)$ and the first excited state $E_\gamma(B_x)$ as a function of B_x. The crystal field V_{CF} was obtained from Refs. [57, 78]. For more details on the crystal field and crystal field parametrization, refer to Section 2.2.

Fig. (3.2)), we henceforth neglect all excited crystal field states and work with a reduced Hilbert space solely spanned by $|\alpha(B_x)\rangle$ and $|\beta(B_x)\rangle$, or equivalently $|\uparrow\rangle$ and $|\downarrow\rangle$. Projecting the single ion Hamiltonian of Eq. (3.8) in this two-dimensional subspace for an arbitrary ion i, we get

$$H_T = \overline{E}(B_x) - \frac{1}{2}\Delta_E(B_x)\sigma^x, \tag{3.10}$$

where $\overline{E}(B_x) = \frac{1}{2}(E_\alpha(B_x) + E_\beta(B_x))$ and $\Delta_E(B_x) = E_\beta(B_x) - E_\alpha(B_x)$. The energy difference between the two lowest states caused by the transverse magnetic field B_x can already be interpreted as an effective transverse field $\Gamma = \frac{\Delta_E(B_x)}{2}$ acting on effective spin-$\frac{1}{2}$ degrees of freedom at each site. The dependence of $\Delta_E(B_x)$ on the magnetic transverse field B_x is plotted in Fig. 3.3.

Since we are working with a two-dimensional subspace for each ion i, we can

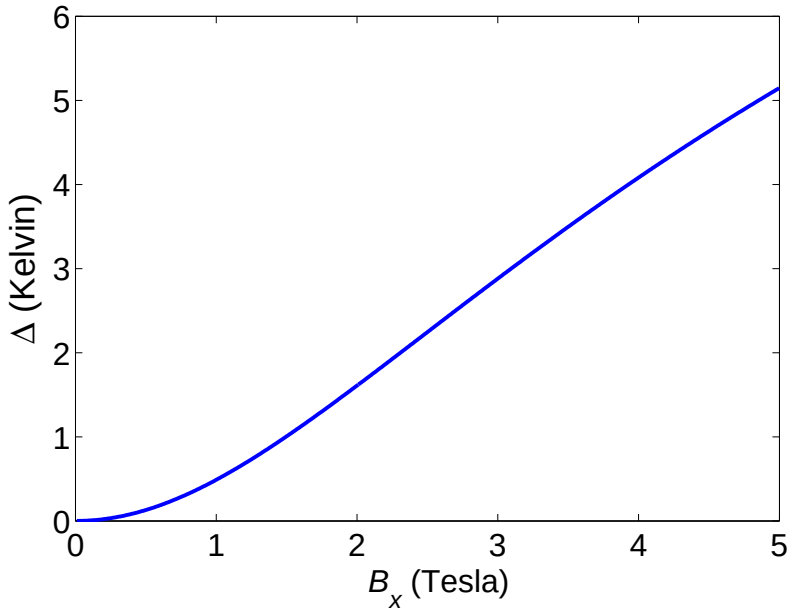

Figure 3.3: The energy splitting of the ground state doublet, $\Delta_E(B_x) \equiv E_\beta(B_x) - E_\alpha(B_x)$, in $LiHoF_4$ as a function of B_x the transverse magnetic field. The crystal field $V_{\rm CF}$ was obtained from Refs. [57, 78]. For more details on the crystal field and crystal field parametrization, refer to Section 2.2.

write the interactions between J_i^μ and J_j^ν in terms of interactions between Pauli matrices. Indeed, any operator in a two-dimensional space can be written as a linear combination of σ_i^μ Pauli matrices plus the unit matrix $\sigma^0 \equiv \mathbf{1}$. In order to express J_i^μ in terms of σ_i^μ, we project J_i^μ in the subspace spanned by $|\uparrow\rangle$ and $|\downarrow\rangle$. Specifically, we write the J^μ operator as

$$\mathrm{J}^\mu = C_{\mu 0}\sigma^0 + \sum_{\nu=x,y,z} C_{\mu\nu}(B_x)\sigma^\nu \ , \tag{3.11}$$

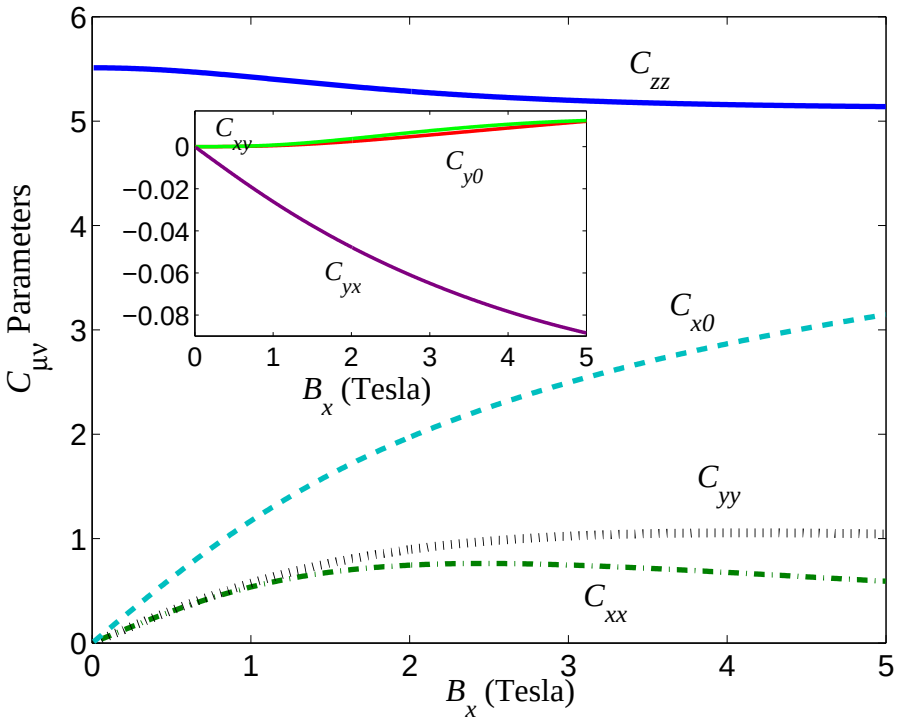

Figure 3.4: The evolution of the $C_{\mu\nu}$ parameters using the crystal field $V_{\rm CF}$ from Refs. [57, 78]. In the inset one can see that $C_{xy} \approx C_{y0}$. Coefficients that are not plotted are zero.

where

$$
\begin{aligned}
C_{\mu 0} &= \frac{1}{2}\left[\langle\uparrow|\mathrm{J}^{\mu}|\uparrow\rangle + \langle\downarrow|\mathrm{J}^{\mu}|\downarrow\rangle\right] \ , \\
C_{\mu z} &= \frac{1}{2}\left[\langle\uparrow|\mathrm{J}^{\mu}|\uparrow\rangle - \langle\downarrow|\mathrm{J}^{\mu}|\downarrow\rangle\right] \ , \\
C_{\mu x} &= \frac{1}{2}\left[\langle\uparrow|\mathrm{J}^{\mu}|\downarrow\rangle + \langle\downarrow|\mathrm{J}^{\mu}|\uparrow\rangle\right] \quad \text{and} \\
C_{\mu y} &= \frac{1}{2i}\left[\langle\uparrow|\mathrm{J}^{\mu}|\downarrow\rangle - \langle\downarrow|\mathrm{J}^{\mu}|\uparrow\rangle\right] \ .
\end{aligned}
$$

Based on the crystal field parameters of Refs. [57, 78], the evolution of the various parameters $C_{\mu\nu}$ and $C_{\mu 0}$ as a function of B_x is plotted in Fig. 3.4. These parameters were obtained by direct numerical diagonalization of the 13×13 matrix representation of $H_{\mathrm{single-ion}}$ given in Eq. (3.8). We see that C_{zz} is the largest term compared to all the other $C_{\mu\nu}$'s.

For the Hamiltonian in Eq. (2.16), the J_i^{μ} operators are substituted by their two dimensional representations given in Eq. (3.11). This leads to a complicated effective spin-$\frac{1}{2}$ Hamiltonian that acts within the Ising subspace of $|\uparrow\rangle$ and $|\downarrow\rangle$. The projection generates various kinds of interactions among the effective spin-$\frac{1}{2}$ spins. Via Eq. (3.9), a specific rotated subspace was chosen, such that $C_{z\mu} = 0$ ($\mu = x, y, 0$; $\sigma^0 \equiv \mathbf{1}$). As shown in the inset of Fig. 3.4, C_{xy}, C_{yx}, and C_{y0} are very small, so the interacting terms containing these coefficients can be safely neglected

for fields below $B_x^c \sim 5$T. Therefore, neglecting these terms, we obtain

$$\begin{aligned} H_{\text{spin}-1/2} &= \frac{1}{2}(g_L\mu_{\text{B}})^2 \,[\, C_{zz}^2(B_x) \sum_{i\neq j} \epsilon_i\epsilon_j L_{ij}^{zz}\sigma_i^z\sigma_j^z \\ &+2C_{zz}(B_x)C_{xx}(B_x) \sum_{i\neq j} \epsilon_i\epsilon_j L_{ij}^{zx}\sigma_i^z\sigma_j^x \\ &+2C_{zz}(B_x)C_{yy}(B_x) \sum_{i\neq j} \epsilon_i\epsilon_j L_{ij}^{zy}\sigma_i^z\sigma_j^y + C_{xx}^2(B_x) \sum_{i\neq j} \epsilon_i\epsilon_j L_{ij}^{xx}\sigma_i^x\sigma_j^x \\ &+C_{yy}^2(B_x) \sum_{i\neq j} \epsilon_i\epsilon_j L_{ij}^{yy}\sigma_i^y\sigma_j^y \,] + \frac{1}{2}\text{J}_{\text{ex}} \sum_{\mu} C_{\mu\mu}^2(B_x) \sum_{i,\text{NN}} \epsilon_i\epsilon_{\text{NN}}\sigma_i^\mu\sigma_{\text{NN}}^\mu \\ &+(g_L\mu_{\text{B}})^2 C_{zz}(B_x)C_{x0}(B_x) \sum_{i\neq j} \epsilon_i\epsilon_j L_{ij}^{zx}\sigma_i^z \qquad (3.12) \\ &+\sum_i \epsilon_i \left[C_{x0}(B_x)C_{xx}(B_x) \left(4\epsilon_{\text{NN}}J_{\text{ex}} + (g_L\mu_{\text{B}})^2 \sum_j \epsilon_j L_{ij}^{xx} \right) \right. \\ &\left. -\frac{\Delta_E(B_x)}{2} \right] \sigma_i^x \ . \end{aligned}$$

When the external magnetic field B_x is equal to zero, only $C_{zz}(0) \neq 0$ and all the other $C_{\mu\nu}$ and $C_{\mu 0}$ are zero. Hence, in absence of an external magnetic field, the system can be described by a simple classical dipolar Ising model [57]. Fortunately, a number of interaction terms are zero or can be neglected with respect to the leading Ising interaction, which is proportional to $C_{zz}^2(B_x)\sum_{i\neq j}\epsilon_i\epsilon_j L_{ij}^{zz}\sigma_i^z\sigma_j^z$. As we can see from Eq. (3.12), an effective $\sigma_i^x\sigma_j^x$ and $\sigma_i^y\sigma_j^y$ pair-wise interactions as well as a linear transverse field along the x direction are induced in the presence of an external magnetic field. As suggested by Fig. 3.5, and already assumed in Ref. [57], we expect the quantum fluctuations induced by these terms via either dipolar or exchange coupling, to be quite small and negligible compared to the quantum fluctuations induced by $\Delta_E(B_x)$. For the pure (disorder free) $LiHoF_4$, where $x = 1$ and $\epsilon_i = 1$, the invariance of the dipolar interactions under lattice mirror symmetries forces $\sum_j L_{ij}^{zx} = 0$. So the linear term with $C_{zz}(B_x)C_{x0}(B_x)\sum_{i\neq j} L_{ij}^{zx}\sigma_i^z$ vanishes. Considering the $C_{zz}(B_x)C_{xx}(B_x)\sum_{i\neq j} L_{ij}^{zx}\sigma_i^z\sigma_j^x$ term, because of lattice mirror symmetry, one has $\sum_{i\neq j} L_{ij}^{zx}\sigma_i^z\left\langle\sigma_j^x\right\rangle = 0$. Therefore, this term can only contribute via thermal fluctuations above the vanishing mean-field contribution. Since $\frac{C_{x0}(B_x)}{C_{zz}(B_x)} < 1$, we expect the (second order) thermal fluctuation contribution effects from the above

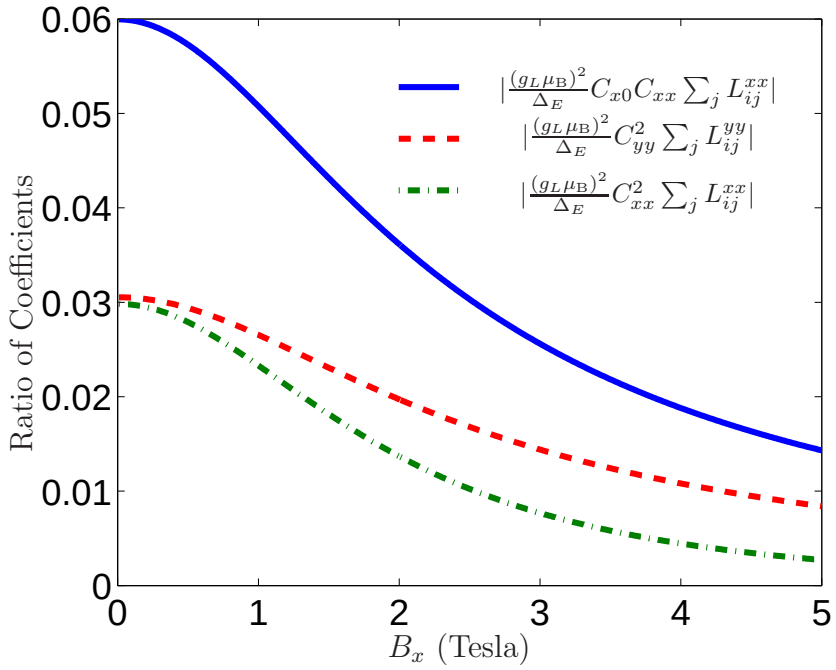

Figure 3.5: The ratio of the typical value of terms neglected in Hamiltonian (3.13) respect to Δ_E, using the crystal field $V_{\rm CF}$ from Refs. [57, 78] and the dipolar sum is performed for a long cylindrical sample.

$\sigma_i^z\sigma_j^x$ term to be small. Hence we neglect the $C_{zz}(B_x)C_{xx}(B_x)\sum_{i\neq j}L_{ij}^{zx}\sigma_i^z\sigma_j^x$ term in the effective spin-$\frac{1}{2}$ Hamiltonian $H_{\text{spin}-1/2}$. Consequently, the spin-$\frac{1}{2}$ Hamiltonian in Eq. (3.12) can be further simplified to a familiar looking transverse field Ising Hamiltonian with a dipolar and nearest-neighbor exchange Ising interaction.

$$\begin{aligned} H_{\text{spin}-1/2}^{\text{pure}} &= \frac{1}{2}C_{zz}^2(B_x)\left[(g_L\mu_{\text{B}})^2\sum_{i\neq j}L_{ij}^{zz}\sigma_i^z\sigma_j^z\right. \\ &+ \left. J_{\text{ex}}\sum_{i,\text{NN}}\sigma_i^z\sigma_{\text{NN}}^z\right] - \frac{\Delta_E(B_x)}{2}\sum_i\sigma_i^x\ . \end{aligned} \tag{3.13}$$

We should emphasize that for diluted $\text{LiHo}_x\text{Y}_{1-x}\text{F}_4$, where $x<1$, since the lattice mirror symmetries are broken, the two latter terms, proportional to $\sum_{i\neq j}L_{ij}^{zx}\epsilon_i\epsilon_j\sigma_i^z$ and $\sum_{i\neq j}\epsilon_i\epsilon_jL_{ij}^{zx}\sigma_i^z\left\langle\sigma_j^x\right\rangle$, can no longer be neglected [72]. However, as discussed in the Introduction, for $B_x>0$, a longitudinal *random field* (RF) term $\propto\sigma_i^z$ emerges. The bilinear $\sigma_i^x\sigma_j^z$ also provides a "mean-field" contribution to the longitudinal RFs, $\langle\sigma_i^x\rangle\sigma_j^z$, as well as transverse RFs, $\langle\sigma_i^z\rangle\sigma_j^x$ [24, 93]. We find that $C_{xx}/C_{x0}\lesssim 1$ for all $B_x>0$ so that the leading correction to H_{TFIM} is indeed a (correlated) random field term $\sim\sum_i h_i^z\sigma_i^z$ with $h_i^z\propto C_{x0}C_{zz}\sum_j\epsilon_jL_{ij}^{xz}$ [72, 24, 56]. Therefore, for the diluted $\text{LiHo}_x\text{Y}_{1-x}\text{F}_4$, by only keeping the leading interactions in the spin-$\frac{1}{2}$ effective Hamiltonian in Eq. (3.12), we obtain the Hamiltonian

$$\begin{aligned} H_{\text{spin}-1/2}^{\text{dil}} &= \frac{1}{2}C_{zz}^2(B_x)\left[(g_L\mu_{\text{B}})^2\sum_{i\neq j}\epsilon_i\epsilon_jL_{ij}^{zz}\sigma_i^z\sigma_j^z + J_{\text{ex}}\sum_{i,\text{NN}}\epsilon_i\epsilon_{\text{NN}}\sigma_i^z\sigma_{\text{NN}}^z\right] \\ &+(g_L\mu_{\text{B}})^2C_{zz}(B_x)\Big[C_{xx}(B_x)\sum_{i\neq j}\epsilon_i\epsilon_jL_{ij}^{zx}\sigma_i^z\sigma_j^x \\ &+C_{x0}(B_x)\sum_{i\neq j}\epsilon_i\epsilon_jL_{ij}^{zx}\sigma_i^z\Big] - \frac{\Delta_E(B_x)}{2}\sum_i\epsilon_i\sigma_i^x\ . \end{aligned} \tag{3.14}$$

3.5 Physical Origin of the Random Fields (a Mean-Field Picture)

Having derived the effective spin-$\frac{1}{2}$ low-energy theory for diluted $\text{LiHo}_x\text{Y}_{1-x}\text{F}_4$ (Eq. (3.14)) and showed how both random longitudinal fields and random bilin-

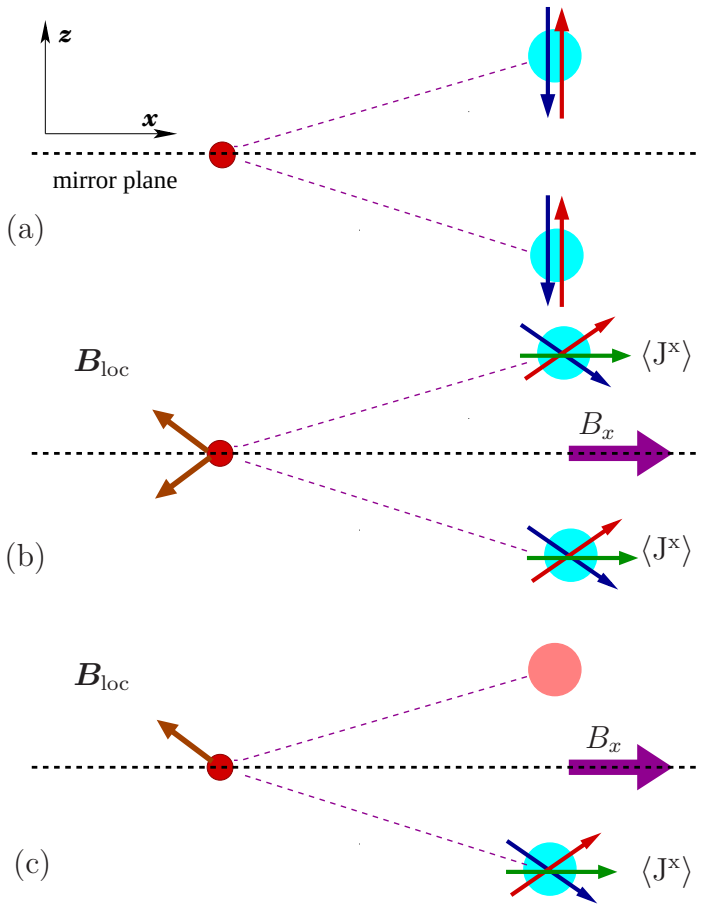

Figure 3.6: The induction of effective local random fields by B_x in the presence of a destructed mirror plane symmetry. Here, we consider the case which the system is in the paramagnetic regime. The magnetic moments of the blue ions fluctuate in the $\hat{z}$ direction. (a) The system is not diluted and B_x=0. Considering a reference point on the mirror plane, the magnetic ions generate no local field at the reference point. (b) The system is not diluted and $B_x \neq 0$. The B_x cants the magnetic moments (green arrow) in the $\hat{x}$ direction. The nonzero $\langle \mathrm{J}^x \rangle$s effectively, generate local $\boldsymbol{B}_{\rm loc}$ fields at the point of reference via dipolor interactions. As it is shown, due to symmetry, the total local field $\boldsymbol{B}_{\rm loc}$ in the $\hat{z}$ direction vanishes. (c) The system is diluted and $B_x \neq 0$. Due to the destruction of symmetry, there is now a nonzero effective field component in the $\hat{z}$ direction.

ear terms develop, it is worthwhile to discuss the physics at play by considering a simple mean-field argument applied to the bare dipole-dipole interaction $H_{\rm dip}$ of Eq. (2.13) as a part of the full microscopic Hamiltonian for $LiHo_xY_{1-x}F_4$ of Eq. (2.16)[8]. Quite simply, the application of a field B_x along $\hat{x}$ breaks the symmetry $J_i^x \to -J_i^x$ in the system. If we consider the single ion Hamiltonian of Eq. (3.8), for $B_x = 0$ the expectation values of J_i^x are

$$\langle\alpha(B_x=0)|J_i^x|\alpha(B_x=0)\rangle = \langle\beta(B_x=0)|J_i^x|\beta(B_x=0)\rangle = 0 \ , \tag{3.15}$$

while for $B_x \neq 0$ we have

$$\langle\alpha(B_x)|J_i^x|\alpha(B_x)\rangle \neq 0 \quad \text{and} \quad \langle\beta(B_x)|J_i^x|\beta(B_x)\rangle \neq 0 \ . \tag{3.16}$$

This non-zero expectation value of J_i^x can be interpreted as a finite "*canting*" of the Ho^{3+} magnetic moments. However, because of this canting, each Ho^{3+} magnetic moment $\boldsymbol{\mu}_i(\boldsymbol{r}_i)$ acts as a source of local internal magnetic field, $\boldsymbol{B}_{\rm loc}(\boldsymbol{r}_j)$, at sites $\boldsymbol{r}_j$. In the pure material, the lattice mirror symmetries make the y and z components of $\boldsymbol{B}_{\rm loc}$ vanish. However, they cease to vanish in the diluted case, and both the y and z components of $\boldsymbol{B}_{\rm loc}$ become random in sign and in magnitude (z being the largest component), generating a random field. In other words, if we consider the off-diagonal term of the dipole-dipole interaction

$$H_{\rm dip}^{xz} = (g_L\mu_{\rm B})^2 \sum_{i\neq j} \epsilon_i\epsilon_j L_{ij}^{xz} \mathrm{J_i^x J_j^z} \ , \tag{3.17}$$

then at a mean-field level we have

$$H_{\rm dip}^{xz} \approx (g_L\mu_{\rm B})^2 \sum_{i\neq j} \epsilon_i\epsilon_j L_{ij}^{xz} \langle \mathrm{J_i^x}\rangle \mathrm{J_j^z} \ , \tag{3.18}$$

where $\boldsymbol{B}_{\rm loc}^z(\boldsymbol{r}_j) = (g_L\mu_{\rm B})\sum_i \epsilon_i L_{ij}^{xz}\langle \mathrm{J_i^x}\rangle$ can be interpreted as an effective local random field acting on the position $\boldsymbol{r}_j$ in the $\hat{z}$ direction. Fig. 3.6 is a schematic picture, illustrating the phenomenology of the random field generation. In Fig. 3.6, to avoid the contributions of the longitudinal Ising interactions in the illustration,

[8]The argument proposed here is quite generic and can be employed to the dipolar spin glass toy model Hamiltonian, $\mathcal{H}^{\rm S}$, of Eq. (3.1).

which would make our drawing more complicated, the system is assumed to be in the paramagnetic phase.

The phenomenon discussed here is valid for any general random spin system for which the effective spin-spin interaction are anisotropic and contain off-diagonal terms which couple to the applied transverse field direction $\hat{x}$.

In Chapter 5, we will see that for $x < 1$, the induced random field interactions lead to a smearing of the nonlinear susceptibility χ_3 at the spin-glass transition with increasing B_x and render the B_x-induced quantum criticality in $LiHo_xY_{1-x}F_4$ likely inaccessible. Now, within the more simple framework of the effective spin-$\frac{1}{2}$ picture, we are able to numerically study the phase diagram of $LiHoF_4$. Also, for the disordered $LiHo_xY_{1-x}F_4$, the effective spin-$\frac{1}{2}$ model is a simple framework to perform a mean field study of the system.

Chapter 4

Quantitative Validity of the Effective Spin-1/2 Description

In Chapter 3, we developed an effective spin-$\frac{1}{2}$ theory, for the $S \geq 1$ model of Eq. (3.1). Subsequently, in a similar way, we developed an effective spin-$\frac{1}{2}$ theory for the microscopic model of $LiHo_xY_{1-x}F_4$ in nonzero B_x for both $x = 1$ and $x < 1$ (see Eq. (3.13) and Eq. (3.14)). Within this framework, for $x < 1$, we found that correlated random fields are induced by the external magnetic field transverse to the Ising direction. In this chapter, the validity of an effective spin-$\frac{1}{2}$ approach is investigated in the context of a spin glass model. All discussions pertaining to the non-diluted material is postponed to Chapter 6.

Schechter and collaborators [24, 25, 89] recently investigated in a series of papers the general phenomenology of induced random fields in $LiHo_xY_{1-x}F_4$. To do so, they considered in Refs. [24, 25] an easy-axis spin-S ($S \geq 1$) dipolar spin glass toy model Hamiltonian, in presence of a nonzero B_x. By using second order perturbation theory, invoking a scaling droplet picture for spin glasses [28], and using an Imry-Ma type argument [46], Schechter *et al.* [24, 25] calculated the finite energy δE required to flip the spins within a spin glass droplet. In their calculations, they found a limit on how large the spin glass correlation length[1] ξ can grow as the system is cooled from the paramagnetic phase. The behaviour of the system,

[1] ξ is the typical length of domains within which the spin glass ordering is maintained [24, 25].

and the corresponding δE, is found to be analogous to that of a spin glass in a random magnetic field which, according to the droplet model, does not show a spin glass transition in nonzero field[2]. As a result, Refs. [24, 25] argue that no spin glass transition can occur in a dipolar spin glass where random off-diagonal dipolar interactions and an applied transverse magnetic field are simultaneously at play.

The results of Refs. [24, 25] as well as ours ours in Section 5 derive from the notion that, the applied transverse field generates effective random fields. The average magnetization along the direction of the applied transverse field induces the random fields via the off-diagonal part of the dipolar interactions, which couple the Ising $\hat{z}$ component with the perpendicular $\hat{x}$ and $\hat{y}$ components (see Section 3.5 and Fig. 3.6). However, what is not clear, is how the random fields in these two calculations are related or if, in fact, whether they are equivalent. In their studies, the authors of Refs. [24, 25] argued, correctly, that consideration of a model with large spin ($S \geq 1$) is crucial in order to understand the weak field response of the spin glass phase in either their toy model or in $LiHo_xY_{1-x}F_4$. Furthermore, exact diagonalization results of an $S = 1$ dipolar spin glass model with easy-axis anisotropy provided further quantitative support to the theoretical arguments as to the scaling behaviour of δE with both B_x and the number of spins in the system [24, 25]. Ref. [25] also considered an effective anisotropic spin-$\frac{1}{2}$ dipolar Ising model in a transverse field, but with the off-diagonal dipolar interactions rescaled compared to the longitudinal Ising coupling. For that model, their numerical results did not conform with those obtained for the "bare" (high-energy) anisotropic $S = 1$ model [24, 25]. Partially on the basis of those results, and seemingly confirming a previous suggestion [24], Ref. [25], concludes that an effective spin-$\frac{1}{2}$ model, such as that developed in Section 3.3 and used in Chapter 5 and Ref. [72], is not sufficient

[2]The argument of Ref. [28] regarding the absence of a spin glass transition in a magnetic field pertains to the case of a *uniform* magnetic field. However, the same conclusion applies to the case of a random field as long as the distribution of couplings is such that one is deep in the spin glass regime and that the randomness in the sign of the random field can be "gauged away". In this context, a recent Monte Carlo study of the Ising spin glass specifically considered the case of *random fields* as opposed to a uniform field in order to check for the existence of a spin glass transition in nonzero random field (and the presence of an Almeida-Thouless line) for a three-dimensional Ising spin glass model (see A. P. Young and H. G. Katzgraber in Ref. [95]).

to capture the physics in the small B_x regime compared to the "bare" microscopic (large-spin) anisotropic dipolar spin glass model $\mathcal{H}^{\rm S}$ of Eq. (3.1). The question of the usefulness of an effective spin-$\frac{1}{2}$ model to describe random field phenomena in the dilute ferromagnetic regime of $LiHo_xY_{1-x}F_4$ [58, 70, 72] was also raised in Ref. [89].

Considering a perspective beyond the specific problematic of $LiHo_xY_{1-x}F_4$, one could interpret the conclusion of Refs. [24, 25, 89], regarding the inadequacies of an effective spin-$\frac{1}{2}$ model to describe $LiHo_xY_{1-x}F_4$ in $B_x \neq 0$, as a counter example of the precise quantitative usefulness of effective low-energy theories for quantum N-body systems. It is therefore of interest to investigate with some scrutiny the mathematical justification for an effective spin-$\frac{1}{2}$ model for $LiHo_xY_{1-x}F_4$ with $B_x \neq 0$. More specifically, the question that we ask here is: to what extent are the explicitly manifest random fields derived in an effective low-energy theory, such as in Ref. [72], related to the random field-like effects at play in perturbation theories, such as used in Refs. [24, 25]? On the basis of analytical calculations and exact diagonalizations, we highlight the fact that an effective spin-$\frac{1}{2}$ Hamiltonian properly derived from an $S = 1$ high-energy toy model $\mathcal{H}$, such as the one proposed in Refs. [24, 25] (see Eq. (1) in Section 4.1), is a quantitatively valid and controlled approach.

This chapter is organized as follows. In Section 4.1 we consider the easy-axis spin-S ($S \geq 1$) dipolar spin glass toy model Hamiltonian of Eq. (3.1) [24, 25], in presence of a nonzero B_x. Similarly to the approach of Schechter *et al.* [24, 25], we employ second order perturbation theory and invoke the scaling droplet picture of Fisher and Huse for spin glasses [28] and an Imry-Ma type argument [46], to calculate the finite energy δE required to flip the spins within a spin glass droplet. A limit on how large the spin glass correlation length ξ can grow to as the system is cooled from the paramagnetic phase is determined [24, 25]. Then in Section 4.2, we follow the same procedure using the effective spin-$\frac{1}{2}$ Hamiltonian of Eq. (3.6) to lowest order. In Section 4.3 results from exact diagonalization calculations are reported. It should be emphasized that the numerical exact diagonalization results reported here, have been obtained by Francois Vernay, who was a postdoctoral fellow in the condensed matter theory group of University of Waterloo from September

2005 to September 2007. The combined analytical work done by the author of this thesis and Dr. Vernay was published in Ref. [56]. The comparison of the numerical results for $S = 1$ and the effective spin-$\frac{1}{2}$ models directly confirms the quantitative validity of the effective Hamiltonian approach. Section 4.4 concludes the Chapter.

4.1 Anisotropic Spin Hamiltonian

Here, just as a reminder, we briefly rewrite the Schechter *et al.* [24, 25] generic anisotropic spin-S toy model Hamiltonian of Eq. (3.1) with long-range dipolar interactions:

$$\begin{aligned} \mathcal{H}^{\rm S} &= -D\sum_i[(S_i^z)^2 - S^2] \\ &- \sum_{i\neq j}\left[\frac{1}{2}V_{ij}^{zz}S_i^zS_j^z + V_{ij}^{zx}S_i^zS_j^x\right] - H_x\sum_i S_i^x \ . \end{aligned}$$

This Hamiltonian is a simplified model that preserves the basic characteristics of the proposed microscopic Hamiltonian [57, 72] of Eq. (2.16) for $LiHo_xY_{1-x}F_4$.

Invoking the spin glass droplet scaling picture of Fisher and Huse [28] and using an Imry-Ma [46] type argument, one can calculate the energy required to flip a spin glass droplet of size L containing $N \sim L^d$ spins, with d the number of space dimensions (here $d = 3$). This energy cost is due to the perturbative quantum term

$$\mathcal{H}_\perp^{\rm S} \equiv -\sum_{i\neq j}V_{ij}^{zx}S_i^zS_j^x - H_x\sum_i S_i^x \ , \tag{4.1}$$

in $\mathcal{H}^{\rm S}$ above, which does not commute with the classical term

$$\mathcal{H}_\parallel^{\rm S} = -D\sum_i[(S_i^z)^2 - S^2] - \frac{1}{2}\sum_{i\neq j}V_{ij}^{zz}S_i^zS_j^z \ . \tag{4.2}$$

We first consider only $\mathcal{H}_\parallel$. We invoke the droplet picture that affirms that there exist only two degenerate ground states related by a global spin flip $S_i^z \to -S_i^z$ symmetry in a spin glass [28]. $|\Phi_S\rangle$ and $|\widetilde{\Phi}_S\rangle$ denote these two collective (doubly-degenerate) Ising spin glass ground states of the system. These two ground states

are related by the global $S_i^z \to -S_i^z$ symmetry, where each spin is either in its $|+S\rangle$ state or its $|-S\rangle$ state. As discussed in Refs. [24, 25], nonzero $\mathcal{H}_\perp$ lifts the ground state degeneracy, as we now review in order to make contact with our own approach and results presented below in Sections 4.2 and 4.3.

The lowest energy excited states (above the otherwise two degenerate $|\Phi_S\rangle$ and $|\widetilde{\Phi}_S\rangle$ ground states) are $|\phi^k_{(S-1)}\rangle$ and $|\widetilde{\phi}^k_{(S-1)}\rangle$ states, in which the k'th spin has its S^z quantum value changed from $+S$ to $+(S-1)$ or from $-S$ to $-(S-1)$. Using standard second order degenerate perturbation theory [82], and considering only excitations to the (intermediate excited) $|\phi_{(S-1)}\rangle$ and $|\widetilde{\phi}^k_{(S-1)}\rangle$ states, the energy difference between $|\Phi_S\rangle$ and $|\widetilde{\Phi}_S\rangle$ is

$$\delta E = \sqrt{\left(H_{\Phi_S,\Phi_S} - H_{\widetilde{\Phi}_S,\widetilde{\Phi}_S}\right)^2 + 4|H_{\Phi_S,\widetilde{\Phi}_S}|^2}\ , \tag{4.3}$$

where

$$\begin{aligned} H_{\Phi_S,\Phi_S} &= -\frac{1}{\Omega_0}\sum_k \left|\left\langle \Phi_S \middle| H_\perp \middle| \phi^k_{(S-1)}\right\rangle\right|^2 , \\ H_{\widetilde{\Phi}_S,\widetilde{\Phi}_S} &= -\frac{1}{\Omega_0}\sum_k \left|\left\langle \widetilde{\Phi}_S \middle| H_\perp \middle| \widetilde{\phi}^k_{(S-1)}\right\rangle\right|^2 , \end{aligned}$$

and

$$\begin{aligned} H_{\Phi_S,\widetilde{\Phi}_S} = &- \frac{1}{\Omega_0}\sum_k \left\langle \Phi_S \middle| H_\perp \middle| \phi^k_{(S-1)}\right\rangle \left\langle \phi^k_{(S-1)} \middle| H_\perp \middle| \widetilde{\Phi}_S\right\rangle \\ &+ \left\langle \Phi_S \middle| H_\perp \middle| \widetilde{\phi}^k_{(S-1)}\right\rangle \left\langle \widetilde{\phi}^k_{(S-1)} \middle| H_\perp \middle| \widetilde{\Phi}_S\right\rangle , \end{aligned}$$

where we have taken the ground state energy to be zero. Here, $\Omega_0 = (2S-1)D$. Since $\langle \Phi_S | H_\perp | \widetilde{\phi}^k_{(S-1)}\rangle = \langle \widetilde{\Phi}_S | H_\perp | \phi^k_{(S-1)}\rangle = 0$, we have $H_{\Phi_S,\widetilde{\Phi}_S} = 0$ Subtracting $H_{\widetilde{\Phi}_S,\widetilde{\Phi}_S}$ from H_{Φ_S,Φ_S}, only the odd terms in H_x remain, with the even terms in H_x canceling each other out. Finally, to lowest order in H_x, we get

$$\delta E = 2S\frac{H_x}{\Omega_0}\sum_{i\neq j} V^{xz}_{ij}\ \langle \Phi_s | S^z_i | \Phi_s\rangle\ . \tag{4.4}$$

Taking the largest V^{xz}_{ij} to have a typical value $V_\perp$, the typical energy gained by flipping a droplet of $N \sim L^d$ spins is, to leading order in H_x,

$$\langle |\delta E|\rangle \propto \frac{S^2 H_x V_\perp \sqrt{N}}{\Omega_0}, \tag{4.5}$$

indicating that the total energy gain increases with H_x linearly to leading order, as first found in Refs. [24, 25].

This decrease in energy is to be compared with the energy cost due to the formation of a spin glass droplet [28]. This energy cost scales with the linear size L of the droplet, $L = N^{1/3}$, as $\approx S^2 V_\parallel L^{\theta_d}$, where $V_\parallel$ is the typical value of the largest V_{ij}^{zz}, which one typically expects to be of the same order as $V_\perp$. Comparing the energy gain $\langle|\delta E|\rangle$ of Eq. (4.5) with the energy cost $S^2 V_\parallel L_d^\theta$ for droplet formation, Refs. [24, 25] find a finite spin-glass correlation length ξ, identified with L, which, for *small* H_x, scales as

$$\xi \approx \left(\frac{\Omega_0 V_\parallel}{H_x V_\perp}\right)^{\frac{1}{3/2-\theta_d}} . \tag{4.6}$$

Based on an argument by Fisher and Huse [28], $\theta_d \leq (d-1)/2$, or $\theta_d < 3/2$ here for $d = 3$. Hence, turning on H_x leads to a reduction of the correlation length $\xi(H_x)$, inhibiting its divergence which occurs when $H_x = 0$. In other words, the presence of the applied transverse H_x leads, via the presence of the off-diagonal V_{ij}^{xz} spin-spin interactions, to a destruction of the spin glass phase with a typical spin glass correlation length ξ decreasing as H_x increases. According to Refs. [24, 25], this is the mechanism via which the non-linear magnetic susceptibility χ_3 no longer diverges in $LiHo_xY_{1-x}F_4$ as H_x is increased from zero [36][3].

4.2 Effective spin-$\frac{1}{2}$ Description

In the previous section we reviewed the arguments of Refs. [24, 25] which lead to the key result of Eq. (4.4). We now proceed to show that the reformulation of the microscopic spin Hamiltonian, Eq. (3.1), in terms of the effective spin-$\frac{1}{2}$ model of

[3] In Chapter 5 we find, using a replica-symmetric mean-field theory calculation (in the static approximation), that χ_3 becomes immediately non-singular as H_x is turned on. However, as that calculation proceeds with a mean-field framework, it makes no comment as per the existence or not of a thermodynamic spin glass transition in presence of nonzero H_x in a *real* three-dimensional system. In other words, in Chapter 5, the elimination of the divergence in the nonlinear susceptibility via the random fields does not eliminate the spin glass transition at finite temperature in infinite dimension, which is signaled by the more complex mathematical concept of replica symmetry breaking rather than the mere divergence of χ_3.

Eq. (3.6), obtained in Chapter 3, leads identically to Eq. (4.4) in the limit of small H_x/D. We focus on a situation where the temperature considered is low compared to Ω_0, and we are able to project the spin S operators onto the two-dimensional subspace formed by the two lowest energy eigenstates.

As a reminder, the effective spin-$\frac{1}{2}$ Hamiltonian of Eq. (3.6)

$$\begin{aligned}\mathcal{H}^{\rm S}_{\rm eff} &= -\frac{1}{2}C^2_{zz}(H_x)\sum_{i\neq j}V^{zz}_{ij}\sigma^z_i\sigma^z_j \\ &\quad -C_{zz}(H_x)\Bigg\{C_{xx}(H_x)\sum_{i\neq j}V^{zx}_{ij}\sigma^z_i\sigma^x_j \\ &\quad -C_{x0}(H_x)\sum_{i\neq j}V^{zx}_{ij}\sigma^z_i\Bigg\}-\frac{1}{2}\Delta_E(H_x)\sum_i\sigma^x_i\ ,\end{aligned}$$

is rewritten here. One is reminded here that, as discussed in Chapter 3, the $C_{\mu\nu}(H_x)$'s are coefficients which connect the $S\geq 1$ operators to the spin-1/2 Pauli operators via the relation

$$S^\mu_i = C_{\mu 0}(H_x)\sigma^0 + \sum_\nu C_{\mu\nu}(H_x)\sigma^\nu_i\ .$$

when the S^μ_i operators are projected onto the two dimensional subspace of the two lowest states. As discussed in Chapter 3, the projection of the $V^{zx}_{ij}S^z_iS^x_j$ term in Eq. (3.1) results in an induced random bilinear coupling, $\propto\sigma^z_i\sigma^x_j$, and a longitudinal random field interaction, $\propto\sigma^z_i$, for $H_x\neq 0$. For low enough transverse field H_x, the Ising dipolar interaction ($\propto V^{zz}_{ij}$) is the dominant term.

Having the effective Hamiltonian of Eq. (3.6), we now repeat the calculation of δE within this effective spin-$\frac{1}{2}$ framework by again bringing in the spin glass droplet picture [28]. For $H_x=0$, we denote $|\psi\rangle$ the ground state of the effective spin-$\frac{1}{2}$ system where $|\psi\rangle$ is a specific realization of the $\uparrow$ and $\downarrow$ (effective) Ising spins configuration[4]. For $H_x=0$, because of time reversal symmetry, the time reversed state $|\widetilde{\psi}\rangle$, which is obtained by flipping all the spins of $|\psi\rangle$, is a ground state of the system as well. We thus have a ground state doublet in the droplet picture for the

[4]For $H_x=0$, $|\uparrow\rangle=|S\rangle$ and $|\downarrow\rangle=|-S\rangle$, which indicates that at $H_x=0$, $|\psi\rangle=|\Phi_S\rangle$.

effective spin model. Carrying on a similar discussion as in the previous section and as in Refs. [24, 25], at low enough H_x within a droplet picture, the symmetry is broken due the presence of the induced random fields in Eq. (3.6). The energy cost to flip the spins over a droplet is,

$$\delta E \equiv \langle\widetilde{\psi}|H_{\rm eff}|\widetilde{\psi}\rangle - \langle\psi|H_{\rm eff}|\psi\rangle$$

which, to lowest order in H_x, gives

$$\delta E \approx 2C_{zz}C_{x0}\sum_{i\neq j} V_{ij}^{xz}\,\langle\psi|\sigma_i^z|\psi\rangle \ . \tag{4.7}$$

Although we have an exact analytical expression for the $C_{\mu\nu}$ coefficients as a function of H_x (which is available for $S \leq 3/2$), in order to compare with Eq. (4.4) above and with Refs. [24, 25], we consider the H_x dependence of the $C_{\mu\nu}$ to leading order in H_x/D. Using standard degenerate perturbation theory, for $S > 1$ and up to second order in H_x[5], the $|\uparrow\rangle$ and $|\downarrow\rangle$ defined in Eq. (3.9) are given by

$$\begin{aligned} |\uparrow\rangle &= \left(1-\frac{H_x^2}{4\Omega_0^2}S\right)|S\rangle + \frac{H_x}{\Omega_0}\sqrt{\frac{S}{2}}|S-1\rangle \\ |\downarrow\rangle &= \left(1-\frac{H_x^2}{4\Omega_0^2}S\right)|-S\rangle + \frac{H_x}{\Omega_0}\sqrt{\frac{S}{2}}|-S+1\rangle \ , \end{aligned} \tag{4.8}$$

recalling that $\Omega_0 = (2S-1)D$. Returning to Eq. (3.4), from which the $C_{\mu\nu}$ are obtained, ($C_{zz} = \frac{1}{2}(\langle\uparrow|S^z|\uparrow\rangle - \langle\downarrow|S^z|\downarrow\rangle)$ and $C_{x0} = \frac{1}{2}(\langle\uparrow|S^x|\uparrow\rangle + \langle\downarrow|S^x|\downarrow\rangle)$), we use Eq. (4.8) to find $C_{zz} \approx S(1-\frac{H_x^2}{2\Omega_0^2})$, $C_{x0} \approx SH_x/\Omega_0$, $C_{xx} \propto (H_x)^{2S-1}$ ($C_{xx} \approx H_x/\Omega_0$ for $S = 1$), while $\Delta_E \propto (H_x)^{2S}$ [6]. Substituting those H_x dependencies back in Eq. (4.7) and keeping terms to lowest order in H_x, the dependence of the energy cost δE is

$$\delta E \approx 2S^2\frac{H_x}{\Omega_0}\sum_{i\neq j} V_{ij}^{xz}\,\langle\psi|\sigma_i^z|\psi\rangle \ . \tag{4.9}$$

[5]For S=1, $|\uparrow\rangle = \left(1-\frac{H_x^2}{4\Omega_0{}^2}\right)|1\rangle + \frac{H_x}{\Omega_0\sqrt{2}}|0\rangle - \frac{H_x^2}{4\Omega_0^2}|-1\rangle$ and $|\downarrow\rangle = \left(1-\frac{H_x^2}{4\Omega_0^2}\right)|-1\rangle + \frac{H_x}{\Omega_0\sqrt{2}}|0\rangle - \frac{H_x^2}{4\Omega_0^2}|1\rangle$, but the final H_x dependence of $C_{\mu\nu}$'s are, to leading order, not changed, and are similar to the $S > 1$ case.

[6]For S=1, using second order degenerate perturbation theory, one finds that $\Delta_E = H_x^2\langle 1|S^x|0\rangle\langle 0|S^x|1\rangle/\Omega_0$. For $S > 1$, one should go to higher orders of perturbation theory obtaining the leading term proportional to $(H_x)^{2S}$.

Referring to Eq. (4.8), we have $S\langle\psi|\sigma_i^z|\psi\rangle \approx \langle\Phi|S_i^z|\Phi\rangle$ to zeroth order in H_x. Hence, we find that the energy cost obtained in the spin-$\frac{1}{2}$ picture is identical to the energy cost given by Eq. (4.4) obtained via a conventional degenerate second order perturbation theory and previously reported in Refs. [24, 25]. Thus, Eq. (4.9) leads to the same RMS energy cost for flipping a droplet, given by Eq. (4.5), and the same H_x dependence of the spin glass correlation length ξ in Eq. (4.6). Hence, we have shown that a formally derived effective spin-$\frac{1}{2}$ Hamiltonian does capture quantitatively the low energy physics of the full S Hamiltonian at low transverse fields. While the argument above was constructed for the toy model of Eq. (3.1), one could proceed identically for the full blown microscopic Hamiltonian of $LiHo_xY_{1-x}F_4$. Indeed, this is the underlying program of Chapter 5.

4.3 Numerical Results

In the same spirit as Ref. [24, 25], My collaborator, François Vernay, performed numerical calculations to back up the analytical perturbative approach described in Section 4.2. This allows us to investigate to what extent our proposed low energy effective spin-$\frac{1}{2}$ model is a good description of the full anisotropic Hamiltonian (3.1) as well as determine the range of transverse field over which the above analytical small H_x results are valid. In this section we present results from exact diagonalizations on finite-size clusters with open boundary conditions[7]. In order to compare the present approach with the previous investigations done by Schechter *et al.*[25, 24], we consider the same constant fixed concentration $x = 18.75\%$.

As stated in chapter 2, $LiHoF_4$ is a compound with space-group $C_{4h}^6\,(I4_1/a)$ with lattice parameters $a = b = 5.175\mathring{A}$, $c = 10.75\mathring{A}$, and with 4 Ho^{3+} ions per unit cell positioned at $(0, 0, 1/2)$, $(0, 1/2, 3/4)$, $(1/2, 1/2, 0)$ and $(1/2, 0, 1/4)$ [76]. For $LiHo_xY_{1-x}F_4$, a dilution of $x = 18.75\%$ is realized by distributing randomly N magnetic moments (holmium, Ho^{3+} ions) in a sample of $\frac{16\times N}{3}$ possible sites. We

[7]Since our goal is merely to compare numerically the energy eigenvalues of two quantum spin models, as opposed to describe a system approaching the thermodynamic limit, we consider here the simplest case of open boundary conditions as opposed to periodic boundary conditions, which could be implemented, for example, using Ewald summation techniques as done in Chapter 6.

chose samples of size $(2a, 2b, c \times \frac{N}{3})$, where N is a multiple of 3. Thus, changing the number N of magnetic ions means changing the size of the sample in the $\hat{z}$ direction in order to keep a constant dilution.

In Eq. (3.1), the dipolar interaction is written as $V_{ij}^{\mu\nu}$, which takes, with the negative coefficient convention used in Eq. (3.1), the explicit form:

$$V_{ij}^{\mu\nu} = \frac{\mu_B^2}{r_{ij}^3}\left[\frac{3r_{ij}^{\mu}r_{ij}^{\nu}}{r_{ij}^2} - \delta_{\mu\nu}\right], \tag{4.10}$$

where r_{ij} is the distance between the ions at positions i and j, and $\mu, \nu = x, y, z$. The dipolar interaction V^{zz} is of the order $\frac{\mu_B^2}{a^3} \approx 4.49 \times 10^{-3}$ K, whereas the on-site anisotropy is taken as $D = 10$ K. In the following, we investigate the behaviour of the gap δE between the ground-state and first excited-state as a function of the applied transverse field H_x. Since we are mainly interested in checking the relations (4.4), (4.5) and (4.9), we present our results in terms of renormalized parameters $(\frac{\delta E}{D\sqrt{N}}, \frac{H_x}{D})$.

To perform a first check of the validity of our approach, we choose a small cluster with a fixed random distribution of $N = 9$ spins and compute the renormalized gap $\delta E/(D\sqrt{N})$, for both models (*i.e.* $S = 1$, Eq. (3.1) and spin-$\frac{1}{2}$, Eq. (3.6)) as a function of the reduced transverse magnetic field H_x/D. The results are shown in Fig. 4.1. In zero transverse field, the ground-state is degenerate and its energetics are governed by the Ising interaction V^{zz}. The application of a transverse field H_x lifts the degeneracy. The splitting energy between the ground-state and the first excited state corresponds to excitation energy δE between the ground state and the excited state with spins flipped. For sufficiently small H_x, the most important interaction remains V^{zz} and the gap δE is found to be proportional to H_x/D (inset of Fig. 4.1), as suggested by the arguments leading to Eqs. (4.4) and (4.9). Upon increasing H_x/D to a sufficiently large value, the transverse field eventually becomes stronger than the dipolar interactions. At that point, the perturbative low H_x regime[8] is no longer valid and the gap δE is no longer proportional to H_x. However, Fig. 4.1 shows that, even for high transverse fields, we observe an almost exact agreement between the $S = 1$ and the effective spin-$\frac{1}{2}$ description.

[8]This low H_x regime corresponds to a region where the transverse field H_x is small compared to the longitudinal part of the dipolar interactions, V^{zz}.

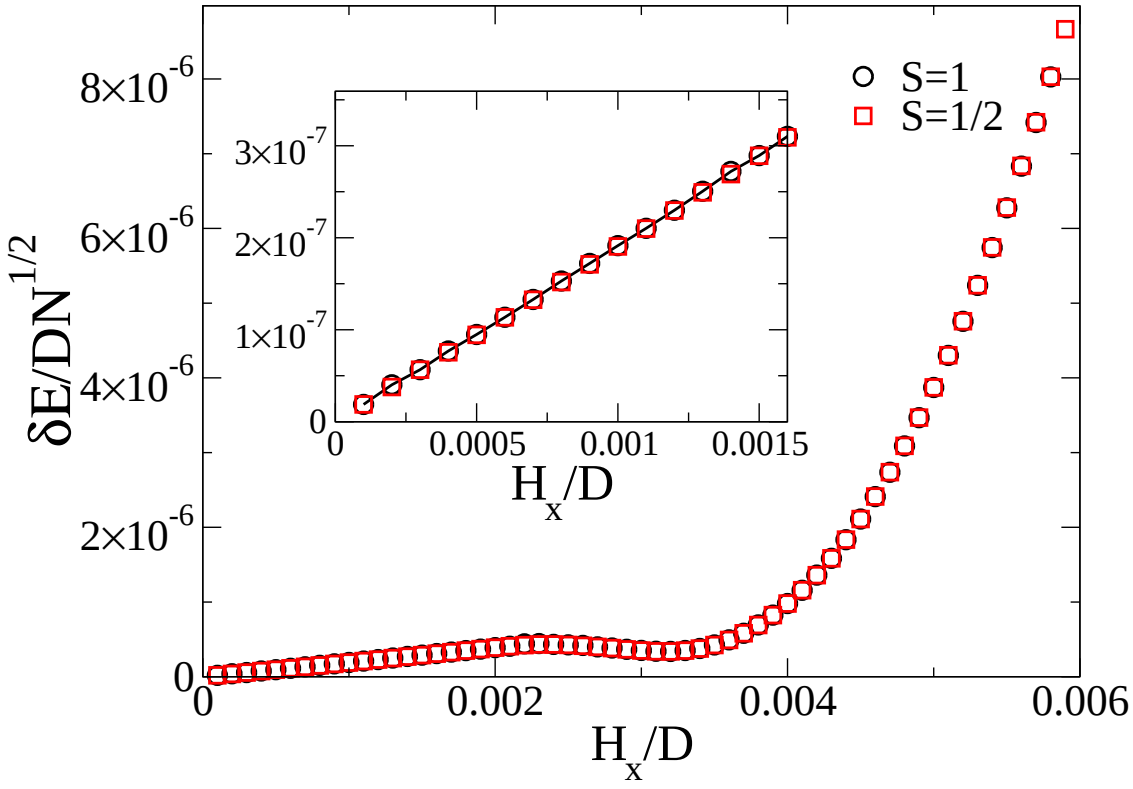

Figure 4.1: Comparison between the $S = 1$ and spin-$\frac{1}{2}$ models for a given sample (e.g. realization of disorder) of $N = 9$ spins: gap $\delta E/(D\sqrt{N})$ as a function of the transverse field H_x/D. δE is the energy gap between the two lowest energy states of the system in presence of both dipolar interactions $V_{ij}^{\mu\nu}$ and the transverse magnetic field H_x. The inset shows the small H_x/D regime for the same sample.

Interestingly, for a specific realization of disorder, in Fig. 4.1, we note a local maximum in δE around $B_x/D \approx 0.0024$, followed by a local minimum, before δE starts diverging with increasing H_x. We investigated the origin of this behaviour and found that it can be understood as arising from the H_x dependence of $C_{zz} \propto (1 - \frac{1}{2}(B_x/\Omega_0)^2)$ vs $C_{x0} \propto H_x/\Omega_0$, both for small H_x/D. The dependence of δE on H_x is controlled not only by the $C_{\mu\nu}$ parameters, but also by a prefactor coming from the dipolar interactions which is proportional to $r_{ij}^z r_{ij}^x$ in Eq. (4.10). Obviously, if this is the case, the random distribution of the magnetic ions in the sample must play a crucial role in the position (or even the existence) of this local maximum/minimum feature. If one takes an extreme case in which all the magnetic ions are aligned on a line along the $\hat{z}$ direction, the resultant $r_{ij}^z r_{ij}^x$ terms are 0, and there is no dip in the curve. To confirm this scenario we show in Fig. 4.2 $\delta E/(D\sqrt{N})$ as a function of the transverse field H_x for twenty different disorder configurations for $N = 6$. One sees that the majority of curves do not show these local maximum/minimum features and, as shown by the inset of Fig. 4.2, the average of δE over those twenty realizations of disorder reveal no such max/min structure.

Having demonstrated the one-to-one correspondence between the $S = 1$ and the effective spin-$\frac{1}{2}$ model for various (specific) realizations of disorder, we now proceed to check the scaling with system size for $\langle|\delta E|\rangle$ predicted by Eq. (4.5) for the $S = 1$ model and also check that it agrees with the one for the effective spin-$\frac{1}{2}$ model. The results for both models are shown in Fig. 4.3. The average gap $\langle|\delta E|\rangle$ was computed over 1000 samples which, for each system size of N spins, we renormalize as $\langle|\delta E|\rangle/(D\sqrt{N})$, and plot for both models ($S = 1$ and effective spin-$\frac{1}{2}$) as a function of the transverse field H_x. As predicted by Eq. (4.5) and previously found in Ref. [24], our numerical results displayed in Fig. 4.3, reveal a regime for which the two models obey $\frac{\langle|\delta E|\rangle}{D\sqrt{N}} \propto \frac{H_x}{D}$ scaling. Indeed, we observe in a good collapse of the results with this scaling behaviour.

One can see that at higher H_x, the scaling relation for different system size N, as well as the proportionality of the gap $\langle|\delta E|\rangle$ with H_x starts to break down. As explained above in the context of Fig. 4.1, this comes from the fact that the transverse field term in the Hamiltonian is larger than the dipolar interaction V_{ij}^{zz}. Thus the droplet picture is not valid and neither are the scaling nor the proportionality

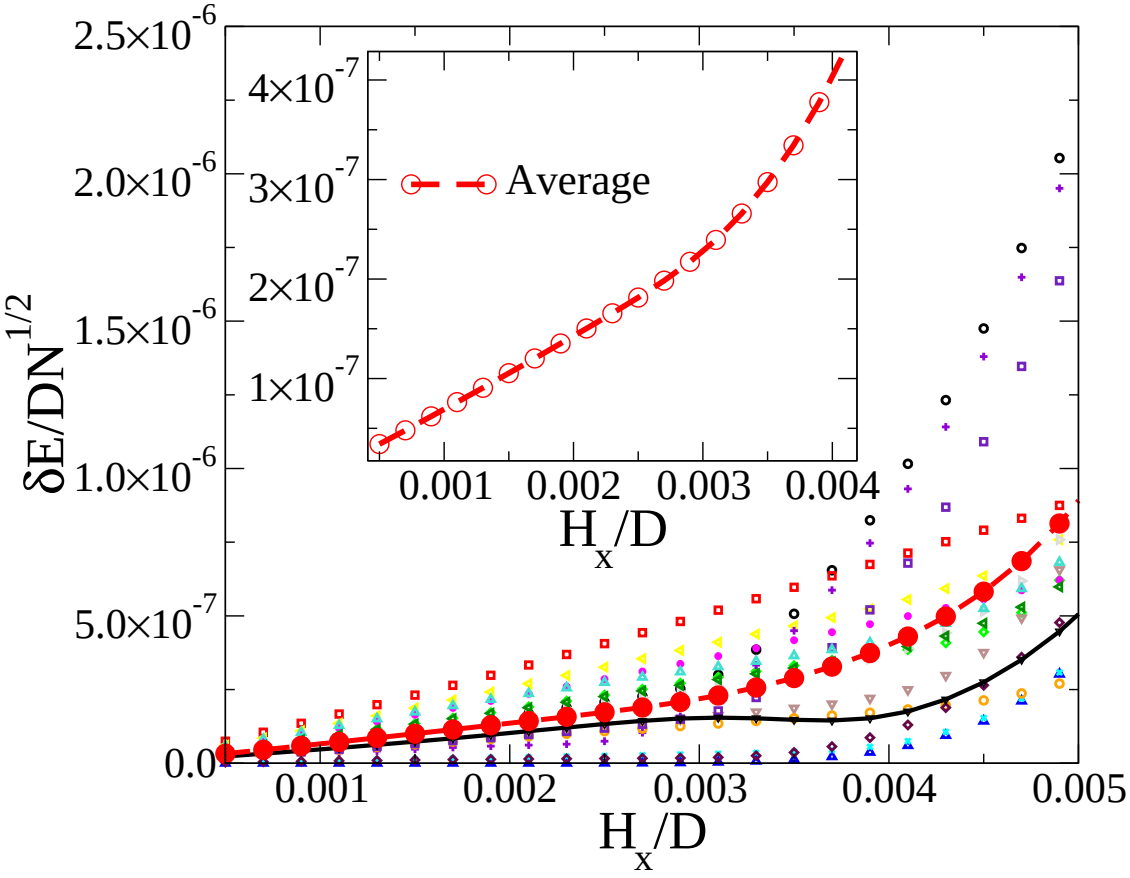

Figure 4.2: Random variations of the disorder configurations for a N=6-spin system for twenty realizations of disorder. Gap $\delta E/(D\sqrt{N})$ as a function of the transverse field H_x/D. Depending on the disorder configuration the curves exhibit a local maximum and a local minimum. The thin (black) curve in the main panel shows the minimum/maximum structure of δE vs H_x for a specific realization of disorder. This structure disappears after taking the average as shown by the thick (red) curve joining the filled (red) circles. The monotonous behaviour for the average of δE, already for 20 samples, is emphasized in the inset.

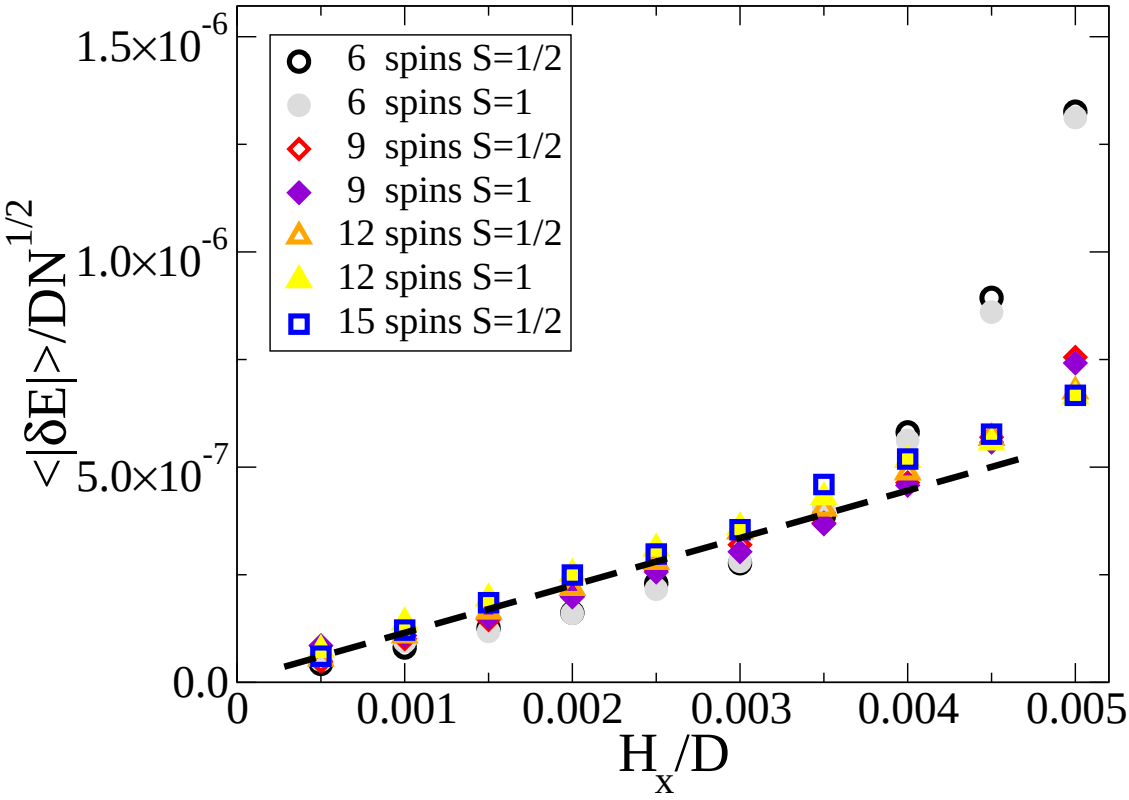

Figure 4.3: Scaling of the renormalized gap $\langle \delta E \rangle / \sqrt{N}$ (average taken over 1000 samples) for various system sizes as a function of the transverse field H_x. The closed symbols are for the $S = 1$ model and the open symbols are for the effective spin-$\frac{1}{2}$ Hamiltonian.

relations in Eq. (4.5) fulfilled. In Fig. 4.3, we also show the results for the effective spin-$\frac{1}{2}$ model (open symbols), demonstrating the agreement with the results for the $S = 1$ model, even when the ($\delta E/\sqrt{N} \propto H_x/D$) regime breaks down. This confirms the correctness of the analytically obtained conclusion, based on Eq. (4.9), and that δE is the same for both the $S = 1$ and the effective spin-$\frac{1}{2}$ models.

4.4 Conclusion

We have shown in this chapter how to rigorously derive an effective spin$-\frac{1}{2}$ Hamiltonian to describe the problem of induced random fields in a spin glass model with strong single-ion Ising anisotropy and subject to a transverse magnetic field. We discussed the relation of this model with the physics of the $LiHo_xY_{1-x}F_4$ material in a magnetic field transverse to the Ho^{3+} Ising spins [36]. We have shown, both analytically and numerically, that the use of such an effective spin$-\frac{1}{2}$ model give results in full quantitative agreement with previously reported perturbation theory calculations on a "large" spin S toy model with strong anisotropy [24, 25, 89]. However, the large hyperfine interactions present in the *real* $LiHo_xY_{1-x}F_4$, and which we ignored here, must ultimately be considered in order to obtain a good quantitative understanding of the low-temperature regime [93].

The approach of Refs. [24, 25] proceeds via the Rayleigh-Schrödinger perturbation theory, while the approach presented in Section 4.2 relies on an effective Hamiltonian approach. To lowest order in the quantum $\mathcal{H}_\perp^{\rm S}$ term in Eq. (4.1), the two approaches are found to give identical results. That is Eq. (4.4) agrees with Eq. (4.9). However, the emergence of induced random fields is more apparent in the spin-$\frac{1}{2}$ effective model approach. The $C_{\mu\nu}$ coefficients needed to construct the effective Hamiltonian are easily calculated, providing an ability to investigate the evolution of δE and ξ with H_x beyond the term linear in H_x and to arbitrarily high order in H_x. Such high order perturbation theory would be more cumbersome to construct when proceeding via a direct Rayleigh-Schrödinger perturbation scheme. In this context, the crucial step connecting the perturbation theory method and the effective spin-$\frac{1}{2}$ approach is in the determination of the H_x dependence of the $C_{\mu\nu}$ transformation parameters in Eq. (3.4). It is the neglect of this H_x dependence of the spin interactions in the effective spin-$\frac{1}{2}$ model that leads to the different results for the effective spin-$\frac{1}{2}$ and $S = 1$ models investigated in Refs. [25, 89], and which lead their authors to argue for the quantitative inadequacies of the effective spin-$\frac{1}{2}$ approach. Per se, the numerical results for the effective spin-$\frac{1}{2}$ and $S = 1$ models reported in Ref. [25] are correct. Indeed, there is no problem in finding a different H_x dependence of the disorder average $|\delta E|$ if one is not interested in making a

formal connection between the $S = 1$ and the effective spin-$\frac{1}{2}$ model. However, in a study aiming at calculating physical quantities defined in the high-energy sector, one may want to formally relate the low-energy description to the "microscopic" (bare) high-energy model.

We note that, in a general case where the V_{ij}^{zx} spin-spin interactions are not much smaller than D, higher-order perturbation theory calculations must be carried out to derive an effective Hamiltonian. The physical result would be that virtual transitions to the excited states induced by the spin-spin interactions lead to an admixing of those states with the low-energy sector. This effect was recently discussed in Ref. [55][9], where it was shown that such effective interaction-induced quantum mechanical effects are seemingly negligible for $LiHo_xY_{1-x}F_4$. For a different magnetic rare-earth system, we note that it was recently found that such interaction-induced admixing can dramatically change the low-energy physics [10].

Having shown that the effective spin-$\frac{1}{2}$ model is a valid description for the problem of induced random fields in a spin glass model with strong single-ion Ising anisotropy and subject to a transverse magnetic field, we use in the next chapter the effective spin-$\frac{1}{2}$ approach to investigate with a mean-field theory the smearing of the nonlinear susceptibility, χ_3, at the spin glass transition with increasing B_x in $LiHo_xY_{1-x}F_4$.

[9] In a recent work, Chin and Eastham derived an effective two-state Hamiltonian for $LiHo_xY_{1-x}F_4$, but for $B_x = 0$. In that work, the effect of admixing of the crystal field levels via the spin interactions was investigated via a second order perturbation theory [55].

[10] A similar approach to that employed in Ref. [55] was recently used to investigate the role of quantum fluctuations in the highly frustrated $Tb_2Ti_2O_7$ pyrochlore antiferromagnet [96].

Chapter 5

Mean Field Study of a Generalized Quantum Spin-Glass Model with a Random Field

In this chapter, we focus on one of the key problems pertaining to the interplay of quantum fluctuation induced by B_x in the presence of random disorder in $LiHo_xY_{1-x}F_4$. In the Introduction, Section 1.2, we mentioned that one of the signatures of the spin-glass transition is a divergence in the nonlinear susceptibility χ_3 [12]. For $LiHo_xY_{1-x}F_4$ with $x < 0.25$ for $B_x = 0$, the system displays a spin glass phase of moments frozen in time but randomly in space, which is observed via a sharp increase of nonlinear susceptibility χ_3 [36] (see Introduction, Footnote 8). As B_x is increased from zero, the χ_3 measurements indicate that the transition to the spin glass phase becomes progressively less singular with no indication of a quantum phase transition at zero temperature [36] (see Fig. 1.5). This is contrary to theoretical expectations [43, 45, 97].

In Section 1.4, we argued that within a transverse field Ising spin-glass model, in the vicinity of the quantum critical point at $T \to 0$, χ_3 is expected to diverge [97]. Such a divergence in χ_3 has been observed, for example, in mean-field studies of an infinite-range transverse field Ising spin glass (see Ref. [97]), where χ_3 has a sharp transition as $T \to 0$. Also, quantum Monte Carlo studies performed to

study the quantum version of an Edward-Anderson model with a transverse field for spatial dimension $d = 2$ [43] and $d = 3$ [45], indicate that at $T = 0$ the nonlinear susceptibility χ_3 diverges at the transverse field Γ_c (see Eqs. (1.1, 1.23)). This is very different from experimental observations of $LiHo_xY_{1-x}F_4$.

In Chapter 3, Section 3.5, we invoked a qualitative argument, to show that in $LiHo_xY_{1-x}F_4$ ($x \neq 0$), an applied magnetic field B_x transverse to the Ising direction $\hat{z}$ induces nonzero magnetic moments along the $\hat{x}$ direction. Because of the destruction of crystalline mirror symmetries, these field-induced magnetic moments couple via the off-diagonal dipolar interactions to the $\hat{z}$ components of the Ho^{3+} magnetic moments. Such couplings can be interpreted as effective random fields along the $\hat{z}$-direction acting on the Ho^{3+} magnetic moments. We believe that the induced random fields, can explain the puzzling behavior observed in the nonlinear susceptibility experiments discussed above. In Chapter 3, we also showed how the general microscopic spin Hamiltonian with strong Ising anisotropy of Eq. (3.1) and the microscopic Hamiltonian of Eq. (3.7) for $LiHo_xY_{1-x}F_4$ can be reformulated in terms of an effective spin-$\frac{1}{2}$ model. We showed that, by using an effective spin-$\frac{1}{2}$ model (see Eqs. (3.6, 3.14)), the induction of random fields by an external magnetic field B_x can be exposed in a rather transparent way. Indeed, the effective random fields emerge naturally in the effective spin-$\frac{1}{2}$ description. The random field physics manifests itself as a random off-diagonal dipole-dipole interaction between σ_i^z and σ_j^z spin degrees of freedom as well as a longitudinal correlated random field in the $\hat{z}$ direction that is linearly coupled to the σ_i^z degrees of freedom. Such interactions have not been typically considered in the idealized transverse field Ising spin glass model of Eq. (1.23) [1].

In Chapter 4, we confirmed the quantitative validity of our effective spin-$\frac{1}{2}$ approach. This confirmation provides us with enough confidence to apply the effective spin-$\frac{1}{2}$ approach to a quantitative study of the influence of the B_x-induced effective random fields on the nonlinear susceptibility χ_3 measurements of $LiHo_xY_{1-x}F_4$ ($x = 0.167$) in the spin glass phase.

[1] In Refs [98, 99], a transverse field Ising spin glass model with a random field (no off-diagonal interaction) has been studied to investigate the effects of quantum fluctuations on the proton glass phase in mixed hydrogen-bonded ferro-antiferroelectric systems.

As discussed in Chapter 4, it has been suggested by the authors of Ref. [24] that the underlying random fields physics destroy the spin glass transition in $LiHo_xY_{1-x}F_4$. In this chapter, we take a more pragmatic approach and ask whether the qualitative behavior of the experimentally observed $\chi_3(B_x, T)$ can be interpreted in terms of underlying B_x-induced effective random fields, by providing some "*quantitative*" evidence, showing that random fields destructs the sharp transitions in χ_3. The rest of this Chapter is organized as follows.

In Section 5.1, inspired by the effective spin-$\frac{1}{2}$ models of Eqs. (3.6, 3.14), we investigate a model which is a generalization of an infinite-range Sherrington-Kirkpatrick (SK) model [21] at the mean-field level. We introduce a spin-$\frac{1}{2}$ Hamiltonian similar to the Hamiltonians of Eqs. (3.6, 3.14). This generalization is achieved by including an infinite range random off-diagonal coupling between σ_z and σ_x components of the spin degrees of freedom, plus a transverse field in the $\hat{x}$ direction and a single site longitudinal random field in the $\hat{z}$ direction. The spin-spin interactions are considered to be infinitely long-range interactions and modeled via Gaussian distribution. Such simplifying assumptions, enable us to perform mostly analytical mean field calculations for this system.

Via the original classical SK model, which is the prototype of an infinite spin glass model, one can qualitatively capture some of the important features of spin glasses such as the existence of a cusp in the linear susceptibility or the critical behavior of the nonlinear susceptibility. Hence, it seems that studying a generalized quantum SK model which incorporates random fields and the transverse field is a quite reasonable theoretical framework to initially investigate the peculiar behavior of $LiHo_xY_{1-x}F_4$ in the SG regime with an applied transverse magnetic field.

By using the standard replica trick [21] and the imaginary time formalism [38] employed in the theory of quantum systems, one can derive a mean-field free energy for the generalized quantum SK model. Having the mean-field free energy one can obtain self-consistent expressions for the order parameters of the theory. In Section 5.2, using the self-consistent equations for the order parameter, we derive an expression for the nonlinear susceptibility χ_3. Unfortunately, because of the complexity of self-consistent equations, the nonlinear susceptibility has to be calculated numerically. In Section 5.3, the range of T and Γ (the transverse field

coupled to the $\hat{x}$ component of the spin-$\frac{1}{2}$ degrees of freedom) over which mean field calculations are stable is investigated. In Section 5.4, we heuristically estimate the dependence of Γ with the the real applied external magnetic field B_x. We also incorporate the external magnetic field B_x dependence of the amplitude of the random interactions, which originally exist in Eqs. (3.6,3.14) in our mean field model and in the calculation of χ_3. We show how the overall trend of the experimental χ_3 data is qualitatively reproduced. In Section 5.5, we summarize the results of this chapter.

5.1 A Generalized Infinite-Range Quantum Spin-Glass Model

Motivated by the effective spin-1/2 model of Eqs. (3.6, 3.14), we introduce here a heuristic model as a generalization of the SK model, which grasps the main phenomenological aspects of the microscopic effective Hamiltonians of Eqs. (3.6,3.14). Our aim is that within this heuristic model, we may compute the nonlinear susceptibility χ_3 and check whether the physics of the B_x-induced effective random fields leads to qualitatively similar behavior to what is observed experimentally for $LiHo_{1.67}Y_{0.833}F_4$ in the presence of an applied B_x.

The Hamiltonian of the generalized SK model is written as

$$\begin{aligned}\mathcal{H}_{\rm SK} = &-\frac{1}{2}\sum_{i,j} J_{ij}\sigma_i^z\sigma_j^z - \frac{1}{2}\sum_{i,j} K_{ij}\sigma_i^z\sigma_j^x \\ &-\sum_i h_i^z\sigma_i^z - h_0^z\sum_i \sigma_i^z - \Gamma\sum_i \sigma_i^x \ . \end{aligned} \tag{5.1}$$

In the original problem of interest, the couplings between the magnetic moments are dipole-dipole long range interactions, where the magnetic ions are randomly diluted with non-magnetic ions. Here, in order to implement a simple mean-field calculation, we make a simplifying assumption for the distribution of the couplings J_{ij}, K_{ij} and the linear random field h_i^z. We consider the couplings J_{ij} and K_{ij} to be independent zero-mean infinite-range interactions with Gaussian distribution

$$P(J_{ij}) = \left(\frac{N}{2\pi J^2}\right)^{1/2} \exp\left(\frac{-N{J_{ij}}^2}{2J^2}\right) \quad \text{and} \tag{5.2}$$

$$P(K_{ij}) = \left(\frac{N}{2\pi K^2}\right)^{1/2} \exp\left(\frac{-N{K_{ij}}^2}{2K^2}\right) . \tag{5.3}$$

The variances of the distributions are respectively denoted by J^2/N and K^2/N. The scaling N^{-1} is necessary in order that the thermodynamical quantities be extensive in the thermodynamic (large N) limit. Here, N is the total number of spins. Also, the distribution of the random field h_i^z is considered Gaussian with a variance of Δ and zero mean as well

$$P(h_i^z) = \frac{1}{\sqrt{2\pi\Delta}} \exp\left(\frac{-h_i^{z2}}{2\Delta}\right) . \tag{5.4}$$

This model is a more generalized version of those studied in Ref. [97] and Refs. [98, 99]. The model that is studied in Ref. [97] is an infinite-range Ising spin glass model with a transverse field. It is similar to the model we propose in Eq. (5.1), with the difference that $K_{ij} = 0$ and $h_i^z = 0$. The model of Refs. [98, 99] was proposed to study the effects of quantum fluctuations on the proton glass phase in mixed hydrogen-bonded ferro-antiferroelectric systems and to calculate linear and nonlinear electrical susceptibility in such systems [98]. The model is similar to our model with the difference that the off-diagonal coupling $K_{ij} = 0$. However, the model in Refs. [98, 99] also possess internal h_i^z random fields.

In the calculation of the free energy, to overcome the difficulty caused by the non-commutation of the spin operators, we use the imaginary time functional method [38, 100] in which the spin operators are regarded as the functions of the imaginary time τ. Thus, the partition function for a specific configuration of random variables $\{J_{ij}, K_{ij}, h_i^z\}$ can be written as

$$Z\{J_{ij}, K_{ij}, h_i^z\} = \mathbf{Tr}\ \mathcal{T} \exp\left[\int_0^\beta d\tau \left\{\frac{1}{2}\sum_{i,j} J_{ij}\,\sigma_i^z(\tau)\sigma_j^z(\tau) + \frac{1}{2}\sum_{i,j} K_{ij}\,\sigma_i^z(\tau)\sigma_j^x(\tau) + \sum_i h_i^z\sigma_i^z(\tau) + h_0^z\sum_i \sigma_i^z(\tau) + \Gamma\sum_i \sigma_i^x(\tau)\right\}\right] . \tag{5.5}$$

Here, a formal dependence of the spin operators on time τ is introduced in order to treat the spin operators as c-numbers [38][2]. $\mathcal{T}$ denotes the time ordering operator, which in the expansion of the exponential of Eq. (5.5) rearranges $\sigma^z(\tau)$ and $\sigma^x(\tau)$ in the order of decreasing time arguments. **Tr** denotes the trace over spin degrees of freedom.

To calculate physical quantities we have to make a disorder average of the free-energy of the system. Therefore, we should calculate $[\ln Z\{J_{ij}, K_{ij}, h_i^z\}]_{\rm av}$. In order to calculate $[\ln Z\{J_{ij}, K_{ij}, h_i^z\}]_{\rm av}$, we use the well known replica trick method (see Section 1.2 of Chapter 1). Practically, to perform the replica trick, we use

$$[\ln Z\{J_{ij}, K_{ij}, h_i^z\}]_{\rm av} = \lim_{n\to 0} \frac{1}{n}\left([Z^n\{J_{ij}, K_{ij}, h_i^z\}]_{\rm av} - 1\right) \ , \tag{5.6}$$

which is valid for $n \to 0$. However, if n is considered as a positive integer, one can express $Z^n\{J_{ij}\}$ in terms of n identical replicas (copies) of the system. Replicating the partition function of Eq. (5.5) we have

$$\begin{aligned}
[Z^n]_{\rm av} &= \mathbf{Tr} \int \left[\prod_i P(h_i^z) dh_i^z \prod_{ij} P(J_{ij})P(K_{ij})\, dJ_{ij} dK_{ij}\right] \\
&\times \mathcal{T} \exp\left[\int_0^\beta d\tau \sum_{\alpha=1}^{n} \left\{\frac{1}{2}\sum_{i,j} J_{ij}\, \sigma_i^{z\alpha}(\tau)\sigma_j^{z\alpha}(\tau)\right.\right. \\
&\left.\left. + \frac{1}{2}\sum_{i,j} K_{ij}\, \sigma_i^{z\alpha}(\tau)\sigma_j^{x\alpha}(\tau) + \sum_i h_i^z \sigma_i^{z\alpha}(\tau) + h_0^z \sum_i \sigma_i^{z\alpha}(\tau) + \Gamma \sum_i \sigma_i^{x\alpha}(\tau)\right\}\right] .
\end{aligned} \tag{5.7}$$

If we average the replicated partition function respect to the random couplings and the random field, then we obtain

$$\begin{aligned}
[Z^n]_{\rm av} &= \mathbf{Tr}\ \mathcal{T} \exp\left[\int_0^\beta d\tau \int_0^\beta d\tau' \left\{\frac{J^2}{4N}\sum_{ij}\sum_{\alpha,\beta} \sigma_i^{z\alpha}(\tau)\sigma_j^{z\alpha}(\tau)\sigma_i^{z\beta}(\tau')\sigma_j^{z\beta}(\tau')\right.\right. \\
&\left. + \frac{K^2}{4N}\sum_{ij}\sum_{\alpha,\beta} \sigma_i^{z\alpha}(\tau)\sigma_j^{x\alpha}(\tau)\sigma_i^{z\beta}(\tau')\sigma_j^{x\beta}(\tau')\right\} \\
&\left. + \frac{\Delta}{2}\sum_i \sum_{\alpha,\beta} \sigma_i^{z\alpha}(\tau)\sigma_i^{z\beta}(\tau') + \int_0^\beta d\tau \sum_i \sum_\alpha \left(h_0^z \sigma_i^{z\alpha}(\tau) + \Gamma \sigma_i^{x\alpha}(\tau)\right)\right] .
\end{aligned} \tag{5.8}$$

[2]By c-number, we mean a classical quantity, as opposed to an operator.

Defining $K/J = k$, and after reorganizing the quadratic terms one gets

$$[Z^n]_{\rm av} = \mathbf{Tr}\ \mathcal{T} \exp\left\{ \int_0^\beta d\tau \int_0^\beta d\tau' \frac{J^2}{4N} \sum_{\alpha,\beta} \left[\left(\sum_i \sigma_i^{z\alpha}(\tau)\sigma_i^{z\beta}(\tau') \right)^2 + \frac{k^2}{4} \left(\sum_i \sigma_i^{z\alpha}(\tau)\sigma_i^{z\beta}(\tau') \right) \left(\sum_i \sigma_i^{x\alpha}(\tau)\sigma_i^{x\beta}(\tau') \right) \right] + \frac{\Delta}{2} \sum_i \sum_{\alpha,\beta} \sigma_i^{z\alpha}(\tau)\sigma_i^{z\beta}(\tau') + \int_0^\beta d\tau \sum_i \sum_\alpha \left(h_0^z \sigma_i^{z\alpha}(\tau) + \Gamma \sigma_i^{x\alpha}(\tau) \right) \right\} . \quad (5.9)$$

The Hubbard-Stratonovitch transformation

$$\exp(\lambda a^2/2) = \left[\frac{\lambda}{2\pi} \right]^{1/2} \int_{-\infty}^{\infty} dx \exp\left[-\frac{\lambda x^2}{2} + a\lambda x \right] , \quad (5.10)$$

can be used in order to linearize the quadratic term $\left(\sum_i \sigma_i^{z\alpha}(\tau)\sigma_i^{z\beta}(\tau') \right)^2$. To linearize the term $\left(\sum_i \sigma_i^{z\alpha}(\tau)\sigma_i^{z\beta}(\tau') \right) \left(\sum_i \sigma_i^{x\alpha}(\tau)\sigma_i^{x\beta}(\tau') \right)$, one can use the $ab \equiv \frac{1}{4}(a+b)^2 - \frac{1}{4}(a-b)^2$ identity to write

$$\left(\sum_i \sigma_i^{z\alpha}(\tau)\sigma_i^{z\beta}(\tau') \right) \left(\sum_i \sigma_i^{x\alpha}(\tau)\sigma_i^{x\beta}(\tau') \right) = \quad (5.11)$$
$$\frac{1}{4} \left[\sum_i \sigma_i^{z\alpha}(\tau)\sigma_i^{z\beta}(\tau') + \sum_i \sigma_i^{x\alpha}(\tau)\sigma_i^{x\beta}(\tau') \right]^2 - \frac{1}{4} \left[\sum_i \sigma_i^{z\alpha}(\tau)\sigma_i^{z\beta}(\tau') - \sum_i \sigma_i^{x\alpha}(\tau)\sigma_i^{x\beta}(\tau') \right]^2 .$$

By implementing a modified version of the Hubbard-Stratonovitch transformation

$$\exp(-\lambda a^2/2) = \left[\frac{\lambda}{2\pi} \right]^{1/2} \int_{-\infty}^{\infty} dx \exp\left[-\frac{\lambda x^2}{2} + ia\lambda x \right] , \quad (5.12)$$

one can linearize the second term in the right-hand-side of Eq. 5.11. Performing

the transformations of Eqs. (5.10,5.12), the free energy per spin is readily obtained

$$\begin{aligned}
-\beta f &= \lim_{n\to 0}\frac{1}{n}\Bigg[\int_{-\infty}^{\infty}\prod_{\alpha\neq\beta}\frac{NJ^2K^2}{2\pi}\left[\frac{NJ^2}{2\pi}\right]^{1/2} d\Lambda_{\alpha\beta}(\tau,\tau')d\Theta_{\alpha\beta}(\tau,\tau')dQ^{zz}_{\alpha\beta}(\tau,\tau') \\
&\quad\times\prod_{\alpha}\frac{NJ^2K^2}{2\pi}\left[\frac{NJ^2}{2\pi}\right]^{1/2} d\omega_{\alpha\alpha}(\tau,\tau')d\theta_{\alpha\alpha}(\tau,\tau')dr^{zz}_{\alpha\alpha}(\tau,\tau') \\
&\quad\exp\left\{-NG(Q^{zz}_{\alpha\beta},\Lambda_{\alpha\beta},\Theta_{\alpha,\beta},r^{zz}_{\alpha\alpha},\omega_{\alpha\alpha},\theta_{\alpha\alpha})\right\}-1\Bigg] ,
\end{aligned}$$

where

$$\begin{aligned}
G(Q^{zz}_{\alpha\beta},\Lambda_{\alpha\beta},\Theta_{\alpha\beta},r^{zz}_{\alpha\alpha},\omega_{\alpha\alpha},\theta_{\alpha\alpha}) &= \frac{1}{4}J^2\int_0^\beta d\tau\int_0^\beta d\tau'\sum_{\alpha\neq\beta}\Big[\left(Q^{zz}_{\alpha\beta}(\tau,\tau')\right)^2 \\
&\quad+\frac{k^2}{4}\left(\Lambda_{\alpha\beta}(\tau,\tau')\right)^2+\frac{k^2}{4}\left(\Theta_{\alpha\beta}(\tau,\tau')\right)^2\Big] \\
&\quad+\sum_{\alpha}\left[\left(r^{zz}_{\alpha\alpha}(\tau,\tau')\right)^2+\frac{k^2}{4}\left(\omega_{\alpha\alpha}(\tau,\tau')\right)^2+\frac{k^2}{4}\left(\theta_{\alpha\alpha}(\tau,\tau')\right)^2\right] \\
&\quad-\mathbf{Tr}\mathcal{L}\left[Q^{zz}_{\alpha\beta},\Lambda_{\alpha\beta},\Theta_{\alpha\beta},r^{zz}_{\alpha\alpha},\omega_{\alpha\alpha},\theta_{\alpha\alpha}\right] \qquad (5.13)
\end{aligned}$$

The explicit form of $\mathcal{L}$ is

$$\begin{aligned}
\mathcal{L} = \quad & \frac{J^2}{2}\int_0^\beta d\tau\int_0^\beta d\tau'\Bigg[\sum_{\alpha\neq\beta}\Bigg\{\left(Q^{zz}_{\alpha\beta}(\tau,\tau')+\Delta\right)\sigma^{z\alpha}(\tau)\sigma^{z\beta}(\tau') \\
&+\frac{k^2}{4}\Lambda_{\alpha\beta}(\tau,\tau')\left[\sigma^{z\alpha}(\tau)\sigma^{z\beta}(\tau')+\sigma^{x\alpha}(\tau)\sigma^{x\beta}(\tau')\right] \\
&+i\frac{k^2}{4}\Theta_{\alpha\beta}(\tau,\tau')\left[\sigma^{z\alpha}(\tau)\sigma^{z\beta}(\tau')-\sigma^{x\alpha}(\tau)\sigma^{x\beta}(\tau')\right]\Bigg\} \\
&+\sum_{\alpha}\Bigg\{r^{zz}_{\alpha\alpha}(\tau,\tau')\sigma^{z\alpha}(\tau)\sigma^{z\alpha}(\tau')+\frac{k^2}{4}\omega_{\alpha\alpha}(\tau,\tau')\left[\sigma^{z\alpha}(\tau)\sigma^{z\alpha}(\tau')+\sigma^{x\alpha}(\tau)\sigma^{x\alpha}(\tau')\right] \\
&+i\frac{k^2}{4}\theta_{\alpha\alpha}(\tau,\tau')\left[\sigma^{z\alpha}(\tau)\sigma^{z\alpha}(\tau')-\sigma^{x\alpha}(\tau)\sigma^{x\alpha}(\tau')\right]\Bigg\}\Bigg] \\
&+\int_0^\beta d\tau\sum_{\alpha}\left(h^z_0\sigma^{z\alpha}(\tau)+\Gamma\sigma^{x\alpha}(\tau)\right) . \qquad (5.14)
\end{aligned}$$

The trace is over the n replicas at a single spin site. Using the method of steepest descent [21, 38], we can apply the saddle point condition $\partial G[y]/\partial y = 0$, where y's are the fields $Q^{zz}_{\alpha\beta}(\tau,\tau'), \Lambda_{\alpha\beta}(\tau,\tau'), \Theta_{\alpha\beta}(\tau,\tau'), r^{zz}_{\alpha\alpha}(\tau,\tau'), \omega_{\alpha\alpha}(\tau,\tau')$ and $\theta_{\alpha\alpha}(\tau,\tau')$. Therefore, as a result, we obtain the following relations

$$Q^{zz}_{\alpha\beta}(\tau,\tau') \equiv \left\langle \mathcal{T}\sigma^{z\alpha}(\tau)\sigma^{z\beta}(\tau')\right\rangle \tag{5.15}$$

$$\Lambda_{\alpha\beta}(\tau,\tau') \equiv \left\langle \mathcal{T}\sigma^{z\alpha}(\tau)\sigma^{z\beta}(\tau')\right\rangle + \left\langle \mathcal{T}\sigma^{x\alpha}(\tau)\sigma^{x\beta}(\tau')\right\rangle \tag{5.16}$$

$$\Theta_{\alpha\beta}(\tau,\tau') \equiv i\left\langle \mathcal{T}\sigma^{z\alpha}(\tau)\sigma^{z\beta}(\tau')\right\rangle - i\left\langle \mathcal{T}\sigma^{x\alpha}(\tau)\sigma^{x\beta}(\tau')\right\rangle \tag{5.17}$$

$$r^{zz}_{\alpha\alpha}(\tau,\tau') \equiv \langle \mathcal{T}\sigma^{z\alpha}(\tau)\sigma^{z\alpha}(\tau')\rangle \tag{5.18}$$

$$\omega_{\alpha\alpha}(\tau,\tau') \equiv \langle \mathcal{T}\sigma^{z\alpha}(\tau)\sigma^{z\alpha}(\tau')\rangle + \langle \mathcal{T}\sigma^{x\alpha}(\tau)\sigma^{x\alpha}(\tau')\rangle \tag{5.19}$$

$$\theta_{\alpha\alpha}(\tau,\tau') \equiv i\langle \mathcal{T}\sigma^{z\alpha}(\tau)\sigma^{z\alpha}(\tau')\rangle - i\langle \mathcal{T}\sigma^{x\alpha}(\tau)\sigma^{x\alpha}(\tau')\rangle \tag{5.20}$$

If we define

$$\begin{aligned} \left\langle \mathcal{T}\sigma^{\mu\alpha}(\tau)\sigma^{\mu\beta}(\tau')\right\rangle &:= Q^{\mu\mu}_{\alpha\beta}(\tau,\tau') \quad \text{and} \\ \langle \mathcal{T}\sigma^{\mu\alpha}(\tau)\sigma^{\mu\alpha}(\tau')\rangle &:= r^{\mu\mu}_{\alpha\alpha}(\tau,\tau')\ , \end{aligned} \tag{5.21}$$

where $\mu = x, y, z$, then the free energy f can be written in terms of $Q^{zz}_{\alpha\beta}(\tau,\tau')$, $Q^{xx}_{\alpha\beta}(\tau,\tau')$, $r^{zz}_{\alpha\beta}(\tau,\tau')$ and $r^{xx}_{\alpha\beta}(\tau,\tau')$. There is no exact analytical solution for Eqs. 5.21. However, we can make the so called "static approximation" [38, 101, 102][3]. This approximation, which is somehow a mean field approximation in the imaginary time direction, neglects the quantum fluctuations in the imaginary time direction. The order parameters above are independent of time by setting $Q^{zz}_{\alpha\beta}(\tau,\tau') = Q^{zz}_{\alpha\beta}$, $Q^{xx}_{\alpha\beta}(\tau,\tau') = Q^{xx}_{\alpha\beta}$, $r^{zz}_{\alpha\alpha}(\tau,\tau') = r^{zz}_{\alpha\alpha}$ and $r^{xx}_{\alpha\alpha}(\tau,\tau') = r^{xx}_{\alpha\alpha}$.

Now, we use the replica-symmetric assumption, where we consider that the system is symmetric under different permutation of the replicas. We set $Q^{zz}_{\alpha\beta} = Q^{zz}$, $\Lambda_{\alpha\beta} := \Lambda = Q^{zz} + Q^{xx}$, $\Theta_{\alpha\beta} := \Theta = i(Q^{zz} - Q^{xx})$, $r^{zz}_{\alpha\alpha} = r^{zz}$, $\omega_{\alpha\alpha} := \omega = r^{zz} + r^{xx}$, and $\theta_{\alpha\alpha} := \rho = i(r^{zz} - r^{xx})$ for all $\alpha \neq \beta$. The spins of two different replica are

[3]For a Heisenberg model with infinite range random couplings, numerical studies show that the static approximation is reasonable in many regimes [102]. However, because it neglects the quantum fluctuations in the imaginary time direction, this approximation is not suitable for studying quantum equilibrium dynamics. Due to the nature of this approximation, it is expected that at low temperatures, where the effect of quantum fluctuations are more significant, static approximation overestimate the critical temperature. See Ref. [101, 102].

coupled to each other. We can decouple the spins of different replicas by applying the Hubbard-Stratonovitch transformation. We rewrite the free energy as

$$\begin{aligned}\beta f &= \frac{1}{4}(\beta J)^2\left[(r^{zz})^2-(Q^{zz})^2\right]+\frac{1}{4}(\beta Jk)^2\left[r^{zz}r^{xx}-Q^{zz}Q^{xx}\right]\\ &\quad-\lim_{n\to 0}\frac{1}{n}\times\ln\frac{1}{2\pi}\int_{-\infty}^{\infty}dzdx\;e^{-(z^2+x^2)/2}\times\\ &\quad\mathbf{Tr}\exp\left\{\frac{(\beta J)^2}{2}\sum_{\alpha}^{n}\left[\left(r^{zz}-Q^{zz}+\frac{k^2}{2}\left(r^{xx}-Q^{xx}\right)\right)\left(\sigma^{z\alpha}\right)^2\right.\right.\\ &\quad\left.\left.+\frac{k^2}{2}\left(r^{zz}-Q^{zz}\right)\left(\sigma^{x\alpha}\right)^2\right]+\beta\sum_{\alpha}^{n}\left[H_z\sigma^z+H_x\sigma^x\right]\right\},\end{aligned}\tag{5.22}$$

where H_x and H_z the random mean fields coupled to the σ^x and σ^z degrees of freedom are

$$H_z = Jz\sqrt{Q^{zz}+\frac{k^2}{2}Q^{xx}+\Delta}+h_0^z,\tag{5.23}$$

$$H_x = Jx\sqrt{\frac{k^2}{2}Q^{zz}}+\Gamma\ .\tag{5.24}$$

For ease of use we define X as

$$\begin{aligned}X &\equiv \mathbf{Tr}_{\alpha}\exp\left\{\frac{(\beta J)^2}{2}\left[\left(r^{zz}-Q^{zz}+\frac{k^2}{2}\left(r^{xx}-Q^{xx}\right)\right)\left(\sigma^{z\alpha}\right)^2\right.\right.\\ &\quad\left.\left.+\frac{k^2}{2}\left(r^{zz}-Q^{zz}\right)\left(\sigma^{x\alpha}\right)^2\right]+\beta\left[H_z\sigma^z+H_x\sigma^x\right]\right\},\end{aligned}\tag{5.25}$$

where the trace is taken over a specific replica at a single spin site. Therefore, the free energy in terms of X is rewritten as

$$\begin{aligned}\beta f &= \frac{1}{4}(\beta J)^2\left[(r^{zz})^2-(Q^{zz})^2\right]+\frac{1}{4}(\beta Jk)^2\left[r^{zz}r^{xx}-Q^{zz}Q^{xx}\right]\\ &\quad-\lim_{n\to 0}\frac{1}{n}\times\ln\frac{1}{2\pi}\int_{-\infty}^{\infty}dzdx\;e^{-(z^2+x^2)/2}X^n\ .\end{aligned}\tag{5.26}$$

In the $n\to 0$ limit we use $X^n=\exp\left(n\ln X\right)\approx 1+n\ln X$ and $\ln(1+nA)\approx nA$. So we write

$$\begin{aligned}&\lim_{n\to 0}\frac{1}{n}\times\ln\frac{1}{2\pi}\int_{-\infty}^{\infty}dzdx\;e^{-(z^2+x^2)/2}X^n\\ &\qquad=\frac{1}{2\pi}\int_{-\infty}^{\infty}dzdx\;e^{-(z^2+x^2)/2}\ln X\ .\end{aligned}\tag{5.27}$$

In a replica symmetric framework $Q^{zz} = \left[\left\langle \sigma^{z\alpha}(\tau)\sigma^{z\beta}(\tau')\right\rangle\right]_{\rm av}$ and $Q^{xx} = \left[\left\langle \sigma^{x\alpha}(\tau)\sigma^{x\beta}(\tau')\right\rangle\right]_{\rm av}$ measure the average overlap of the z and x components of the spin configuration in two replica of a system with quenched disorder. The magnetization in the $\hat{z}$ and $\hat{x}$ direction are denoted as $M^z = \left[\langle\sigma^{z\alpha}(\tau)\rangle\right]_{\rm av}$, and $M^x = \left[\langle\sigma^{x\alpha}(\tau)\rangle\right]_{\rm av}$. In a replica symmetric picture, Q^{zz} is the spin glass order parameter [12, 21]. In a paramagnetic phase $M^z = Q^{zz} = 0$, while $M^z = 0$ and $Q^{zz} \neq 0$ indicates the the z component of the spins are in a randomly frozen state. For Q^{zz}, Q^{xx}, M^z and M^x the following self-consistent equations are at last obtained:

$$\begin{aligned}
Q^{zz} &= \frac{1}{2\pi}\int_{-\infty}^{\infty} dzdx\; e^{-(z^2+x^2)/2}\left[\frac{H_z}{H_{xz}}\right]^2 \tanh^2\left[\beta H_{xz}\right] \;, \\
Q^{xx} &= \frac{1}{2\pi}\int_{-\infty}^{\infty} dzdx\; e^{-(z^2+x^2)/2}\left[\frac{H_x}{H_{xz}}\right]^2 \tanh^2\left[\beta H_{xz}\right] \;, \\
M_z &= \frac{1}{2\pi}\int_{-\infty}^{\infty} dzdx\; e^{-(z^2+x^2)/2}\left[\frac{H_z}{H_{xz}}\right] \tanh\left[\beta H_{xz}\right] \text{ and }, \\
M_x &= \frac{1}{2\pi}\int_{-\infty}^{\infty} dzdx\; e^{-(z^2+x^2)/2}\left[\frac{H_x}{H_{xz}}\right] \tanh\left[\beta H_{xz}\right] \;,
\end{aligned}$$

where

$$H_{xz} = \sqrt{H_x^2 + H_z^2}\;.$$

In Fig. 5.1, we have plotted Q_{zz} and Q_{xx} as a function of temperature and Γ for $K = \Delta = 0$, where in this case the model is simply denoting a transverse Ising spin glass model. Subfigures 5.1(a) and 5.1(c), subsequently show Q^{zz} as a function of T and Γ. Q^{zz} shows a sharp transition to zero at $T_g(\Gamma)$. By going to higher Γ, $T_g(\Gamma)$, the temperature at which Q^{zz} vanishes, decreases. Subfigures 5.1(b) and 5.1(d) show Q^{xx} as a function of T and Γ. As it is expected for $\Gamma = 0$, Q^{xx} is zero and, by increasing Γ, Q^{xx} increases from zero to the maximum value of $Q^{xx} = 1$, where the spins tend to align parallel with Γ ($\hat{x}$ direction.) By increasing the temperature, Q^{xx} monotonically decreases to zero at $T \to \infty$.

In Fig. 5.2, Q_{zz} and Q_{xx} are shown as a function of temperature for different transverse field values and different choices of nonzero K or Δ. Generally, Q_{zz} decreases as the temperature T and transverse field increase. In Subfigure 5.2(a)

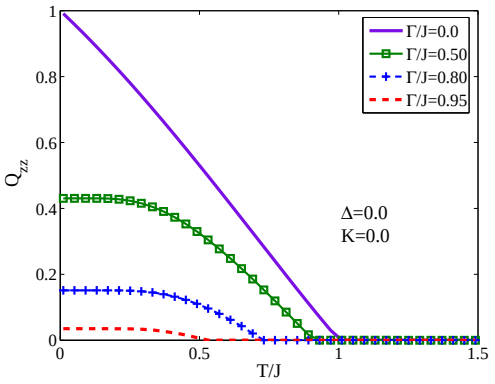

(a) Q_{zz} as a function of T/J .

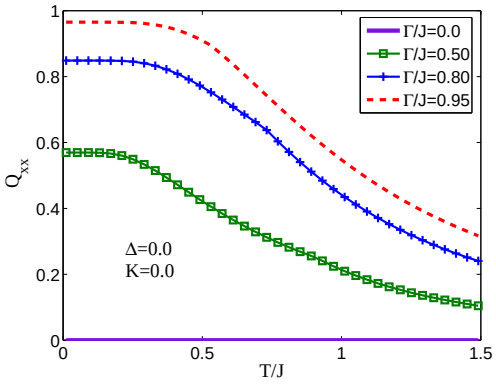

(b) Q_{xx} as a function of T/J .

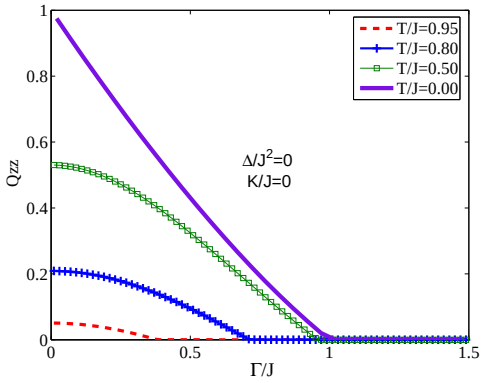

(c) Q_{zz} as a function of Γ/J .

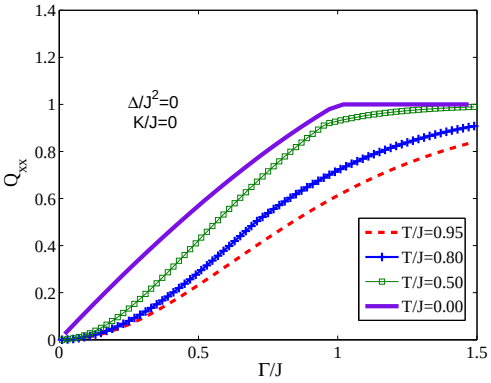

(d) Q_{xx} as a function of Γ/J .

Figure 5.1: The plot of Q_{zz} and Q_{xx} are illustrated as a function of temperature and Γ for K=Δ=0 .

the result of the existence of a finite random field $\Delta \neq 0$ in the $\hat{z}$ direction is that Q_{zz} looses its sharp transition to zero. However, the temperature where there is an inflection point, similar to Fig. 5.1(a), where $\Delta = K = 0$, decreases by increasing Γ.

As it is shown in Subfigure 5.2(c), $K \neq 0$ has the similar effect of destroying the sharp transition of Q_{zz}. One can just consider a mean field like contribution of $\propto \langle \sigma^x \rangle \sigma^z$ arising from the $K_{ij}\sigma^x\sigma^z$ term in the Hamiltonian of Eq. (5.1). Now, the difference with the case that $\Delta \neq 0$ is that because $\langle \sigma^x \rangle$ increases by increasing Γ, therefore by going to higher Γs the inflection point is more rounded. Subfigure 5.2(f) shows Q_{zz} as a function of T, when both K and Δ are nonzero. As it is shown in Subfigures 5.2(b), 5.2(d), and 5.2(f), Q_{xx} decreases by going to high temperatures and low Γs, similar to what is seen in Fig. 5.1(a).

Now, having a method to calculate Q_{zz}, Q_{xx}, M_z and M_x in a self-consistent way numerically, one can derive a self-consistent equation for the nonlinear susceptibility by differentiating M_z with respect to h_0^z. In the next section, we describe the calculation of χ_3 in some detail.

5.2 Calculating the Nonlinear Susceptibility

In the previous section we derived a mean field expression for M_z the magnetization in the $\hat{z}$ direction. In this section we derive the mean-field nonlinear susceptibility for the model we studied. The nonlinear susceptibility is calculated using $\chi_3 = -\frac{1}{6}\frac{\partial^3 M_z}{\partial {h_0^z}^3}$, where M_z is written as $M_z = \frac{1}{2\pi}\int_{-\infty}^{\infty} dzdx\ e^{-(z^2+x^2)/2} m_z$. m_z is defined as $m_z \equiv \left[\frac{H_x}{H_{xz}}\right] \tanh\left[\beta H_{xz}\right]$. Therefore χ_3 is

$$\chi_3 = -\frac{1}{12\pi}\int_{-\infty}^{\infty} dzdx\ e^{-(z^2+x^2)/2}\ \frac{\partial^3 m_z}{\partial {h_0^z}^3}\bigg|_{h_0^z=0}\ , \tag{5.28}$$

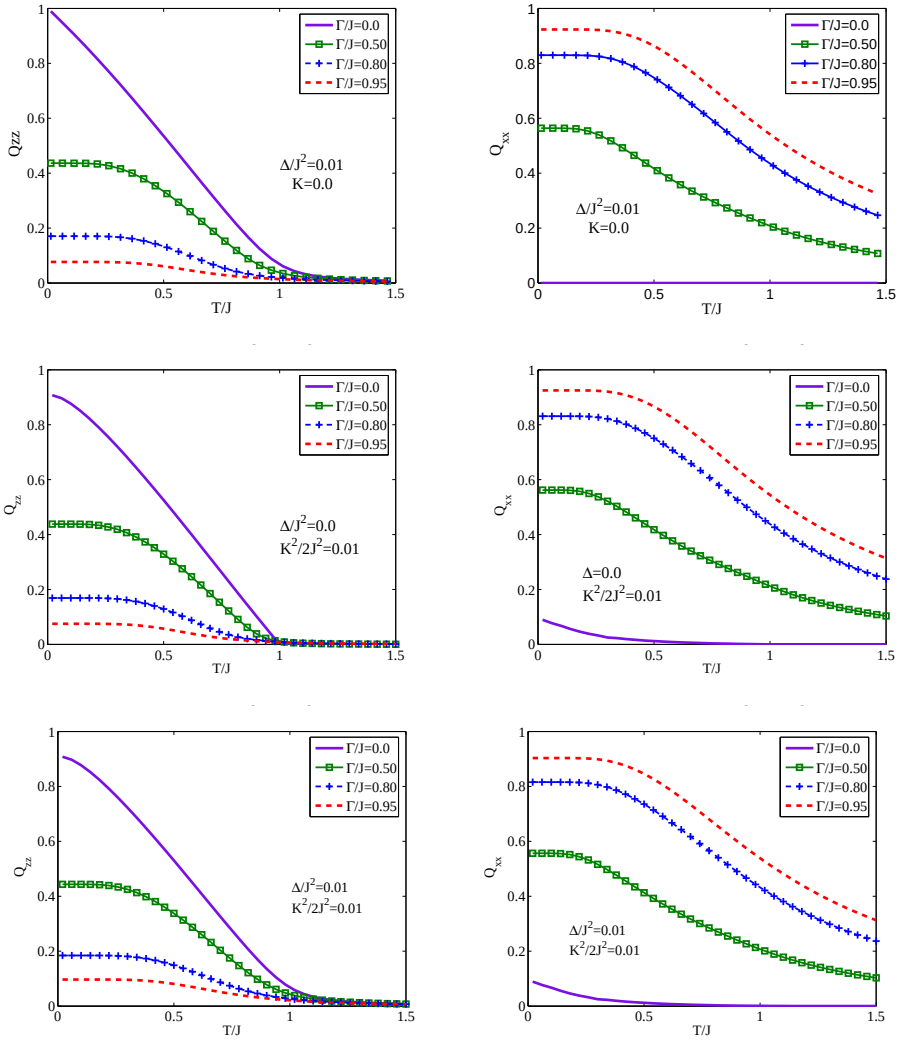

(e) Q_{zz} for $\Delta/J^2 = K^2/2J^2 = 0.01$. (f) Q_{xx} for $\Delta/J^2 = K^2/2J^2 = 0.01$.

Figure 5.2: The plot of Q_{zz} and Q_{xx} are illustrated as a function of temperature for different transverse field values and different choices of K and Δ.

which for $\frac{\partial^3 m_z}{\partial h_0^{z\,3}}|_{h_0^z=0}$ we need to calculate a set of self-consistent equations

$$\begin{aligned}
\left.\frac{\partial Q^{zz}}{\partial h_0^z}\right|_{h_0^z=0} &= \frac{1}{2\pi}\int_{-\infty}^{\infty} dzdx\; e^{-(z^2+x^2)/2}\left[2m_z\frac{\partial m_z}{\partial h_0^z}\right]\Bigg|_{h_0^z=0}\,, \\
\left.\frac{\partial Q^{xx}}{\partial h_0^z}\right|_{h_0^z=0} &= \frac{1}{2\pi}\int_{-\infty}^{\infty} dzdx\; e^{-(z^2+x^2)/2}\left[2m_x\frac{\partial m_x}{\partial h_0^z}\right]\Bigg|_{h_0^z=0}\,, \\
\left.\frac{\partial H_z}{\partial h_0^z}\right|_{h_0^z=0} &= 1+\frac{J^2 z}{2H_z}\left[\frac{\partial Q^{zz}}{\partial h_0^z}+\frac{k^2}{2}\frac{\partial Q^{xx}}{\partial h_0^z}\right]\Bigg|_{h_0^z=0} \text{ and} \\
\left.\frac{\partial H_x}{\partial h_0^z}\right|_{h_0^z=0} &= \frac{J^2 x}{2H_x}\left[\frac{k^2}{2}\frac{\partial Q^{xx}}{\partial h_0^z}\right]\Bigg|_{h_0^z=0}.
\end{aligned}$$

This set of self-consistent equations is applied in order to derive the nonlinear susceptibility of Eq. (5.28)in the form of

$$\chi_3 = \left(\frac{3b}{ad-bc}-2\right)\mathcal{C}-\frac{3a}{ad-bc}\mathcal{F}\,, \tag{5.29}$$

where $\mathcal{C}$, $\mathcal{F}$, c, d, a and b represent the following equations:

$$\begin{aligned}
\mathcal{C} &= \frac{1}{2\pi}\int_{-\infty}^{\infty} dzdx\,\frac{e^{-(z^2+x^2)/2}}{H_{xz}^7}\times \\
&\Big\{3H_x^2\left(4H_z^2-H_x^2\right)\left(\tanh\left[\beta H_{xz}\right]-\beta H_{xz}\mathrm{sech}^2\left[\beta H_{xz}\right]\right) \\
&-12\beta^2 H_{xz}^2(H_x^2H_z^2)\tanh\left[\beta H_{xz}\right]\mathrm{sech}^2\left[\beta H_{xz}\right] \\
&-2\beta^3 H_{xz}^3H_z^4\mathrm{sech}^2\left[\beta H_{xz}\right]\left(1-3\tanh^2\left[\beta H_{xz}\right]\right)\Big\}\,,
\end{aligned}$$

$$\begin{aligned}
\mathcal{F} &= \frac{1}{2\pi}\int_{-\infty}^{\infty} dzdx\,\frac{e^{-(z^2+x^2)/2}}{H_{xz}^7}\times \\
&\Big\{\left(2H_{xz}^4-15(H_zH_x)^2\right)\tanh\left[\beta H_{xz}\right] \\
+\;&\beta H_{xz}(-2H_{xz}^4+3H_x^2H_z^2)\mathrm{sech}^2\left[\beta H_{xz}\right] \\
&-2\beta^2 H_{xz}^2(H_{xz}^4-6H_x^2Hz^2)\tanh\left[\beta H_{xz}\right]\mathrm{sech}^2\left[\beta H_{xz}\right] \\
&-2\beta^3 H_{xz}^3(H_x^2H_z^2)\mathrm{sech}^2\left[\beta H_{xz}\right]\left(1-3\tanh^2\left[\beta H_{xz}\right]\right)\Big\}\,,
\end{aligned}$$

$$
\begin{aligned}
a &= \frac{-J^2}{2\pi}\int_{-\infty}^{\infty} dzdx\, \frac{e^{-(z^2+x^2)/2}}{H_{xz}^6} \times \\
&\left\{ H_x^2\left(-3H_z^2+H_x^2\right)\tanh\left[\beta H_{xz}\right]^2 \right. \\
&+5\beta H_{xz}H_x^2H_z^2\tanh\left[\beta H_{xz}\right]\mathrm{sech}^2\left[\beta H_{xz}\right] \\
&\left. +\beta^2 H_{xz}^2H_z^4\mathrm{sech}^2\left[\beta H_{xz}\right]\left(1-3\tanh^2\left[\beta H_{xz}\right]\right)\right\},
\end{aligned}
$$

$$
\begin{aligned}
b &= \frac{2}{k^2}-\frac{J^2}{2\pi}\int_{-\infty}^{\infty} dzdx\, \frac{e^{-(z^2+x^2)/2}}{H_{xz}^6} \times \\
&\left\{ H_z^2\left(3H_x^2-H_z^2\right)\tanh\left[\beta H_{xz}\right]^2 \right. \\
&+\beta H_{xz}H_z^2\left(-4H_x^2+H_z^2\right)\tanh\left[\beta H_{xz}\right]\mathrm{sech}^2\left[\beta H_{xz}\right] \\
&\left. +\beta^2 H_{xz}^2H_z^2H_x^2\mathrm{sech}^2\left[\beta H_{xz}\right]\left(1-3\tanh^2\left[\beta H_{xz}\right]\right)\right\},
\end{aligned}
$$

,

$$
\begin{aligned}
c &= 1+a-\frac{(kJ)^2}{2\pi}\int_{-\infty}^{\infty} dzdx\, \frac{e^{-(z^2+x^2)/2}}{H_{xz}^6} \times \\
&\left\{ H_x^2\left(3H_z^2-H_x^2\right)\tanh\left[\beta H_{xz}\right]^2 \right. \\
&+\beta H_{xz}H_x^2\left(-4H_z^2+H_x^2\right)\tanh\left[\beta H_{xz}\right]\mathrm{sech}^2\left[\beta H_{xz}\right] \\
&\left. +\beta^2 H_{xz}^2H_z^2H_x^2\mathrm{sech}^2\left[\beta H_{xz}\right]\left(1-3\tanh^2\left[\beta H_{xz}\right]\right)\right\}
\end{aligned}
$$

$$
\begin{aligned}
d &= -\frac{2}{k^2}+b+\frac{-(kJ)^2}{2\pi}\int_{-\infty}^{\infty} dzdx\, \frac{e^{-(z^2+x^2)/2}}{H_{xz}^6} \times \\
&\left\{ H_z^2\left(-3H_x^2+H_z^2\right)\tanh\left[\beta H_{xz}\right]^2 \right. \\
&+5\beta H_{xz}H_x^2H_z^2\tanh\left[\beta H_{xz}\right]\mathrm{sech}^2\left[\beta H_{xz}\right] \\
&\left. +\beta^2 H_{xz}^2H_x^4\mathrm{sech}^2\left[\beta H_{xz}\right]\left(1-3\tanh^2\left[\beta H_{xz}\right]\right)\right\}
\end{aligned}
$$

In Fig. 5.3 and Fig. 5.4, χ_3 is plotted as a function of temperature T/J or the transverse field Γ/J for different choices of Δ and K. The dotted lines indicate the region where the mean-field replica symmetric calculation is unstable. In the next section the calculation of the stability condition is discussed in detail. In Subfigure. 5.3(a) it is observed that for $\Delta = K = 0$ the nonlinear susceptibility χ_3 shows a very sharp peak at a critical temperature $T_g(\Gamma)$. This sharp peak persists as we lower the temperature to $T \to 0$. In Subfigures 5.3(b) and 5.4(a) it is shown that a nonzero random field with a variance $\Delta \neq 0$, smears the singularity of the nonlinear susceptibility. For $K = 0$, the results we obtained for χ_3, using the imaginary time replica formalism, is consistent with the results obtained for an infinite range transverse Ising spin-glass model with a longitudinal random field reported in Ref. [98]. The model in Ref. [98] was performed to study the effects of quantum fluctuations on the proton glass phase in mixed hydrogen-bonded ferro-antiferroelectric systems. However, as it is shown in Subfigures 5.3(b) and 5.4(a), a constant $\Delta \neq 0$ does not show the decreasing of the χ_3 peak by going to lower temperatures, which is what experimentally observed for $LiHo_xY_{1-x}F_4$ in an applied transverse magnetic field [36] (See Chapter 1, Fig. 1.5.) Subfigure 5.4(b) shows that a nonzero $K \neq 0$ gives a qualitative decreasing in the height of the peak. Subfigures 5.3(c) and 5.4(c), subsequently show χ_3 as a function of T ans Γ. As it is easily noticed from Fig. 5.3 and Fig. 5.4, the sudden sharpening of the nonlinear susceptibility, which is observed in real diluted $LiHo_xY_{1-x}F_4$ systems as the classical $T_g(\Gamma = 0)$ is approached (see Fig. 1.5), is not captured from a model in which Δ and K are considered nonzero and constant. This indicates the necessity of bringing the simplified model of Eq. (5.1) into better contact with the realistic microscopic model for the diluted $LiHo_xY_{1-x}F_4$ material [72], In Section 5.4, we discuss how by considering Δ and K to be dependent on the external magnetic field B_x, one can obtain a qualitative behavior that is more similar to what is observed in the real system.

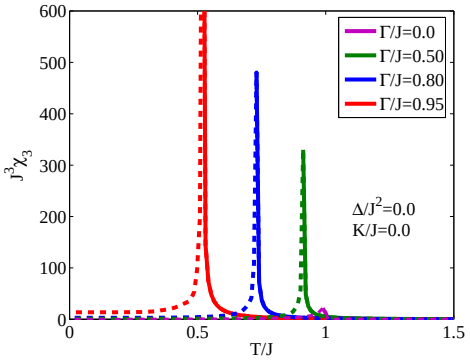

(a) χ_3 as a function of T/J for $\Delta = K = 0.0$. χ_3 is divergent going from $\Gamma = 0$ to higher Γ.

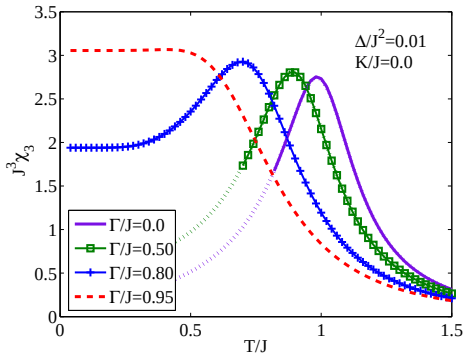

(b) χ_3 as a function of T/J for Δ/J^2= 0.01 and K=0.0. $\Delta \neq 0$ smears the sharp peak of χ_3.

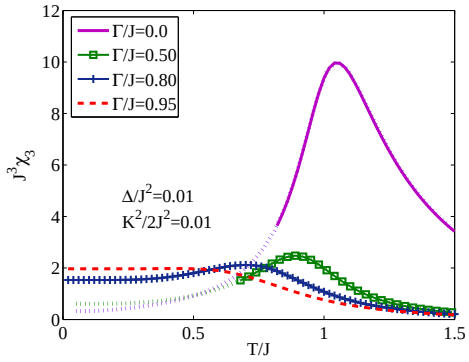

(c) χ_3 as a function of T/J for Δ/J^2=$K^2/2J^2$=0.01. The sharp peaks of χ_3 are rounded and show a decrease in the height of the peaks as going to lower Ts.

Figure 5.3: The nonlinear susceptibility χ_3 is plotted as a function of T/J for different choices of K and Δ. The region where replica symmetric solution is unstable (see next section) is plotted with dotted lines.

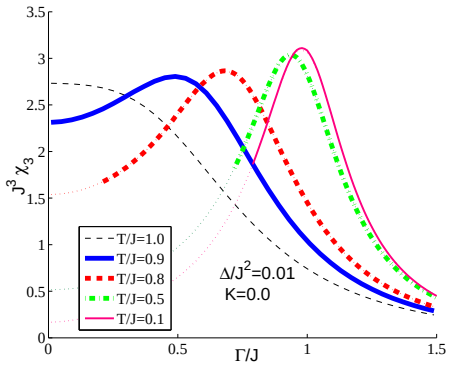

(a) χ_3 as a function of Γ/J for Δ/J^2= 0.01 and K=0.0. The nonzero random field smears the sharp peak of χ_3.

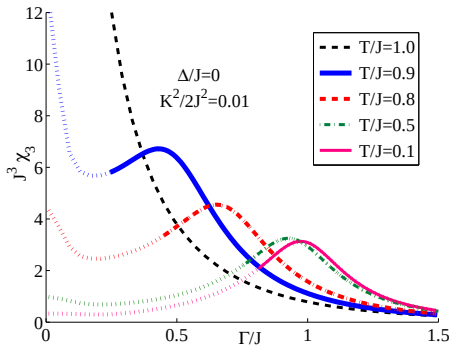

(b) χ_3 as a function of Γ/J for Δ= 0.0 and $K^2/2J^2$=0.01. The height of χ_3 peaks decreases as going to lower Ts.

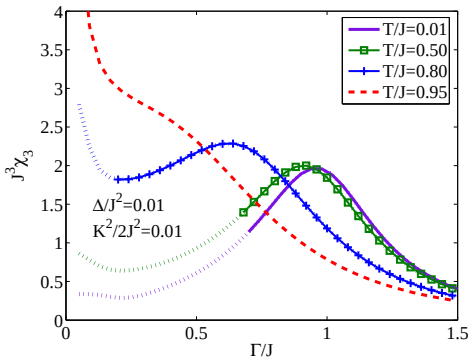

(c) χ_3 as a function of Γ/J for Δ/J^2=$K^2/2J^2$=0.01. The sharp peaks of χ_3 are rounded and show a decrease in the height of the peaks as going to lower temperatures.

Figure 5.4: The nonlinear susceptibility χ_3 is plotted as a function of the transverse field Γ/J for different choices of K and Δ. The region where replica symmetric solution is unstable (see next section) is plotted with dotted lines.

5.3 De Almeida-Thouless Stability Condition

In this section we want to find the stability condition for the replica symmetric solutions. For our mean field replica symmetric calculations it is essential to investigate the condition for which the replica symmetric assumption is a valid assumption. De Almeida-Thouless[22] have shown that for an infinite range SK model, the mean field solution becomes unstable below a critical temperature. Therefore, the replica symmetry is broken and the replica symmetric solution is not correct anymore. In the previous sections, we performed a mean field calculation using the replica symmetry assumption to calculate the order parameters and the nonlinear susceptibility. Therefore, it is crucial to determine the range of T and Γ in which the mean field replica symmetric solution is stable. To do this, we allow a small fluctuation of $Q^{zz}_{\alpha\beta}$, $\Lambda_{\alpha\beta}$, $\Theta_{\alpha\beta}$, $r^{zz}_{\alpha\alpha}$, $\omega_{\alpha\alpha}$ and $\theta_{\alpha\alpha}$ by a small amount around their respective stationary values

$$\begin{aligned}
Q^{zz}_{\alpha\beta}(\tau,\tau') &\longrightarrow Q^{zz} + \delta Q^{zz}_{\alpha\beta}(\tau,\tau') \\
\Lambda_{\alpha\beta}(\tau,\tau') &\longrightarrow \Lambda + \delta\Lambda_{\alpha\beta}(\tau,\tau') \\
\Theta_{\alpha\beta}(\tau,\tau') &\longrightarrow \Theta + \delta\Theta_{\alpha\beta}(\tau,\tau') \\
r^{zz}_{\alpha\alpha}(\tau,\tau') &\longrightarrow r^{zz} + \delta r_{\alpha\alpha}(\tau,\tau') \\
\omega_{\alpha\alpha}(\tau,\tau') &\longrightarrow \omega + \delta\omega_{\alpha\alpha}(\tau,\tau') \\
\theta_{\alpha\alpha}(\tau,\tau') &\longrightarrow \theta + \delta\theta_{\alpha\alpha}(\tau,\tau') \ .
\end{aligned} \tag{5.30}$$

The free energy $G(Q^{zz}_{\alpha\beta}, \Lambda_{\alpha\beta}, \Theta_{\alpha\beta}, r^{zz}_{\alpha\alpha}, \omega_{\alpha\alpha}, \theta_{\alpha\alpha})$ has to be expanded up to the second order in the fluctuations. Referring to the work of De Almeida and Thouless [22], in order to have a stable solution, the deviation of G from the stationary value $\left(\delta G \approx \sum_{y,y'} \partial^2 G[y]/\partial y \partial y'\right) \delta y \delta y'$, should be positive definite, where y and y' are of the $Q^{zz}_{\alpha\beta}$, $\Lambda_{\alpha\beta}$, $\Theta_{\alpha\beta}$, $r^{zz}_{\alpha\alpha}$, $\omega_{\alpha\alpha}$, and $\theta_{\alpha\alpha}$. Therefore, the eigenvalues of the stationary matrix, which its elements consists of $\partial^2 G[y]/\partial y \partial y'$ should be all real and positive. For simplicity, we define $\mathbf{Q}_{\alpha\beta}(\tau,\tau')$ as a three component array in the form of

$$\mathbf{Q}_{\alpha\beta}(\tau,\tau') = \begin{pmatrix} Q^{zz}_{\alpha\beta}(\tau,\tau') \\ \Lambda_{\alpha\beta}(\tau,\tau') \\ \Theta_{\alpha\beta}(\tau,\tau') \end{pmatrix} \ , \tag{5.31}$$

while for the self interacting terms[4] $r^{zz}_{\alpha\alpha}$, $\omega_{\alpha\alpha}$ and $\theta_{\alpha\alpha}$ we define a three component array $\mathbf{W}_{\alpha\alpha}(\tau,\tau')$ as

$$\mathbf{W}_{\alpha\alpha}(\tau,\tau') = \begin{pmatrix} r^{zz}_{\alpha\alpha}(\tau,\tau') \\ \omega_{\alpha\alpha}(\tau,\tau') \\ \theta_{\alpha\alpha}(\tau,\tau') \end{pmatrix} . \tag{5.32}$$

Their stationary replica symmetric equivalents are written as $\mathbf{Q} = \begin{pmatrix} Q^{zz} \\ \Lambda \\ \Theta \end{pmatrix}$ and $\mathbf{W} = \begin{pmatrix} r^{zz} \\ \omega \\ \theta \end{pmatrix}$. The deviation of the elements of the array $\mathbf{Q}_{\alpha\beta}(\tau,\tau')$ with respect to their stationary values of $\mathbf{Q}$ are defined as an array of fluctuation fields

$$\boldsymbol{\eta}_{\alpha\beta}(\tau,\tau') = \begin{pmatrix} \delta Q^{zz}_{\alpha\beta}(\tau,\tau') \\ \delta\Lambda_{\alpha\beta}(\tau,\tau') \\ \delta\Theta_{\alpha\beta}(\tau,\tau') \end{pmatrix} , \tag{5.33}$$

and subsequently the deviation of the array of self-interacting terms $\mathbf{W}_{\alpha\alpha}(\tau,\tau')$ with respect to the stationary values of $\mathbf{W}$ are defined as an array of the fluctuation fields

$$\boldsymbol{\xi}_{\alpha\alpha}(\tau,\tau') = \begin{pmatrix} \delta r^{zz}_{\alpha\alpha}(\tau,\tau') \\ \delta\omega_{\alpha\alpha}(\tau,\tau') \\ \delta\theta_{\alpha\alpha}(\tau,\tau') \end{pmatrix} . \tag{5.34}$$

Referring to the work of De Almeida and Thouless [22], the stability condition is fulfilled if all the eigenvalues of the stability matrix $\mathbf{G}''$ are real and positive. The elements of the stability matrix are $\partial^2 G[y]/\partial y \partial y'$, where y and y' are the different permutations of the elements of $\mathbf{Q}_{\alpha\beta}$ ($Q^{zz}_{\alpha\beta}(\tau,\tau')$, $\Lambda_{\alpha\beta}(\tau,\tau')$, $\Theta_{\alpha\beta}(\tau,\tau')$), and the elements of $\mathbf{W}_{\alpha\alpha}$ ($r^{zz}_{\alpha\alpha}(\tau,\tau')$, $\omega_{\alpha\alpha}(\tau,\tau')$, and $\theta_{\alpha\alpha}(\tau,\tau')$). In the stability matrix the derivatives are calculated with respect to the stationary values under static approximation. After a rather involved calculation, which is found in Appendix E, for $n \to 0$, where n is the number of replicas, the stability condition of our mean

[4]Self interacting terms are those terms, where the overlap between the spin-$\frac{1}{2}$ degrees of freedom are calculated within a single replica (see Eq. (5.18)).

field replica symmetric solution is satisfied if the eigenvalues of the 3×3 matrix $\mathbf{M} = \tilde{\boldsymbol{P}} - 2\tilde{\boldsymbol{Q}} + \tilde{\boldsymbol{R}}$, is positive definite. $\tilde{\mathbf{P}}$, $\tilde{\mathbf{Q}}$, and $\tilde{\mathbf{R}}$ only include a permutation of the second order derivatives of the free energy $\partial^2 G/\partial Q^i_{\alpha\beta}\partial Q^j_{\mu\nu}$ respect to the non-self-interacting terms[5] such as $Q^{zz}_{\alpha\beta}$, $\Lambda_{\alpha\beta}$, and $\Theta_{\alpha\beta}$.

Here, α, β, μ, and ν denotes different replicas, while i and j labels the specific elements of the fluctuation field arrays $\boldsymbol{\eta}_{\alpha\beta}$ defined in Eqs (5.33).

As discussed in Appendix E, the 3×3 matrix elements of $\tilde{\mathbf{P}}$, $\tilde{\mathbf{Q}}$, and $\tilde{\mathbf{R}}$ denotes the three different types, which one can consider for α, β, μ, and ν, such as

$$\begin{aligned}
\tilde{P}_{ij} &= \frac{\partial^2 G}{\partial Q^i_{\alpha\beta}\partial Q^j_{\alpha\beta}} && \alpha = \mu \texttt{ and } \beta = \nu, \\
\tilde{Q}_{ij} &= \frac{\partial^2 G}{\partial Q^i_{\alpha\beta}\partial Q^j_{\alpha\nu}} && \alpha = \mu \texttt{ and } \beta \neq \nu, \\
\tilde{R}_{ij} &= \frac{\partial^2 G}{\partial Q^i_{\alpha\beta}\partial Q^j_{\mu\nu}} && \alpha \neq \mu \texttt{ and } \beta \neq \nu,
\end{aligned}$$

where $Q^i_{\alpha\beta}$ and $Q^j_{\alpha\beta}$ denotes one of the three non-self-interacting fields $Q^{zz}_{\alpha\beta}, \Lambda_{\alpha\beta}$ and $\Theta_{\alpha\beta}$ of the array $\boldsymbol{Q}_{\alpha\beta}$.

Considering G, which was originally defined in Eq. (5.13), to calculate the elements of matrix $\mathbf{M}$, we have to calculate expressions such as

$$\left\langle \mathcal{T}\sigma^{x_l\alpha}(\tau)\sigma^{x_l\beta}(\tau')\sigma^{x_m\mu}(\tau'')\sigma^{x_m\nu}(\tau''')\right\rangle - \left\langle \mathcal{T}\sigma^{x_l\alpha}(\tau)\sigma^{x_l\beta}(\tau')\right\rangle\left\langle \mathcal{T}\sigma^{x_m\mu}(\tau'')\sigma^{x_m\nu}(\tau''')\right\rangle \ .$$

To write the stability matrix elements in a more compact form we define $O^{\alpha\beta\mu\nu}_{x_l x_m}$ as

$$\begin{aligned}
O^{\alpha\beta\mu\nu}_{x_l x_m}(\tau,\tau',\tau'',\tau''') \ \equiv \ & \left\langle \mathcal{T}\sigma^{x_l\alpha}(\tau)\sigma^{x_l\beta}(\tau')\sigma^{x_m\mu}(\tau'')\sigma^{x_m\nu}(\tau''')\right\rangle \\
& - \left\langle \mathcal{T}\sigma^{x_l\alpha}(\tau)\sigma^{x_l\beta}(\tau')\right\rangle\left\langle \mathcal{T}\sigma^{x_m\mu}(\tau'')\sigma^{x_m\nu}(\tau''')\right\rangle \ , \quad (5.35)
\end{aligned}$$

where we trace with respect to the effective Hamiltonian $\mathcal{L}$ for the n replicated single ion system in the $n \to 0$ limit.
Here, x_l and x_m are either z or x, identifying σ^x and σ^z.

[5]The fluctuation of the non-self-interacting terms, where the overlap of the spin-$\frac{1}{2}$ degrees of freedom are calculated between two different replicas play a crucial role in the stability of the replica symmetric free energy G and the concept of replica symmetry breaking.

The matrix $\mathbf{M} = \tilde{\boldsymbol{P}} - 2\tilde{\boldsymbol{Q}} + \tilde{\boldsymbol{R}}$, only includes the non-self-interacting terms $Q^{zz}_{\alpha\beta}$, $\Lambda_{\alpha\beta}$, and $\Theta_{\alpha\beta}$. The elements of the stability matrix not including the self-interacting terms are listed as below

$$\begin{aligned}
\frac{\delta^2 G}{\delta Q^{zz}_{\alpha\beta}\delta Q^{zz}_{\mu\nu}} &= (\beta J)^2\delta_{(\alpha,\beta)}\delta_{(\mu,\nu)} - (\beta J)^4 O^{\alpha\beta\mu\nu}_{zz}(\tau,\tau',\tau'',\tau''') \\
\frac{\delta^2 G}{\delta Q^{zz}_{\alpha\beta}\delta \Lambda_{\mu\nu}} &= -\frac{(\beta J)^4 k^2}{4}\left[O^{\alpha\beta\mu\nu}_{zz}(\tau,\tau',\tau'',\tau''') + O^{\alpha\beta\mu\nu}_{zx}(\tau,\tau',\tau'',\tau''')\right] \\
\frac{\delta^2 G}{\delta Q^{zz}_{\alpha\beta}\delta \Theta_{\mu\nu}} &= -\frac{i(\beta J)^4 k^2}{4}\left[O^{\alpha\beta\mu\nu}_{zz}(\tau,\tau',\tau'',\tau''') - O^{\alpha\beta\mu\nu}_{zx}(\tau,\tau',\tau'',\tau''')\right] \qquad (5.36) \\
\frac{\delta^2 G}{\delta \Lambda_{\alpha\beta}\delta \Lambda_{\mu\nu}} &= (\beta J\frac{k}{2})^2\delta_{(\alpha,\beta)}\delta_{(\mu,\nu)} \\
&\quad -(\beta J\frac{k}{2})^4\left[O^{\alpha\beta\mu\nu}_{zz}(\tau,\tau',\tau'',\tau''') + O^{\alpha\beta\mu\nu}_{xx}(\tau,\tau',\tau'',\tau''') + 2O^{\alpha\beta\mu\nu}_{zx}(\tau,\tau',\tau'',\tau''')\right] \\
\frac{\delta^2 G}{\delta \Theta_{\alpha\beta}\delta \Theta_{\mu\nu}} &= (\beta J\frac{k}{2})^2\delta_{(\alpha,\beta)}\delta_{(\mu,\nu)} \\
&\quad +(\beta J\frac{k}{2})^4\left[O^{\alpha\beta\mu\nu}_{zz}(\tau,\tau',\tau'',\tau''') + O^{\alpha\beta\mu\nu}_{xx}(\tau,\tau',\tau'',\tau''') - 2O^{\alpha\beta\mu\nu}_{zx}(\tau,\tau',\tau'',\tau''')\right] \\
\frac{\delta^2 G}{\delta \Lambda_{\alpha\beta}\delta \Theta_{\mu\nu}} &= -i(\beta J\frac{k}{2})^4\left[O^{\alpha\beta\mu\nu}_{zz}(\tau,\tau',\tau'',\tau''') - O^{\alpha\beta\mu\nu}_{xx}(\tau,\tau',\tau'',\tau''')\right]
\end{aligned}$$

In Eq. (5.35), regarding the definition of $O^{\alpha\beta\mu\nu}_{x_l x_m}$, it can be shown that after applying the static approximation and the replica symmetry assumption in the $n \to 0$ limit and performing the Hubbard-Stratonovitch transformation, we obtain

$$\begin{aligned}
O^{\alpha\beta\mu\nu}_{x_l x_m} - 2O^{\alpha\beta\alpha\nu}_{x_l x_m} + O^{\alpha\beta\alpha\beta}_{x_l x_m} &= \frac{1}{2\pi}\int_{-\infty}^{\infty} dzdx\ e^{-(z^2+x^2)/2}\left[\langle\sigma^{x_l}\sigma^{x_m}\rangle - \langle\sigma^{x_l}\rangle\langle\sigma^{x_m}\rangle\right]^2 \\
&\equiv \frac{1}{2\pi\beta}\int_{-\infty}^{\infty} dzdx\ e^{-(z^2+x^2)/2}\left[\chi_{x_l,x_m}(x,z)\right]^2\ , \qquad (5.37)
\end{aligned}$$

where x_l and x_m denotes either z or x. We have defined $\chi_{x_l,x_m}(x,z)$ as

$$\chi_{x_l,x_m}(x,z) = \frac{\partial^2 \ln\left[\cosh\left(\beta H_{xz}\right)\right]}{\partial H_{x_l}\partial H_{x_m}}\ . \qquad (5.38)$$

Referring to the matrix elements in relation (5.37), we are now able to calculate the matrix elements of, $\mathbf{M} = \tilde{\boldsymbol{P}} - 2\tilde{\boldsymbol{Q}} + \tilde{\boldsymbol{R}}$, which we list below

$$
\begin{aligned}
M_{Q^{zz},Q^{zz}} &= (\beta J)^2 \left\{ 1 - \frac{1}{2\pi} \int_{-\infty}^{\infty} dz dx \; e^{-(z^2+x^2)/2} \chi_{zz}^2 \right\}, \\
M_{Q^{zz},\Lambda} &= -\frac{1}{2\pi} \left(\beta J \frac{k}{2} \right)^2 \int_{-\infty}^{\infty} dz dx \; e^{-(z^2+x^2)/2} \left[\chi_{zz}^2 + \chi_{zx}^2 \right], \\
M_{Q^{zz},\Theta} &= -i \frac{1}{2\pi} \left(\beta J \frac{k}{2} \right)^2 \int_{-\infty}^{\infty} dz dx \; e^{-(z^2+x^2)/2} \left[\chi_{zz}^2 - \chi_{zx}^2 \right], \\
M_{\Lambda,\Lambda} &= (\beta J \frac{k}{2})^2 \left\{ 1 - \frac{1}{2\pi} \frac{k^2}{4} \int_{-\infty}^{\infty} dz dx \; e^{-(z^2+x^2)/2} \left[\chi_{zz}^2 + \chi_{xx}^2 + 2\chi_{zx}^2 \right] \right\}, \\
M_{\Theta,\Theta} &= (\beta J \frac{k}{2})^2 \left\{ 1 + \frac{1}{2\pi} \frac{k^2}{4} \int_{-\infty}^{\infty} dz dx \; e^{-(z^2+x^2)/2} \left[\chi_{zz}^2 + \chi_{xx}^2 - 2\chi_{zx}^2 \right] \right\}, \\
M_{\Lambda,\Theta} &= -i \frac{1}{2\pi} \left(\beta J \frac{k^2}{4} \right)^2 \int_{-\infty}^{\infty} dz dx \; e^{-(z^2+x^2)/2} \left[\chi_{zz}^2 - \chi_{xx}^2 \right].
\end{aligned}
$$

where

$$
\chi_{zz} = \frac{H_x^2}{H_{xz}^3} \tanh\left[\beta H_{xz}\right] + \beta \left[\frac{H_z}{H_{xz}} \right]^2 \mathrm{sech}^2\left[\beta H_{xz}\right] \tag{5.39}
$$

$$
\chi_{xx} = \frac{H_z^2}{H_{xz}^3} \tanh\left[\beta H_{xz}\right] + \beta \left[\frac{H_x}{H_{xz}} \right]^2 \mathrm{sech}^2\left[\beta H_{xz}\right] \tag{5.40}
$$

$$
\chi_{zx} = -\frac{H_x H_z}{H_{xz}^3} \tanh\left[\beta H_{xz}\right] + \beta \frac{H_x H_z}{H_{xz}^2} \mathrm{sech}^2\left[\beta H_{xz}\right]. \tag{5.41}
$$

The origin of the complex matrix elements is due to the relation of Θ with Q_{zz} and Q_{xx} (see Eq. (5.17).) Θ is a complex function of the real parameters Q_{zz} and Q_{xx}. The condition that the eigenvalues of this matrix should be all real and positive definite, provides us with a condition for the stability of the replica symmetric calculation. The matrix elements of $\mathbf{M}$ are calculated numerically. By calculating all the matrix elements of $\mathbf{M}$, $\lambda_{\mathbf{M}}$, the eigenvalues of matrix $\mathbf{M}$, can then be determined.

In Fig. 5.5, we plotted [AT] $= \frac{T^2}{J^2} \lambda_{\mathbf{M}}^{\min}$ as a function of Γ/J, where $\lambda_{\mathbf{M}}^{\min}$ is the smallest eigenvalue of the matrix $\mathbf{M}$ [6]. Where ever [AT] intersects the horizontal axis, beneath the horizontal axis [AT] is negative, $\lambda_{\mathbf{M}}^{\min}$ is negative, and the replica

[6] The matrix elements of $\mathbf{M}$ have a common factor of J^2/T^2. In calculating [AT], we have divided the elements of $\mathbf{M}$ by J^2/T^2.

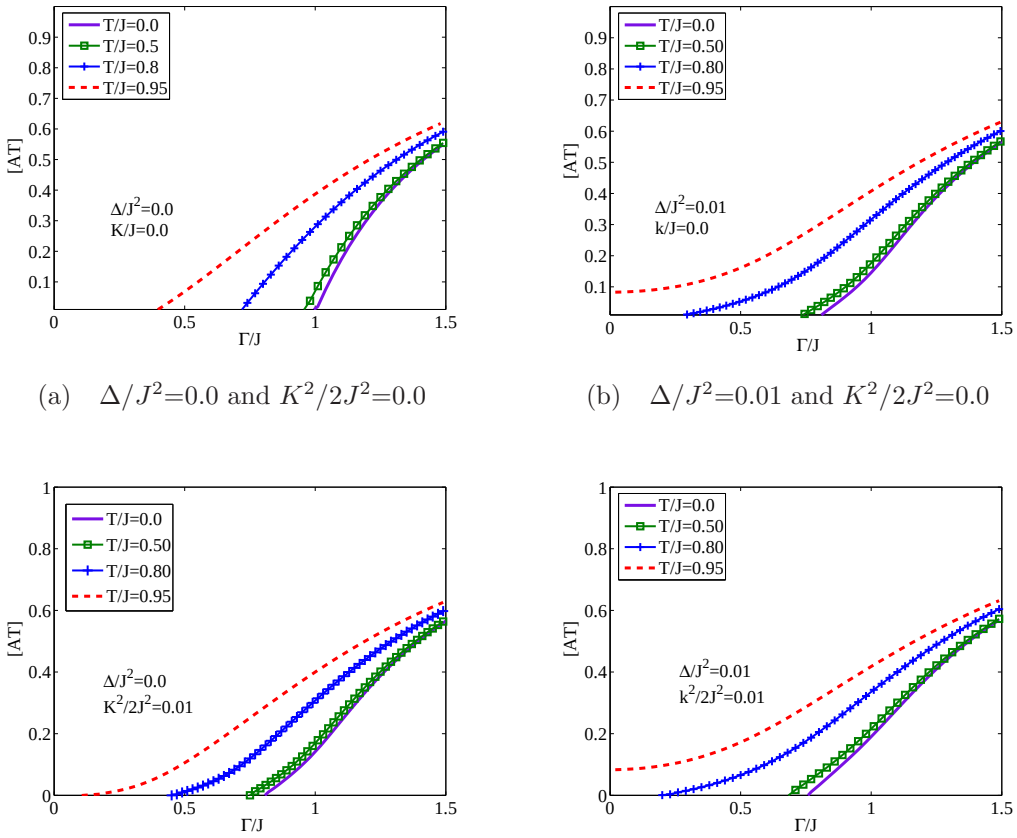

(a) Δ/J^2=0.0 and $K^2/2J^2$=0.0

(b) Δ/J^2=0.01 and $K^2/2J^2$=0.0

(c) Δ/J^2=0.0 and $K^2/2J^2$=0.01

(d) Δ/J^2=0.01 and $K^2/2J^2$=0.01

Figure 5.5: $[\mathrm{AT}] = \frac{T^2}{J^2}\lambda_{\mathbf{M}}^{\min}$ as a function of Γ/J for different choices of the distribution variances of K^2 and Δ and different values of T/J. The transverse field Γ_c is the Γ, where the [AT] plot intersects with the [AT] = 0 line. For $\Gamma < \Gamma_c$, [AT] becomes negative. The replica symmetric solution is not stable anymore.

symmetric mean field solution is unstable. In Fig. 5.5(a) for $\Delta = K = 0$, one can see that below the transition point where χ_3 shows a singular behavior the replica symmetric solution in not stable. For $\Delta \neq K \neq 0$, the field Γ and temperature T for which the solution become unstable decreases. The instability point occur at lower temperatures compared where χ_3 shows a peak. As plotted in Fig. 5.5(b) and Fig. 5.5(d), there exist conditions in which the system remains stable even down to zero transverse field.

5.4 Obtaining a Qualitative Match with Real $LiHo_xY_{1-x}F_4$

Comparing Fig. 5.4(a) with the experimental $\chi_3^{\rm exp}(B_x)$ (the top left inset of Fig. 5.4), one finds that although the singularity in χ_3 is smeared down, the dependence of χ_3 upon Γ in Fig. 5.4(a) does not show a decrease in magnitude as T is decreased. If we consider that in the microscopic spin-1/2 effective Hamiltonian of the realistic system $\gamma(B_x)$ is simply an increasing function of B_x, then the lack of magnitude reduction in Fig. 5.4(a) is inconsistent with experimental observations for the real system. Also, while χ_3 shows a decreasing amplitude with decreasing T in Fig. 5.4(b), it does not reveal the rapid sharpening at $\Gamma > 0$ seen in experiments as the classical $T_g(\Gamma = 0)$ critical temperature is approached. The transverse field Γ of is a function of the Therefore, to make a closer connection with the real material, we compare the random couplings, the random field and the transverse field Γ of the generalized infinite range Hamiltonian introduced in Eq. (5.1) with their equivalent counterparts of the microscopic spin-1/2 effective Hamiltonian of the realistic system, when the system is randomly diluted and some of the magnetic Ho^{3+} ions are substituted with non-magnetic Y^{3+}. If we compare Eq. (5.1) with Eq. (3.14), we see that J_{ij} couplings correspond to $-C_{zz}^2(B_x)\epsilon_i\epsilon_j L_{ij}^{zz}$, K_{ij} correspond to $-2C_{zz}(B_x)C_{xx}(B_x)\epsilon_i\epsilon_j L_{ij}^{zz}$, and h_i^z correspond to $-2C_{zz}(B_x)C_{x0}(B_x)\epsilon_i \sum_j \epsilon_j L_{ij}^{zz}$. Here, ϵ_i denotes the dilution of site i, such that if site i is occupied by a magnetic Ho^{3+} ion, $\epsilon_i = 1$; otherwise $\epsilon_i = 0$. From the comparison of Eq. (5.1) with Eq. (3.14), it turns out that the key physics ingredient missing in these calcula-

tions is the underlying *microscopic* dependence of the distribution width of J_{ij}, K_{ij}, and h_i^z upon B_x. This dependence on B_x is tied to the general phenomenology of random field development in $LiHo_xY_{1-x}F_4$. In Chapter 3, we discussed that for a general random spin system for which the effective spin-spin interactions are anisotropic and contain off-diagonal terms, an applied transverse magnetic field B_x may induce random fields in the system. The amplitude of these random fields is expected to increase for increasing B_x. Therefore, the corresponding variances are expected to increase with B_x as well. If Eq. (5.1) is compared with Eq. (3.14), one can see that the B_x dependence of $J(B_x)$, $K(B_x)$, and $\Delta(B_x)$ originates from the $C_{\mu\nu}(B_x)$ transformation coefficients, which are B_x dependent. As a result, from Fig. 3.4, one can conclude that $J(B_x)$ decreases slowly with B_x, while $K(B_x)$, and $\Delta(B_x)$ increase asymptotically with B_x. Also, by comparing Γ in Eq. (5.1) with the transverse field term appeared in Eq. (3.14), one can conclude that the magnitude of $\Gamma(B_x)$ also increases asymptotically with B_x. As a result, at higher temperatures, where χ_3 has a peak at lower transverse fields, the amplitude of the induced random fields are weak compared with low temperatures, where χ_3 has a peak at higher transverse fields. Therefore, this B_x dependence of $K(B_x)$ and $\Delta(B_x)$ can qualitatively explain the abrupt decrease of the magnitude of χ_3 as B_x increases. To obtain a further match with experiment, one may bring Eq. (5.1) in contact with the relevant microscopic model describing the system.

One may expect that a B_x dependence of $J(B_x)$, $K(B_x)$, $\Delta(B_x)$, and $\Gamma(B_x)$ can be obtained from a one-to-one match between the terms of Eq. (5.1) and Eq. (3.14). Unfortunately, the effective spin-$\frac{1}{2}$ Hamiltonian of Eq. (3.14) does not incorporate the nuclear ion hyperfine interactions. Previously, in Chapter 3, we discussed that hyperfine interactions can not be neglected when $LiHo_xY_{1-x}F_4$ is in the spin glass regime [93, 94]. The physical importance of these interactions, which are important in Ho-based materials [1, 57], is discussed in Refs. [93, 94]. One of the main problems which may occur as a result of neglecting hyperfine interactions is the relation between Γ, the transverse field coupled to the spin-$\frac{1}{2}$ degrees of freedom and the applied magnetic field B_x. Experimental results obtained from AC susceptibility measurements on $LiHo_{0.167}Y_{0.833}F_4$ indicate that at zero temperature, the spin glass to paramagnet transition occurs at a critical field of $B_x^c = 12.0 \pm 0.4$ kOe [36, 71]. If

the effective spin-$\frac{1}{2}$ Hamiltonian of Eq. (3.14) is assumed to be the model describing $LiHo_{0.167}Y_{0.833}F_4$, then B_x^c corresponds to a ground state doublet splitting of $\Gamma \sim 1.0$ K. Such a value of Γ contradicts theoretical expectations indicating that $\Gamma \sim T_g(B_x = 0) = 133$ mK. The experimental B_x^c is therefore a factor of 10 higher than the naively expected theoretical B_x^c. Therefore, it is not correct to naively use $\frac{1}{2}\Delta_E(B_x)$, the energy splitting gap of Eq. (3.14) as the Γ of Eq. (5.1). The authors of Refs. [93, 94] found that hyperfine interactions lead to a renormalization of the pairwise interactions and the critical transverse field in SG samples of $LiHo_xY_{1-x}F_4$, when T_g is substantially below the hyperfine energy scale ($A = 39$ mK). In order to obtain a phenomenological relation between Γ in Eq. (5.1) and the real physical field B_x, for x=0.167 we set

$$\Gamma(B_x)/J(B_x) = 1.05(B_x/B_x^c)^{0.35} \ . \tag{5.42}$$

Here, $B_x^c = 1.2$ T is the zero temperature experimental critical magnetic field for x=0.167 [71]. In Ref. [71], for x=0.167 the T_g-B_x phase diagram of $LiHo_xY_{1-x}F_4$ is obtained experimentally by measuring the AC susceptibility. The measured $T_g(B_x)$ can be plotted as a function of B_x. The spin glass transition temperature depends on the transverse magnetic field via the relation

$$T_g(B_x) = T_g(0)[1 - (B_x/B_x^c)^{\phi}] \tag{5.43}$$

relation, where ($\phi = 1.7 \pm 0.1$). On the other hand, from Eq. (5.1), as a result of our theoretical mean field calculations, we obtain a theoretical phase diagram for T_g as a function of Γ. For $K = \Delta = 0$, one can derive a theoretical relation for T_g in the form of

$$T_g(\Gamma) \approx T_g(0)[1 - a\,(\Gamma/T_g(0))^{\psi}] \tag{5.44}$$

by fitting to the theoretical phase diagram, where we find $a \approx 0.79$ and $\psi \approx 4.82$). By matching the theoretical T_g of Eq. (5.44) with the experimental T_g of Eq. (5.43), we derive the relation between Γ and B_x, which we use to obtain the parametrization of Eq. (5.42).

To obtain the B_x dependent variances, $J^2(B_x)$, $K^2(B_x)$ and $\Delta(B_x)$ of the infinite range generalized SK model of Eq. (5.1), we first calculate the disorder average of

the dipole-dipole couplings of the first, second and third lattice sums in Eq. (3.14), respectively. We have

$$J^2 = (g\mu_{\rm B})^4[C_{zz}(B_x)C_{xx}(B_x)]^2[\frac{1}{N_0}\sum_{(i,j)}\epsilon_i\epsilon_j(L_{ij}^{zz})^2]_{\rm av}\ , \tag{5.45}$$

$$K^2 = 4(g\mu_{\rm B})^4[C_{zz}(B_x)C_{xx}(B_x)]^2[\frac{1}{N_0}\sum_{(i,j)}\epsilon_i\epsilon_j(L_{ij}^{xz})^2]_{\rm av}\ , \text{ and} \tag{5.46}$$

$$\Delta = (g\mu_{\rm B})^4[C_{zz}(B_x)C_{x0}(B_x)]^2[\frac{1}{N_0}\sum_{i}\epsilon_i(\sum_{j\neq i}\epsilon_j L_{ij}^{xz})^2]_{\rm av}. \tag{5.47}$$

where $[\ldots]_{\rm av}$ signifies an average over the bimodal lattice occupancy probability distribution, N_0 is the total number of sites, $P(\epsilon_i) = x\delta(\epsilon_i - 1) + (1-x)\delta(\epsilon_i)$, where x is the concentration ratio of the Ho^{3+} ions. Motivated by the results of Refs. [93, 94], where dipole-dipole interactions are renormalized for relatively low temperatures, in order to incorporate the role of hyperfine effects on h_i^z and K_{ij}, and to obtain results comparable with experimental results, we rescale K and Δ calculated from their microscopic origin in Eq. (5.45) by a scale factor $\eta = 0.15$ that repositions the peak of $\chi_3^{\rm theo}(B_x)$ at $B_x \sim 5$ kOe for $T_g(B_x)/T_g(0) = 0.75$. Without this rescaling, χ_3 would peak at relatively lower temperatures compared to experiment [36]. As shown in Fig. 5.4, including the B_x dependence of K/J and Δ/J^2 in the χ_3 calculation provides a qualitative description for χ_3 behavior similar to what is observed in experiments.

5.5 Summary and Conclusion

To address the puzzling behavior of the nonlinear susceptibility measurements of $LiHo_xY_{1-x}F_4$ subject to an external transverse magnetic field B_x in the spin glass phase, and to give a qualitative analytical description of how random field effects induced by an applied B_x explains the smearing of the nonlinear susceptibility at the spin glass transition with increasing B_x, we studied a generalized SK transverse field Ising SG model as a mean field variant of Eqs. (3.6, 3.14). The standard SK Ising spin glass model was generalized, such that it possess the relevant interactions pertaining to induced random fields in $LiHo_xY_{1-x}F_4$. To do so, we were inspired

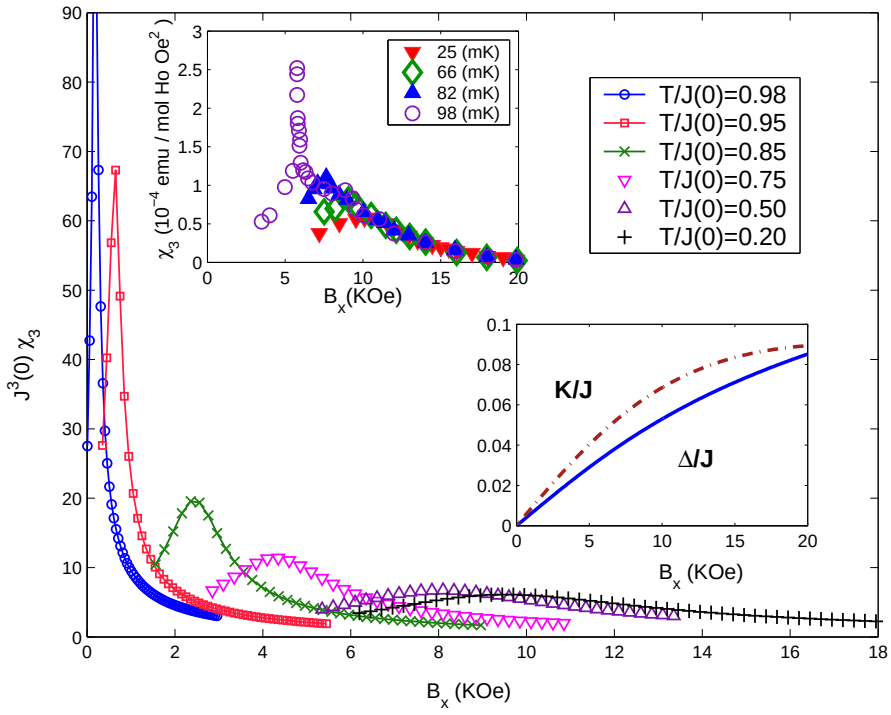

Figure 5.6: χ_3 vs B_x for different temperatures given by the model of Eq. (5.1) and considering Δ, K and J to be variating functions of B_x, which were first reported in Ref. [72]. The top inset shows $\chi_3^{\rm exp}$ from Ref. [36]. The parameters K and Δ are computed using $x = 0.167$ from Eq. (5.45). To incorporate in a phenomenological way the role of hyperfine effects, both K and Δ have been rescaled by a scale factor $\eta = 0.15$ to position the peak of $\chi_3^{\rm theo}(B_x)$ at $B_x \sim 5$ kOe for $T_g(B_x)/T_g(0) = 0.75$. The $\eta-$rescaled $K(B_x)$ and $\Delta(B_x)$ are shown in the bottom inset. Similarly, $\Gamma(B_x)$ is scaled to match the experimental $T_c(B_x)$.

by the low energy effective spin-$\frac{1}{2}$ description of diluted $LiHo_xY_{1-x}F_4$ subject to an external B_x, where the random field effect directly manifest as a linear random field coupled to σ_i^z and a random off-diagonal coupling between σ_i^z and σ_i^x.

We performed a mean field calculation on a generalized SK model, employing the imaginary time formalism and the replica trick to derive the (replicated) free-energy of the system. To further simplify the calculations, we made a static approximation for the replica-symmetric solution in the PM phase. Via this mean field procedure, we derived self-consistent equations for magnetizations, M^z, M^x and spin-glass order parameters Q^{xx}, Q^{zz}. We obtained χ_3 from $\chi_3 = \frac{1}{6}\partial^3 M_z/\partial {h_0^z}^3$, by solving numerically the resulting four coupled self-consistent equations for M^z, M^x and spin-glass order parameters Q^{xx}, Q^{zz}. Following a standard procedure, first introduced by De Almeida and Thouless [22], we determined the limit of stability of the replica symmetric solution. We found that a finite random field smears the sharp peak of χ_3. However, χ_3 does not show a decrease in magnitude as T is decreased, similar to what observed experimentally [36]. Also, we found that, while for a finite variance of the random off-diagonal couplings χ_3 shows a decreasing amplitude with decreasing T, it does not reveal the rapid sharpening seen in experiment as T is reduced. We found that the crucial physics missing is the underlying dependence of the amplitude of the random field and the off-diagonal random coupling with the external B_x. While the amplitudes are zero at $B_x = 0$, they progressively grow by increasing B_x. This B_x dependence of the random field is understood from the original effective spin-$\frac{1}{2}$ model of Eqs. (3.6, 3.14). Although, a B_x dependent effective random fields explains the general trend observed in experiment, to bring our calculations to a closer contact with real $LiHo_xY_{1-x}F_4$, we estimated the relation of $\Gamma(B_x)$ with B_x by fitting with experimental data and estimated the variance of our field-dependent random interactions and random field to be proportional to the variance of the site diluted interactions and effective random fields of the effective spin-$\frac{1}{2}$ model for $LiHo_xY_{1-x}F_4$ with an applied B_x of Eq. (3.14).

In conclusion, by comparing numerical and analytical results with experimental data we have obtained compelling evidence that induced random fields are indeed at play and "observed" in $LiHo_xY_{1-x}F_4$. As a result, $LiHo_xY_{1-x}F_4$ in a transverse field is identified as a new class of random field (RF) Ising system.

Now that we have obtained some persuasive evidence of how effective spin-$\frac{1}{2}$ description of $LiHo_xY_{1-x}F_4$ is useful to obtain a better understanding of the random field physics in such materials, in the next chapter we shift gear and exploit the effective spin-$\frac{1}{2}$ model derived for pure $LiHoF_4$, to numerically revisit the phase diagram of $LiHoF_4$ in an applied B_x (in particular small B_x) in the vicinity of the classical critical temperature (see Fig. 1.6). As we discussed in the Introduction of the thesis, our goal in the next chapter is to address the origin of the discrepancy between the experimental phase diagram and the one obtained in Ref. [57] numerically using stochastic series expansion quantum Monte Carlo [103, 104] and which persists down to the classical transition temperature.

Chapter 6

Perturbative Quantum Monte Carlo Study of $LiHoF_4$ in a Transverse Magnetic Field

6.1 $LiHoF_4$ as a TFIM

In addition to the phenomena arising in the diluted regime of $LiHo_xY_{1-x}F_4$, the $LiHoF_4$ ($x = 1$) system also turns out to be interesting. There still exist problems for the pure $LiHoF_4$, requiring its properties in nonzero B_x to be re-investigated more thoroughly. It is just recently that the properties of $LiHoF_4$ in a transverse external magnetic field have been studied in quantitative detail starting from a truly microscopic spin Hamiltonian [57]. In Ref. [57], which reported results from a quantum Monte Carlo (QMC) study using the stochastic series expansion (SSE) technique [74], a general qualitative agreement between the microscopic model and experimental data [1] was obtained. However, as we discussed in the Introduction and re-illustrate in Fig. 6.1, there is significant quantitative discrepancy between the Monte Carlo results of Ref. [57] and the experimental data of Ref [1]. In particular, the discrepancy between experiment and QMC results persists asymptotically close to the classical ferromagnetic to paramagnetic phase transition, where B_x/T_c and quantum fluctuations are *perturbatively small*. For very low temperatures and

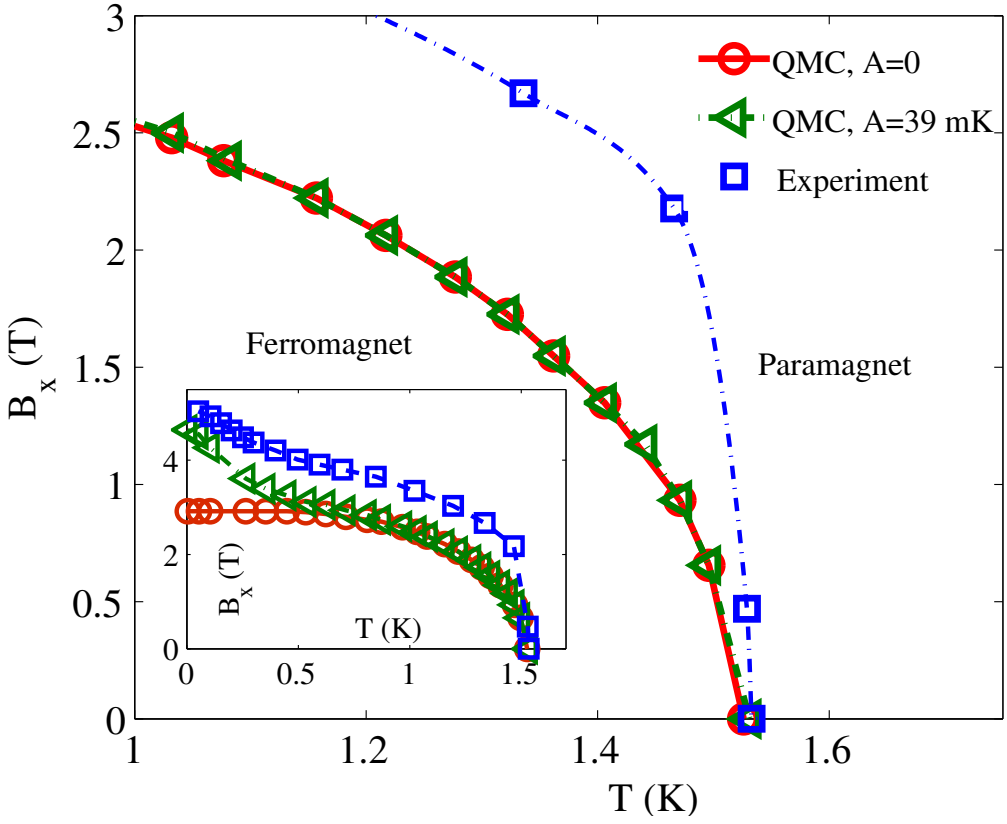

Figure 6.1: The discrepancy between the experimental [1] phase diagram of $LiHoF_4$ and quantum Monte Carlo (QMC) simulations using stochastic series expansion for small B_x from Ref. [57]. The whole phase diagram is shown in the inset. At low temperature and high B_x, neglecting the large hyperfine interaction A, generates a large discrepancy between the experimental quantum critical point and the one obtained from simulation. However, at low B_x and close to the classical critical point, the hyperfine interaction is not a quantitatively important parameter. Other possibilities for the origin of this discrepancy has to be investigated in this regime.

high B_x, it is crucial to consider the hyperfine interaction in order to explain the behaviour of the phase diagram close to the quantum critical point [1, 57, 75]. However, for very small B_x/T_c, the numerical results shown in Fig. 6.1 indicate that the effect of the hyperfine interaction is not important close to the classical transition at T_c.

It was suggested in Ref. [57] that the discrepancy between simulation and experiment, close to the classical transition, may be related to some uncertainty in the crystal field parameters (CFP) used in the crystal field Hamiltonian, which enters in the transverse field Ising model (TFIM) description of $LiHoF_4$ (see Eq. (3.13)), and which is simulated via QMC. Indeed a number of CFP sets obtained from different experimental works, such as susceptibility measurements [54], neutron scattering [78], and electron paramagnetic resonance experiments [79], provide somewhat different values for the CFP. Specifically, different CFP would lead to different field (B_x) dependent effective coupling parameters in the TFIM description of $LiHoF_4$, which would result in different B_x vs T_c phase diagrams.

Yet, there are other factors of strictly computational nature which may be at the origin of the discrepancy illustrated in Fig. 6.1. For example, because of the difficulties associated with dipolar interactions, calculations incorporating long-range dipolar interactions should be performed carefully. Because of the long-range nature and angular dependence of dipolar interactions, the dipolar sum $U(i) = 1/N \sum_j (1 - 3\cos^2\theta_{ij})/r_{ij}^3$ is conditionally convergent [105, 106][1], i.e the value of the sum depends on the shape of the external boundary of the system studied. Here, r_{ij} is the distance between site i and j, and θ_{ij} is the angle between r_{ij} and the Ising spin axis. For example, the conditional convergence of dipolar

[1]The sum of an infinite number of dipole-dipole interactions is conditionally convergent and depends on the order of the summation. For example, if the dipole-dipole interactions of a central unit cell with unit cells located on an ever-increasing long needle-shaped sample, the energy converges to a different value than if the interaction energies is summed spherically. Roughly speaking, this conditional convergence arises because the number of interacting dipoles on a shell of radius R grows like R^2, while the strength of a single dipole-dipole interaction falls like $1/R^3$, and the mathematical $\sum_{n=1}^{\infty} \frac{1}{n}$ summation diverges. The value that the sum converges to depends on the shape of the boundary of the system. In the present work, the effect of the geometry of the boundary is incorporated via the Ewald summation technique. See Ref. [106].

sums has been studied by Luttinger and Tisza [105]. They performed the dipolar sum for a number of spin structures for systems with different external boundary shapes. For example, they considered an infinitely large system of dipoles on a body centered cubic lattice. They found that when the external boundary is spherical, the ground state is antiferromagnetic, while it is ferromagnetic for a needle-shaped sample. Later, Griffiths rigorously proved that for zero external field, the free energy for a dipolar lattice system has to be independent of the sample shape in the thermodynamic limit [107]. The immediate consequence of Griffiths' theorem is that, in zero external field, the net magnetization of the sample has to be zero. Otherwise, the field originating from the magnetic moments sitting on the boundary of the sample would couple to the dipolar moments of the sample, making the free energy shape dependent. Therefore, as a result of Griffiths' theorem [107], domains are formed in the sample, such that in the thermodynamical limit, the total magnetization of the sample is zero. Griffiths' theorem is contrary to Luttinger and Tisza [105] results, where the spin configurations were assumed uniform, and the formation of domain walls were neglected in their work. The reason Luttinger and Tisza's results do not conform with Griffith's theory is that the former authors assumed a uniform ground state spin configuration and ignored the possibility of domain formation. This discussion emphasizes the complication of studying systems with long range dipolar interactions and the caution which should be taken when dealing with such systems (e.g. the choice of the boundary geometry, boundary conditions and the shape of the domain walls.) Finite size effects are another issue that needs to be handled quite carefully in systems where ions interact via long-range interactions.

There are different ways to incorporate dipolar interactions in a computationally efficient way. The method implemented in Ref. [57] is the reaction field method [108], which truncates the sum of the long-range interactions at the boundary of a sphere, with the dipoles outside the sphere treated in a mean-field fashion. Due to the semi mean-field nature of this method, the reaction field method overestimates the critical temperature, T_c. In the presence of quantum fluctuations, this overestimation is still at play and can possibly influence the B_x-T_c phase diagram

near $T_c(B_x = 0)$ as well. The Ewald summation method [109, 110, 111, 112][2] is another method to treat the long-range dipolar interactions. In the Ewald summation method, a specified volume is periodically replicated. Then, by summing instead two absolutely convergent series effectively representing the dipolar interactions between magnetic moments i and j, and all the periodically repeated images of j, an effective dipole-dipole interaction between two arbitrary magnetic moments i and j within the finite size sample to be numerically simulated can be derived. From a general perspective point of view, it would appear quite worthwhile to investigate the applicability and usefulness of the Ewald summation method to determine the low B_x vs T_c phase diagram of $LiHoF_4$. Indeed, the Ewald summation method, unlike the reaction field one, is less prone to mean field over-estimations, and can be used as another methodology to investigate $LiHoF_4$ via simulations [63].

Another factor whose influence on the $B_x - T$ phase diagram should be studied is the role of the nearest neighbor exchange interaction $J_{\rm ex}$ in $LiHoF_4$. Although for a $4f$ ion such as Ho^{3+}, the dipole-dipole interaction is the predominant interaction, however, $J_{\rm ex}$ is not that smaller to be completely neglected. The strength of $J_{\rm ex}$ is unknown, but can be determined such that the numerically determined classical critical temperature matches the experimental value for $B_x = 0$. The estimated value of $J_{\rm ex}$ is highly sensitive to the method used to handle the external sample boundaries and finite size effects in simulations, both of which having significant effects when using the reaction field (RF) method, as already discussed in Ref. [57].

6.2 Scope of this Chapter

The above discussion should make it clear that there are two rather distinct avenues to pursue in order to seek an explanation for the discrepancy between the experimental [1] B_x vs T_c phase diagram of $LiHoF_4$ and the one obtained via QMC [57]. One avenue, is that the current microscopic model is incomplete. Specifically, as

[2]For example, the Ewald summation method has proved quite efficient to allow a characterization of the thermodynamic properties of rare-earth spin ice materials, such as $Ho_2Ti_2O_7$ and $Dy_2Ti_2O_7$, and a determination of the exchange in these materials. See Ref. [112] and references therein.

mentioned above, and suggested in Ref. [57], one possible source for this incompleteness may be an inaccurate set of CFP. Another possible source is that other interactions other than long-range magnetic dipolar interactions and nearest neighbor exchange may be at play [113]. Examples of other interactions include higher order multipole interactions and virtual phonon exchange [113]. The other avenue is related to the ensemble of computational pitfalls and ensuing numerical errors that may arise when one deals with long range dipolar interactions through simulations. Therefore, before one delves into exploring a more complex microscopic Hamiltonian, there is a clear need to re-investigate the "simpler" problem that solely considers long-range dipole-dipole interactions and nearest neighbor exchange.

In this work we aim to scrutinize the individual role of each of the computational issues as potential culprits for the discrepancy observed in Fig. 6.1. Because QMC and experiment do not match at $B_x/T_c \to 0$, we have developed a tool that allow us to achieve the goal in an efficient and computationally simple way. Since this discrepancy appears at low enough B_x near the classical T_c, where quantum fluctuations are *perturbatively* small, we can expand the partition function Z in terms of the transverse magnetic field B_x, and recast the partition function as a sum over strictly classical states, using a new effective *classical* Hamiltonian $H_{\text{eff}}(T)$. In $H_{\text{eff}}(T)$, the quantum effects are incorporated perturbatively, giving us the ability to calculate all thermodynamical quantities in presence of small quantum fluctuations within a classical Monte Carlo method. Therefore classical Monte Carlo simulations can be easily performed using $H_{\text{eff}}(T)$ in a very simple way, without the need to perform complicated QMC [57, 74] simulations when interested in a regime with weak quantum fluctuations[3]. Therefore, we can focus on the region close to the classical transition and investigate the different possible origins of the discrepancy in detail.

In summary, (i) the complexity of the QMC SSE method, (ii) the problematic conditional convergence of dipolar lattice sums, (iii) the question of controlled finite

[3]The quantum Monte Carlo method (QMC) based on stochastic series expansion (SSE) of Ref. [74] amounts to a numerical summation of βH to high powers, where H is the Hamiltonian and $\beta = 1/k_{\text{B}}T$. The method we use splits H into the classical Ising sector, H_0, and the quantum transverse field term, H_1, and resums "analytically" all the terms in βH_0 and retains only the leading $(\beta H_1)^2$ term when evaluating thermodynamic averages.

size effects and its role on the consistent determination of the nearest-neighbor exchange $J_{\rm ex}$, and (iv) the possible sensitivity of the $T_c(B_x)$ dependence on the choice of CFP altogether warrant a new numerical investigation of the $T_c(B_x)$ phase diagram in the $LiHoF_4$ transverse field Ising material. Below, we will show that either fortunately or unfortunately, depending on one's disposition, the factors proposed in the previous section as the possible origins of the discrepancy between experiment and simulation (see Fig. 6.1) are apparently not the issue. Therefore, the origin of the discrepancy remains unexplained. However, the perturbative cumulant Monte Carlo tool that we have devised can be used effectively to search for the cause of discrepancy. Without it, the discovery of the irrelevance of the above factors through a quantum Monte Carlo simulation would have been a more CPU time consuming burden. Ultimately, the same tool can also be used to explore the role of the small B_x when $x \neq 0$ [24, 25, 58, 72]. Indeed, constructing the whole x-$T_c(B_x)$ phase diagram in the "small B_x" vicinity of the classical x-T_c phase diagram (see Fig. 6.1) by performing solely classical Monte Carlo, was an original key motivation for the development of the method presented in this Chapter.

In Section 6.3, we explain how, from a generic TFIM such as the one introduced in Eq. (3.13), a *perturbative* effective Hamiltonian can be derived. To do this, the transverse field term is incorporated perturbatively via a cumulant expansion. In Section 6.4, the perturbative effective Hamiltonian obtained in Section 6.3, is employed in classical Monte Carlo simulations for small B_x. We discuss the results obtained using either the reaction field or Ewald summation method for the long-range dipole interactions. We also investigate how $J_{\rm ex}$ is estimated and investigate the sensitivity of the determined value upon the choice of the numerical method. Finally, we compare the B_x-T_c phase diagrams originating from two different sets of crystal field parameters. Section 6.5 summarizes our results.

6.3 Effective Classical Temperature-Dependent Hamiltonian – Perturbation Expansion

In this section, with a focus on the effective spin-$\frac{1}{2}$ Hamiltonian for pure $LiHoF_4$ of Eq. (3.13), we aim to implement a cumulant perturbative Monte Carlo method for a general spin-$\frac{1}{2}$ transverse Ising model [114] [4]. For small quantum fluctuations, close to the classical critical temperature, we are able to derive a classical perturbative effective Hamiltonian analytically, where quantum fluctuations are incorporated perturbatively. Using such effective perturbative Hamiltonian, we can then perform classical MC simulations. To set the stage, we first consider a general transverse field Ising Hamiltonian such as

$$\begin{aligned} \mathcal{H} &= \frac{1}{2}\sum_{i,j}\mathcal{L}_{ij}^{zz}\sigma_i^z\sigma_j^z + \frac{1}{2}\mathcal{J}_{\rm ex}\sum_{i,\rm NN}\sigma_i^z\sigma_{\rm NN}^z \\ &\quad -\Gamma\sum_i\sigma_i^x - h_0^z\sum_i\sigma_i^z. \end{aligned} \tag{6.1}$$

Γ is a general transverse field in the $\hat{x}$ direction coupled to the σ^x degrees of freedom and h_0^z denotes an external longitudinal field along the $\hat{z}$ direction. For the sake of compactness, the dipole-dipole and nearest neighbor exchange interactions are written in the forms of $\mathcal{L}_{ij}^{zz}$ and $\mathcal{J}_{\rm ex}$. The parameters Γ, h_0^z, $\mathcal{L}_{ij}^{zz}$, and $\mathcal{J}_{\rm ex}$ should be matched up with their equivalent counterparts in the original effective spin-$\frac{1}{2}$ microscopic Hamiltonian $H_{\rm spin-1/2}^{\rm pure}$ of Eq. (3.13). The partition function Z for a system with Hamiltonian (6.1) is

$$\begin{aligned} Z &= {\rm Trace}(e^{-\beta\mathcal{H}}) \\ &= \sum_{\{\psi_i\}}\langle\psi_i|e^{-\beta\mathcal{H}}|\psi_i\rangle, \end{aligned} \tag{6.2}$$

where Z is obtained by tracing over ψ_i 's which are, for example, direct product of σ^z eigenvectors ($|\uparrow\rangle$ and $|\downarrow\rangle$) and $\beta \equiv 1/k_{\rm B}T$. We can write the Hamiltonian (6.1) as $\mathcal{H} = H_0 + H_1$. H_0 is the classical part of the Hamiltonian, for which the ψ_i 's are eigenvectors. $H_1 \equiv -\Gamma\sum_i\sigma_i^x$ is the quantum term, which does not commute

[4] We follow closely the method laid out in Ref. [114] as well as adopt their notation. However, we provide somewhat more details to assist the reader.

with H_0. The existence of these two non-commuting terms in $\mathcal{H}$ prevents us from applying classical Monte Carlo techniques directly to the system. However, we can derive an effective classical Hamiltonian as a functional of ψ_i, such that

$$e^{-\beta H_{\text{eff}}[\psi_i]} = \langle\psi_i|e^{-\beta\mathcal{H}}|\psi_i\rangle \ . \tag{6.3}$$

Referring to the definition above in Eq. (6.3), since the right hand side of Eq. (6.3) is the matrix element with respect to $|\psi_i\rangle$, $H_{\text{eff}}\left[\psi_i\right]$ is a functional depending only on the set of σ_i^z eigenvalues. The partition function can then be written as a classical partition function

$$Z = \sum_{\{\psi_i\}} e^{-\beta H_{\text{eff}}[\psi_i]} \ . \tag{6.4}$$

By finding an explicit expression for $H_{\text{eff}}\left[\psi_i\right]$, one can calculate the thermodynamical properties of the system described by $\mathcal{H}$ by performing *classical* Monte Carlo simulations using H_{eff} instead of $\mathcal{H}$.

To proceed, we write the matrix element $\langle\psi|e^{-\beta\mathcal{H}}|\psi\rangle$ in terms of a cumulant expansion [115]

$$\langle\psi|e^{-\beta\mathcal{H}}|\psi\rangle = \exp\left[-\beta\langle\psi|\mathcal{H}|\psi\rangle + \sum_{n>1}^{\infty}\frac{(-\beta)^n}{n!}\langle\psi|\left(\mathcal{H}-\langle\psi|\mathcal{H}|\psi\rangle\right)^n|\psi\rangle\right] \ . \tag{6.5}$$

To make the notation more compact, we use $|\psi\rangle$ as a typical $|\psi_i\rangle$ eigenvector. Using Eq. (6.5) we can derive the effective Hamiltonian $H_{\text{eff}}\left[\psi_i\right]$ perturbatively. The details of the derivation of $H_{\text{eff}}\left[\psi_i\right]$ are presented in Appendix B. $H_{\text{eff}}\left[\psi_i\right]$, is to order $O(\Gamma^2)$, given by

$$\begin{aligned} H_{\text{eff}} &= H_0 + \beta\Gamma^2\sum_i\Big\{\sigma_i^z F_1\left[2\beta(h_i+h_0^z)\right] \\ &\quad -F_0\left[2\beta(h_i+h_0^z)\right]\Big\}. \end{aligned} \tag{6.6}$$

In Eq. (6.6), h_i is the total local field affecting the spin at site i caused by all the other spins, and which is

$$h_i = -\sum_{j\neq i}\mathcal{L}_{ij}^{zz}\sigma_j^z - \mathcal{J}_{\text{ex}}\sum_{\text{NN}}\sigma_{\text{NN}}^z \ , \tag{6.7}$$

and h_0^z is the external longitudinal field in the z direction. The functions $F_0(x)$ and $F_1(x)$ are defined as

$$F_0(x) \equiv \frac{\cosh(x) - 1}{x^2},$$
$$F_1(x) \equiv \frac{\sinh(x) - x}{x^2}. \tag{6.8}$$

In this effective Hamiltonian, the effect of quantum fluctuations is taken into account perturbatively to order $O(\beta\Gamma^2/[H_0])$, where $[H_0]$ denotes the order of magnitude of H_0, the classical part (first two terms) of Eq. (6.1). To obtain the thermodynamical properties of the system for small transverse fields we can perform a classical Monte-Carlo on H_{eff} as a classical counterpart to the real quantum mechanical Hamiltonian. Since we are interested in thermal averages, we can calculate thermodynamical quantities by differentiating the partition function, which is written in terms of $H_{\text{eff}}[\psi_i]$, with respect to h_0^z, Γ or β. The effective Hamiltonian has an explicit h_0^z and β dependence. For each true thermodynamical quantum-mechanical quantity, we obtain a pseudo-operator counterpart. For example the pseudo-operators corresponding to $\langle E\rangle$, $\langle M_z\rangle$, $\langle M_x\rangle$, $\langle M_z^2\rangle$, and $\langle M_z^4\rangle$ are calculated in Appendix C, where E, M_z and M_x are the energy and magnetization operators along the $\hat{z}$ and $\hat{x}$ direction. $\langle \dots \rangle$ stands for the Boltzmann thermal average.

Because of its perturbative nature in $(\beta\Gamma)$, this method is not reliable for large transverse fields or low temperatures. To illustrate the range of validity of this method we consider a simple one-dimensional nearest-neighbor transverse-field Ising model Hamiltonian

$$H = -J\sum_i \sigma_i^z\sigma_{i+1}^z - \Gamma\sum_i \sigma_i^x$$

with periodic boundary conditions. For a one-dimensional chain of 10 ions, we are able to calculate the exact total energy of the chain by exact diagonalization. To check our perturbative MC technique, we calculated the energy of the Ising chain as a function of temperature for a given transverse field. To make a comparison, we also performed a quantum Monte-Carlo (QMC) simulation on the system. In this QMC simulation, we used the Trotter-Suzuki [116, 11] formalism (see Appendix A)

and applied a continuous time cluster algorithm with the same method used in Ref. [117], which we refer to "time cluster QMC". In Fig. 6.2, for a quite large transverse field $\Gamma/J = 1$, we plot the average thermal energy as a function of temperature obtained from exact diagonalization, time cluster QMC and "perturbative MC" using the effective perturbative Hamiltonian of Eq. (6.6). Although, for the region where $\beta\Gamma^2/J$ is relatively large, the perturbative MC results are not reliable, this tests confirms the quantitative correctness of the perturbative Monte Carlo scheme at small $\beta\Gamma^2/J$.

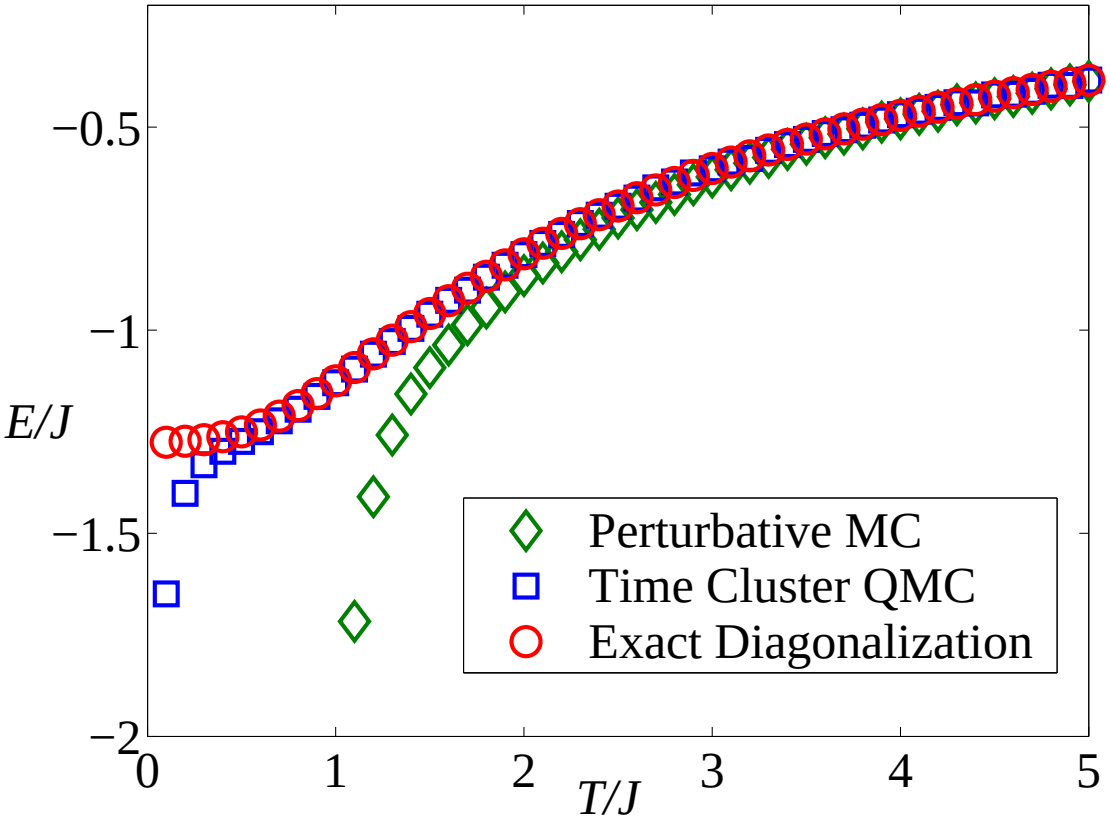

Figure 6.2: Energy per spin as a function of temperature for a simple one dimensional nearest-neighbor Ising chain with a transverse field of $\Gamma = J$ and $N = 10$ spins and periodic boundary conditions. The energy is obtained by exact diagonalization of the Hamiltonian, a time-cluster QMC algorithm, and a classical Monte-Carlo algorithm of the perturbative effective Hamiltonian.

Before we present our Monte Carlo results for $LiHoF_4$, we should remind the reader that through this thesis, we use two different notion of "*effective* Hamiltonian", which should not be mixed up. To avoid any possible confusion, let us summarize:

1. As discussed in Section 3.4, since the spin-spin interactions and $T_c(B_x)$ are small compared to the gap between the low-lying states $|\alpha(B_x)\rangle$ and $|\beta(B_x)\rangle$ with respect to the excited state $|\gamma(B_x)\rangle$, we can recast the full microscopic model of $LiHoF_4$ in terms of an effective spin-$\frac{1}{2}$ transverse field Ising model with effective spin-spin interactions and effective transverse field $\Gamma(B_x)$ that depend on the real physical applied magnetic field B_x (see Eq. (3.14).

2. As discussed in this section, since we are interested in a regime where B_x/T_c is small, we can develop a perturbation expansion of the partition function in powers of B_x/T and recast the thermal averages of real physical observables in terms of quantities that can be determined via a classical Monte Carlo simulation of a further effective classical Hamiltonian in which quantum fluctuations are incorporated perturbatively.

Having shown that the perturbative cumulant MC can quantitatively describe the TFIM at small $\beta\Gamma^2/[H_0]$, we proceed in the next section to describe how we use this method to study $LiHoF_4$ at small transverse field B_x.

6.4 Perturbative Monte Carlo Study of $LiHoF_4$

In this section we report results from the perturbative Monte Carlo (MC) simulation to study the low transverse field B_x properties of $LiHoF_4$, using the low field perturbative effective Hamiltonian in Eq. (6.6) and using Eq. (6.7) for the definition of the local h_i fields. As discussed in the Introduction, our primary goal here is to check the quantum Monte Carlo results from stochastic series expansion of Ref. [57], and investigate the contradictory results with the transverse field B_x phase diagram of Ref. [1] for small B_x (See Fig. 6.1).

In the following subsections, first as a reminder, we recall the effective spin-$\frac{1}{2}$ Hamiltonian for $LiHoF_4$ of Eq. (3.13) as the model we are interested to study. In order to simplify the numerical calculations and apply the method introduced in the previous section, we write a renormalized version of the Hamiltonian. We define a renormalized temperature and a renormalized magnetic field based on the real temperature T and magnetic field B_x, with the goal to implement them in Eq. (6.6). Next, we discuss the reaction field (RF) and the Ewald summation (ES) methods that we use to deal with the long range dipolar interactions, and discuss how the Monte Carlo results in the classical regime, where $B_x = 0$, are affected by the choice of the method we use. Then, we discuss the sensitivity of the $J_{\rm ex}$ estimates at zero B_x to finite-size effects, boundary conditions and choice of the method to handle the dipolar lattice sum. We also consider the effect of different $J_{\rm ex}$ on the phase digram, when $B_x \neq 0$ and B_x/T is small. Finally, we investigate to what extent the final results depend on the set of crystal field parameters chosen to describe the Ho^{3+} single ion properties.

6.4.1 Renormalizing the Hamiltonian, Temperature and the Magnetic Field

Let us, rewrite the effective spin-$\frac{1}{2}$ Hamiltonian for $LiHoF_4$ of Eq. (3.13), which was presented in Section 3.4 as follows:

$$H^{\rm pure}_{\rm spin-1/2} = \frac{1}{2}C^2_{zz}(B_x)\left[(g_L\mu_{\rm B})^2\sum_{i\neq j}L^{zz}_{ij}\sigma^z_i\sigma^z_j + J_{\rm ex}\sum_{i,{\rm NN}}\sigma^z_i\sigma^z_{\rm NN}\right] - \frac{\Delta_E(B_x)}{2}\sum_i\sigma^x_i \ .$$

To simplify the calculations, and in order to be consistent with the notation of Ref. [57] as well as for further comparison between our simulation results and those of Ref. [57], we lump the whole B_x dependence in the transverse field term into a renormalization factor $\epsilon(B_x)$ defined as

$$\epsilon(B_x) = \frac{C_{zz}(B_x)}{C_{zz}(0)} \ , \tag{6.9}$$

where $C_{zz}(B_x)$ is defined in Section 3.4. We renormalize the Hamiltonian as

$$H^{\rm pure}_{\rm spin-1/2} = \left[\epsilon(B_x)\right]^2\widetilde{\mathcal{H}} \ , \tag{6.10}$$

with, according to Eq. (3.13), $\widetilde{\mathcal{H}}$ is

$$\begin{aligned}\widetilde{\mathcal{H}} &= \frac{1}{2}C_{zz}^2(0)\left[(g_{\rm L}\mu_{\rm B})^2\sum_{i\neq j}L_{ij}^{zz}\sigma_i^z\sigma_j^z + J_{\rm ex}\sum_{i,\rm NN}\sigma_i^z\sigma_{\rm NN}^z\right] \\ &\quad -g_{\rm L}\mu_{\rm B}C_{zz}(0)\widetilde{\mathcal{B}}_x\sum_i\sigma_i^x\ . \end{aligned} \tag{6.11}$$

The renormalized effective transverse magnetic field, $\widetilde{\mathcal{B}}_x$, is related to the real applied B_x via

$$\widetilde{\mathcal{B}}_x = \frac{\Delta_E(B_x)}{2g_{\rm L}\mu_{\rm B}C_{zz}(0)\times\left[\epsilon(B_x)\right]^2}\ , \tag{6.12}$$

in accordance with Ref. [57]. In discussing Monte Carlo simulations below, we also define a renormalized temperature, $\widetilde{T}$, in conjunction with $\widetilde{\mathcal{H}}$, with $\widetilde{T}$ defined as

$$T = \left[\epsilon(B_x)\right]^2\widetilde{T}, \tag{6.13}$$

where T is the real physical temperature.

All results presented in the Monte Carlo simulation subsections below were obtained by considering the renormalized Hamiltonian (6.11), and performing the simulations with respect to the renormalized $\widetilde{T}$ and $\widetilde{\mathcal{B}}_x$. Regarding Eq. (6.11), the transverse field Γ used in the perturbative effective Hamiltonian (6.6) is $\Gamma = g_{\rm L}\mu_{\rm B}C_{zz}(0)\widetilde{\mathcal{B}}_x$, where $\widetilde{\mathcal{B}}_x$ is defined in Eq. (6.12). For the local field h_i, defined in Eq. (6.7), we have $\mathcal{L}_{ij}^{zz} = C_{zz}^2(0)(g_{\rm L}\mu_{\rm B})^2L_{ij}^{zz}$ and $\mathcal{J}_{\rm ex} = C_{zz}^2(0)J_{\rm ex}$, where C_{zz} is defined in Section 3.4 .

6.4.2 Reaction Field Method vs Ewald Summation Method

As already alluded to earlier, Griffiths' theorem [107] states that in the absence of an external field the free energy for a dipolar lattice system has to be independent of the sample shape in the thermodynamical limit. Therefore, as an immediate consequence, in the absence of an external field, the net magnetization $\mathcal{M}$ of the sample has to be zero. Otherwise, for a uniform $\mathcal{M}\neq 0$, a shape dependent demagnetization field would couple to the dipolar moments of the sample, making

the free energy shape dependent. Here, the demagnetization field is the field originating from the magnetic moments sitting on the boundary of the sample. Hence, in the thermodynamic limit, domains form in order for the system to have a zero magnetization, $\mathcal{M} = 0$.

Experiments on $LiHoF_4$ show that the results (i.e. susceptibility measurements) are shape independent, confirming Griffiths' theorem and domain formation [118, 119]. There is evidence that in $LiHoF_4$ long needle-shaped domains form along the c axis [118, 119]. If we assume that there is a uniform macroscopic bulk magnetization $\mathcal{M}_z$ within a long needle-shaped domain and the external magnetic field acting on the domain is $B_z^{\rm ext}$, then the susceptibility χ of the domain is

$$\chi = \mathcal{M}_z / B_z^{\rm ext} \ . \tag{6.14}$$

It should be noted that the macroscopic bulk magnetization $\mathcal{M}_z$, is given by $\mathcal{M}_z = n_0 g_{\rm L} \mu_{\rm B} \langle J^z \rangle$, where $n_0 = 4/a^2 c$ is the number of dipoles per unit of volume with $a^2 c$ the volume of the unit cell. Using $\mathrm{J}^z = C_{zz}\sigma^z$, the bulk magnetization $\mathcal{M}_z$ is related to the total moment of the effective Ising spins, $M_z = \sum_i \sigma_i^z$, in the effective spin-$\frac{1}{2}$ picture by

$$\mathcal{M}_z = \frac{4}{N} \frac{g_{\rm L}\mu_{\rm B} C_{zz}(B_x)}{a^2 c} \langle M_z \rangle \ , \tag{6.15}$$

where N is the total number of dipoles.

Let us consider an imaginary *macroscopic* spherical cavity deep inside a needle-shaped domain. The magnetization inside the sphere should be equal to the uniform bulk magnetization of the long needle-shaped domain. Apart from the external magnetic field $B_z^{\rm ext}$, spins enclosed in the sphere experience an additional field that originates from the spins on the outer boundary of the imaginary sphere. The magnetic surface charge density on the surface of the needle-shaped domain with uniform magnetization $\mathcal{M}_z$ produces an internal magnetic field $B_{\rm needle} = 4\pi\mathcal{M}_z$. Meanwhile, the magnetic surface charge density on the surface of the uniformly magnetized sphere with magnetization of $\mathcal{M}_z$ induces a (demagnetization) magnetic field $\frac{8\pi}{3}\mathcal{M}_z$ inside the sphere that is in the opposite direction to the applied field and to $B_{\rm needle}$. Therefore, the total field $B_z^{\rm sph}$ inside the spherical cavity is [120]

$$B_z^{\rm sph} = B_z^{\rm ext} - \frac{8\pi}{3}\mathcal{M}_z + 4\pi\mathcal{M}_z \ , \tag{6.16}$$

with $\mathcal{M}_z$ uniform throughout the whole sample. Now, instead of considering a bulk needle-shaped sample, we can also study an isolated spherical sample which an effective $B_z^{\rm sph}$ field is applied to it. If we substitute $B_z^{\rm ext}$ with $\mathcal{M}_z/\chi$ and $B_z^{\rm sph}$ with $\mathcal{M}_z/\chi_{\rm sph}$, where $\chi_{\rm sph}$ is the susceptibility of the spherical domain, then we can write χ as a function of $\chi_{\rm sph}$

$$\chi = \frac{\chi_{\rm sph}}{1 - \frac{4\pi}{3}\chi_{\rm sph}}. \tag{6.17}$$

If $\chi_{\rm sph}$ is obtained via some calculation procedure for a spherical sample, one can use Eq. (6.17) to determine the macroscopic susceptibility of the bulk sample within which the sphere is embedded. Specifically, simulations can be performed on a finite size sphere, and the effect of the macroscopic bulk surrounding the sphere is incorporated in a mean-field manner by considering an effective field $B_z^{\rm sph}$ interacting with the spins inside the spherical sample. Using this method, called the reaction field (RF) method, Chakraborty *et al.* calculated the finite size sphere susceptibility $\chi_{\rm sph}$ by using the stochastic series expansion quantum Monte-Carlo method [57, 74]. They considered an N spin system enclosed by a sphere, where the susceptibility of the sphere is obtained from the spin-spin correlation. Referring to Eq. (6.17), the paramagnetic to ferromagnetic transition (criticality) within the macroscopic long needle-shaped domain occurs at the temperature for which $\chi_{\rm sph} = \frac{3}{4\pi}$ occurs for a spherical sample. It should be noted that this criteria is derived for macroscopic systems in the thermodynamic limit. Therefore, as discussed in Ref. [111], because of the fluctuation of magnetic moments on the boundary of a finite size surface, quantities such as specific heat and susceptibility obtained via the reaction field method, are quite sensitive to finite size effects.

The Ewald summation (ES) method [109, 110, 111] is an alternative approach used to obtain reliable quantitative results to describe real dipolar materials in a periodic boundary condition (PBC) setting [112]. In the ES method, in order to treat long-range dipolar interactions with PBC, the system is modeled by replicating the simulation cell of linear size L into a large array of image copies. The ES method generates an effective dipole-dipole interaction $\sum_{\mu,\nu} L_{\rm eff}^{\mu\nu}(\mathbf{r}_{ij})\mu_i^\mu\mu_j^\nu$ between two arbitrary magnetic moments, $\boldsymbol{\mu}_i$ and $\boldsymbol{\mu}_j$ within the simulation cell. Here, $\boldsymbol{\mu}_i = g_{\rm L}\mu_{\rm B}\mathbf{J}_i$, $\mu, \nu{=}x, y, z$, and $\mathbf{r}_j - \mathbf{r}_i$, where $\mathbf{r}_i$ is the position of moment i. This is done by periodically replicating the simulation cell with a volume of $v_0 = L^3a^2c$

and summing convergently the interactions between the real spins i and j in the specified volume of the simulation cell of size L [5], and all the periodically repeated images of j as

$$L^{\mu\nu}_{\text{eff}}(\mathbf{r}_{ij}) = \sum_{\mathbf{n}} L^{\mu\nu}(\mathbf{r}_{ij} + \mathbf{n}) \ , \tag{6.18}$$

where $\mathbf{n} = (n_x La, n_y La, n_z Lc)$ with n_x, n_y, n_z integers. Here,

$$L^{\mu\nu}(\mathbf{r}_{ij}) = L^{\mu\nu}_{ij} \equiv \left[\delta^{\mu\nu}|\mathbf{r}_{ij}|^2 - 3\mathrm{r}^{\mu}_{ij}\mathrm{r}^{\nu}_{ij}\right] / |\mathbf{r}_{ij}|^5 \tag{6.19}$$

are dipolar couplings, which can be written in a more compact form as

$$L^{\mu\nu}(\mathbf{r}_{ij}) = \nabla^{\mu}_i \nabla^{\nu}_j |\mathbf{r}_{ij}|^{-1} \ . \tag{6.20}$$

Therefore,

$$L^{\mu\nu}_{\text{eff}}(\mathbf{r}_{ij}) = \nabla^{\mu}_i \nabla^{\nu}_j \sum_{\mathbf{n}} |\mathbf{r}_{ij} + \mathbf{n}|^{-1} \ . \tag{6.21}$$

The sum $\sum_{\mathbf{n}} |\mathbf{r}_{ij} + \mathbf{n}|^{-1}$ is calculated using the Ewald method, such that the sum contain a real space sum plus a reciprocal space sum minus a self term [109, 110, 111]

$$\begin{aligned} \sum_{\mathbf{n}} |\mathbf{r}_{ij} + \mathbf{n}|^{-1} \ &= \ \sum_{\mathbf{n}} \frac{\text{erfc}(\kappa|\mathbf{r}_{ij} + \mathbf{n}|)}{|\mathbf{r}_{ij} + \mathbf{n}|} \\ &\quad + \frac{1}{\pi v_0} \sum_{\mathbf{k}\neq 0} \frac{4\pi^2}{k^2} e^{-k^2/4\kappa^2} \cos\left(\mathbf{k} \cdot \mathbf{r}_{ij}\right) \\ &\quad - \frac{\kappa}{\sqrt{\pi}} \delta_{ij} \ . \end{aligned} \tag{6.22}$$

Here $\text{erfc}(x) = (2/\sqrt{\pi}) \times \int_x^{\infty} \exp -t^2 dt$ and $\mathbf{k} = (2\pi m_x/La, 2\pi m_y/La, 2\pi m_z/Lc)$ denotes the reciprocal vectors of the simulation cell, with m_x, m_y, m_z integers. The convergence factor κ is chosen such that the real space sum and the reciprocal space sum converge about equally rapidly [109, 110, 111]. The simulation cell and all its replicated images are embedded altogether in a continuous medium. Additionally, each spin experiences a demagnetization field, which is originating from the magnetic moments on the boundary of the system [111]. This boundary contribution depends on the shape of the boundary of the macroscopic sample that we are

[5] Having the unit cell of $LiHoF_4$ denoted by (a, a, c), a simulation cell of size L denotes a volume with a size of (La, La, Lc), where L is dimensionless.

interested in modeling. For example, for a long needle-shaped sample, the demagnetization field correction to the ES representation of the dipole-dipole interactions is zero [111]. However, for a bulk spherical sample, the magnetic polarization of the magnetic moments on the boundary of the sphere induces a demagnetization field proportional to the magnetization of the sample $\mathcal{M} = \frac{1}{v_0}\sum_i \boldsymbol{\mu}_i$, which creates an additional effective field acting on the the magnetic moments. This results in an extra effective interaction

$$\frac{4\pi}{2\mu'+1}\frac{\boldsymbol{\mu}_i \cdot \boldsymbol{\mu}_j}{v_0} \tag{6.23}$$

between magnetic moments $\boldsymbol{\mu}_i$ and $\boldsymbol{\mu}_j$ to be incorporated in the simulation [111]. In practice, the term in Eq. (6.23) is merely added to $L^{\mu\nu}_{\rm eff}(\mathbf{r}_{ij})$ in Eq. (6.21), which itself is calculated via the ES expression of Eq. (6.22). Here, as before, L is the linear system size, $\boldsymbol{\mu}_i = g_{\rm L}\mu_{\rm B}\mathbf{J}_i$, and μ' is the magnetic permeability of the surrounding continuum. For a sample surrounded by vacuum $\mu' = 1$ [6]. This interaction is added to the effective dipolar interaction between spins i and j, derived by the ES technique [112].

As a result, within the ES method, each spin interacts with all the "real" spins in the specified simulation cell of linear size L, and with all its replicated periodic images. Therefore, one would expect the system to behave more like a macroscopic system than in the reaction field method. However, there are still some finite size effects due to the artifact of having a periodic sequence of cells of finite size L. Once an effective dipole-dipole interaction between spins i and j within the simulation cell has been derived via the ES technique, one can perform Monte Carlo simulations using the standard Metropolis algorithm. Xu *et al.* [121] used the ES technique

[6] The magnetic permeability μ' is usually not known beforehand. In general, as discussed in Ref [111], it can be estimated rigorously in a self consistent way. In the problem that we are interested in here, we simulate an isolated sphere, where the effect of the infinite continuum surrounding it is incorporated via $B_z^{\rm sph}$ as defined in Eq. (6.16). We are interested in the situation where $\chi_{\rm sph} = 3/4\pi$. When this situation is fulfilled the whole long needle-shaped bulk is in the paramagnetic regime where in the thermodynamic limit the macroscopic magnetization of the bulk is zero. We consider μ'=1 for the spherical sample for which the simulation is being carried without embarking into complex self-consistent calculations, which are beyond the scope of this paper, specially since at the end the results so obtained are consistent with those found when considering a long needle-shaped bulk with no demagnetization effects.

to simulate long-range dipolar Ising interactions for both the body-centered cubic (BCC) and body centered tetragonal lattices in zero applied field. In a more recent work [63, 64], the ES technique was implemented in a Monte Carlo simulation study of $LiHo_xY_{1-x}F_4$ in zero applied field. In the next subsection we discuss the results of MC simulations using the cumulant perturbative method. In our simulations, we incorporate the long-range dipolar interactions using either the reaction field method as discussed in Ref. [57] and the ES method. The influence of each method on the MC results is investigated in some detail.

6.4.3 Perturbative Monte Carlo Simulations Results

In this subsection we describe the Monte-Carlo results obtained using the effective perturbative Hamiltonian (6.6) and which employ different ways to handle the dipolar lattice sums. We first report results obtained using the reaction field method for a spherical sample embedded in a long needle-shaped domain. The main purpose of doing so is to corroborate the results of Ref. [57]. We also report results from simulations using the ES method for both a long needle-shaped sample and a spherical sample embedded in a long needle-shaped domain.

Results from reaction field method

To establish a comparison of the effective perturbative Hamiltonian with previous QMC results [57], we first performed Monte-Carlo simulations for a finite size sample with open spherical boundary condition, containing $N = 295$ spins and with $J_{\rm ex}$ in Eq. (6.11) set to zero. These conditions are identical to those in Ref. [57]. As in Ref. [57], we used the reaction field criterion, set by the divergence of χ when $\chi_{\rm sph} = \frac{3}{4\pi}$ (see Eq. (6.17)), to find the effective critical temperature $\widetilde{T}_c(\widetilde{B}_x)$ as a function of the effective field $\widetilde{B}_x$, where $\widetilde{T}$ and $\widetilde{B}_x$ are defined in Eqs. (6.12) and (6.13). $\chi_{\rm sph}$ is calculated using

$$\chi_{\rm sph} = \frac{1}{k_B \widetilde{T}} \frac{\alpha}{N} \left\langle M_z^2 \right\rangle \ , \tag{6.24}$$

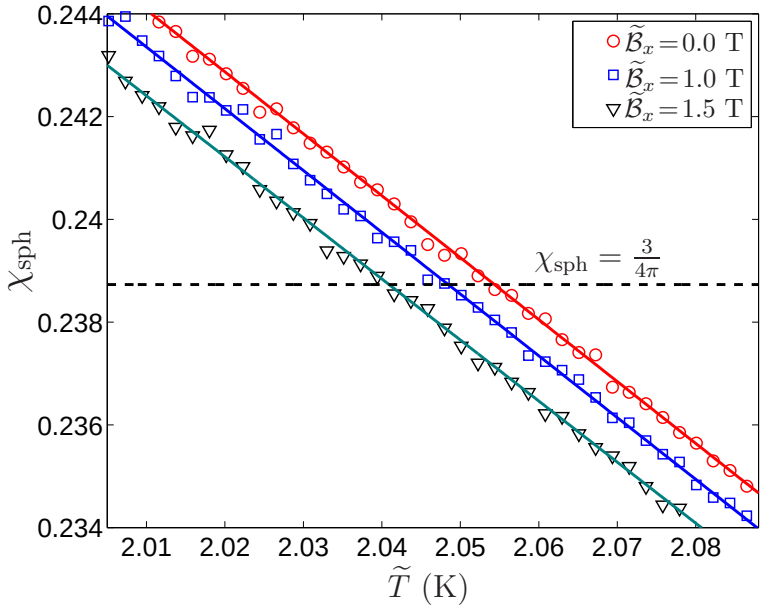

Figure 6.3: Finding $\widetilde{T}_c$ using the perturbative Monte-Carlo for a sphere of N=295 spins by using the reaction field $\chi_{\rm sph} = \frac{3}{4\pi}$ criterion at criticality, using $J_{\rm ex} = 0$.

where the prefactor α is given by

$$\alpha = \frac{4}{a^2 c} \left(g_{\rm L}\mu_{\rm B} C_{zz}(0)\right)^2 \ . \tag{6.25}$$

In the perturbative MC method, for determining $\langle M_z^2 \rangle$, we used the pseudo-operator defined by Eq. (C.4). The results for $\widetilde{\mathcal{B}}_x$=0 T,0.5 T, and 1.5 T are shown in Fig. 6.3.

The phase diagram as a function of the effective temperature $\widetilde{T}$ and the effective field $\widetilde{B}_x$, using the effective perturbative Hamiltonian (6.6) and the above cumulant expansion is shown in Fig. 6.4. At low enough fields, close to the classical phase transition, our perturbative Monte Carlo results, using the same reaction field method as in Ref. [57], closely match the quantum Monte Carlo results of Ref. [57]. Using the reaction field method for $B_x = 0$ we get a $\widetilde{T}_c = 2.03$ K similar to what reported in Ref. [57], where $T_c(B_x = 0) = \widetilde{T}_c(B_x = 0)$ since $\epsilon(B_x = 0) = 1$.

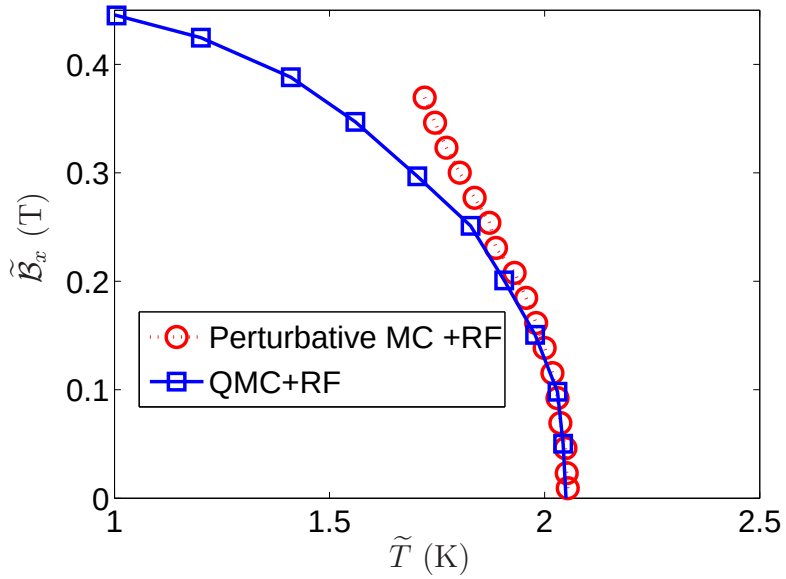

Figure 6.4: Comparing the phase diagram of the perturbative Monte-Carlo with Quantum Monte Carlo results [57] as a function of effective temperature and effective magnetic field for a sphere of N=295 spins and $J_{\rm ex} = 0$, using the reaction field method of Ref. [57].

Results from Ewald summation method – needle-shaped sample

The simulations using the Ewald summation (ES) method were performed with simulation boxes of size $L = 7, 8, 9$, with each box containing $N = 4 \times L^3$ spins, where 4 is the number of ions per unit cell. The dipolar interactions of ions inside the simulation boxes were derived via the ES technique and assuming an infinitely long needle-shaped sample [122]. That is, the additional demagnetization term correction from Eq. (6.23) is not incorporated into the Ewald representation of the dipolar interactions between ions i and j. We determined the critical temperature by finding the temperature at which the magnetization Binder ratio [123],

$$Q = 1 - \frac{1}{3} \left\langle M_z^4 \right\rangle / \left\langle M_z^2 \right\rangle^2 \ ,$$

for system sizes $L = 7, 8$, and 9 intersect. The intersection point shown in Fig. 6.5 is at $T_c = 1.92$ K which is the critical temperature. $\langle M_z^4 \rangle$ and $\langle M_z^2 \rangle$ are calculated using Eqs. (C.4) and (C.9) within the perturbative effective Hamiltonian scheme.

As demonstrated in the inset of Fig. 6.5, plotting Q as a function of $L^{1/\nu}(T - T_c)$ shows a good data collapse for system sizes $L = 7, 8$, and 9, with the mean field exponent $\nu = 1/2$. This is consistent with the argument that the upper critical dimension for dipolar interactions is $d = 3$. A more rigorous analysis of three dimensional ferromagnetic dipolar systems shows logarithmic finite size scaling corrections [121, 124]. We have not investigated these corrections in this study as it is outside the scope of this work.

Results from Ewald summation method − spherical sample

We have repeated the perturbative MC simulations using the ES technique but with a slightly different twist to it. Instead of simulating a long needle-shaped bulk sample and using the Binder method to obtain the critical temperature, we simulate a sample with a spherical domain. We derived the effective dipolar interactions between the spins by using the ES technique for a spherical cavity The effect of the spherical boundary is taken into account by incorporating the additional effective interaction of Eq. (6.23) between spins i and j. Now, one can assume that this sphere is embedded in a long-needle-shaped bulk sample. Therefore, by recalling the derivation of Eq. (6.17) from Eq. (6.16), where an effective field $B_z^{\rm sph}$ is applied to the magnetic moments of the sphere, one can determine the macroscopic χ of the bulk, by calculating $\chi_{\rm sph}$ via the ES method for a spherical sample. The procedure that we use here is similar to the procedure above that employed the reaction field for a finite size system and which led to the phase diagram in Fig. 6.4. The difference between the ES technique within a spherical boundary and the reaction field method implemented above and in Ref. [57] is the following. Instead of using an open spherical boundary condition, and considering only bare dipolar interaction between a finite number of spins within a cutoff sphere, a simulation box with periodic boundary condition is considered. The effective dipolar interactions of ions inside the simulation box is derived via the Ewald summation technique. In this approach a spherical boundary is considered for the whole simulation box and all the replicated images of the real box. In this case, each effective pairwise dipolar interactions described by the ES representation has added to it the extra interaction term given by Eq. 6.23. Once again, the origin of this additional interaction is

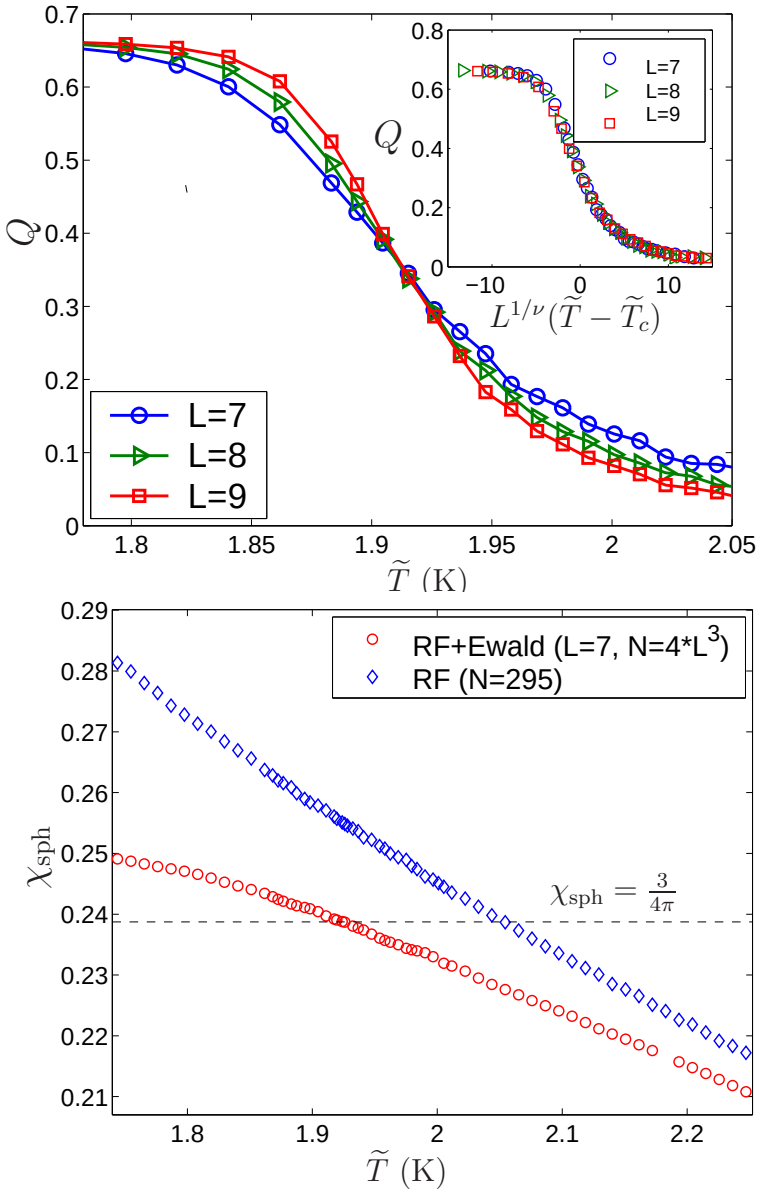

Figure 6.5: (a) The Binder ratio crossing for $L = 7, 8, 9$ system sizes, performing MC and using ES technique for a long needle-shaped sample, with $B_x = 0$, $J_{\rm ex} = 0$. $\widetilde{T} = T$ for $B_x = 0$. The inset shows that the Binder ratios collapse for the mean field exponent $\nu = 1/2$ to a very good degree. (b) $\chi_{\rm sph}$ calculated by performing MC simulation, using Eq. (6.24). The diamonds are for a finite size sphere using the reaction field scheme similar as in Ref. [57] (i.e. same results as shown in Fig. 6.3 for the $\widetilde{\mathcal{B}}_x = 0$ data). For the circles, we have obtained the interaction between the ions by the ES technique for $L = 7$ system size and incorporating the spherical boundary effect via the demagnetization term of Eq. (6.23) and using $B_x = 0$ and $J_{\rm ex} = 0$, with again $\widetilde{T} = T$ for $B_x = 0$. As one can see, the $\widetilde{T}_c \approx 1.92$ K obtained here agrees with the $\widetilde{T}_c$ obtained using the Binder ratio crossing.

the demagnetization field, due to the polarization of the magnetic moments on the spherical boundary. In this approach, the system behaves much more like a macroscopic sphere compared to the one above that uses the reaction field method. It is further assumed that this macroscopic sphere is embedded inside a macroscopic long macroscopic needle-shaped domain. Therefore, by employing the perturbative Monte Carlo method and using Eq. (6.24), we calculate $\chi_{\rm sph}$ to obtain the critical temperature. Based on Eq. (6.17), the critical temperature is calculated by finding where the $\chi_{\rm sph} = \frac{3}{4\pi}$ criticality criterion is satisfied. As shown in Fig. 6.5b, for a simulation box of $L = 7$, we obtain $T_c = 1.92$ K for a zero transverse field and $J_{\rm ex} = 0$, very close to the T_c previously derived using ES technique for a long needle-shaped sample and shown in Fig. 6.5a. Thus, the two approaches using ES technique lead to similar results. We believe that the difference between the classical T_c obtained via ES technique and the $T_c(B_x = 0)$ obtained using the reaction field method [57] is because, in the reaction field method, the number of spins inside the cut-off sphere, which is embedded in the needle-shaped domain, is of too limited size. By implementing Eq. (6.17) in the reaction field method, the effect of the spins on the spherical boundary for a limited size is in essence incorporated in a mean field manner in the simulation. For a limited size boundary, thermal fluctuations on the boundary are underestimated, hence resulting in an overestimated T_c. This overestimation of T_c, which decreases by increasing the size of the spherical boundary, is expected to vanish in the thermodynamic limit $L \to \infty$.

6.4.4 Nearest-Neighbor Exchange Interactions

The zero transverse field critical temperature of 1.92 K obtained above lies quite far above the experimental critical temperature of 1.53 K. As suggested by Chakraborty *et al.*, it is reasonable to assume that the discrepancy may be related to a nearest-neighbor Heisenberg antiferromagnetic exchange interaction. Indeed, in the related $LiTbF_4$ material, it has long been known that an antiferromagnetic $J_{\rm ex}$ coupling exists [84]. There has been no direct determination for the magnitude of this nearest-neighbor exchange in $LiHoF_4$. However, there have been indirect estima-

tions, considering J_{ex} as a free parameter [7], such that the specific heat [76] and susceptibility [77] calculations based on mean field theory fit to the equivalent experimental measurements. Another procedure to determine J_{ex}, would be to fit theoretical calculation with neutron scattering data, similar to the procedure followed for $LiTbF_4$ [84]. Recently, Rønnow *et al.* [78] have performed inelastic neutron scattering measurements on $LiHoF_4$. Considering J_{ex} as a free parameter, they used the so called *effective-medium theory* to modify the mean field random phase approximation parameters. They estimated J_{ex} such that a best fit with the experimental phase diagram is obtained. For example, although for J_{ex}=1.16 mK there is good agreement with experiment when $2.0 < B_x < 4.0$ Tesla, as is common in calculations of mean field theory type, the critical temperature is overestimated by 14 percent compared with the experimental critical temperature at zero applied field $B_x = 0$.

In this thesis, we use Monte Carlo techniques and consider the exchange interaction as a free parameter. We can estimate the J_{ex} strength by adjusting its value such that the experimental T_c is reproduced, as was done in Ref. [57]. Using the reaction field method performed for finite spheres in Ref. [57], for $N = 295$ spins, $J_{ex} = 6.07$ mK was obtained. As a check, we repeated our Monte Carlo simulations, also using the reaction field method for the same number of spins, and fitted J_{ex} such that the experimental zero-field critical temperature $T_c = 1.53$ K is reproduced. We obtained the same $J_{ex} = 6.07$ mK as in Ref. [57]. It should be noted that, as reported in Ref. [57], one does not obtain a unique J_{ex} value when performing simulations for different sphere sizes. The J_{ex} value strongly depends on the number of spins considered. In Ref. [57], for the largest system size considered (N=3491), a $J_{ex} = 5.25$ mK was required to obtain a Monte Carlo estimate of T_c of 1.53 K.

There are two sources of errors that affect the value of the estimated J_{ex} obtained by the reaction field method of Ref. [57]. Firstly, for a given number of spins, when Monte Carlo simulations are performed to calculate T_c, the reaction field method estimates a higher value for T_c compared to the ES method. The sources of these errors are finite size effects and the underestimation of thermal fluctuations at the

[7] See Eq. (2.15) and Eq. (3.14) for the convention we used, denoting J_{ex} in our calculations.

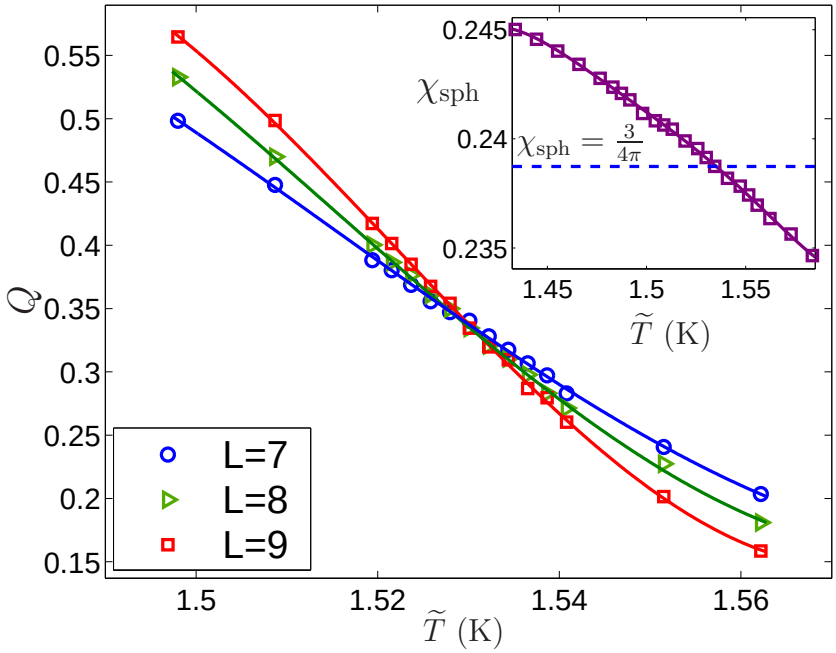

Figure 6.6: The Binder ratio crossing for $L = 7, 8, 9$ system sizes, performing MC and using ES technique for a cylindrical boundary with $B_x = 0$. $J_{\rm ex} = 3.91$ mK is set such that the critical temperature $T_c \approx 1.53$ K is obtained. $\widetilde{T} = T$ for $B_x = 0$. In the inset $\chi_{\rm sph}$ is calculated by performing Monte Carlo simulations, using Eq. (6.24). The interaction between the ions is obtained by the ES technique for $L = 7$ system size and using a spherical boundary condition for $B_x = 0$. The same $J_{\rm ex} = 3.91$ mK used and a similar $T_c \approx 1.53$ K is obtained. Recall that $\widetilde{T} = T$ for $B_x = 0$.

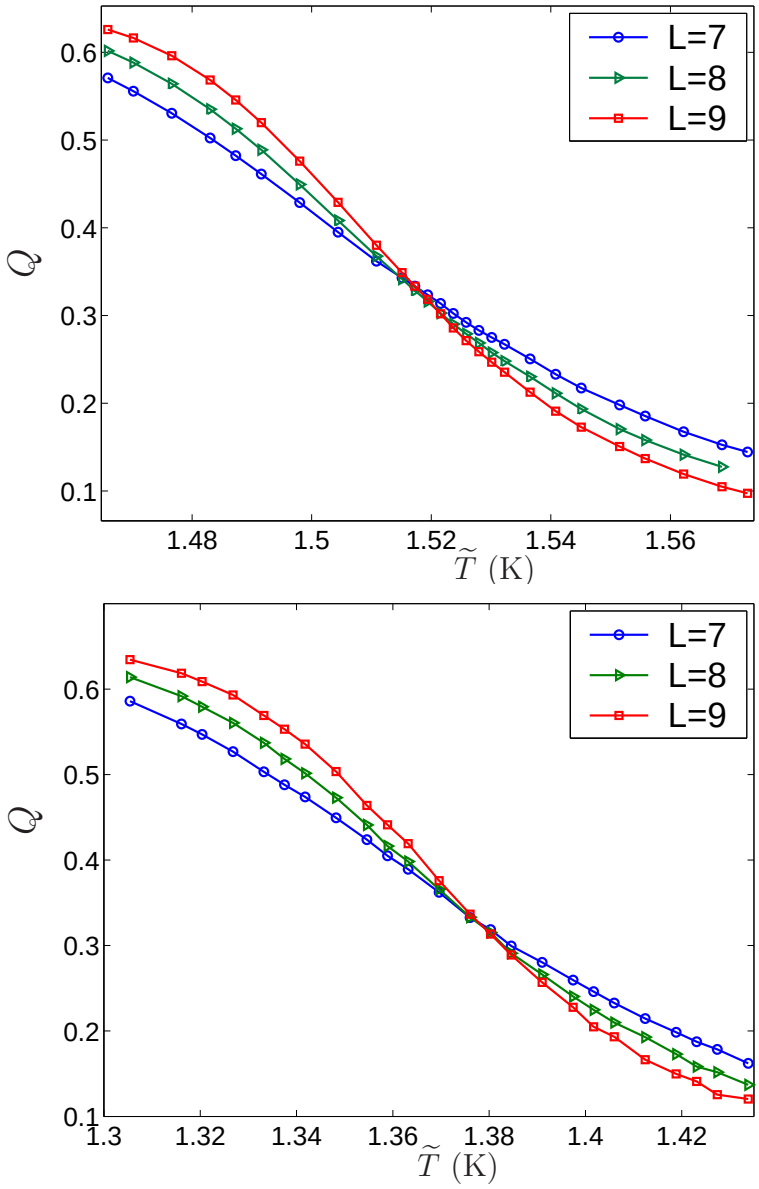

Figure 6.7: The Binder cumulant crossing for $L = 7, 8, 9$ system sizes, employing perturbative MC and using ES technique for a long needle-shaped sample with $J_{\rm ex} = 3.91$ mK. In (a) we have $\widetilde{B}_x = 0.05$ T and in (b) we have $\widetilde{B}_x = 0.15$ T.

boundary, as we now explain. To push down the value of T_c obtained for $J_{\rm ex} = 0$ such that it matches the experimental value for T_c, an antiferromagnetic $J_{\rm ex}$ is required. For $J_{\rm ex} = 0$, the reaction field method generates a higher T_c compared to the ES method. Therefore, in order to push down the T_c obtained from Monte Carlo simulation to match the experimental value for T_c, a larger value for the antiferromagnetic $J_{\rm ex}$ is required than the one required when using the ES method. A second source of error affects the value of the estimated $J_{\rm ex}$ obtained by the reaction field method. It comes from the number of surface bonds, which depends on the radius of the chosen cut-off sphere. For ions close to the surface, some of the nearest-neighbors fall inside the spherical boundary while some remain outside. Because of the missing number of exchange interactions on the boundary, the overall exchange estimated is forced to be larger than the actual value. When the ES technique is used in conjunction with periodic boundary conditions, this boundary effect problem no longer exists, making the ES technique a more reliable tool for estimating $J_{\rm ex}$ [112].

To estimate $J_{\rm ex}$ using our Monte Carlo simulations, we used the Binder ratio crossing method and employed both the ES technique for a long needle-shaped sample and the ES technique for a macroscopic sphere embedded in a long needle-shaped sample. For the latter case, the interactions of Eq. (6.23), originating from the magnetic polarizations of the magnetic moments on the spherical boundary were considered as well. The two $J_{\rm ex}$ values so determined are the same, which is approximately $J_{\rm ex} = 3.91$ mK, as illustrated in Fig. 6.6. Note that this value of $J_{\rm ex} = 3.91$ mK is consistent with the one recently determined in Ref. [63]. The definition of the exchange constant of 0.12 K in Ref. [63] for Ising spins corresponds to $J_{\rm ex}C_{zz}(B_x = 0)^2$ in our case (see Eq. (2.15)). Using $J_{\rm ex} = 3.91$ mK and $C_{zz}(B_x = 0) = 5.51$ from Fig. 3.4, we get $J_{\rm ex}C_{zz}(B_x = 0)^2 \approx 0.119$ K, in excellent agreement with the 0.119 K value of the Ref. [63].

6.4.5 Transverse Field vs Temperature Phase Diagram

Having determined a seemingly consistent value for $J_{\rm ex}$, we are now ready to perform Monte Carlo simulations for small transverse magnetic fields B_x, and attempt to

compare the $T_c(B_x)$ phase diagram from Monte Carlo with the experimental one in Fig. 6.1. The effect of quantum perturbations are incorporated through the effective Hamiltonian Eq. (6.6), which is derived from the B_x-rescaled Hamiltonian Eq. (6.11). To obtain the real temperature T and external transverse magnetic field B_x from the effective values $\widetilde{T}$ and $\widetilde{B}_x$ used in the simulations we employ relations Eqs. (6.12) and (6.13). To illustrate the procedure, we show the crossing of the Binder ratio Q for $\widetilde{B}_x = 0.05$ T and $\widetilde{B}_x = 0.15$ T in Fig. 6.7.

Interestingly, using each of the numerical methods discussed above to obtain the phase diagram, it seems that for small B_x the final phase diagrams illustrating the critical transverse field as a function of temperature are affected very little in respect to which specific technique is used. Figure 6.8 shows the phase diagrams, using the perturbative Monte Carlo method implementing the reaction-field method and the Ewald summation technique, compared with QMC [57] results and experiment [1]. We use Eq. (6.12) and Eq. (6.13) to obtain the real physical transverse magnetic field, B_x and temperature T from $\widetilde{T}$ and $\widetilde{B}_x$. As one can see, all the phase diagrams obtained from the effective perturbative method show a good agreement with the quantum Monte Carlo result of Chakraborty *et al.* [57], for small transverse fields up to a "real" physical transverse magnetic field $B_x \approx 1.5$ Tesla, where we presume the lowest order cumulant formulation of the effective classical Hamiltonian model breaks down. This is the main result of this Chapter.

In conclusion, we confirm the results of Ref. [57] but, perhaps unfortunately, we fail to explain the discrepancy between numerical and experimental results. We are thus led to ponder on theoretical reasons that may explain this discrepancy. We explore one such possibility in the next subsection and which is also the one that was put forward in Ref. [57].

6.4.6 Other Crystal Field Parameters

As reported in Ref. [57], we find that the numerical phase diagrams show a discrepancy with the experimental phase diagram, even at asymptotically small transverse fields. Indeed, this was one of the main motivations for the present work. As can be seen in Fig. 6.8, our efforts in considering (i) a different Monte Carlo scheme and

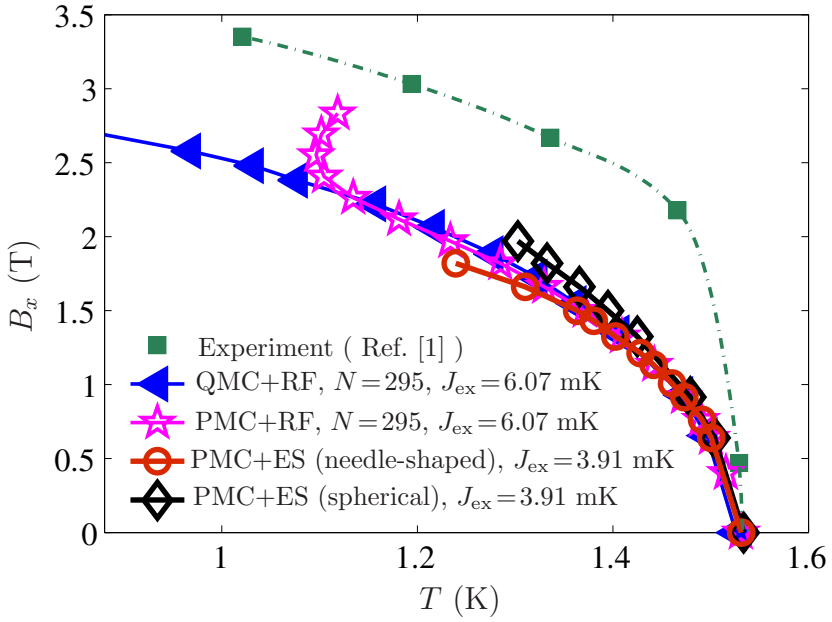

Figure 6.8: The phase diagram of the critical transverse field as a function of temperature for $LiHoF_4$. The closed boxes are the experimental phase digram [1]. The closed triangles are the phase diagram obtained by QMC [57] using the reaction field method for a finite sphere with $N = 295$ spins. The open stars are the result from perturbative Monte Carlo (PMC) using the same reaction field (RF) method used in Ref. [57] for a sphere with $N = 295$ spins. Quite importantly, as discussed in the text, the reaction field method leads to a considerable overestimate of J_{ex}. The open circles are obtained, using the perturbative Monte Carlo in a needle-shaped domain using ES method. The open diamonds are obtained, using perturbative Monte Carlo in a bulk sphere embedded in a needle-shaped domain, using ES method and the spherical boundary effect of Eq. (6.23).

(ii) other ways to handle the long-range dipole-dipole interactions have not allowed us to resolve the discrepancy between the results from numerical simulations of Ref. [57] and the experimental phase diagram of Ref. [1]. Chakraborty *et al.* [57] suggested that this discrepancy may be related to uncertainties in the crystal field parameters. We now briefly explore this possibility.

As discussed in Section 2.2, crystal field parameters are usually obtained such that theoretical calculations match with experimental data from electron paramagnetic resonance (EPR) [79], inelastic neutron scattering (INS) [78] or susceptibility measurements [54]. Recalling the discussion that led to the derivation of the effective spin-$\frac{1}{2}$ description of $LiHoF_4$ in Eq. (3.13), one realizes that the parameters $C_{zz}(B_x)$ and $\Delta_E(B_x)$ are implicit functions of the crystal field level energies and crystal field level wave functions. As a result, the mapping of the problem to a spin-$\frac{1}{2}$ model depends on the chosen values of the B_n^α crystal field parameters (See Section 2.2) parameterizing the crystal field Hamiltonian $V_{\rm CF}$. This state of affairs is rendered particularly important, since, unfortunately, there appears to be some ambiguity in the literature about the empirical values of the B_n^α parameters. All the numerical results that we obtained in the previous sections are based on the set of recent crystal field parameters reported in Refs. [78], and which were also used in the stochastic series expansion quantum Monte Carlo of Ref. [57], and which were determined by fitting theoretically determined crystal field levels with those resolved in inelastic neutron scattering data. Recently, new electron paramagnetic resonance (EPR) spectroscopy experiments have been performed, in which the crystal field parameters were also determined [79]. Based on the EPR data reported in Ref. [79], spectral parameters were refined in order to fit the observed dependencies of the resonance frequencies on the external magnetic field, giving a new set of crystal field parameters and an effective Landé g-factor $g_{\rm L}$ reduced from its pure ${}^5I_8$ $g_{\rm L} = 5/4$ value down to an effective $g_{\rm L}^{\rm eff} = 1.21$. Using this new set of crystal-field parameters, we obtain a different renormalization factor $\epsilon(B_x)$ (Eq. (6.9)) and effective transverse field $\widetilde{\mathcal{B}}_x$ (Eq. (6.12)) and, as a result, different $C_{zz}(B_x)$ and $\Delta_E(B_x)$. One of the consequences of obtaining a different C_{zz}, with the new CFP is that, referring to Eq. (3.13), a different $T_c(B_x = 0)$ is obtained. Having determined a different T_c via this new set of CFP, the value of $J_{\rm ex}$ required

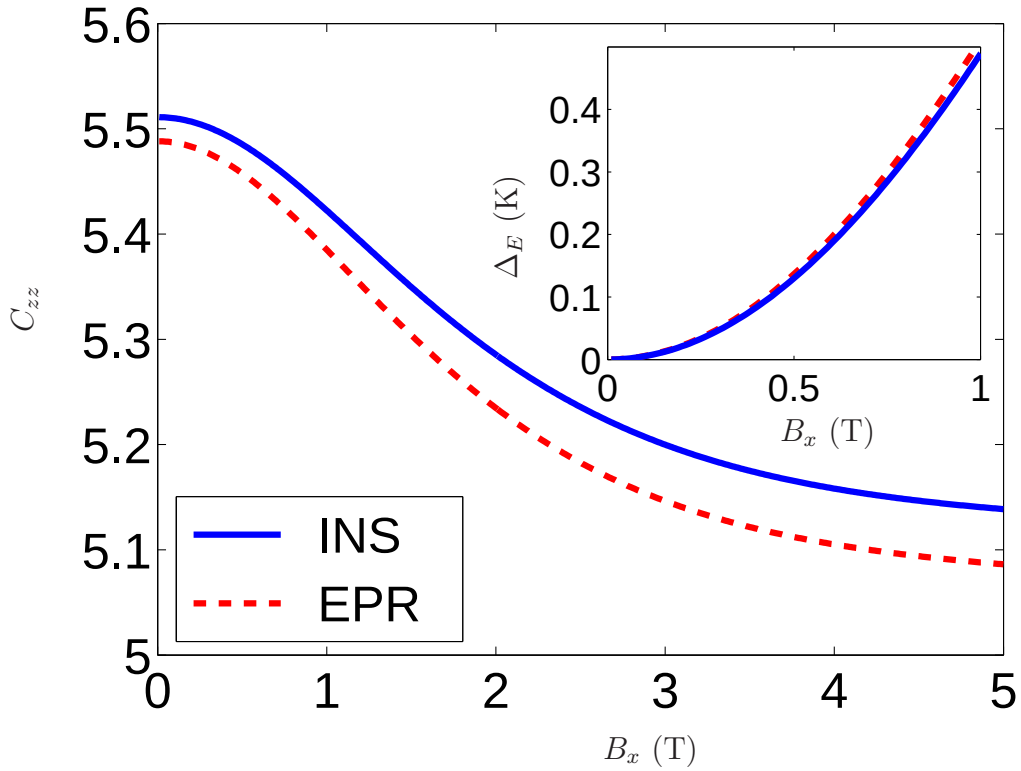

Figure 6.9: Comparing C_{zz} and Δ_E as a function of B_x, calculated using two different crystal field parameters (CFP). The solid line is obtained, using Refs. [57, 78] CFP based on inelastic neutron scattering (INS) experiment. The dashed lines is obtained, using Ref. [79] based on electron paramagnetic resonance (EPR) experiment.

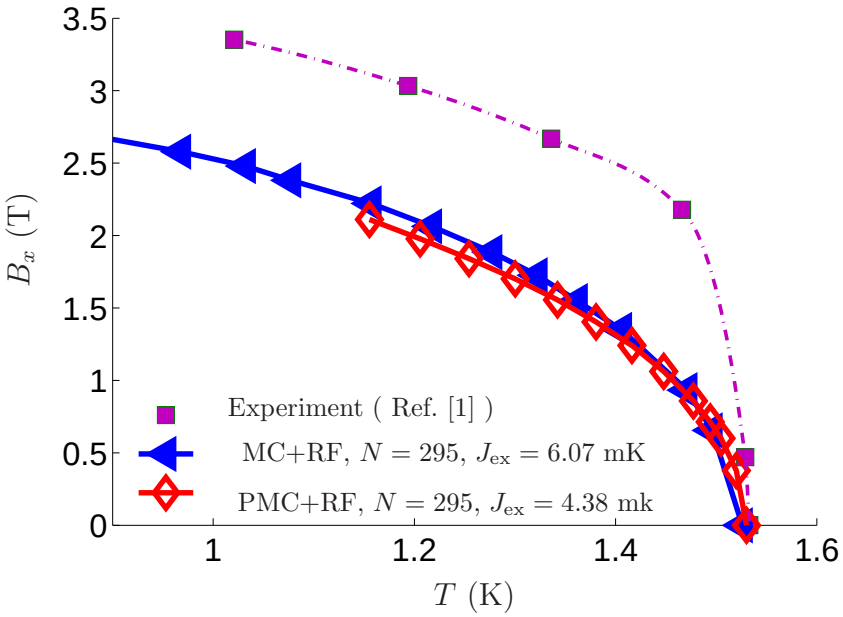

Figure 6.10: Comparing the phase diagrams of the critical transverse field as a function of temperature for $LiHoF_4$, based on two different set of crystal field parameters. The closed triangles are the QMC results of Ref. [57], using the reaction field method for a finite sphere with $N = 295$, based on the CFP of Ref. [78]. The open diamonds are obtained from our perturbative Monte-Carlo, using the same reaction field method used in Ref. [57] for a sphere with $N = 295$ spins, based on the CFP reported in Ref. [79].

to match the experimental $T_c = 1.53$ K is therefore different. In order to scrutinize "only" the effect of using a new set of CFP and to compare the phase diagram obtained using this new set of parameters with the results of Ref. [57] in a rather simple way, we repeated the perturbative Monte Carlo simulations, using the same reaction field method used above and done in Ref. [57] for a finite size sphere of $N = 295$ spins and a newly determined $J_{\rm ex} = 4.38$ mK. At the end, after in essence repeated all the work discussed in Section 6.4.3, a new phase diagram is derived. This phase diagram is plotted in Fig. 6.10. As it can be seen, this *new* phase diagram is consistent with the previous theoretical work, (*e.g.* Ref. [57] and Fig. 6.8). Interestingly it therefore does not appear at this time that the different crystal field Hamiltonians available for $LiHoF_4$ [54, 57, 78, 79] are able to explain the significant discrepancy between the $B_x - T$ phase diagram obtained by simulations compared to experimental results of Ref. [1]. Finally, we need to emphasize that there is no difference in the results for this new set of CFP provided $J_{\rm ex}$ is adjusted as well. On the other hand, different CFP lead to a systematically different T_c if $J_{\rm ex}$ is not adjusted.

6.5 Conclusion

With a perturbative Hamiltonian derived from a low energy effective spin-$\frac{1}{2}$ description of $LiHoF_4$, we have re-investigated the $B_x - T$ phase diagram with an independent approach from Ref. [57] for small B_x/T_c where quantum fluctuations are weak. The method we used to incorporate perturbatively weak quantum fluctuations within a semiclassical Hamiltonian, because of its simple numerically tractable form, allows one to directly address possible factors behind the discrepancy between results from experiments and from classical Monte Carlo simulations in the vicinity of T_c. This method can be easily generalized to more complicated quantum magnetic Ising models, where the Ising-like term is the dominant term and the other non commuting terms are considered as weak perturbations. In particular, if one is interested in studying numerically the effect of nonzero B_x in the diluted regime of $LiHo_xY_{1-x}F_4$, this perturbative method should be directly applicable by performing Monte Carlo simulations of the appropriate low energy Hamiltonian [56, 72].

To perform semi-classical Monte Carlo simulations that handle the magnetostatic long-range dipole-dipole interactions properly, we applied the Ewald summation technique for two different geometries. In order to determine T_c, we used the Binder magnetization ratio crossing for a long needle-shape sample, and we used the $\chi_{\rm sph} = \frac{3}{4\pi}$ criterion for a spherical sample embedded inside a long needle-shaped domain. We obtained the same T_c for both cases and, consequently, determined the same value for $J_{\rm ex}$. The values of the T_c and $J_{\rm ex}$ that we calculated are somewhat different from the T_c and $J_{\rm ex}$ values found in Ref. [57]. This difference originates from using open boundary conditions and a finite spherical cutoff in Ref. [57], which underestimates the thermal fluctuations at the boundary. We found that although we used a different method and found a different $J_{\rm ex}$, the final $B_x - T$ phase diagram obtained here is the same in the low B_x/T_c limit as in the previous results [57]. As a result, we tentatively conclude that the discrepancy between the theoretical and experimental results is *not* of computational origin. To explore a possible explanation for the discrepancy, we considered a different set of crystal field parameters.

A consideration of different crystal field parameters (CFP), which lead to a different estimate for $J_{\rm ex}$ does not, however, at the end produce a dramatically different T_c vs B_x phase diagram. This preliminary result, that only considers one set of alternative CFP, goes against the suggestion of Ref. [57] that a possible origin of the discrepancy might be due to the ambiguity in CFP. It is perhaps surprising that the consideration of a rather different set of CFP compared to those used in Ref. [57] affects the phase diagram so little once $J_{\rm ex}$ has been re-adjusted to match the experimental $T_c(B_x = 0) = 1.53$ K value. Therefore the origin of the discrepancy between numerics and experiment remains fully unexplained.

The method we obtained in the present work could be used to carry on further investigation of the cause of the discrepancy. Without this tool, it would have been somewhat less straightforward to have investigated the relevance of the various factors that we investigated in this paper. The disagreement with the experimental phase diagram of Ref. [1], would suggest that it may be worthwhile to revisit the experimental determination of the B_x vs T_c phase diagram. On the other hand, in both the work presented here and in that of Ref. [57], a very simple spin Hamiltonian was considered. Specifically, only long-range magnetostatic dipole-dipole and

isotropic (Heisenberg) nearest-neighbor exchange interactions were considered. The faster decreasing $T_c(B_x)$, compared to the experimental case indicates that perhaps there are effects at play in the real material that weaken quantum fluctuations for small B_x.

In other words, there may be other couplings in the effective theory in addition to those in the simplest transverse field Ising model (TFIM) of Eq. (6.1). As illustrated in Fig. 3.5, the terms that we ignored when passing from Eq. (3.12) to Eq. (3.13) seem too small to be able to resolve this issue. It might be necessary to consider the possibility that not completely negligible anisotropic exchange, higher order multipolar exchange interaction, or magneto-elastic couplings may be at play in $LiHoF_4$.

Finally, we note that it would be interesting if one could study other magnetic materials similar to the $LiHoF_4$ compound and that could provide another realization of a TFIM. Recently, a mean-field theory calculation has concluded that $Ho(OH)_3$, which is an insulating hexagonal dipolar Ising ferromagnet, is very well described by a TFIM when a magnetic field B_x is applied perpendicular to the Ising spin direction [6]. This material constitutes a close analogue of $LiHoF_4$ and, when diamagnetically diluted with Y^{3+}, may potentially be an analogue of $LiHo_xY_{1-x}F_4$. The existence of another experimental candidate for the study of the TFIM with long-range dipolar interaction presents the opportunity to re-investigate the puzzling properties of pure and diluted $LiHoF_4$ in a new material, shedding light on the physics of dipolar Ising systems in both zero and nonzero applied transverse field. The method we have employed in this work is a suitable tool to study these new proposed quantum magnetic Ising materials beyond mean field theory and provides a tool to make comparison with future experiments performed on these proposed TFIM materials.

To conclude, we hope that the work presented in this chapter stimulates further theoretical and experimental studies of $LiHoF_4$ in the regime of small transverse field B_x where the classical paramagnetic to ferromagnetic transition is only perturbatively affected by B_x.

Chapter 7

Conclusion and Avenues for Future Work

7.1 Summary of Conclusions

In this thesis, in Chapter 3, we explained how to derive an effective spin$-\frac{1}{2}$ Hamiltonian for the $LiHo_xY_{1-x}F_4$ magnetic material in a magnetic field B_x transverse to the Ho^{3+} Ising spins for either $x = 1$ or $x < 1$. For $x < 1$, via a general mean field discussion and also, more rigorously, via an effective spin$-\frac{1}{2}$ picture, we showed that by randomly diluting magnetic Ho^{3+} ions with nonmagnetic Y^{3+} ions, the magnetization induced by B_x, combined with the destruction of the spatial symmetry surrounding each Ho^{3+}, consequently generates effective local random fields via the long-range off-diagonal interactions between the magnetic Ho^{3+} ions.

To affirm the soundness of our effective spin$-\frac{1}{2}$ approach, in Chapter 4, we presented analytical and numerical evidence for the validity of an effective $S_{\text{eff}} = \frac{1}{2}$ approach to the description of random field generation in $S \geq 1$, and especially for an $S = 1$, dipolar spin glass models with strong uniaxial Ising anisotropy and subject to weak external magnetic field B_x transverse to the Ising direction.

We proposed that the effective B_x induced random fields are the key explanation to the long standing experimental puzzle of the smearing of the nonlinear

susceptibility χ_3 at the spin glass transition with increasing B_x. To provide a quantitative description of how random fields influence the behaviour of χ_3, in Chapter 5, based on the effective spin$-\frac{1}{2}$ model for $LiHo_xY_{1-x}F_4$ with an applied B_x, we studied a mean field model, which generalizes the standard Sherrington-Kirkpatrick model for a quantum spin glass model. We assumed a Gaussian distribution for the random interactions and considered the amplitude of the random interactions are B_x dependent. Then, using the standard replica trick and the imaginary time formalism employed in the theory of quantum systems, we derived the free energy and obtained self-consistent relations for the magnetization and spin-glass order parameters. Calculating χ_3 for our proposed model, we successfully reproduced the overall trend of the experimental χ_3 data.

We believe, that by comparing experimental data with our theoretical results, it can be concluded that induced random field physics is at play and observed in $LiHo_xY_{1-x}F_4$. The significance of this piece of work is that, firstly, we have proposed a novel realization of a three dimensional random field Ising model within a magnetic setting and, secondly, have solved a long standing experimental puzzle. $LiHo_xY_{1-x}F_4$ with $B_x \neq 0$ is a realization of a RF Ising model and provides a new venue for studying the RF problem. The RF physics can be probed directly by measuring bulk properties such as magnetization and susceptibility.

In another part of this thesis, in Chapter 6, we used Monte Carlo simulations to investigate the phase diagram of disorder-free $LiHoF_4$ in weak B_x. A previous quantum Monte Carlo simulation [57] had found that even for small B_x close to the classical critical point, there is a discrepancy between experiment and the quantum Monte Carlo results. This discrepancy persists asymptotically close to the classical ferromagnet to paramagnet phase transition where quantum fluctuations are perturbatively small. In our work, we aimed to scrutinize the potential culprits for the discrepancy. We revisited this problem, using an alternative approach. We focused on weak transverse fields close to the classical critical point. We started with the effective spin$-\frac{1}{2}$, which we had previously derived for pure $LiHoF_4$. Then, we took the quantum fluctuations into account by applying a so-called cumulant expansion. We derived an effective perturbative classical Hamiltonian analytically, on which we performed classical Monte Carlo simulations. The "simple" numer-

ically treatable form of our model allows one to directly address possible factors behind the discrepancy between experiment and Monte Carlo simulation in the vicinity of T_c. We used the Ewald summation technique, which incorporates long range interactions more systematically compared to the reaction technique used in the previous work of Ref. [57]. By performing a systematic finite-size scaling, we found a more accurate estimate for the nearest-neighbor exchange interaction than in Ref. [57]. The crystal field from the ions surrounding each Ho ion is described by an empirical Hamiltonian. Although the ambiguity in the empirical Hamiltonian leads to different estimations for the exchange interaction, surprisingly, the phase diagram we calculated does not produce a dramatically different change compared to quantum Monte Carlo results of Ref. [57]. We found that the factors proposed as the possible origins of the discrepancy are not the issue. Possibly other sources, for example, interactions other than long-range magnetic dipolar interactions and nearest-neighbor exchange may be at play. However, our Monte Carlo method can be effectively used to carry out further investigations of the likely causes of the discrepancy. Without this tool, the discovery of the irrelevance of the above factors would have been less straightforward. The advantage of our perturbative Monte Carlo method is that it can be applied to any magnetic spin-$\frac{1}{2}$ system for which the effects of quantum fluctuations close to the classical phase transition are of interest, including case with disorder such as $LiHo_xY_{1-x}F_4$.

Up to now, significant experimental and theoretical efforts have been devoted to obtain a better understanding of the underlying physics of the magnetic material $LiHo_xY_{1-x}F_4$. Although, from a contribution of the total efforts, some of the puzzling behaviours of $LiHo_xY_{1-x}F_4$ have been unraveled, still, there are many questions opened regarding the physics of this material. In the next section, we briefly mention a few interesting open problems related to the $LiHo_xY_{1-x}F_4$ material that may warrant further study.

7.2 Open Questions and Prospects for Future Work

7.2.1 The Perturbative Quantum Monte Carlo Method

The method we used in Chapter 6 to incorporate perturbatively weak quantum fluctuations within a semiclassical Hamiltonian for dilution free $LiHoF_4$ ($x = 1$) with a weak B_x, can be generalized to more complicated Hamiltonians, where there is a dominant Ising interaction plus non-commuting weak quantum interactions. These non-commuting terms are perturbations to the Ising interaction. One of the immediate applications of this method is to employ it for $LiHo_xY_{1-x}F_4$ in the diluted regime. Therefore, by deriving a perturbative semiclassical Hamiltonian for $LiHo_xY_{1-x}F_4$ with a weak B_x in the diluted regime ($x < 1$), one can study the diluted system numerically by performing Monte Carlo simulations. If we compare the effective spin-$\frac{1}{2}$ Hamiltonian of Eq. (3.14), which was derived for randomly disordered $LiHo_xY_{1-x}F_4$, with the effective spin-$\frac{1}{2}$ Hamiltonian of Eq. (3.13) for pure $LiHoF_4$, we see that Eq. (3.14) has an extra non-commuting term of $2C_{zz}(B_x)C_{xx}(B_x)\sum_{i\neq j}\epsilon_i\epsilon_j L_{ij}^{zx}\sigma_i^z\sigma_j^x$, compared to the Hamiltonian of Eq. (3.13).

The reason that this term is neglected in Eq. (3.13) is that, in the non diluted system, because of lattice mirror symmetry, $\sum_{i\neq j} L_{ij}^{zx}\sigma_i^z\left\langle\sigma_j^x\right\rangle = 0$. Therefore, this term can only contribute via (thermal) fluctuations above the vanishing mean-field contribution. Since $\frac{C_{x0}(B_x)}{C_{zz}(B_x)} < 1$, the (second order) thermal fluctuation contribution effects from the above $\sigma_i^z\sigma_j^x$ term is considered to be small. However, for $x < 1$ the spatial symmetry of the Ho^{3+} ions is broken and this argument is no more valid. Indeed, this term contributes when $x < 1$. Interestingly, the amplitude of these random off-diagonal couplings are induced by B_x. Therefore, at low B_x, their contributions are weak and these terms can be incorporated perturbatively to derive a semiclassical effective Hamiltonian via cumulant expansion. We can apply this newly derived semiclassical Hamiltonian to perform Monte Carlo simulations in the vicinity of the classical regime, where $B_x/T \to 0$. Therefore, one can fruitfully apply this perturbative semiclassical approach to numerically study the physics of induced random fields in diluted $LiHo_xY_{1-x}F_4$ in a regime where B_x is weak. In the diluted regime, due to these non-comuting off-diagonal dipole-dipole interactions, performing a full quantum Monte Carlo simulation is somehow complicated. There-

fore, such a perturbative semiclassical method would be a useful tool for possible numerical studies of $LiHo_xY_{1-x}F_4$ in a weak B_x/T regime.

7.2.2 Hyperfine Interactions

As we previously discussed, in $LiHo_xY_{1-x}F_4$, the electronic and nuclear moments of the Ho^{3+} ions are coupled via a hyperfine interaction $H_{\rm hyp} = A\sum_i \epsilon_i(\mathbf{I}_i \cdot \mathbf{J}_i)$, with a relatively large coupling constant $A \approx 39$ mK [1, 57, 93, 94]. $LiHo_xY_{1-x}F_4$ in the spin glass regime (i.e $x \sim 0.1$) at $B_x = 0$ has a transition temperature ~ 100 mK. At $B_x = 0$ the classical transition temperature is a measure of the typical energy of the dipolar interactions. Comparing the typical energy scale of the average dipole-dipole interactions and the energy scale of the hyperfine interactions indicates that these hyperfine interactions can not be neglected. Thus, at low enough temperatures a study of $LiHo_xY_{1-x}F_4$ without considering the hyperfine interactions at a microscopic level is incomplete. In particular, at $T = 0$ hyperfine interactions enhance the critical transverse magnetic field B_x^c for either $x = 1$ and $x < 1$ [1, 57, 93]. If $A = 0$, one would expect the order of magnitude of B_x^c to be the same as $T_c(B_x = 0)$. $A \neq 0$ leads to a significant increase of B_x^c, compared to $T_c(B_x = 0)$.

Schechter *et al.* [93, 94] have theoretically studied the physics of hyperfine interactions at $T \to 0$. The AI^zJ^z contribution to the hyperfine interaction splits the electronic ground state doublet into eight doubly degenerate states, with separation ~ 205 mK between adjacent levels [93, 94]. Each of the ground states can be associated with nuclear spins of equal magnitude and opposite sign. Schechter *et al.*, correctly discuss that, if only AI^zJ^z is considered, then a $B_x \ll \Omega$ cannot couple or induce quantum fluctuations between these degenerate states. However, $A(I^+J^+ + I^-J^-)$ in the presence of $B_x \neq 0$ can couple the ground state and allow for quantum fluctuations, but these quantum fluctuations are significantly weaker compared to the B_x induced quantum fluctuations, when $A = 0$ [93, 94]. Subsequently, the authors of Refs. [93, 94], by including the hyperfine interactions and for $T \to 0$, derived an effective spin-$\frac{1}{2}$ Hamiltonian written in the subspace of the two lowest degenerate electro-nuclear ground states. The difference compared to the

effective spin-$\frac{1}{2}$ written in the subspace of the electronic degenerate ground state in the absence of A is a much weaker effective transverse field and a renormalized dipole-dipole interaction. From the work of Ref. [93, 94] one can understand the origin of the high B_x^c at $T = 0$ much better.

In this thesis, we were specifically interested in the general phenomenology of the induced random fields generated by applied B_x and the physics behind it, rather than obtaining a precise quantitative description of *diluted* $LiHo_xY_{1-x}F_4$. In our calculations, to focus only on the phenomena pertaining to random field physics and to avoid the complexity of including hyperfine interactions, we therefore, did not consider the hyperfine interactions explicitly in our modeling in the microscopic level. We incorporated the role of hyperfine interactions by deriving the transverse field $\Gamma(B_x)$ relation with B_x from a fitting with experiment and renormalizing the amplitude of our dipole-dipole interactions such that we have a better match with experiment. To have a further quantitative contact with experiments, we have to somehow incorporate these hyperfine interactions. Unfortunately a spin-$\frac{1}{2}$ framework similar to what introduced in Refs. [93, 94] for $T \to 0$ is not suitable for the energy scales we are interested in. Unlike the case that $A = 0$ and the higher electronic states are well separated from the degenerate ground state, for $A \neq 0$ the eightfold degenerate electro nuclear states associated to the electronic ground state are very close to each other, therefore all the 16 electro nuclear states should be incorporated in our analysis. For example one of the questions that may arise is: Can the microscopic Hamiltonian of Eq. (2.16) be somehow projected properly in the subspace of the lowest 16 electro nuclear states, such that each pair of the eightfold degenerate states (when $A(I^+J^+ + I^-J^-)$ is neglected) be described by a series of eight spin-$\frac{1}{2}$ pseudo spins [94]? Can we develop a mean field theory, such that the thermodynamical quantities (i.e magnetization, non linear susceptibility, ...) be quantitatively derived, either numerically or analytically?

7.2.3 Random Strain

In systems consisting of odd number of electrons, the Kramers theorem dictates that, by time reversal symmetry, the ground state is at least a doublet (Kramers

doublet). The Kramers doublet, which are time conjugates of each other can not be split by any electrostatic field. In $LiHo_xY_{1-x}F_4$, Ho^{3+} is an even electron ion (non-Kramers ion). Therefore, if the local tetragonal symmetry is somehow broken (e.g. by strain) then, new crystal field interactions such as $B_2^{\pm 2}O_2^{\pm 2}$ may be locally induced. Such crystal field operators have nonzero matrix elements between the two degenerate ground states. The degeneracy may be lifted, which in the effective spin-$\frac{1}{2}$ picture reads as local transverse fields coupled to the $\hat{x}$ component of the spin-$\frac{1}{2}$ degrees of freedom. Therefore, these locally induced transverse fields compete with collective magnetic ordering and may destruct the ordered phase. In diluted $LiHo_xY_{1-x}F_4$ the random substitution of Ho^{3+} with Y^{3+} may induce "random" strains in the system, and lead to random transverse fields [125]. Such random transverse fields have been identified in samples with very dilute Ho^{3+} in $LiYF_4$ [79, 126].

These stain-induced random transverse fields open an interesting possible scenario to explain the destruction of the spin glass phase in highly diluted $LiHo_xY_{1-x}F_4$. It would be worthwhile to develop a mean field spin glass model including strain-induced random transverse fields to investigate the possibility of the destruction of the spin glass phase by these local random strains[1].

7.2.4 Other Candidate Transverse Field Ising Materials

It would be very interesting if one could study other dipolar Ising magnetic materials similar to the $LiHoF_4$ compound and which could be easily diamagnetically diluted, providing another realization of a TFIM. In the context of these new materials, one can address specific problems such as: (i) Whether the proposal of B_x-induced effective random fields valid in other diluted dipolar Ising materials [24, 56, 72]. (ii) How do quantum fluctuations manifest in other possible transverse field Ising materials where hyperfine interactions are much smaller than the hyperfine interactions within Ho^{3+} ions? (iii) Does the antiglass phenomenon [7, 8, 67] occur in other diluted dipolar Ising materials?

[1]However, it might be possible that the quantum fluctuations induced by these random strains be somehow blocked by hyperfine interactions (see the previous subsection).

Recently, a mean-field theory calculation has concluded that $Ho(OH)_3$, which is an insulating hexagonal dipolar Ising ferromagnet, is very well described by a TFIM when a magnetic field B_x is applied perpendicular to the Ising spin direction [6]. This material constitutes a close analogue of $LiHoF_4$ and, when diamagnetically diluted with Y^{3+}, may potentially be an analogue of $LiHo_xY_{1-x}F_4$. The existence of another experimental candidate for the study of the TFIM with long-range dipolar interaction presents the opportunity to re-investigate the puzzling properties of pure and diluted $LiHoF_4$ in a new material, shedding light on the physics of dipolar Ising systems in both zero and nonzero applied transverse field. The analytical and theoretical methods we have employed in this thesis to study $LiHo_xY_{1-x}F_4$ for both $x = 1$ and $x < 1$, are suitable tools to study these new proposed quantum magnetic Ising materials and provides benchmarking tools to make comparison with future experiments performed on these proposed TFIM materials.

The work presented in this thesis covers a small part of the challenges offered by $LiHo_xY_{1-x}F_4$, with apparently more left to understand than has so far been understood. We hope that this work stimulates further theoretical and experimental studies of this system and other related materials.

Appendix A

The Trotter-Suzuki Method

The Trotter-Suzuki method [11] is a useful tool that helps us to derive an effective classical Ising Hamiltonian as a map to the quantum Ising Hamiltonian in such a way that their partition function is the same. This general method can be used to study the simple transverse Ising model by using Monte Carlo simulation. With the aid of Trotter-Suzuki method, one can derive an effective classical Hamiltonian with commuting terms, providing us with the ability to perform simulations.

If we have two non-commuting operators, A_1 and A_2, we know that

$$\exp\left(A_1 + A_2\right) \neq \exp A_1 \exp A_2 \ .$$

Trotter has shown [127] that, in the case that $M \to \infty$, then

$$\exp\left(A_1 + A_2\right) = \lim_{M\to\infty} \left[\exp A_1/M \exp A_2/M\right]^M ,$$

even when $[A_1, A_2] \neq 0$. For the TFIM Hamiltonian

$$H_{\text{TFIM}} = -\frac{1}{2}\sum_{i,j} J_{ij}\sigma_i^z\sigma_j^z - \Gamma\sum_i \sigma_i^x = \mathcal{H}_0 + \mathcal{V}, \tag{A.1}$$

The partition function is then

$$Z = \mathbf{Tr} e^{-\beta(\mathcal{H}_0+\mathcal{V})}.$$

By applying the Trotter formula, Z reads

$$Z = \sum_{l}^{2^N} \lim_{M\to\infty} \langle\psi_l| \left[\exp\left(-\beta\mathcal{H}_0/M\right) \exp\left(-\beta\mathcal{V}/M\right)\right]^M |\psi_l\rangle. \tag{A.2}$$

Here ψ_l represent the l-th set of spin configuration $\{\sigma_1, \sigma_2, \cdots, \sigma_N\}$ of the whole 2^N configurations of the system, and the above summation runs over all such possible configurations denoted by l. Here, $\sigma = \pm 1$ denotes the up and down eigenvalues of σ^z. Introducing M number of identity operators

$$\mathcal{I} = \sum_{l}^{2^N} |\psi_{l,k}\rangle\langle\psi_{l,k}|, \qquad k = 1, 2, ...M.$$

in between the M product of exponentials we have

$$Z = \lim_{M\to\infty} \mathbf{Tr} \prod_{k=1}^{M} \langle\sigma_{1,k}...\sigma_{N,k}| \exp\left(\frac{-\beta\mathcal{H}_0}{M}\right) \exp\left(\frac{-\beta\mathcal{V}}{M}\right) |\sigma_{1,k+1}\sigma_{2,k+1}...\sigma_{N,k+1}\rangle.$$

For the classical Ising term $\mathcal{H}_0$, we have,

$$\prod_{k=1}^{M} \langle\sigma_{1,k}...\sigma_{N,k}| \exp\left(\frac{\beta J_{ij}}{2M} \sum_{i,j=1}^{N} \sigma_i^z \sigma_j^z\right) |\sigma_{1,k+1}...\sigma_{N,k+1}\rangle = \exp\left[\sum_{i,j=1}^{N} \sum_{k=1}^{M} \frac{\beta J_{ij}}{2M} \sigma_{i,k}\sigma_{j,k}\right] \tag{A.3}$$

while for the term with transverse field interaction we have

$$\begin{aligned} &\prod_{k=1}^{M} \langle\sigma_{1,k}...\sigma_{N,k}| \exp\left[\frac{\beta\Gamma}{M} \sum_i \sigma_i^x\right] |\sigma_{1,k+1}...\sigma_{N,k+1}\rangle \\ &= \left(\frac{1}{2}\sinh\left[\frac{2\beta\Gamma}{M}\right]\right)^{\frac{NM}{2}} \exp\left[\frac{1}{2}\ln\coth\left(\frac{\beta\Gamma}{M}\right) \sum_{i=1}^{N} \sum_{k=1}^{M} \sigma_{i,k}\sigma_{i,k+1}\right]. \end{aligned} \tag{A.4}$$

The last step follows because

$$e^{a\sigma^x} = e^{-i(ia\sigma^x)} = \cos\left(ia\sigma^x\right) - i\sin\left(ia\sigma^x\right) = \cosh\left(a\right) + \sigma^x \sinh\left(a\right),$$

and then

$$\langle\sigma|e^{a\sigma^x}|\sigma'\rangle = \left[\frac{1}{2}\sinh\left(2a\right)\right]^{1/2} \exp\left[(\sigma\sigma'/2)\ln\coth\left(a\right)\right],$$

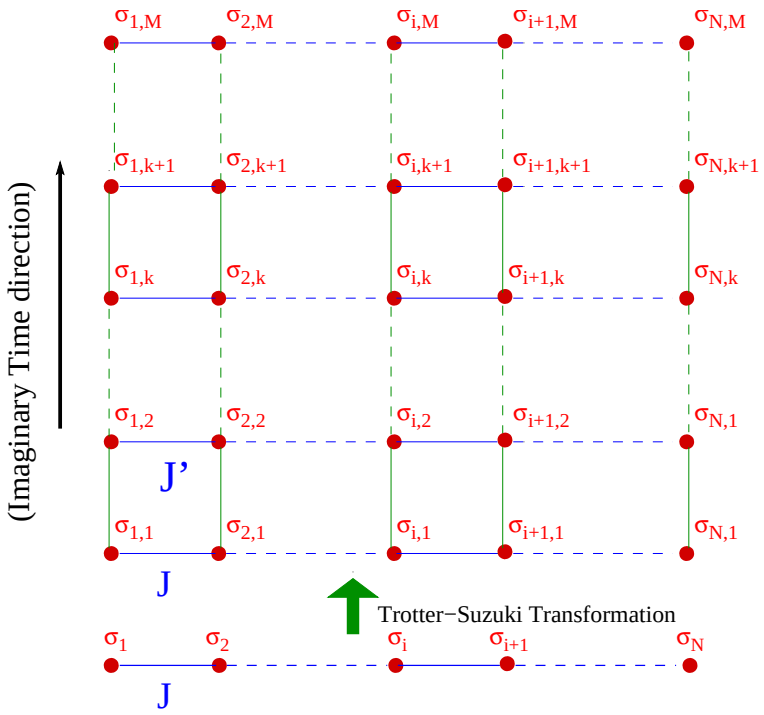

Figure A.1: The Trotter-Suzuki equivalence of a quantum one dimensional chain and a (1+1) dimensional classical system. J' indicates the additional interaction in the Trotter (imaginary time) direction.

since

$$\langle\uparrow|e^{a\sigma^x}|\uparrow\rangle = \left[\frac{1}{2}\sinh(2a).\coth(a)\right]^{1/2} = \cosh(a) = \langle\downarrow|e^{a\sigma^x}|\downarrow\rangle$$

and

$$\langle\uparrow|e^{a\sigma^x}|\downarrow\rangle = \left[\frac{1}{2}\sinh(2a)/\coth(a)\right]^{1/2} = \sinh(a) = \langle\downarrow|e^{a\sigma^x}|\uparrow\rangle.$$

Thus the partition function becomes

$$Z = C^{\frac{NM}{2}}\mathbf{Tr}_\sigma(-\beta\mathcal{H}_{\rm TS}[\sigma]) \quad ; \quad C = \frac{1}{2}\sinh\frac{2\beta\Gamma}{M} \tag{A.5}$$

where the effective classical Hamiltonian is

$$\mathcal{H}_{\rm TS}(\sigma) = \frac{1}{2}\sum_{i,j}^{N}\sum_{k=1}^{M}\left[-\frac{J_{ij}}{M}\sigma_{ik}\sigma_{jk} - \frac{\delta_{ij}}{2\beta}\ln\coth\left(\frac{\beta\Gamma}{M}\right)\sigma_{ik}\sigma_{ik+1}\right]. \tag{A.6}$$

The Hamiltonian $\mathcal{H}_{\rm TS}$ is a classical one, since the variables $\sigma_{i,k}$'s involved are merely the eigen values of σ^z, and hence there is no non-commuting part in $\mathcal{H}_{\rm TS}$. For $T \to 0$, $M \to \infty$, and the Hamiltonian represents a system of spins in a (d+1)-dimensional lattice, which is one dimension higher than the original d-dimensional Hamiltonian, as is evident from the appearance of one extra label k for each spin variable (see Fig. A). Thus, corresponding to each single quantum spin variable σ_i in the original Hamiltonian, we have an array of M number of classical replica spins σ_{ik}. This new (time-like) dimension along which these classical spins are spaced is known as the *imaginary time* (Trotter) dimension. From the explicit form of $\mathcal{H}_{\rm TS}$, we see that in addition to the previous interaction (J) term ($-\sum_{i,j}^{N} J_{ij}\sigma_i\sigma_j$), there is an additional nearest neighbor interaction (J') between the Trotter replicas corresponding to the same original spin, along the Trotter direction, given by the term ($\sum_{i,j}^{N}\sum_{k=1}^{M} -\frac{\delta_{ij}}{2\beta}\ln\coth(\beta\Gamma/M)\sigma_{ik}\sigma_{ik+1}$).

Appendix B

Perturbative Cumulant Expansion for Small Quantum Fluctuations

In this appendix, starting from Eq. (6.5), we give the details of the derivation of the effective perturbative Hamiltonian $H_{\text{eff}}[\psi_i]$ by a cumulant expansion, when quantum fluctuations are small. Deriving $H_{\text{eff}}[\psi_i]$, as defined by Eq. (6.4), one can rewrite the partition function of the system in a classical form.

Referring to Eq. (6.5) and recalling that $|\psi\rangle$ is a direct product of σ_i^z eigenstates, the expectation value $\langle\psi|\sigma_x|\psi\rangle$ is zero, so $\langle\psi|\mathcal{H}|\psi\rangle = \langle\psi|H_0|\psi\rangle$. Defining $E_0(\psi) \equiv \langle\psi|H_0|\psi\rangle$, we can write $\langle\psi|\left(\mathcal{H} - \langle\psi|\mathcal{H}|\psi\rangle\right)^n|\psi\rangle = \langle\psi|(\mathcal{H} - E_0(\psi))^n|\psi\rangle$.
Performing a polynomial expansion on $\left(\mathcal{H} - E_0(\psi)\right)^n = \left[(H_0 - E_0(\psi)) + H_1\right]^n$, and keeping terms to order of $O(\Gamma^2)$ in the polynomial expansion ($H_1 \propto \Gamma$), we have

$$\begin{aligned}
\langle\psi|\left(\mathcal{H} - E_0(\psi)\right)^n|\psi\rangle &= \langle\psi|\left[(H_0 - E_0(\psi)) + H_1\right]^n|\psi\rangle \\
&\cong \sum_{n_1,n_2,n_3} \delta(n_1+n_2+n_3, n-2) \\
&\quad \times \left[\langle\psi|(H_0 - E_0(\psi))^{n_1} H_1 (H_0 - E_0(\psi))^{n_2} H_1 (H_0 - E_0(\psi))^{n_3}|\psi\rangle\right] \\
&\cong \langle\psi|H_1\left[H_0 - E_0(\psi)\right]^{n-2} H_1|\psi\rangle \ . \qquad \text{(B.1)}
\end{aligned}$$

To write Eq. (B.1) we have used the fact that

$$\langle\psi|\left(H_0 - E_0(\psi)\right)^n|\psi\rangle = 0 \qquad \text{(B.2)}$$

and

$$\langle\psi|(H_0 - E_0(\psi))^m H_1 (H_0 - E_0(\psi))^k|\psi\rangle = 0 \ , \tag{B.3}$$

for integer numbers m and k. The effect of σ_i^x on $|\psi\rangle$ is to flip the spin i. We define $\sigma_i^x|\psi\rangle = |f_i\psi\rangle$, where $f_i\psi$ means that the i'th spin has flipped, such that if the i'th spin was in the $|\uparrow\rangle$ or the $|\downarrow\rangle$ eigenstate of σ_i^z, it changes into the $|\downarrow\rangle$ or $|\uparrow\rangle$ state respectively. In Eq. (B.1), using $H_1 = -\Gamma \sum_i \sigma_i^x$, we get

$$\begin{aligned} &\langle\psi|H_1 \left[H_0 - E_0(\psi)\right]^{n-2} H_1|\psi\rangle \\ &= \Gamma^2 \textstyle\sum_{i,j} \langle\psi|\sigma_i^x \left[H_0 - E_0(\psi)\right]^{n-2} \sigma_j^x|\psi\rangle \\ &= \Gamma^2 \textstyle\sum_{i,j} \langle f_i\psi| \left[H_0 - E_0(\psi)\right]^{n-2} |f_j\psi\rangle \ . \end{aligned} \tag{B.4}$$

Here $\langle f_i\psi| \left[H_0 - E_0(\psi)\right]^{n-2} |f_j\psi\rangle$ is zero, unless $i = j$. Thus, Eq. (B.1) can be written as

$$\langle\psi| \left(\mathcal{H} - E_0(\psi)\right)^n |\psi\rangle = \Gamma^2 \sum_i \left[E_0(f_i\psi) - E_0(\psi)\right]^{n-2} . \tag{B.5}$$

Considering the definition of H_{eff}, by substituting $E_0(f_i\psi) - E_0(\psi) = 2(h_i + h_0^z)\sigma_i^z$ in Eq. (6.5), we obtain

$$\begin{aligned} H_{\text{eff}} &= H_0 - \beta\Gamma^2 \sum_i \sum_{n>1}^{\infty} \frac{1}{n!} \left[-2\beta(h_i + h_0^z)\right]^{n-2} \\ &= H_0 + \beta\Gamma^2 \sum_i \{\sigma_i^z F_1 \left[2\beta(h_i + h_0^z)\right] - F_0 \left[2\beta(h_i + h_0^z)\right]\}. \end{aligned} \tag{B.6}$$

In Eq. (B.6), h_i is the total local field affecting the spin at site i by other spins , which is

$$h_i = -\sum_{j\neq i} \mathcal{L}_{ij}^{zz} \sigma_j^z - \mathcal{J}_{\text{ex}} \sum_{\text{NN}} \sigma_{\text{NN}}^z \ , \tag{B.7}$$

and h_0^z is the external longitudinal field in the z direction. The functions $F_0(x)$ and $F_1(x)$ are defined as

$$\begin{aligned} F_0(x) &= \frac{\cosh(x) - 1}{x^2}, \\ F_1(x) &= \frac{\sinh(x) - x}{x^2}. \end{aligned} \tag{B.8}$$

Appendix C

Pseudo-Operator Counterparts of Thermodynamical Quantum-Mechanical Quantities

In this appendix, we establish the relationship between the real thermodynamical quantities of physical observables and their corresponding pseudo-operator representations, which can be calculated using the perturbative effective classical Hamiltonian of Eq. (6.6). To obtain the numerical values of these thermodynamical quantities, the derived pseudo-operators should be averaged by employing our perturbative classical Monte Carlo simulations.

Writing the partition function in terms of the perturbative effective Hamiltonian $H_{\text{eff}}[\psi_i]$, the pseudo-operators corresponding to $\langle E \rangle$, $\langle M_z \rangle$, $\langle M_x \rangle$, $\langle M_z^2 \rangle$, and $\langle M_z^4 \rangle$, which need to be calculated to obtain thermodynamical quantities using Monte

Carlo simulations, are given by

$$\langle E\rangle = -\frac{1}{Z}\frac{\partial Z}{\partial\beta} = \left\langle H_{\rm eff} + \beta\frac{\partial H_{\rm eff}}{\partial\beta}\right\rangle \tag{C.1}$$

$$\langle M_z\rangle = \left\langle -\frac{\partial H_{\rm eff}}{\partial h_0^z}\right\rangle \tag{C.2}$$

$$\langle M_x\rangle = \left\langle -\frac{\partial H_{\rm eff}}{\partial \Gamma}\right\rangle \tag{C.3}$$

$$\langle M_z^2\rangle = \left\langle \left(\frac{\partial H_{\rm eff}}{\partial h_0^z}\right)^2 - \frac{1}{\beta}\frac{\partial^2 H_{\rm eff}}{\partial {h_0^z}^2}\right\rangle \tag{C.4}$$

$$\langle M_z^4\rangle = \frac{1}{\beta^4}\left\langle -\beta\frac{\partial^4 H_{\rm eff}}{\partial {h_0^z}^4} + 4\beta^2\frac{\partial^3 H_{\rm eff}}{\partial {h_0^z}^3}\frac{\partial H_{\rm eff}}{\partial h_0^z}\right. \tag{C.5}$$

$$\left. -6\beta^3\frac{\partial^2 H_{\rm eff}}{\partial {h_0^z}^2}\left(\frac{\partial H_{\rm eff}}{\partial h_0^z}\right)^2 + 3\beta^2\left(\frac{\partial^2 H_{\rm eff}}{\partial {h_0^z}^2}\right)^2 + \beta^4\left(\frac{\partial H_{\rm eff}}{\partial h_0^z}\right)^4\right\rangle, \tag{C.6}$$

where E, M_z and M_x are the energy and magnetization in the z and x direction and their equivalent pseudo-operators to be calculated are on the right. The thermal average is denoted by $\langle\ldots\rangle$. Applying the derivatives and using the perturbative effective Hamiltonian (6.6), we find:

$$\begin{aligned} E &= E_0 + 2\beta\Gamma^2\sum_i\{\sigma_i^z F_1\left[2\beta(h_i+h_0^z)\right] \\ &\quad -F_0\left[2\beta(h_i+h_0^z)\right]\} \\ &\quad +\beta\Gamma^2\sum_i 2\beta(h_i+h_0^z)\{\sigma_i^z F_1^{(1)}\left[2\beta(h_i+h_0^z)\right] \\ &\quad -F_0^{(1)}\left[2\beta(h_i+h_0^z)\right]\}\ , \end{aligned} \tag{C.7}$$

while M_x is

$$\begin{aligned} M_x &= -2\beta\Gamma\sum_i\{\sigma_i^z F_1\left[2\beta(h_i+h_0^z)\right] \\ &\quad -F_0\left[2\beta(h_i+h_0^z)\right]\} \end{aligned} \tag{C.8}$$

and M_z

$$\begin{aligned} M_z &= \sum_i \sigma_i^z - 2\beta^2\Gamma^2 \sum_i \{\sigma_i^z F_1^{(1)}\left[2\beta(h_i + h_0^z)\right] \\ &\quad -F_0^{(1)}\left[2\beta(h_i + h_0^z)\right]\} \ , \end{aligned} \tag{C.9}$$

with $F_i^{(n)}(x)$ defined as $F_i^{(n)} = \frac{d^n F_i(x)}{dx^n}$, where $i = 1, 0$.
In order to find an expression for $\langle M_z^2 \rangle$ and $\langle M_z^4 \rangle$, we need to calculate $\frac{\partial H_{\rm eff}}{\partial h_0^z}$, $\frac{\partial^2 H_{\rm eff}}{\partial h_0^{z\,2}}$, $\frac{\partial^3 H_{\rm eff}}{\partial h_0^{z\,3}}$, and $\frac{\partial^4 H_{\rm eff}}{\partial h_0^{z\,4}}$. We find:

$$\begin{aligned} \frac{\partial H_{\rm eff}}{\partial h_0^z} &= -\sum_i \sigma_i^z + 2\beta^2\Gamma^2 \sum_i \{\sigma_i^z F_1^{(1)}\left[2\beta(h_i + h_0^z)\right] \\ &\quad -F_0^{(1)}\left[2\beta(h_i + h_0^z)\right]\} \ , \end{aligned} \tag{C.10}$$

$$\begin{aligned} \frac{\partial^2 H_{\rm eff}}{\partial h_0^{z\,2}} &= 4\beta^3\Gamma^2 \sum_i \{\sigma_i^z F_1^{(2)}\left[2\beta(h_i + h_0^z)\right] \\ &\quad -F_0^{(1)}\left[2\beta(h_i + h_0^z)\right]\} \ , \end{aligned} \tag{C.11}$$

$$\begin{aligned} \frac{\partial^3 H_{\rm eff}}{\partial h_0^{z\,3}} &= 8\beta^4\Gamma^2 \sum_i \{\sigma_i^z F_1^{(3)}\left[2\beta(h_i + h_0^z)\right] \\ &\quad -F_0^{(3)}\left[2\beta(h_i + h_0^z)\right]\} \quad \text{and} \end{aligned} \tag{C.12}$$

$$\begin{aligned} \frac{\partial^4 H_{\rm eff}}{\partial h_0^{z\,4}} &= 16\beta^5\Gamma^2 \sum_i \{\sigma_i^z F_1^{(4)}\left[2\beta(h_i + h_0^z)\right] \\ &\quad -F_0^{(4)}\left[2\beta(h_i + h_0^z)\right]\} \ . \end{aligned} \tag{C.13}$$

Appendix D

Lanczos Method

The Lanczos method [128, 129] is a useful numerical method for diagonalizing and calculating the eigenvalues of a sparse matrix. The basic idea of the Lanczos method is that a basis can be constructed iteratively, such that a general Hamiltonian $\widehat{H}$ has a tridiagonal representation. The first step is to choose an arbitrary state $|\phi_0\rangle$ in the Hilbert space of $\widehat{H}$. If no information about the ground state is available then $|\phi_0\rangle$ is chosen randomly. If there is any symmetry information about the ground state then it is convenient to choose a state from a subspace which satisfies the ground state symmetry of the system. After selecting an arbitrary $|\phi_0\rangle$, we can construct a set of n orthogonal states. We apply $\widehat{H}$ to the initial state. therefore, we obtain another state $\widehat{H}|\phi_0\rangle$. If we subtract the projection of the new state over $|\phi_0\rangle$ we obtain

$$|\phi_1\rangle = \widehat{H}|\phi_0\rangle - \frac{\langle\phi_0|\widehat{H}|\phi_0\rangle}{\langle\phi_0|\phi_0\rangle}|\phi_0\rangle \ , \tag{D.1}$$

where $|\phi_1\rangle$ is orthogonal to $|\phi_0\rangle$ and $\langle\phi_1|\phi_0\rangle = 0$. This procedure can be continued and we can construct a new states that is orthogonal to $|\phi_1\rangle$ and $|\phi_0\rangle$. This new state reads as

$$|\phi_2\rangle = \widehat{H}|\phi_1\rangle - \frac{\langle\phi_1|\widehat{H}|\phi_1\rangle}{\langle\phi_1|\phi_1\rangle}|\phi_1\rangle - \frac{\langle\phi_1|\phi_1\rangle}{\langle\phi_0|\phi_0\rangle}|\phi_0\rangle \ , \tag{D.2}$$

The procedure can be generalized. Hence, with the recursive relation

$$|\phi_{n+1}\rangle = \widehat{H}|\phi_n\rangle - a_n|\phi_n\rangle - b_n^2|\phi_{n-1}\rangle \ , \tag{D.3}$$

one can construct orthogonal basis for $n = 0, 1, 2, \ldots$. The coefficients are given by $a_n = \frac{\langle\phi_n|\widehat{H}|\phi_n\rangle}{\langle\phi_n|\phi_n\rangle}$ and $b_n^2 = \frac{\langle\phi_n|\phi_n\rangle}{\langle\phi_{n-1}|\phi_{n-1}\rangle}$. It should be noted that in the general Eq. (D.3), $b_0 = 0$ and $|\phi_{-1}\rangle = 0$. Therefore, using this new set of orthogonal states the Hamiltonian matrix of $\widehat{H}$ can be written as a tridiagonal matrix in the form of

$$\widehat{H} = \begin{vmatrix} a_0 & b_1 & 0 & 0 & \cdots \\ b_1 & a_1 & b_2 & 0 & \cdots \\ 0 & b_2 & a_2 & b_3 & \cdots \\ \vdots & \vdots & \vdots & \vdots & \end{vmatrix} . \tag{D.4}$$

This matrix can be diagonalized using standard numerical techniques. However, if one is interested in the low energy ground state properties of the interaction of Hamiltonian $\widehat{H}$, then the ground state information is obtained more rapidly after a number of iterations. The rapid convergence to the ground state can be obtained by proceeding via a 2×2 step diagonalization procedure. Instead of using the whole set of $|\phi_n\rangle$ basis, we only consider the $|\phi_0\rangle$ and $|\phi_1\rangle$. The Hamiltonian is diagonalized in the 2×2 subspace of $|\phi_0\rangle$ and $|\phi_1\rangle$. The lowest energy state is a better approximation to the actual ground state than $|\phi_0\rangle$. Therefore this new state is used as the initial state of another 2×2 iteration. The iteration is repeated as many times needed until a sufficiently high accuracy is reached.

Appendix E

Some Details of the De Almeida-Thouless Stability Condition Calculation

In this appendix we discuss the details of the derivation for the De Almeida-Thouless [22] stability condition of the replica symmetric solution under the static approximation for the generalized infinite range model with random interactions defined in Eq. (5.1). As discussed in Chapter 5, Section 5.3, in order for the mean field replica solution to be stable, the deviation of G, which is defined in Eq. (5.13), should be positive definite. As an immediate consequence, the eigenvalues of the stability matrix, of which the elements are $\partial^2 G[y]/\partial y \partial y'$, should all be real and positive. Here, y and y' denote one of the $Q^{zz}_{\alpha\beta}$, $\Lambda_{\alpha\beta}$, $\Theta_{\alpha\beta}$, $r^{zz}_{\alpha\alpha}$, $\omega_{\alpha\alpha}$, and $\theta_{\alpha\alpha}$. In the stability matrix, the derivatives are calculated with respect to the stationary values under the static approximation. Taking n as the number of replicas, then the order of the stability matrix is of $3 \times \frac{1}{2}n(n-1) + 3 \times n = \frac{3}{2}n(n+1)$.

When the free energy is variated from its saddle point, the elements of the stability matrix are associated with either $\eta^i_{\alpha\beta}\eta^j_{\mu\nu}$, $\eta^i_{\alpha\beta}\xi^j_{\mu\mu}$, and $\xi^i_{\alpha\alpha}\xi^j_{\beta\beta}$ fluctuation fields introduced in Eqs. (5.33, 5.34). Here, α, β, μ, and ν denotes different replicas, while i and j labels the specific elements of the fluctuation field arrays $\boldsymbol{\eta}_{\alpha\beta}$ and $\boldsymbol{\xi}_{\alpha\alpha}$ defined in Eqs (5.33, 5.34). Therefore, we consider three subcategories for the

matrix elements of the stability matrix:

(i) $\partial^2 G/\partial Q^i_{\alpha\beta}\partial Q^j_{\mu\nu}$ terms, which are associated with $\eta^i_{\alpha\beta}\eta^j_{\mu\nu}$ fluctuation fields. These $\partial^2 G/\partial Q^i_{\alpha\beta}\partial Q^j_{\mu\nu}$ terms can be represented as a 3×3 block matrix. Here i and j, are used to label one of the three elements of the previously defined arrays $\boldsymbol{\eta}_{\alpha\beta}$ or $\boldsymbol{Q}_{\alpha\beta}$. The value of the 3×3 matrix elements depends on the relation between α, β, μ, and ν, which has three different types such as

$$\begin{aligned}
\tilde{P}_{ij} &= \frac{\partial^2 G}{\partial Q^i_{\alpha\beta}\partial Q^j_{\alpha\beta}} && \alpha=\mu \texttt{ and } \beta=\nu,\\
\tilde{Q}_{ij} &= \frac{\partial^2 G}{\partial Q^i_{\alpha\beta}\partial Q^j_{\alpha\nu}} && \alpha=\mu \texttt{ and } \beta\neq\nu,\\
\tilde{R}_{ij} &= \frac{\partial^2 G}{\partial Q^i_{\alpha\beta}\partial Q^j_{\mu\nu}} && \alpha\neq\mu \texttt{ and } \beta\neq\nu,
\end{aligned}$$

where $Q^i_{\alpha,\beta}$ and $Q^j_{\alpha,\beta}$ are chosen among the different permutations of the three non-self-interacting fields $Q^{zz}_{\alpha\beta}, \Lambda_{\alpha\beta}$ and $\Theta_{\alpha\beta}$ of the array $\boldsymbol{Q}_{\alpha\beta}$.

(ii) In a similar way, the $\partial^2 G/\partial W^i_{\alpha\alpha}\partial W^j_{\beta\beta}$ terms are associated with the $\xi^i_{\alpha\alpha}\xi^j_{\beta\beta}$ fluctuation fields in the free energy, and represented as a 3×3 block matrix. These matrix elements have two different types of

$$\begin{aligned}
\tilde{G}_{ij} &= \frac{\partial^2 G}{\partial W^i_{\alpha\alpha}\partial W^j_{\alpha\alpha}} && \alpha=\beta\\
\tilde{E}_{ij} &= \frac{\partial^2 G}{\partial W^i_{\alpha\alpha}\partial W^j_{\beta\beta}} && \alpha\neq\beta\ ,
\end{aligned}$$

where $W^i_{\alpha\alpha}$ are the different permutations of choosing the three self-interacting fields $r^{zz}_{\alpha\alpha}$, $\omega_{\alpha\alpha}$, and $\theta_{\alpha\alpha}$ of the $\boldsymbol{R}_{\alpha\alpha}$ array.

(iii) Finally, the $\partial^2 G/\partial Q^i_{\alpha\beta}\partial W^j_{\mu\mu}$ terms associated to the $\eta^i_{\alpha\beta}\xi^j_{\mu\mu}$ fluctuating fields in the free energy, can be represented as a 3×3 matrix. The matrix elements have

two different types of

$$\begin{aligned} \tilde{C}_{ij} &= \frac{\partial^2 G}{\partial Q^i_{\alpha\beta}\partial W^j_{\alpha\alpha}} && \alpha = \mu \\ \tilde{D}_{ij} &= \frac{\partial^2 G}{\partial Q^i_{\alpha\beta}\partial W^j_{\mu\mu}} && \alpha \neq \mu \text{ and } \beta \neq \mu, \end{aligned}$$

The replica symmetric mean field solution is stable if all the eigenvalues of the stability matrix are positive definite. The eigenvectors of the stability matrix are denoted as

$$\boldsymbol{\mu} = \begin{pmatrix} \{\boldsymbol{\eta}_{\alpha\beta}\} \\ \{\boldsymbol{\xi}_{\alpha\alpha}\} \end{pmatrix} \qquad (\beta < \alpha = 1, 2, ..., n)\ . \tag{E.1}$$

For a number of n replicas, considering the column vector $\{\boldsymbol{\eta}_{\alpha\beta}\}$, there is $\frac{1}{2}n(n-1)$ number of α and β pairs, and a three component $\boldsymbol{\eta}_{\alpha\beta}$ array is assigned to each pair. For $\{\boldsymbol{\xi}_{\alpha\alpha}\}$ there is a number of n $\boldsymbol{\xi}_{\alpha\alpha}$ arrays, which each array consists of three elements. As discussed in Refs [22, 97], in order to solve the eigenvalue problem for the stability matrix in the $n \to 0$ limit three conditions must be met. These are:

1. First, we consider an eigenvector $\boldsymbol{\mu}_1$ where the elements are such that $\eta^i_{\alpha\beta} = a_i$ for all α and β and $\xi^i_{\alpha\alpha} = b_i$ for all α. In this case the eigenvalue equations become

$$\begin{aligned} \sum_{j=1}^{3} \Big\{ \big[\tilde{P}_{ij} + 2(n-2)\tilde{Q}_{ij} + \frac{1}{2}(n-2)(n-3)\tilde{R}_{ij}\big] a_j + \big[2\tilde{C}_{ij} + (n-2)\tilde{D}_{ij}\big] b_j \Big\} \\ = \lambda a_i \\ \sum_{j=1}^{3} \Big\{ \big[(n-1)\tilde{C}_{ij} + \frac{1}{2}(n-1)(n-2)\tilde{D}_{ij}\big] a_j + \big[\tilde{G}_{ij} + (n-1)\tilde{E}_{ij}\big] b_j \Big\} \\ = \lambda b_i \end{aligned} \tag{E.2}$$

In the $n \to 0$ limit Eq. (E.2) can be solved by calculating the eigenvalues of the 9×9 matrix

$$\mathbf{A} = \begin{pmatrix} \tilde{\boldsymbol{P}} - 4\tilde{\boldsymbol{Q}} + 3\tilde{\boldsymbol{R}} & 2(\tilde{\boldsymbol{C}} - \tilde{\boldsymbol{D}}) \\ -\tilde{\boldsymbol{C}} + \tilde{\boldsymbol{D}} & \tilde{\boldsymbol{G}} - \tilde{\boldsymbol{E}} \end{pmatrix} \tag{E.3}$$

2. The other eigenvector which can be considered is $\boldsymbol{\mu}_2$, where $\eta^i_{\alpha\beta} = a_i$ if α or $\beta = \phi$, $\eta^i_{\alpha\beta} = b_i$ for α, $\beta \neq \phi$, $\xi^i_{\alpha\alpha} = c_i$ for $\alpha = \phi$ and $\xi^i_{\alpha\alpha} = d_i$ for $\alpha \neq \phi$. The eigenvector $\boldsymbol{\mu}_2$ should be orthogonal to $\boldsymbol{\mu}_1$. Therefore $a_i = -\frac{1}{2}(n-2)b_i$ and $c_i = -(n-1)d_i$. The eigenvalue equations in this case are

$$\begin{aligned} \sum_{j=1}^{3} \Big\{ \big[\tilde{P}_{ij} + (n-4)\tilde{Q}_{ij} - (n-3)\tilde{R}_{ij}\big] a_j + \big\{(n-2)/(n-1)\big\} \big[\tilde{C}_{ij} - \tilde{D}_{ij}\big] c_j \Big\} \\ = \lambda a_i \\ \sum_{j=1}^{3} \Big\{ (n-1)\big[\tilde{C}_{ij} - \tilde{D}_{ij}\big] a_j + \big[\tilde{G}_{ij} - \tilde{E}_{ij}\big] c_j \Big\} \\ = \lambda c_i \ , \end{aligned} \tag{E.4}$$

which in the $n \to 0$ limit Eq. (E.4) leads to the determination of the eigenvalues of a 9×9 matrix exactly identical to matrix $\mathbf{A}$ in Eq. (E.3).

3. Finally the last eigenvector set which can be considered is $\boldsymbol{\mu}_3$, where $\eta^i_{\alpha\beta} = a_i$ for $\alpha = \phi$ and $\beta = \psi$, $\eta^i_{\alpha\beta} = b_i$ for $\alpha = \phi, \psi$ and $\beta \neq \phi, \psi$, $\eta^i_{\alpha\beta} = c_i$ for $\alpha, \beta \neq \phi, \psi$, $\xi^i_{\alpha\alpha} = d_i$ for $\alpha = \phi, \psi$, and $\xi^i_{\alpha\alpha} = e_i$ for $\alpha \neq \phi, \psi$. The orthogonality of $\boldsymbol{\mu}_3$ with $\boldsymbol{\mu}_1$ and $\boldsymbol{\mu}_2$ indicates that $d_i = e_i = 0$, while $a_i = -(n-2)b_i$ and $c_i = -\frac{1}{2}(n-3)b_i$. In the $n \to 0$ limit, the eigenvalues of the instability matrix are the eigenvalues of the 3×3 matrix

$$\mathbf{M} = \tilde{\boldsymbol{P}} - 2\tilde{\boldsymbol{Q}} + \tilde{\boldsymbol{R}} \ . \tag{E.5}$$

It can be numerically shown that for the case of eigenvectors $\boldsymbol{\mu}_1$ and $\boldsymbol{\mu}_2$, the eigenvalues of matrix $\boldsymbol{A}$ in Eq. (E.3) are always positive definite. Therefore to check the positivity of the eigenvalues of the stability matrix we should check the positivity of the eigenvalues of matrix $\mathbf{M}$ in Eq. (E.5).

Bibliography

[1] D. Bitko, T. F. Rosenbaum, and G. Aeppli, Phys. Rev. Lett. **77**, 940 (1996).

[2] P. G. de Gennes, Solid State Commun. **1**, 132 (1963).

[3] R. J. Elliott, P. Pfeuty, and C. Wood, Phys. Rev. Lett. **25**, 443 (1970).

[4] S. Sachdev, *Quantum Phase Transitions*, Cambridge University Press, Cambridge, 1999.

[5] B. K. Chakrabarti, A. Dutta, and P. Sen, *Quantum Ising Phases and Transitions in Transverse Ising Models*, Spinger-Verlag, Heidelberg, 1996.

[6] P. Stasiak and M. J. P. Gingras, *unpublished*.

[7] D. H. Reich, B. Ellman, J. Yang, T. F. Rosenbaum, G. Aeppli, D. P. Belanger Phys. Rev. B **42**, 4631 (1990).

[8] S. Ghosh, T. F. Rosenbaum, G. Aeppli, and S. N. Coppersmith, Nature **425**, 48 (2003).

[9] P. E. Jönsson, R. Mathieu, W. Wernsdorfer, A. M. Tkachuk, and B. Barbara, Phys. Rev. Lett. **98**, 256403 (2007).

[10] S. L. Sondhi, S. M. Girvin, J. P. Carini, and D. Shahar, Rev. Mod. Phys. **69**, 315 (1997).

[11] M. Suzuki, Prog. Theor. Phys. **46**, 1337 (1971).

[12] K. Binder and A. P. Young, Rev. Mod. Phys. **58**, 801 (1986).

[13] H. G. Ballesteros, A. Cruz, L. A. Fernández,V. Martín-Mayor, J. Pech, J. J. Ruiz-Lorenzo, A. Tarancón, P. Téllez, C. L. Ullod,and C. Ungil, Phys. Rev. B **62**, 14237 (2000).

[14] M. A. Ruderman and C. Kittel, Phys. Rev. **96**, 99 (1954).

[15] T. Kasuya, Prog. Theor. Phys. **16**, 45 (1956).

[16] K. Yosida, Phys. Rev. **106**, 893 (1957).

[17] V. Cannella and J. A. Mydosh, Phys. Rev. B **6**, 4220 (1972).

[18] S. Nagata, P. H. Keesom, and H. R. Harrison, Phys. Rev. B **19**, 1633 (1979).

[19] H. Maletta and W. Felsch, Phys. Rev. B **20**, 1245 (1979).

[20] S. Edwards and P. W. Anderson, J. Phys. F **5**, 965 (1975).

[21] D. Sherrington and S. Kirkpatrick, Phys. Rev. Lett. **35**, 1792 (1975).

[22] J. R. L. de Almeida and D. J. Thouless, J. Phys. A **11**, 983 (1978).

[23] G. Parisi, Phys. Rev. Lett. **43**, 1754 (1979).

[24] M. Schechter and N. Laflorencie, Phys. Rev. Lett. **97**, 137204 (2006).

[25] M. Schechter, P. Stamp, and N. Laflorencie, J. Phys.: Condens. Matter **19**, 145218 (2007).

[26] W. L. McMillan, J. Phys. C **17**, 3179 (1984).

[27] A. J. Bray and M. A. Moore, *Heidelberg Colloquium on Glassy Dynamics*, volume 275, Springer, Berlin, 1986.

[28] D. S. Fisher and D. A. Huse, Phys. Rev. Lett. **56**, 1601 (1986).

[29] D. S. Fisher and D. A. Huse, Phys. Rev. B **38**, 373 (1988).

[30] D. S. Fisher and D. A. Huse, Phys. Rev. B **38**, 386 (1988).

[31] J. Chalupa, Solid State Commun **22**, 315 (2007).

[32] B. K. Chakrabarti, Phys. Rev. B **24**, 4062 (1981).

[33] P. Ray, B. K. Chakrabarti, and A. Chakrabarti, Phys. Rev. B **39**, 11828 (1989).

[34] M. Guo, R. N. Bhatt, and D. A. Huse, Phys. Rev. Lett. **72**, 4137 (1994).

[35] D. S. Fisher, Phys. Rev. B **50**, 3799 (1994).

[36] W. Wu, B. Ellman, T. F. Rosenbaum, G. Aeppli, and D. H. Reich, Phys. Rev. Lett. **67**, 2076 (1991).

[37] R. N. Bhatt, Quantum spin glasses, in *Spin Glasses and Random Fields*, edited by A. P. Young, World Scientific, Singapore, 1998.

[38] A. J. Bray and M. A. Moore, J. Phys. C **13**, L655 (1980).

[39] R. B. Griffiths, Phys. Rev. Lett. **23**, 17 (1969).

[40] B. M. McCoy, Phys. Rev. Lett. **23**, 383 (1969).

[41] T. Vojta, Journal of Physics A: Mathematical and General **39**, R143 (2006).

[42] D. S. Fisher, Phys. Rev. Lett. **69**, 534 (1992).

[43] H. Rieger and A. P. Young, Phys. Rev. Lett. **72**, 4141 (1994).

[44] H. Rieger and A. P. Young, Phys. Rev. B **54**, 3328 (1996).

[45] M. Guo, R. N. Bhatt, and D. A. Huse, Phys. Rev. B **54**, 3336 (1996).

[46] Y. Imry and S.-K. Ma, Phys. Rev. Lett. **35**, 1399 (1975).

[47] G. T. P. Lacour-Gayet, J. Physique **35**, 425 (1974).

[48] G. Grinstein, Phys. Rev. Lett. **37**, 944 (1976).

[49] A. Aharony, Y. Imry, and S.-K. Ma, Phys. Rev. Lett. **37**, 1364 (1976).

[50] J. Villain, J. Physique **43**, L551 (1982).

[51] A. A. S. Fishman, J. Phys. C **12**, L729 (1979).

[52] J. L. Cardy, Phys. Rev. B **29**, 505 (1984).

[53] R. Nattermann, Theory of the random field ising model, in *Spin Glasses and Random Fields*, edited by A. P. Young, World Scientific, Singapore, 1998.

[54] P. E. Hansen, T. Johansson, and R. Nevald, Phys. Rev. B **12**, 5315 (1975).

[55] A. Chin and P. R. Eastham, cond-mat/0610544.

[56] S. M. A. Tabei, F. Vernay, and M. J. P. Gingras, Phys. Rev. B **77**, 014432 (2008).

[57] P. B. Chakraborty, P. Henelius, H. Kjønsberg, A. W. Sandvik, and S. M. Girvin, Phys. Rev. B **70**, 144411 (2004).

[58] D. M. Silevitch, D. Bitko, J. Brooke, S. Ghosh, G. Aeppli, and T. F. Rosenbaum, Nature **448**, 567 (2007).

[59] T. F. Rosenbaum, Journal of Physics: Condensed Matter **8**, 9759 (1996).

[60] K. Kjaeri, J. Als-Nielsen, I. Laursen, and F. K. Larsen, J. Phys.: Condens. Matter **1**, 5743 (1989).

[61] W. Wu, D. Bitko, T. F. Rosenbaum, and G. Aeppli, Phys. Rev. Lett. **71**, 1919 (1993).

[62] J. Snyder and C. C. Yu, Phys. Rev. B **72**, 214203 (2005).

[63] A. Biltmo and P. Henelius, Phys. Rev. B **76**, 054423 (2007).

[64] A. Biltmo and P. Henelius, arxiv:0803.0851.

[65] P. E. Jönsson, R. Mathieu, W. Wernsdorfer, A. M. Tkachuk, and B. Barbara, arxiv:0803.1357.

[66] C. Ancona-Torres, D. M. Silevitch, G. Aeppli, and T. F. Rosenbaum, Phys. Rev. Lett. **101**, 057201 (2008).

[67] S. Ghosh, R. Parthasarathy, T. F. Rosenbaum, and G. Aeppli, Science **296**, 2195 (2002).

[68] J. A. Mydosh, *Spin Glasses: an Experimental Introduction*, Taylor & Francis, London, 1993.

[69] M. J. Stephen and A. Aharony, J. Phys. C **14**, 1665 (1981).

[70] J. Brooke, Ph.D. thesis, U. of Chicago, 2000.

[71] W. Wu, Ph.D. thesis, U. of Chicago, 1992.

[72] S. M. A. Tabei, M. J. P. Gingras, Y.-J. Kao, P. Stasiak, and J.-Y. Fortin, Phys. Rev. Lett. **97**, 237203 (2006).

[73] Z. Fisk, Nature **48**, 546 (2007).

[74] A. W. Sandvik and J. Kurkijärvi, Phys. Rev. B **43**, 5950 (1991).

[75] M. Schechter and P. C. E. Stamp, Phys. Rev. Lett. **95**, 267208 (2005).

[76] G. Mennenga, L. J. de Jongh, and W. J. Huiskamp, J. Magn. Magn. Matter **44**, 59 (1984).

[77] P. Beauvillain, J. P. Renard, I. Laursen, and P. J. Walker, Phys. Rev. B **18**, 3360 (1978).

[78] H. M. Rønnow, J. Jensen, R. Parthasarathy, G. Aeppli, T. F. Rosenbaum, D. F. McMorrow, and C. Kraemer, Phys. Rev. B **75**, 054426 (2007).

[79] G. S. Shakurov, M. V. Vanyunin, B. Z. Malkin, B. Barbara, R. Yu. Abdulsabirov, and S. L. Korableva Appl. Magn. Reson. **28**, 251 (2005).

[80] J. Magarino, J. Tuchendler, P. Beauvillain, and I. Laursen, Phys. Rev. B **21**, 18 (1980).

[81] M. T. Hutchings, Solid State Phys. **16**, 227 (1964).

[82] K. Hecht, *Quantum Mechanics*, Springer-Verlag, New York, 2000.

[83] K. W. H. Stevens, Proc. Phys. Soc. A **65**, 209 (1952).

[84] L. M. Holmes, J. Als-Nielsen, and H. J. Guggenheim, Phys. Rev. B **12**, 180 (1975).

[85] D. J. Klein, J. Chem. Phys. **61**, 786 (1974).

[86] A. L. Chernyshev, D. Galanakis, P. Phillips, A. V. Rozhkov, and A.-M. S. Tremblay, Phys. Rev. B **70**, 235111 (2004).

[87] A. H. MacDonald, S. M. Girvin, and D. Yoshioka, Phys. Rev. B **37**, 9753 (1988).

[88] J.-Y. P. Delannoy, M. J. P. Gingras, P. C. W. Holdsworth, and A.-M. S. Tremblay, Phys. Rev. B **72**, 115114 (2005).

[89] M. Schechter, Phys. Rev. B **77**, 020401(R) (2008).

[90] H. M. Rønnow, R. Parthasarathy, J. Jensen, G. Aeppli, T. F. Rosenbaum, and D. F. McMorrow, Science **308**, 389 (2005).

[91] A. P. Ramirez and J. Jensen, J. Phys.: Condens. Matter **6**, L215 (1994).

[92] S. T. Bramwell et al., Phys. Rev. Lett. **87**, 047205 (2001).

[93] M. Schechter and P. C. E. Stamp, Phys. Rev. Lett. **95**, 267208 (2005).

[94] M. Schechter and P. C. E. Stamp, arxiv:0801.2889v2.

[95] A. P. Young and H. G. Katzgraber, Phys. Rev. Lett. **93**, 207203 (2004).

[96] H. R. Molavian, M. J. P. Gingras, and B. Canals, Phys. Rev. Lett. **98**, 157204 (2007).

[97] D.-H. Kim and J.-J. Kim, Phys. Rev. B **66**, 054432 (2002).

[98] T. K. Kopec, R. Pirc, B. Tadic, and R. Blinc, Z. Phys B **78**, 493 (1990).

[99] R. Pirc, B. Tadić, and R. Blinc, Phys. Rev. B **36**, 8607 (1987).

[100] Y. V. Federov and E. F. Shender, JETP Lett **43**, 681 (1986).

[101] A. Georges, O. Parcollet, and S. Sachdev, Phys. Rev. B **63**, 134406 (2001).

[102] D. R. Grempel and M. J. Rozenberg, Phys. Rev. Lett. **80**, 389 (1998).

[103] A. W. Sandvik and J. Kurkijärvi, Phys. Rev. B **43**, 5950 (1991).

[104] A. W. Sandvik, Phys. Rev. E **68**, 056701 (2003).

[105] J. M. Luttinger and L. Tisza, Phys. Rev. **70**, 954 (1946).

[106] L. N. Kantorovich and I. I. Tupitsyn, J. Phys.: Condens. Matter **11**, 6159 (1999).

[107] R. B. Griffiths, Phys. Rev. **176**, 655 (1968).

[108] J. A. Barker and R. O. Watts, Mol. Phys. **26**, 789 (1973).

[109] J. M. Ziman, *Principles of the Theory of Solids*, Cambridge Univ. Press, Cambridge, ed. 2, 1972.

[110] M. Born and S. Huang, *Dynamical Theory of Crystal Lattices*, Oxford Univ. Press, New York, 1968.

[111] S. W. de Leeuw, J. W. Perram, and E. R. Smith, Ann. Rev. Phys. Chem. **37**, 245 (1986).

[112] R. G. Melko and M. J. P. Gingras, J. Phys.: Condens. Matter **16**, R1277 (2004).

[113] J. Jensen and A. R. Mackintosh, *Rare Earth Magnetism*, Oxford Univ. Press, Oxford, 1991.

[114] R. J. Creswick, H. A. Farach, J. M. Knight, and C. P. Poole, Phys. Rev. B **38**, 4712 (1988).

[115] M. L. Bellac, *Quantum and Statistical Field Theory*, Oxford Univ. Press, New York, 1992.

[116] M. Suzuki, *Quantum Monte Carlo Methods*, Springer-Verlag, Heidelberg, 1987.

[117] H. Rieger and N. Kawashima, Eur. Phys. J. B **9**, 233 (1999).

[118] A. H. Cooke, D. A. Jones, J. F. A. Silva, and M. R. Wells, J. Phys. C: Sol. St. Phys. **8**, 4083 (1975).

[119] J. E. Battison, A. Kasten, M. J. M. Leask, J. B. Lowry, and B. M. Wanklyn, J. Phys. C: Sol. St. Phys. **77**, 4089 (1975).

[120] J. D. Jackson, *Classical Electrodynamics*, Wiley, New York, 1998.

[121] H.-J. Xu, B. Bergesen, and Z. Racz, J. Phys.: Condens. Matter **64**, 214420 (1992).

[122] I. I. Tupizin and I. V. Abarenkov, Phys. Status Solidi B **82**, 99 (1977).

[123] K. Binder, Z. Phys. B **43**, 119 (1981).

[124] A. I. Larkin and D. Khmel'nitskii, Soviet Physics JETP **29**, 1123 (1969).

[125] J.-Y. Fortin and M. J. P. Gingras, *unpublished* .

[126] S. Bertaina, B. Barbara, R. Giraud, B. Z. Malkin, M. V. Vanuynin, A. I. Pominov, A. L. Stolov, and A. M. Tkachuk, Phys. Rev. B **74**, 184421 (2006).

[127] H. F. Trotter, Proc. Am. Math. Soc. **10**, 545 (1950).

[128] C. Lanczos, J. Res. Natn. Bur. Stand. **45**, 255 (1950).

[129] J. T. Edwards, D. C. Licciardello, and D. J. Thouless, IMA J Appl Math **23**, 277 (1979).